IMPERIAL COLLEGE LONDON
Department of Materials
London Centre for Nanotechnology

Magnetic and structural properties of molecular films, blends and nanostructures based on cobalt phthalocyanines

Thesis submitted for the degree of
DOCTOR OF PHILOSOPHY

Michele Serri

Abstract

Organic semiconductors are a class of materials based on conjugated molecules which has been the subject of intensive research in the past two decades for applications in organic light-emitting diodes (OLEDs), organic thin film transistors (OTFT), photovoltaic cells, sensors and optical amplifiers/lasers. These molecular materials have recently become of interest for spintronic applications, since long spin relaxation times and magnetoresistance have been experimentally measured in these systems. The properties of organic materials can be easily manipulated and combined in novel ways, while their molecular nature paves the way for devices that operate at a single molecule/single spin level and really approach the ultimate limit of the atomic scale.

In order to exploit the full potential of organic spintronics, it is essential to increase the temperatures at which the spin effects can be observed. This thesis is concerned with the development of novel organic magnetic materials, which could be of interest for spintronic devices operating above cryogenic temperatures. The work focuses on organic thin films and other nanostructures containing cobalt phthalocyanine and its derivatives. It is shown that some forms of these compounds, in particular α-CoPc, exhibit antiferromagnetic spin correlations above the boiling point of liquid nitrogen (77 K), suggesting that phthalocyanine materials may be suitable for high temperature organic spintronic applications.

Declaration of Authorship

This thesis is the result of my own work and includes nothing which is the outcome of work done in collaboration except where specifically indicated in the text.

Michele Serri

Date: 30 November 2013

Copyright

The copyright of this thesis rests with the author and is made available under a Creative Commons Attribution Non-Commercial No Derivatives licence. Researchers are free to copy, distribute or transmit the thesis on the condition that they attribute it, that they do not use it for commercial purposes and that they do not alter, transform or build upon it. For any reuse or redistribution, researchers must make clear to others the licence terms of this work

Publications

The following publication is directly related to the work presented in this thesis:

M. Serri, W. Wu, L.R. Fleet, N.M. Harrison, C.F. Hirjibehedin, C.W.M. Kay, A.J. Fisher, G. Aeppli and S. Heutz **"High-temperature antiferromagnetism in molecular semiconductor thin films and nanostructures"**. *Nat. Commun.* 5:3079 doi: 10.1038/ncomms4079 (2014)

Which has the abstract: *The viability of dilute magnetic semiconductors in applications is linked to the strength of the magnetic couplings, and room temperature operation is still elusive in standard inorganic systems. Molecular semiconductors are emerging as an alternative due to their long spin-relaxation times and ease of processing, but, with the notable exception of vanadium-tetracyanoethylene, magnetic transition temperatures remain well below the boiling point of liquid nitrogen. Here we show that thin films and powders of the molecular semiconductor cobalt phthalocyanine exhibit strong antiferromagnetic coupling, with an exchange energy reaching 100 K. This interaction is up to two orders of magnitude larger than in related phthalocyanines and can be obtained on flexible plastic substrates, under conditions compatible with routine organic electronic device fabrication. Ab initio calculations show that coupling is achieved via superexchange between the singly occupied a_{1g} (d_{z^2}) orbitals. By reaching the key milestone of magnetic coupling above 77 K, these results establish quantum spin chains as a potentially useable feature of molecular films.*

Acknowledgements

I would like to express my gratitude to my supervisor, Dr Sandrine Heutz for all the invaluable advice, patience and support along my PhD. I would also like to extend my thanks to Prof Andrew Fisher, Prof Nicholas Harrison and Dr Wei Wu for the calculations of the exchange interactions in cobalt phthalocyanine and for patiently discussing with me about the theoretical issues related to my work. I am very grateful to the scientists in the London Centre for Nanotechnology (LCN) who have been very helpful, especially Prof Gabriel Aeppli, Prof Cyrus Hirjibehedin, Prof Chris Kay with whom I had many inspiring discussions about experimental results. I am indebted to Richard Sweeney, Dr Mahmoud Ardakani, Prof Mark Ellerby, Dr Richard Thorogate, Dr Robert Palgrave, Benjamin Chan and Dr Marc Warner for the assistance with using the experimental equipment and analysing data. I would like to thank the Engineering and Physical Sciences Research Council of the United Kingdom for providing funding for my research and the attendance to conferences. Special thanks go to all my colleagues in the Heutz group, Din, Zhenlin, Leo, Soumaya, Solveig, Junwei, Luke, Hsiang-Han, Jimmy, Alex, Jasvir, Sharon and Peter, the members of the Natalie Stingelin's group, and the many other friends in the department for making my PhD so enjoyable. Finally I would like to thank my parents for the encouragement and the exceptional support during my staying in London.

Contents

1 Introduction **31**

1.1 Organic Spintronics 31

1.1.1 Spintronics 31

1.1.2 Organic Spintronics 32

1.1.3 Spin diffusion in organic semiconductors 33

1.1.4 Challenges and current understanding of organic spintronics 34

1.1.5 All-organic spintronics devices 36

1.2 Molecule based magnets 37

1.2.1 Magnetism 38

1.2.2 Spin Hamiltonian 42

1.2.3 Dimensionality of the spin 46

1.2.4 Dimensionality of the magnetic lattice 46

1.2.5 Spin coupling mechanisms 47

1.3 Phthalocyanine and metal phthalocyanines 48

1.3.1 Fluorinated phthalocyanines 55

1.3.2 Magnetic ordering in metal phthalocyanines 57

1.3.3 Cobalt phthalocyanine 58

1.4 Thesis layout 60

2 Experimental methods **62**

2.1 Purification of materials 62

2.2 Growth of organic nanostructures 63

2.2.1 OMBD growth of thin films 63

2.2.2 OVPD growth of nanowires 65

2.2.3 Preparation of nanopowders (acid paste) 66

2.3 Characterization of the organic nanostructures 67

2.3.1 Scanning electron microscope 68

2.3.2 X-ray diffraction 69

2.3.3 UV-Visible absorption spectroscopy 73

2.3.4 X-ray photoelectron spectroscopy 76

2.3.5 Inductively Coupled Plasma Atomic Emission Spectroscopy (ICP-AES) 77

2.3.6 Electron Paramagnetic Resonance 78

2.3.7 Superconducting Quantum Interference Device (SQUID) magnetometry 79

2.4 Calculation of the magnetic properties of antiferromangetic chains . 86

3 Cobalt phthalocyanine (CoPc) powders and thin films **89**

3.1 Determination of the purity of CoPc 89

3.2 Characterization of α- and β-CoPc materials 92

3.2.1 Identification of the polymorph type 92

3.2.2 UV-Visible spectroscopy of CoPc materials 96

3.2.3 Investigation of the morphology 98

3.2.4 Analysis of the crystalline coherence length 102

3.3 Magnetism of α- and β-CoPc 105

3.3.1 Electron paramagnetic resonance of CoPc powders 105

3.3.2 SQUID magnetometry of CoPc samples 111

4 Cobalt phthalocyanine (CoPc) nanowires **125**

4.1 Identification of the nanowire phase 126

4.2 Magnetic properties of CoPc nanowires 134

4.3 Discussion and conclusions 136

5 Hexadecafluoro cobalt phthalocyanine (F_{16}CoPc) **140**

5.1 Introduction 141

5.2 Morphology of F_{16}CoPc films 142

5.3 UV-Vis spectroscopy of films on glass 146

5.4 X-ray diffraction of the F_{16}CoPc films 148

5.5 Magnetic characterization of F_{16}CoPc films on kapton 154

6 Co-deposited CoPc:F_{16}CoPc films **160**

6.1 Morphology of the films 160

6.2 X-ray diffraction measurements of the films 162

6.3 UV-Visible spectroscopy 166

6.4 X-ray Photoelectron Spectroscopy 169

6.5 Magnetic characterization of the films 174

7 Conclusions **185**

A CoPc powders and films **208**

A.1 Main ICP-AES lines of atomic emission spectra of Co and potential contaminants 208

A.2 Finite chain fits of the magnetic properties of α-CoPc 209

List of Figures

1.1 Plot of inverse susceptibility in paramagnetic, antiferromagnetic and ferromagnetic materials. For the antiferromagnetic case, the trend at low temperature is extrapolated, as the experimental data deviates from linearity below the Néel temperature T_N. The Weiss temperatures are shown. The slope is inversely proportional to the effective magnetic moment squared 41

1.2 Magnetization curve of a paramagnet (blue line) and of a ferromagnet (red line) below the Curie temperature T_C. The definitions of coercive field (H_C), magnetization at saturation (M_S) and remnant magnetization (M_R) are shown. 42

1.3 Chemical structure of metal free phthalocyanine H_2Pc (a) and of metal phthalocyanine MPc (b) 50

1.4 Definition of the geometrical parameters describing the arrangement of phthalocyanine molecules stacked in a column (a). Possible mutual arrangements of the columns in a crystal: (b) brick-stack and (c) herringbone arrangement. For the herringbone structure, the unit cell is doubled. 50

1.5 Possible molecular displacement directions inside the phthalocyanine columns: at 45° with the directions defined by the four lobes of the molecule (a); along the direction of the lobes (b) 51

1.6 Crystal structure of β-CuPc, as determined by Brown [19]: a) is a representation of the crystal lattice, b) a schematics of the unit cell occupation by the phthalocyanine, c) is a projection of the stacking geometry on the plane of the molecules 52

1.7 Crystal structure of α-CuPc, as determined by Hoshino [43]: a) is a representation of the crystal lattice, b) a schematics of the unit cell occupation by the phthalocyanine, c) is a projection of the stacking geometry on the plane of the molecules 53

1.8 Absorption spectrum of a 20 nm copper phthalocyanine (CuPc) film deposited on glass 54

1.9 Splitting of the d levels of transition metals in ligand fields of cubic and tetragonal symmetry. The z axis is defined by the C_4 symmetry axis of the molecule 55

1.10 Canted ferromagnet with ordered (opposed) spins. Individual spins are represented by black arrows; the rows of spins represent spin chains coupled ferromagnetically. The resultant magnetization of the material is shown by the red arrow. The two possible orientations of the magnetization can be determined by an external magnetic field, or by the inter-chain magnetic coupling 57

2.1 Schematics of the OMBD chamber. QCM are quartz-crystal microbalances used to monitor the growth rate; the substrate shutter is opened only when the sublimation rate stabilizes at the desired value, and is closed again when the desired thickness is achieved. . . 64

2.2 Schematics of the OVPD system used for the growth of CoPc nanowires. The steady-state temperature profile was measured by Zhenlin Wu [104] 65
2.3 Differences in diffraction patterns of acid paste α-CoPc powders precipitated in isopropanol and water. The conditions of re-precipitation control the average grain size in the powder. A simulated α-CoPc pattern with a peak FWHM=0.424° is also shown 68
2.4 Schematics of the X-ray diffractometer in a Bragg-Brentano configuration 71
2.5 Left: energy diagram of an electronic transition in an isolated molecule and in a solid. The ground and excited levels can be modified by dispersion interactions in the solid state. The intermolecular interaction of the chromophores in the solid leads to a splitting of the excited state into, at least, two excitonic levels, with different oscillator strengths, f_1 and f_2. Right: the oscillator strengths of the excitonic transitions are shown in the case of a sideways (H aggregate) and a head to tail (J aggregate) alignment of the molecular transition dipoles. 74
2.6 Schematics of the MPMS-7 Quantum Design system. From [24] . . 80
2.7 Schematics of the second order gradiometer in a SQUID magnetometer 81
2.8 Mounting on a plastic straw of a capsule filled with CoPc powder for SQUID measurement 83
2.9 Organic film sample for SQUID characterization. The sample is shown rolled inside the sample straw (bottom) 84
2.10 $M(H)$ curves for chains of 13 and 14 spins with $g = 2$ and $J/k_B = 80K$, calculated with the Bonner Fisher method. The curve of the 14 spins chain has been scaled by a factor of 10^6. 87

2.11 $\chi(T)$ curves for chains of length N, with $g = 2$ and $J/k_B = 80K$, calculated with the Bonner Fisher method. The infinite chain susceptibility was calculated with the Johnston formula [48]. For the definition of $\chi(T)$ and its units refer to Equation 2.12 88

3.1 Results of the calibration procedure of the ICP analysis. The photon counts per second for the different elements (wavelengths) analysed are shown as a function of the concentration of the standard solution and fitted to a straight line 91

3.2 X-ray diffraction patterns of the four CoPc sample typologies investigated. The stick pattern of the α (red) and β-CoPc (black) shown were calculated using the structures published by Ballirano *et al.* [6] 95

3.3 Structure of perylene-3,4,9,10-tetracarboxylic dianhydride (PTCDA), used in this work for templating the texture of phthalocyanine films 96

3.4 XRD scans of CoPc films grown on glass (left) and kapton film (right). The stick pattern at the bottom refers to the peaks of the α-CoPc structure 97

3.5 UV-Visibile absorption spectra of CoPc in solution and in α and β-CoPc solid samples (powders and films). The solution is $2.61\,\mathrm{mg\,l^{-1}}$ in 1-Chloronaphthalene:Pyridine (5:1). The spectrum of the α-CoPc powder was measured on a film obtained by drying a drop-casted suspension of the α-CoPc acid paste powder in hexane. The α-CoPc film was evaporated on bare glass or onto a 20 nm PTCDA layer (dashed (solid) line shows spectrum before (after) subtraction of PTCDA absorption). The β-CoPc film is the product of the annealing of an α-CoPc film deposited on glass. 98

3.6 Scanning electron microscope image (a) of particles found in CoPc powder re-precipitated with the acid paste method. (b) shows the distribution of particle sizes in a group of 28 particles 99

3.7 Top view scanning electron microscope images of a 200nm CoPc non templated (a) and templated (c) films with their relative cross-sections (b) and (d) 100

3.8 Statistics on the apparent size of randomly chosen grains visible in the SEM images of a 200 nm CoPc templated film. Figure (a) represents a group of 91 grains in the top view image 3.7c, while (b) refers to 89 grains in the cross section image 3.7d 100

3.9 Atomic force microscope topography images of a 200nm CoPc non-templated (a) and templated (c) films on kapton with their relative phase images (b) and (d) 101

3.10 SEM images (50kX magnification in (a) and 200kX in (b)) of a β-CoPc film obtained by annealing of a 200 nm film on glass 101

3.11 Bright field optical microscope transmission image (20x magnification) of a β-CoPc film on glass (a) The contrast highlights domains of different thickness. Same area observed with a 90° angle between the polariser and the analyser (b). The contrast highlights domains with different orientation 102

3.12 HRTEM image of a 50 nm CoPc film grown on a Cu grid with carbon film. The spacing between the fringes is 12.1 Å, in agreement with the 100 plane distance. Based on this observation, the a* direction of the reciprocal lattice is drawn perpendicular to the fringes, while the b direction of the unit cell lies along them. The regions highlighted by dashed lines contain grain boundaries with seemingly shorter fringes and possibly a higher concentration of structural defects. TEM image courtesy of Dr Luke Fleet 104

3.13 EPR spectrum (9.40 GHz) of α-CoPc acid paste powder at room temperature. The spectrum is composed of a broad component and a fine structure, which have been deconvoluted using a low pass and a high pass filter. The simulation of the spectrum of α-CoPc based on the parameters by Assour[3] (Table 3.3) was performed with Easyspin and is shown for reference 107

3.14 Temperature dependence of the EPR spectrum (9.40 GHz) of α-CoPc (a) and β-CoPc (b) powders. Simulations of the spectra using the spin paramenters by Assour (Table 3.3) were calculated using Easyspin and are shown here for reference 109

3.15 (a) Magnetic moment per Co atom as a function of field at 2 K in β-CoPc powder (black triangles, scaled by a factor of 0.1), α-CoPc powder (black circles), α-CoPc 200 nm film (red squares) and α-CoPc 200 nm/PTCDA 20 nm film (green diamonds). The black solid line represents the fit of the β-CoPc data with the Bonner Fisher model of a Heisenberg spin chain (S=1/2, g_z=1.9 $g_{x,y}$=2.9, J =1.86 K, average of two spin chains with 13 and 14 spins) (b) H/T scaling in α-CoPc powder (circles), 200 nm film (squares) and 200 nm film on 20 nm PTCDA (diamonds) after subtraction of field independent susceptibility χ_0^{MH} (values in Table 3.5). Colours indicate the temperature of the measurement: 2 K (black), 4 K (red), 6 K (green), 8 K (purple), 10 K (magenta), 15 K (cyan). Red lines are fit using the Brillouin function and g values in Table 3.4 113

3.16 (a) Magnetic susceptibility $\chi(T)$ of CoPc as a function of temperature: α-CoPc ($\circ$) and β-CoPc powders ($\triangle$); the main plot shows detail of the high temperature susceptibility, while the inset includes the full data range. The red line is a fit of $\chi(T)$ in α-CoPc powder with a model based on the Johnston antiferromagnetic chain formula and a Curie correction (Equation 3.3) to include finite size effects. The black line is the Curie Weiss fit of β-CoPc powder (8 K–310 K). $\chi(T)$ is calculated (Equation 2.13) as the incremental ratio of $M(T)$ between fields of 500 Oe and 1000 Oe; for an explanation of units refer to section 2.3.7 and Equation 2.12. Inset: Plot of the reciprocal of $\chi(T)$. Dashed black line is the linear fit of α-CoPc powder at low temperature. Solid lines represent the fits shown in the main figure. (b). Susceptibility of α-CoPc films and powders; the $\chi(T)$ values in the films are calculated from $M(T)$ measurements at 5000 Oe and 10 kOe (Equation 2.13). Solid lines are fits using Equation 3.3. Inset: preferential orientation of CoPc molecule in templated and non-templated films 115

3.17 (a) definition of the stacking (ϕ) and sliding (ψ) angles in CoPc chains. (b) contour plot of the calculated exchange energy as a function of the stacking and sliding angles in CoPc crystals. Note that the height scale is linear from -3K to 3K, and logarithmic thereafter. Contour lines are drawn at 0 K, 10 K, 50 K, and then for every 100 K increment from 100 K to 400 K. The points corresponding to the α, β and η CoPc structures have been highlighted with a square, a triangle and a circle respectively. The structure of η-CoPc is assumed to be identical to that of η-CuPc nanowires [95]; this assumption could be incorrect, as discussed in Chapter 4 118

3.18 Example of a spin chain length distribution in CoPc materials reflecting a bimodal character, as defined in Equation 3.4. In this example 60 % of the CoPc molecules are part of the grain boundaries (group A), having an average length of 3.5 molecules, while the remaining 40 % belong to the core of the grains (group B) and have an average length of 12.5 molecules. 120

3.19 Results of the fit of the α-CoPc powder susceptibility using the finite chain model (Equation 3.5). Residuals and values of the fitted parameters are shown in the color map for all combinations of chain lengths. (a) Weighted root mean square error of the fit; (b) values of the exchange energy J/k_B; (c) values of the temperature independent correction χ_0; (d) fraction f of paramagnetic spins . . 122

3.20 Characteristic fits of the susceptibility of α-CoPc powder highlighting that the inflection at low T ($\approx 30\,\mathrm{K}$) (see inset) and the high temperature susceptibility requires contributions from both long and short chains 123

3.21 (a) Projection of the CoPc unit cell along the b^* axis, highlighting that the cross-section area of a CoPc chain can be approximated by the product ac. (b) Scaling of the fraction of paramagnetic spins in α-CoPc samples with the fraction of surface molecules corresponding to chain ends, and which can be approximated by $3b/2r$, where b is the lattice vector ($b = 3.75$Å) and r is the particle radius as estimated from the Scherrer equation (Table 3.2). The fractions of spins and their error bars were determined by averaging the values obtained from the $M(H)$ and $\chi(T)$ experiments. The solid lines represent the fraction of paramagnetic spins expected if their origin is either all the surface molecules corresponding to chain ends (slope=1, purple) or only one spin per odd chain (slope=1/4, blue). The dotted line is a fit through the film data and has a slope of 2.2. The cartoon is a schematic representation of the S=1/2 ground state for a chain of 5 spins 124

4.1 (a) SEM image of a carpet of CoPc nanowires lifted from a silicon substrate after manipulation. (b) Photographic image of the kapton film covered by CoPc nanowires after the growth. The scale indicates the position in the tube, according to the convention defined in this chapter. In the inner part of the kapton film, the nanowires from a mesh with a film-like appearance; in the outer region strands of nanowires are observed. 127

4.2 SEM images (50kX) of CoPc nano-structures obtained by OVPD at different positions in the tube: (a) 70 cm, (b) 75 cm, (c) 80.5 cm, (d) 87.5 cm, (e) 95 cm, (f) 102.5 cm 127

4.3 (a) UV-Vis absorption spectrum of CoPc nanostructures obtained by OVPD in different tube positions. The transition through a region of the OVPD tube where mixed phase growth occurs (75cm) is shown by the evolution of the spectrum. (b) Distinction from the α and β-CoPc spectra confirms the presence of a new polymorph. The absorption is remarkably similar to that of CuPc nanowires [95] 129

4.4 XRD of the CoPc nanostructures collected along the tube. Peak characteristic of the nanowire phase have been highlighted by red dashed lines at the following 2θ positions: 5.05°, 8.72°, 10.09°, 17.53°. Peaks that can be assigned to β-CoPc are highlighted by green vertical lines at these positions: 7.09°, 9.28°, 10.65°, 12.61°, 14.16°, 18.62°, 18.73° 130

4.5 High Resolution TEM (HRTEM) image of a CoPc nanowire (a); the insets show a zoomed image of the diffraction fringes within the nanowire and its Fast Fourier Transform (FFT). The profile of the intensity across the wire is shown in (b), highlighting a spacing of 1.07 nm between the fringes. Courtesy of Dr Luke Fleet. 133

4.6 Schematics of the mounting of CoPc nanowires samples in plastic straws for SQUID measurements 135

4.7 Magnetic analysis of the CoPc nanowires. The susceptibility, shown in (a), follows the Curie-Weiss law. A fit of χ^{-1} between 3 K and 48 K extracts the parameters shown in table 4.2. The $\chi(T)$ values are calculated from $M(T)$ measurements at 500 Oe and 1000 Oe (Equation 2.13); for an explanation of the units refer to section 2.3.7 and Equation 2.12. The $M(H)$ curves in CoPc nanowires at 2 K and 4.5 K are shown in (b); the dashed lines represent the fits with the Brillouin function (S=1/2). Solid lines are simulations with the g value extracted from the $\chi(T)$ curve 137

5.1 SEM images of F_{16}CoPc films grown at room temperature on kapton, glass and silicon. Cross-section images were obtained from freshly cleaved films grown on silicon. The scale bars correspond to 100 nm 143

5.2 SEM images of F_{16}CoPc films deposited on a 20 nm PTCDA layer on a silicon substrate: (a) top view of a 50 nm F_{16}CoPc/20 nm PTCDA film and (b) relative cross-section view; (c) top and (d) cross-section view of a 200 nm F_{16}CoPc/20 nm PTCDA film 145

5.3 From top to bottom: normalized UV-visible absorption spectra of 200 nm F_{16}CoPc film, CoPc nanowires, 200 nm α-CoPc film, 200 nm β-CoPc film, F_{16}CoPc solution in pyridine and CoPc solution in 5:1 1-Chloronaphthalene/pyridine mixture. The spectrum of F_{16}CoPc in solution is taken from Schuster *et al.*[86]. 147

5.4 (a) Absorption spectra of films of increasing thickness on glass.(b) Spectra after normalization of the optical density at λ=645 nm. . . 148

5.5 UV-Visible absorption spectra of templated F_{16}CoPc films on glass. (a) shows the overall absorption of 50 nm and 200 nm thick F_{16}CoPc films grown on a 20 nm thick PTCDA layer. The dashed lines show the data after subtraction of the PTCDA absorption. In (b) the absorption profile of the same films, corrected for the PTCDA absorption and normalized to unity, is compared with the spectrum of a 253 nm thick film deposited directly on glass, also normalized. The vertical dashed lines suggest the position of the absorption bands 150

5.6 XRD scans of films grown on (a) silicon (thickness 25 nm, 50 nm, 75 nm, 100 nm, 200 nm), (b) glass (thickness 25 nm, 50 nm, 75 nm, 100 nm, 200 nm) and (c) kapton (thickness 25 nm and 200 nm) substrates 151

5.7 Schematics of the proposed crystalline structure of thick F_{16}CoPc films grown on non interacting substrates (glass, silicon, kapton). At the interface with the substrate, the film grows in the structure proposed by Pandey [77], with the (001) plane oriented parallel to the substrate. Above this interfacial layer, which might have a thickness of some tens of nm, the structure switches to the one proposed by Yoon *et al.*[112], which exhibits a herringbone pattern between consecutive layers. Stacking faults may lead to the growth in a tilted direction with respect to the substrate, causing the nucleation of needles. 153

5.8 XRD patterns of 50 nm and 200 nm F_{16}CoPc films grown on a 20 nm thick PTCDA layer grown on a glass substrate. The diffraction from a 20 nm PTCDA film is shown for reference 154

5.9 Possible crystallographic planes of texture in F_{16}MPc films grown on PTCDA and their respective interplanar spacing d: (a) shows the orientation of the (1-2-2) plane in the F_{16}CuPc crystal structure proposed by Pandey *et al.*[77], (b) depicts the orientation of the (1-22) and the (1-2-2) planes in the F_{16}CuPc crystal structure proposed by Yoon *et al.*[112] 155

5.10 Magnetic characterization of F_{16}CoPc films. Isothermal magnetization curves of a 200 nm F_{16}CoPc film grown on kapton (a). The net magnetic moment per F_{16}CoPc molecule along the direction of the applied field is expressed in units of Bohr magnetons (μ_B). Inset: magnetic moment as a function of the ratio of field over temperature (H/T). The solid curve is a simulation of a paramagnet with S=1/2 and g=2. Temperature dependence of the differential susceptibility χ(T) (b). The $\chi(T)$ values are calculated from $M(T)$ measurements at 5000 Oe and 10 kOe (Equation 2.13); for an explanation of the units refer to section 2.3.7 and Equation 2.12. Inset: reciprocal of χ(T) and linear fit according to the Curie-Weiss law. The value of the Weiss temperature θ is equal to -1.3 K 157

5.11 Magnetic characterization of F_{16}CoPc films grown on PTCDA. Isothermal magnetization curves of a 200 nm F_{16}CoPc film grown on a 20 nm PTCDA layer on kapton (a). The net magnetic moment per F_{16}CoPc molecule along the direction of the applied field is expressed in units of Bohr magnetons (μ_B). Inset: magnetic moment as a function of the ratio of field over temperature (H/T). The solid curve is a simulation of a paramagnet with S=1/2 and g=2. Temperature dependence of the differential susceptibility χ(T) (b). Inset: reciprocal of χ(T) and linear fit according to the Curie-Weiss law. The $\chi(T)$ values are calculated from $M(T)$ measurements at 5000 Oe and 10 kOe (Equation 2.13); for an explanation of the units refer to section 2.3.7 and Equation 2.12. The value of the Weiss temperature θ is equal to -2 K 158

6.1 SEM top view image of a 50 nm F_{16}CoPc:CoPc (1:1) mixed film deposited on silicon (a) and its cross-section (b). Images (c) and (d) refer to films of the same composition but larger thickness (200 nm) 161

6.2 SEM top view image of a 50 nm F_{16}CoPc:CoPc (1:1) mixed film deposited on a 20 nm PTCDA layer on silicon (a) and its cross-section (b). 161

6.3 X-ray diffraction patterns of F_{16}CoPc:CoPc (1:1) mixed films; the background signal has been subtracted for clarity. The black line shows the measurement on a 50 nm film grown on silicon, the blue line refers to a 50 nm film grown on glass, while the red line represents the measurement of a 50 nm film grown on a 20 nm PTCDA layer on glass. All XRD scans have been normalized to unity. The data between 2θ=14.5°and 2θ=24.5°is omitted because it did not contain any diffraction peak. The position of the (102) peak of PTCDA has been marked for reference 163

6.4 X-ray diffraction pattern of 50 nm F_{16}CoPc:CoPc (1:1) mixed films grown on kapton (black line); the background signal from the kapton substrate is shown for reference (red line). Inset: the diffraction peak of the organic film at 2θ=6.5°(black line) and fit with a Lorentzian function (red line) 164

6.5 UV-Visible absorption spectrum of a 50 nm F_{16}CoPc:CoPc (1:1) mixed film (black line), compared with the spectra of a 100 nm CoPc film (red line, scaled by 0.5) and a 50 nm F_{16}CoPc film (blue line) 167

6.6 (a) UV-Visible absorption spectrum of a 50 nm F_{16}CoPc:CoPc (1:1) mixed film (black line), compared with the spectra of a 100 nm CoPc film (red line, scaled by 0.5) and a 50 nm F_{16}CoPc film (blue line). (b) spectra of 50 nm F_{16}CoPc:CoPc (1:1) mixed film on 20 nm PTCDA layer(black line), 50 nm CoPc film (red line, scaled by 0.5) and a 50 nm F_{16}CoPc film (blue line) both on PTCDA. The absorption of the 20 nm PTCDA layer (already subtracted from the other spectra) is shown for reference (dashed line). (c) Normalized spectra of F_{16}CoPc:CoPc (1:1) films: 50 nm film (black), 200 nm film (blue) and 50 nm film on 20 nm PTCDA (red); the absorption of PTCDA has been subtracted from all the spectra 168

6.7 XPS survey data of CoPc, F_{16}CoPc and mixed F_{16}CoPc:CoPc films. The species responsible for the main peaks are labelled accordingly, whilst the data are offset for clarity. 170

6.8 High resolution C 1s XPS profiles of the (a) CoPc 200nm/PTCDA 20 nm, (b) F_{16}CoPc 75nm, (c) F_{16}CoPc:CoPc 50nm and (d) F_{16}CoPc:CoPc 50nm/PTCDA 20nm films on silicon. The profiles in the pure CoPc and F_{16}CoPc films have been deconvoluted with Voigt peak shapes (30% Lorentzian, 70% Gaussian) and the background has been modelled by the Shirley algorithm. The spectra of the mixed films have been simulated by a 1:1 mixture of the spectra of the pure films. The top of each figure shows the residuals of the fit or of the simulation 172

6.9 High resolution XPS profiles of the (a) N 1s, (b) O 1s, (c) F 1s and (d) Co 2p. In (d) the spectra are shifted for clarity. 175

6.10 Magnetic characterization of F_{16}CoPc:CoPc (1:1) 200 nm film on kapton: (a) low temperature isothermal magnetization curve, expressed as the net magnetic moment in μ_B per phthalocyanine molecule. The magnetic moment as a function of the ratio of field over temperature (H/T) is shown in (b). Inset: the same data after subtraction of a magnetic moment $H\chi_0^{MH}$, where χ_0^{MH}=1.9x10$^{-3}\mu_B T^{-1}$. The red line shows the Brillouin function fit ($g = 2.224$) which returns a fraction of paramagnetic spins $f = 3.8\%$. The isothermal magnetization curves between 50 K and 300 K, shown in (c), exhibit a linear increase of the magnetization; lines of best fit are shown in red. The fits extrapolate to a negative intercept with the magnetization axis, owing to an impurity in the film (see text) . . . 178

6.11 Magnetic characterization of F_{16}CoPc:CoPc (1:1) 200 nm film grown on a PTCDA layer on kapton: (a) low temperature isothermal magnetization curve, expressed as the net magnetic moment in μ_B per phthalocyanine molecule. The net magnetic moment per molecule as a function of the ratio of field over temperature (H/T) is shown in (b). Inset: the same data after subtraction of a magnetic moment $H\chi_0^{MH}$, where χ_0^{MH}=2.5x10$^{-3}\mu_B T^{-1}$. The red line shows the Brillouin function fit ($g = 2.42$) which returns a fraction of paramagnetic spins $f = 2.4\%$. The isothermal magnetization curves between 50 K and 300 K, shown in (c), exhibit a linear increase of the magnetization; lines of best fit are shown in red. The fits extrapolate to a positive intercept with the magnetization axis, owing to an impurity in the film (see text) 179

6.12 (a) Temperature dependence of the magnetic susceptibility $\chi(T)$ of a 200 nm F_{16}CoPc:CoPc (1:1) mixed film on kapton; empty symbols are values of differential susceptibility calculated as $\Delta M/\Delta H$ from two M(T) measurements at different fields (H_{ave} is the average field); filled (magenta) diamonds values were calculated as M_{corr}/H from a single M(T) measurement at H=40 kOe, where M_{corr} is the magnetization after subtraction of the spurious signal do to a ferromagnetic impurity (M_0=-3.4x$10^{-3}\mu_B$, see Figure 6.10c); the filled (yellow) circles are the gradients of the M(H) curves in Figure 6.10c. For an explanation of units refer to section 2.3.7 and Equation 2.12. (b) Detail of the high temperature part of $\chi(T)$ and fit with the model based on the infinite antiferromagnetic chain (Equation 3.3). 181

6.13 (a) Temperature dependence of the magnetic susceptibility $\chi(T)$ of a 200 nm F_{16}CoPc:CoPc (1:1) mixed film grown on 20 nm PTCDA on kapton; empty symbols are values of differential susceptibility calculated as $\Delta M/\Delta H$ from two M(T) measurements at different fields (H_{ave} is the average field); filled (magenta) diamonds values were calculated as M_{corr}/H from a single M(T) measurement at H=40 kOe, where M_{corr} is the magnetization after subtraction of the spurious signal do to a ferromagnetic impurity (M_0=+1.49$^{-3}\mu_B$, see Figure 6.11c); the filled (yellow) circles are the gradients of the M(H) curves in Figure 6.11c. For an explanation of units refer to section 2.3.7 and Equation 2.12. (b) Detail of the high temperature part of $\chi(T)$ and fit with the model based on the infinite antiferromagnetic chain (Equation 3.3). 182

A.1 Results of the fit of the magnetic susceptibility of α-CoPc 200 nm film on kapton using the finite chain model (Equation 3.5). Residuals and values of the fitted parameters are shown in the color map for all combinations of chain lengths. (a) Weighted root mean square error of the fit; (b) values of the exchange energy J/k_B; (c) values of the temperature independent correction χ_0; (d) fraction f of paramagnetic spins 210

A.2 Characteristic fits of the susceptibility of α-CoPc 200 nm film on kapton 211

A.3 Results of the fit of the susceptibility of the α-CoPc templated film (200 nm on 20 nm PTCDA) on kapton using the finite chain model (Equation 3.5). Residuals and values of the fitted parameters are shown in the color map for all combinations of chain lengths. (a) Weighted root mean square error of the fit; (b) values of the exchange energy J/k_B; (c) values of the temperature independent correction χ_0; (d) fraction f of paramagnetic spins 212

A.4 Characteristic fits of the susceptibility of α-CoPc 200 nm templated film on kapton 213

List of Tables

2.1 Sensitivity of the SQUID magnetometer in different ranges of magnetic field strength 80

3.1 Results of the ICP analysis of CoPc samples. The first column shows the solutions analysed, with their theoretical concentration of cobalt indicated with the symbol $[Co]_{calc}$ in ppm units. The following columns report the measured concentration of each element (Co, Cu, Fe, Mn) and the line (λ) of the atomic emission spectrum used for the measurement. The standard deviation of the values of concentration are given in brackets. 93

3.2 Summary of the Scherrer analysis performed on the α-CoPc samples XRD patterns. The peaks used in the calculation are the (001) and the (2-11) peaks of the α-CoPc structure. For each peak, the table shows the (hkl) index, the experimental diffraction angle ($2\theta_0$), the observed width of the peak ($w_{2\theta}^{obs}$), the Scherrer grain size (Size) and the estimated number of CoPc molecules (N) stacked along the b direction in an average crystallite. The number of molecules N was calculated by dividing the Scherrer size by the lattice constant b=3.75Å along the stacking direction 103

3.3 Values of the g factors and hyperfine constants ($A_{\parallel}$, $A_{\perp}$) of CoPc extracted from EPR measurements on α-phase and β-phase samples. Fitting of the fine structure of the α-phase powder gave the values of both the g and the hyperfine tensors. When the fine structure was not resolved, values were estimated from the position of the maximum and minimum of the broad signal envelope. The values determined by Assour *et al.*[3] in spin diluted samples at low temperature (77 K) are also shown for reference. 110

3.4 Average value of g calculated for the orientation of α-CoPc powder, α-CoPc films and α-CoPc film on PTCDA. The calculation used the g tensor parameters from Assour (Table 3.3). 112

3.5 Magnetic parameters extracted from SQUID measurements. J is the exchange energy, χ_0^{χ} is the temperature independent correction to the $\chi(T)$ curves, χ_0^{MH} is the temperature and field independent correction applied to M(H) curves, f^{χ} is the fraction of paramagnetic spins calculated from the Curie constant fitting the low temperature trend of $\chi(T)^{-1}$ (with g as in Table 3.4), while f^{MH} is the fraction of paramagnetic spins obtained by fitting the $M(H)$ curves. 117

3.6 Summary of the results of the finite chain fits of the CoPc susceptibility (Equation 3.5). The chain length range defines the chain distributions (Equation 3.4) that result in the best fits (*i.e.* WRMSE $<4 \times 10^{-3}\,\mu_{\mathrm{B}}\mathrm{T}^{-1}$); WRMSE is the weighted root mean of squared errors, where the squared errors are weighted by the density of data points at each temperature; RMSE is the root mean of squared errors. J/k_B is the exchange energy in K, χ_0^{χ} is the temperature independent correction, f is the fraction of paramagnetic spins predicted at low temperature, calculated with Equation 3.6 121

4.1 Peak parameters of CoPc nanostructures samples grown by OVPD collected at different positions along the furnace tube. For each sample the table gives the Bragg angle of the peaks observed, their width and integrated area, the corresponding Scherrer size and lattice spacing, and the assignment to either the β or η polymorphs, with the relative Miller indices (hkl). The question mark indicate peaks that could not be assigned 131

4.2 Magnetic parameters extracted from the fit of the measurements in Figure 4.7 136

5.1 Peak parameters from the fit of the XRD patterns of F_{16}CoPc samples, using pseudo-Voigt line shape. 149

6.1 Best fit parameters of the diffraction XRD peaks of F_{16}CoPc:CoPc (1:1) 50 nm films. The peaks are modelled with a Lorentzian function: $2\theta_0$ is the centre of the peak, $w_{2\theta}^{obs}$ is the experimental full width at half maximum in degrees of 2θ 162

6.2 Calculated relative abundance of the species detected in CoPc, F_{16}CoPc and mixed F_{16}CoPc:CoPc films (1:1 ratio) (from Figures 6.8 and 6.9) after correcting for the empirical sensitivity factors relative to the F(1s) level (from [93]) 171

6.3 Binding energies and relative intensities of fitted peaks for the high resolution XPS spectra of CoPc, F_{16}CoPc and mixed F_{16}CoPc:CoPc films (1:1 ratio), in Figures 6.8 and 6.9. The intensity profiles are fitted using a Voigt line shape with 30 % Lorentzian and 70 % Gaussian component. The C 1s signal of the mixed films has not been fitted owing to its complex structure. Without any further correction, all values of the binding energy are in reasonably good agreement (within 0.4 eV) with those reported by Niwa *et al.*[74] and Ottaviano *et al.*[76] 176

A.1 Atomic emission lines for Mn, Fe, Co. For each element, the emission wavelength λ, the intensity and the oxidation state of the ion (in parentheses) are given 208

A.2 Atomic emission lines for Cu and Ni. For each element, the emission wavelength λ, the intensity and the oxidation state of the ion (in parentheses) are given 209

Chapter 1

Introduction

1.1 Organic Spintronics

1.1.1 Spintronics

Spintronics is a multidisciplinary research field which studies phenomena arising from the spin of electrons and ways of manipulating the spin degree of freedom in solid-state systems [114]. One of the goals of spintronics is to exceed conventional electronics through the development of novel devices where the spin is exploited for achieving enhanced sensitivity, faster operation speed, lower power consumption and/or additional functionality [36]. The most successful achievement of spintronics so far has been the discovery of the so-called giant magneto-resistance (GMR) effect and the invention of the spin valve, a device based on such effect which has found application as a high sensitivity magnetic field sensor for hard disk read heads. The simplest spin valve is a three layer device, where a non-magnetic conductive material is sandwiched between ferromagnetic electrodes: one of the electrodes injects in the non-magnetic material a spin polarized current, which is collected by the second electrode. The magnetization in the two electrodes can be oriented either parallel or antiparallel and one configuration determines a higher electrical resistance compared to the other, due to the spin dependent scattering

of the charge carriers. This magneto-resistive effect is described as giant (GMR) in order to differentiate it from the much weaker ordinary magneto-resistance (anisotropic magneto-resistance, AMR) [25]. A similar effect, named tunnelling magneto-resistance (TMR), is observed in magnetic tunnelling junctions, where the spin carriers tunnel from magnetic contacts through a thin insulating barrier. The magnitude of the magneto-resistive effects is quantified by the percentile change in resistance, generally with respect to the configuration having lower resistance; it is common to use the term positive (negative) magneto-resistance to refer to the case when the parallel (antiparallel) configuration yields the lower resistance.

1.1.2 Organic Spintronics

Organic semiconductors have been an increasingly active subject of scientific research since when their application in electronic and optoelectronic devices such as light emitting diodes [90, 21], transistors [92] and photovoltaic cells [99, 16] has been demonstrated. Some of these applications have already reached the stage of industrial production and are challenging existing commercial products thanks to the low costs of production of organic semiconductor devices, combined with the ease of processability on large areas and on flexible substrates. Organic semiconductors recently became materials of interest for spintronic applications. Magneto-resistive effects in organic materials were first observed by Dediu *et al.* in hybrid spin-valves containing an organic semiconductor film bridging magnetic inorganic for spin current injection and detection [30]. The report of giant magneto-resistance in organic hybrid devices at low temperature ($\Delta R \approx 40\%$ at 11K) [105], triggered a number of studies on organic spintronics which confirmed the magneto-resistance effects and measured spin transport through organic materials [84, 31], establishing the field on solid experimental grounds. Other studies revealed that

organic semiconductors exhibit an intrinsic magneto-resistance (OMAR, organic magneto-resistance) and magnetic modulation of electroluminescence even in absence of spin polarizing electrodes [44]. In this regard, organic semiconductors are attractive especially because of the weakness of the spin-scattering mechanism in such materials, which increases significantly the lifetime of non-equilibrium spin populations and the diffusion length of spin polarized currents involved in the operation of spintronic devices [31], bringing the realization of practical organic spintronics closer to reality. Furthermore, this technology could be easily integrated into existing organic electronic applications.

1.1.3 Spin diffusion in organic semiconductors

Key parameters in organic spintronics are the spin diffusion length (λ_s), which corresponds to the distance that a spin carrier can travel within the material before its spin polarization is lost, and the spin relaxation time τ_s, that measures the timescale of spin scattering events; these two quantities are linked by the carrier mobility in the organic material. Organic semiconductors can exhibit spin relaxation times which are several orders of magnitude longer than those in inorganic materials [114, 73], as shown by electron spin resonance experiments [52] and spin transport measurements; values of τ_s up to 1 s have also been reported in spin-valves containing the organic semiconductor Alq_3 [80]. Spin diffusion lengths measured in organics are of the order of 100 nm [84, 31] and the values are currently limited by the low carrier mobility, which generally is around $10^{-4}\,cm^2\,V^{-1}\,s^{-1}$–$10^{-3}\,cm^2\,V^{-1}\,s^{-1}$ in organic thin films; however, the mobility can exceed $10\,cm^2\,V^{-1}\,s^{-1}$ at room temperature, in the case of organic single crystals [49, 78]. An issue regarding the measurement of spin diffusion length in organic spintronic devices is that this data is not easily accessible. The value of λ_s is generally extracted from magneto-resistance measurements, where a single measurement

cannot resolve different contributions to the spin scattering (e.g. interface, bulk) and therefore can only provide a lower estimate for the spin diffusion length in the organic layer [33]. In order to discern these contributions it is necessary to perform magneto-resistance measurements on a series of devices of different channel length but with otherwise identical properties. This could require significant effort, considering that the interfaces between organic semiconductors and the electrodes are subject to a high degree of variability. It should be mentioned that direct and depth-resolved measurements of the spin polarization has been performed in working organic spin valves using the low energy muon spin rotation technique [33].

1.1.4 Challenges and current understanding of organic spintronics

The magneto-resistance effects observed in macroscopic organic samples and devices are generally the sum of several components with possibly different functional dependence on experimental parameters like applied magnetic field or voltage bias. How fundamental processes such as spin scattering at the interface, spin injection or the intrinsic organic magneto-resistance affect the overall characteristics of the device probably depends on a series of factors like the spin polarization in the electrode, the quality of the interfaces between the electrodes and the organic material, the molecular orientation of the organic thin film, if crystalline, the density of defects and traps. The complexity of these systems and the lack of common metrology rules among the organic spintronics community is slowing the development of a theoretical understanding of the subject [31], although significant progress has been made recently, especially in controlling interfaces and understanding their role [84]. A limitation of magneto-transport experiments on spintronic devices is that they average out device properties over a relatively large

area. However organic devices can exhibit markedly inhomogeneous interfaces, due to the softness of the organic films and their intrinsic disorder. For example, it was observed that the deposition of ferromagnetic electrodes on organic layers forms an ill-defined interface, where the metal atom islands sometimes protrude up to 50 or 100 of nm inside the organic layer; this was found to jeopardize reproducibility of the characteristics and cause a dramatic reduction of the operating temperature and magnitude of the magneto-resistive effects [30, 94, 89]. Better injection interfaces were fabricated by protecting the organic layer with a thin layer of an robust insulating material (e.g. Al_2O_3) [31], or by deposition of the magnetic electrode in the form of nanodots [89], which reduce diffusion in the organic layer. These precautions brought about improvement of the temperature dependence of the magneto-resistance, which was measured even at room temperature [31], and giant negative magneto-resistance behaviour at low temperature ($\Delta R \approx 300\%$ at 11K) in spin valves based on the organic semiconductor Alq_3 [89]. The issues of inhomogeneity and metal penetration are even more serious in magnetic tunnel junctions, where nanometre thick organic films are required. These problems were circumvented by Barraud *et al.* who fabricated nanosized organic magnetic tunnel junctions devices through a nano-indentation process, and measured a sizeable, positive giant magneto resistance through an Alq_3 tunneling barrier at low temperature ($\Delta R \approx 300\%$ at 11K) [8]. Theoretical and experimental evidence suggest that the polarization of spin currents injected in organic devices is highly sensitive to the degree of orbital hybridization with the magnetic electrode. This process broadens the density of states in the molecule in a spin-dependent fashion, in the case of contacts with spin-polarized electrodes, and also depends on the molecular adsorption geometry on the surface of the electrode and on the possible formation of chemical bonds. In the strong coupling limit, where the broadening exceeds the energy separation between the molecular acceptor states and the Fermi level, an inversion of spin polarization around the Fermi level is predicted to occur in

the adsorbed molecules [8]; this causes a preferential injection of minority spin carriers in the organic film at low applied bias, while injection of majority spin carriers was postulated at larger biases. These predictions are in agreement with the spin density of states observed on phthalocyanine monolayers on iron with spin polarized STM [5, 17], which showed inversion of the spin polarization near the Fermi level. These results may help to understand why both positive and negative magneto-resistive effects have been observed in the literature, even on the same organic semiconductor. Furthermore they suggest that it would be possible to control the spin polarization in the organic semiconductor by adjusting the bias applied to the injecting electrode in a spintronic device.

1.1.5 All-organic spintronics devices

Most studies in the organic spintronics literature focused on the spin- and magneto-transport in diamagnetic organic conjugated molecules, which have been used only as "passive" spacers between inorganic spin-polarizing electrodes. The materials generally used for spin injectors are managanites and magnetic metals like cobalt and iron. Lanthanum strontium manganite (LSMO) is the most widely used material for spin injectors in organic devices and it has provided the largest magneto-resistance effects [89] and spin-valve operation at room temperature [31]. LSMO offers high spin polarization efficiency and chemical stability; however its use has several practical disadvantages, such as the need to recur to pulsed laser deposition, a costly and low throughput method, and the incompatibility with flexible or stretchable substrates. There is currently great interest in the use of organic based magnets as spin injectors in all-organic spintronics devices, which would benefit from cheap and low temperature synthetic routes, large area processing, mechanical flexibility and tuning of the magnetic and electronic properties using organic chemistry methodologies. The field of organic- and molecular-based mag-

nets, which will be discussed in the next section, has been growing significantly in the past decades [70, 69], leading to the synthesis of magnetic molecular materials with transition temperature above room temperature [64], and to the discovery of single molecule magnets (SMM). The potential of organic-based magnets as spin-polarizing materials was shown theoretically [28, 27] and a recent breakthrough experiment demonstrated the operation of a spin-valve device employing an organic-based magnetic semiconductor in both the spin-injector/detector electrodes [59]. Following the trend to ever-smaller devices, conjugated molecules and single molecule magnets have also been investigated in molecular junctions between magnetic electrodes for application as spin valves or spin transistors [83, 84, 14]. This research direction is receiving remarkable interest motivated by the rich physics observed on these relatively simple systems, and by the ultimate goal of shrinking the size of electronic devices to the atomic/molecular scale.

1.2 Molecule based magnets

Molecule based magnets have been an active area of research in the past four decades [70, 69]. In the initial definition, this class of materials included all the compounds in which the magnetism arised exclusively from spin centres in s or p orbitals of light elements such as carbon, nitrogen, oxygen and sulphur, although nowadays the family of molecule based magnets also include metallorganic materials where both transition metals and organic moieties play an active role in the magnetic behaviour [70]. Molecule based magnets offer several advantages over conventional metal and ceramic magnets: while the latter require high temperature and energy consuming processes, the former can be synthesized in solution or by chemical vapour deposition under milder conditions. This has both economic and environmental advantages and might also lead to novel magneto electronic

devices, previously not feasible because of incompatible processing routes. Furthermore the properties of molecule based magnets can be easily tuned using chemical modification of the organic groups, similarly to what has been done on organic semiconductors; for example, appropriate choice of the organic moiety can tailor the magnetic interaction between the spins, or introduce new functionalities in the material, such as photo-responsivity. Finally, this methodology allows a larger degree of freedom in the way the spins can be combined to form magnetic materials and therefore allows the synthesis of model systems where spin-physics theories can be tested and new phenomena can be observed.

1.2.1 Magnetism

The macroscopic magnetization of a molecular based magnet is principally due to the magnetic moments generated by the spin angular momentum of unpaired electrons. In these materials, the unpaired electrons are (partially) localized, for example, on free radicals or transition metal ions, which we will call spin centres. The magnetic moment of a spin centre, μ_S, is linked to its spin quantum number, S, by the following relation:

$$\mu_S = g\mu_B\sqrt{S(S+1)} \tag{1.1}$$

where μ_B is the Bohr magneton and g is a dimensionless quantity called the g-factor; S is equal to ½ for an unpaired electron, and is equal to n½ in a spin centre containing n unpaired electrons. The magnetic properties of a molecular based magnet depend on the coupling interactions existing between the spin centres. When these are not interacting, no correlation between the spin centres is observed and the material is paramagnetic. At low magnetic fields, the magnetization of paramagnets is proportional to the magnetic field, with a proportionality constant χ called the magnetic susceptibility. χ is more generally defined as the derivative

of the magnetization with respect to the magnetic field. When the applied field is weak, the susceptibility is inversely proportional to the temperature, as described by the Curie law:

$$\chi = \frac{C}{T} \tag{1.2}$$

The Curie constant C is given by

$$C = \frac{N}{V}\frac{\mu_0 \mu_{eff}^2 \mu_B^2}{3k_B} \tag{1.3}$$

where μ_0 is the vacuum permeability, needed when using SI units, N is the number of paramagnetic centres in the sample, V is the sample volume, k_B is the Boltzmann constant and μ_{eff} is the effective magnetic moment, which expresses the magnetic moment in units of Bohr magnetons:

$$\mu_{eff} = g\sqrt{S(S+1)} \tag{1.4}$$

At very large magnetic fields the net magnetic moment per spin reaches a saturation value equal to gS, which is obtained when the spins are fully aligned with the magnetic field. The magnetic moment per unit of volume (magnetization M_V) of the sample can be calculated analytically at any field with the Brillouin function, as shown below:

$$M_V = \frac{N}{V} g\mu_B S B_S(\eta) \tag{1.5}$$

where η is equal to

$$\eta = \frac{g\mu_0\mu_B H}{k_B T} \tag{1.6}$$

and $B_S(\eta)$ is the Brillouin function:

$$B_S(\eta) = \frac{1}{S}\left[\left(S+\frac{1}{2}\right)\coth\left[\left(S+\frac{1}{2}\right)\eta\right] - \frac{1}{2}\coth\left(\frac{\eta}{2}\right)\right] \tag{1.7}$$

In the weak field limit, where the value of η is much less than 1, Equation 1.5 is approximated by

$$M_V = \chi H \tag{1.8}$$

Paramagnetic materials are generally not attractive from the technological point of view. More interesting are the cases where the spins in the material are coupled and have a preferential relative orientation. When the interaction favours a parallel alignment of the spins the coupling is said to be ferromagnetic, while an antiferromagnetic coupling tends to align neighbouring spins anti-parallel. In the high temperature regime, where k_BT is larger than the energy of the spin-spin interaction, the low field susceptibility can be expressed as a function of temperature using the Curie-Weiss formula:

$$\chi = \frac{C}{T - \theta} \tag{1.9}$$

where θ, the Weiss constant, takes a positive or negative value for ferromagnetic or antiferromagnetic materials respectively, and is a measure of the strength of the spin-spin coupling. A simple way of classifying a magnetic material as paramagnetic, ferromagnetic or antiferromagnetic is to plot the inverse of susceptibility against temperature, which results in having straight lines that intersect the x-axis at $T = \theta$, giving the value of the Weiss constant, as shown in Figure 1.1; the inverse of the slope of the line allows the determination of the effective magnetic moment, which is linked to the Curie constant C by Equation 1.3.

The Curie-Weiss formula is the result of a mean-field treatment of the spin-spin interaction: the coupling is taken into account by means of an internal magnetic field, generated by the magnetization of the material, which is acting on the spin centres. The internal field adds up to the external field in the case of ferromagnetically coupled spins, making them further aligned with the magnetic field; in the case of antiferromagnetic coupling, the internal field partially cancels the applied

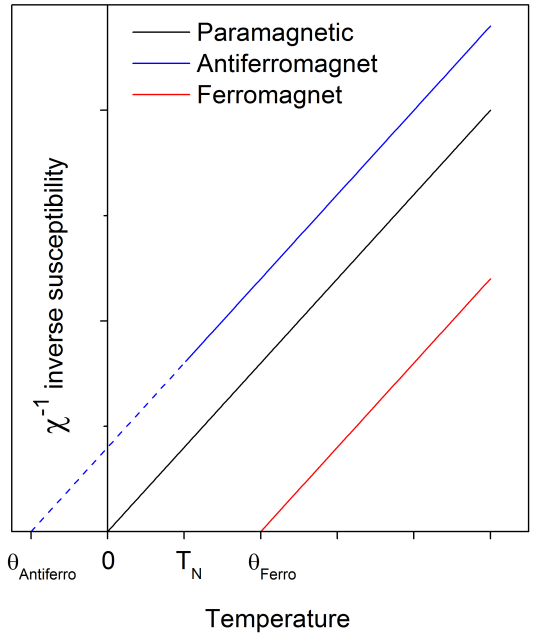


Figure 1.1: Plot of inverse susceptibility in paramagnetic, antiferromagnetic and ferromagnetic materials. For the antiferromagnetic case, the trend at low temperature is extrapolated, as the experimental data deviates from linearity below the Néel temperature T_N. The Weiss temperatures are shown. The slope is inversely proportional to the effective magnetic moment squared

one and causes a reduction of the alignment of spins along the field. Although the Curie-Weiss formula can give an accurate quantitative description of the magnetic susceptibility as a function of temperature, the microscopic model made of spin centres interacting only through classical dipolar forces is actually wrong, as the coupling is mainly a quantum-mechanical effect.

Systems of coupled spins can show transitions from paramagnetic to ordered magnetic phases at lower temperatures. The transition temperature is called the Curie temperature for ferromagnetic materials and Néel temperature for antiferromagnets. While the Curie temperature is generally very similar to the Weiss constant of the material, the Néel temperature can be significantly smaller than the absolute value of θ [13].

An important property of ferromagnetically ordered materials is magnetic hys-

teresis, shown if Figure 1.2. A ferromagnet can keep a permanent magnetization, called remanent magnetization (M_R), even in absence of an external field. This magnetization can only be cancelled when a sufficiently strong magnetic field (H_C, the coercive field) is applied in the opposite direction.

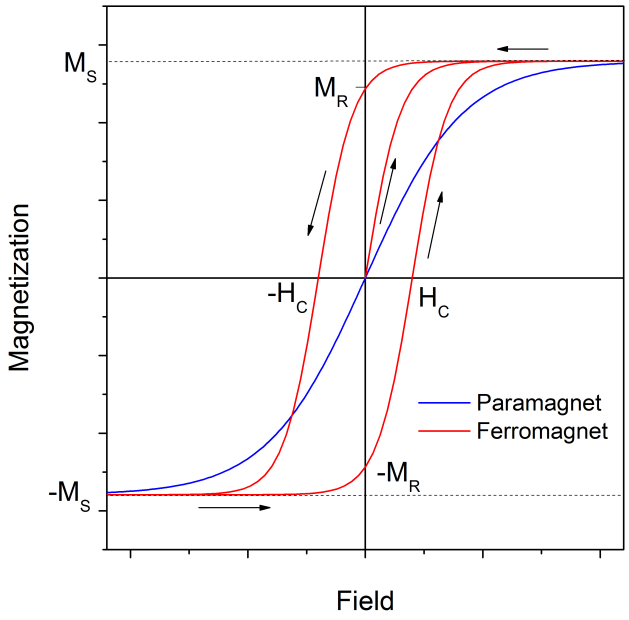


Figure 1.2: Magnetization curve of a paramagnet (blue line) and of a ferromagnet (red line) below the Curie temperature T_C. The definitions of coercive field (H_C), magnetization at saturation (M_S) and remnant magnetization (M_R) are shown.

1.2.2 Spin Hamiltonian

The susceptibility and magnetization are physical quantities that describe the magnetism of a material at a macroscopic scale and are relatively easy to measure experimentally. However, they provide little detail about the origin of the magnetism. A convenient description of the system at a microscopic scale is provided by the spin Hamiltonian operator $\hat{\mathcal{H}}_{spin}$, which includes the main interactions regarding the spin centres of the system and allows the calculation of spin eigenstates and their relative energies (eigenvalues). Once the eigenvalues of the

spin Hamiltonian are known, it is possible to compute the macroscopic quantities such as susceptibility or magnetization by using statistical mechanics. The spin Hamiltonian used for molecular based magnets typically includes three terms, the Zeeman interaction ($\hat{\mathcal{H}}_{Zeeman}$), the spin-spin interaction ($\hat{\mathcal{H}}_{spin-spin}$) and the zero field interaction ($\hat{\mathcal{H}}_{ZFI}$), as shown in Equation 1.10

$$\hat{\mathcal{H}}_{spin} = \hat{\mathcal{H}}_{Zeeman} + \hat{\mathcal{H}}_{spin\text{-}spin} + \hat{\mathcal{H}}_{ZFI} \tag{1.10}$$

These three contributions are discussed individually in the following sections.

The Zeeman interaction

The Zeeman Hamiltonian describes the interaction of the spin with the magnetic field and, for a single spin centre can be written as following:

$$\hat{\mathcal{H}}_{Zeeman} = g\mu_B B\hat{S}_z \tag{1.11}$$

where B is the magnitude of the magnetic field, whose direction defines the z axis, and $\hat{S}_z$ is the z component in the spin operator. Equation 1.11 describes an isotropic Zeeman interaction, not depending on the relative orientation of the sample with respect to the magnetic field. This result is obtained, for example, when the spin centre is in an environment with cubic local symmetry [20]. In the general case, the Zeeman Hamiltonian has to be written in a tensorial form:

$$\hat{\mathcal{H}}_{Zeeman} = \mu_B \vec{B}\bar{\bar{g}}\hat{S} \tag{1.12}$$

where $\vec{B}$ is the magnetic flux density vector, $\hat{S} = \left(\hat{S}_x\hat{S}_y\hat{S}_z\right)$ is the Pauli spin operator and $\bar{\bar{g}}$ is a 3×3 tensor. In most cases $\bar{\bar{g}}$ is symmetric and therefore it can

be written in a diagonal form as in Equation 1.13:

$$\begin{pmatrix} g_{xx} & 0 & 0 \\ 0 & g_{yy} & 0 \\ 0 & 0 & g_{zz} \end{pmatrix} \tag{1.13}$$

with x, y and z being the principal axes of the tensor. Like the g value, the magnetic moment is non-isotropic and its components are linked to the g_{ii} components of the g tensor in a way similar to the isotropic case (Equation 1.4). The primary reason for the deviation of the g_{ii} values from $g_e = 2.0023$, the *free* electron value, is the interaction existing between the spin and the orbital angular momenta (spin-orbit coupling, SOC) of the unpaired electrons. When the spin-orbit coupling is weak (like in most molecular based magnets), the result is a mixing of the ground state with excited states that add orbital contribution to the magnetic moment and hence change the g tensor; for a spin ½ system, with quenched orbital angular momentum ($L = 0$) in the ground state and no low lying excited states, the values of the g tensor can be estimated with the following formula derived from perturbation theory [57, 20]:

$$g_{ij} = g_e\delta_{ij} + \lambda \sum_{m \neq 0} \frac{\langle m|\hat{L}_i|0\rangle\langle 0|\hat{L}_j|m\rangle}{E_0 - E_m} \tag{1.14}$$

where δ_{ij} is the Kronecker delta, λ is the spin-orbit coupling constant, E_0, E_m are the energies of the singly occupied molecular orbital (SOMO) and of the m orbital respectively, L_i is the i component ($i = x, y, z$) of the angular momentum operator, $\langle m|\hat{L}_i|0\rangle$ is the matrix element of L_i calculated between the ground state ($|0\rangle$) and the m state ($\langle m|$). Using this model, the g tensor can give information about the electronic spin wavefunction. For instance, a g_{ii} value less than g_e indicates orbital mixing with empty orbitals (lying at higher energy), while a positive deviation of g_{ii} results from mixing with filled orbitals. Furthermore, in

the case of transition metal ions, a g_{zz} value close to g_e is expected when the SOMO is based on the d_z^2 orbital, because it has zero angular momentum along the z direction and therefore all the matrix elements vanish (i.e. the L_z operator does not couple the d_z^2 orbital to any other orbital) [20]. Although Equation 1.14 is just an approximation, it can provide a guideline for the interpretation of the electronic structure of paramagnetic compounds.

Spin-spin coupling

The simplest Hamiltonian describing the spin-spin interaction between two centres is:

$$\hat{\mathcal{H}}_{spin\text{-}spin} = J\hat{S}_1 \cdot \hat{S}_2 \tag{1.15}$$

where $\hat{S}_1$, $\hat{S}_2$ are the spin Pauli operators and J is the coupling constant that, in our convention, assumes positive (negative) values for a antiferromagnetic (ferromagnetic) coupling. Similarly to the Zeeman interaction, the spin-spin coupling can contain non isotropic contributions, although the isotropic term in Equation 1.15 is often dominant in molecular based magnets and allows a sufficiently accurate description of the system. This is a phenomenological model, which does not provide information about the origin of the spin-spin coupling; the main mechanism for spin-spin coupling will be reviewed in section 1.2.5.

Zero field interaction

When the spin quantum number of a spin centre is larger than ½, because it contains two or more unpaired electrons, the zero field interaction is observed. This interaction actually originates from spin-orbit coupling and dipolar interactions between the unpaired electrons populating the spin centre. The Hamiltonian of

the zero field interaction can be written as following:

$$\hat{\mathcal{H}}_{ZFI} = D\hat{S}_z^2 + E\left(\hat{S}_x^2 - \hat{S}_y^2\right) \tag{1.16}$$

where $|E/D| < 1/3$ by definition. The first term, depending on D, causes a splitting of the $\hat{S}_z$ spin eigenstates even in absence of an external magnetic field. Its effect is to define the easy axis z, when D is negative, or the easy plane xy, when D is positive, along which the spin magnetic moment will lie preferentially; for this reason D is also called magnetic anisotropy or zero field splitting. The second term of Equation 1.16 depends on E, which describes the rombicity of the system and is equal to 0 for a system with axial symmetry; a finite E causes a mixing of the $\hat{S}_z$ eigenstates.

1.2.3 Dimensionality of the spin

The spin angular momentum is in general described by a three dimensional vector, as we assumed in the discussion of the spin Hamiltonian: this model is called the Heisenberg spin model. However the treatment of the spin can be simplified in systems that feature spin quantum numbers higher than ½ and large magnetic anisotropy: when the zero field splitting is stronger than any other interaction in the spin Hamiltonian and the parameter D is negative, then the Ising model applies, which takes into account only the S_z component of the spin; in the case of positive D, the XY model is used, which considers just the x and y components of the spin.

1.2.4 Dimensionality of the magnetic lattice

In a structurally ordered molecular magnet, the spin centres are arranged into a crystal lattice; when studying the spin-spin coupling between these centres we generally consider only the nearest neighbour interaction, which expresses the

strongest contribution. The spin-spin coupling might have different coupling constants J along the crystal directions and the directions which are most relevant for the spin coupling determine the dimensionality of the magnetic lattice. When the interaction is much stronger in one or two dimensions, the system can be safely considered as having a 1- or 2-dimensional magnetism, at least in the temperature range where the weakest couplings are disrupted by thermal fluctuations. The dimensionality of the magnetic lattice is a factor which affects enormously the properties of magnetic materials; for example, pure 1D or 2D ferromagnetic systems cannot exhibit a thermodynamically stable bulk magnetic ordering [13]. However, low dimensional systems such as single molecule or chain magnets can display a slow dynamics of the magnetization that leads to magnetic hysteresis effects on the time-scale of the measurement.

1.2.5 Spin coupling mechanisms

In section 1.2.2 we introduced a phenomenological description of the coupling between spin centres, based on the spin-spin Hamiltonian (Equation 1.15); in this paragraph we will review some of the main coupling mechanisms observed in molecular based magnets. A first distinction in the coupling mechanism is between the *classical* interaction, due to the dipole-dipole forces experienced by two magnetic moments, and the quantum mechanical coupling, also called the exchange interaction. The dipolar interaction between magnetic moments depends on the separation and the mutual alignment of the magnetic moments, as shown in the following energy equation:

$$E = \frac{\mu_0 g^2 \mu_B^2}{4\pi r^3} \left[\vec{S}_1 \cdot \vec{S}_2 - \frac{3}{r^2} \left(\vec{S}_1 \cdot \vec{r} \right) \left(\vec{S}_2 \cdot \vec{r} \right) \right] \tag{1.17}$$

Dipolar interactions are often much weaker than quantum-mechanical exchange interactions: in the case of spin ½ centres with $g = 2$ separated by $r \approx 1$ Å, the

dipolar interaction is equivalent to about 3 K in temperature. Three pathways for exchange interaction, which could be important in molecular based magnets, will be defined here. The first one is the *direct exchange*, which originates from the exchange term of the Coulomb interaction between localized electrons and can be relevant if there is a significant overlap between the densities of the interacting electrons wavefunctions (orbitals); it favours a ferromagnetic configuration when the orbitals containing the unpaired electrons are orthogonal, as summarized by the Hund's rule of spin multiplicity. A second mechanism is called *superexchange* and is particularly relevant for molecule based magnets. In the superexchange mechanism the coupling is mediated by transfer of electron density of the ligand onto the metal. In this work, the exchange mechanism responsible for the antiferromagnetic coupling in α-CoPc is also named superexchange, since it involves partial transfer (hopping) of electron density between the Co atoms, although the ligand is not involved in this process [101]. The third mechanism is called *indirect exchange* and consists of a magnetic coupling mediated by the polarization of the spin density on the bridging organic ligands; the coupling here is due to electron-electron repulsion interactions between the spin centre and the ligand electrons [102]. Both the superexchange and the indirect exchange mechanisms can be relevant in molecular based magnets where the magnetic atoms are separated by non-magnetic ligands (having filled orbitals) such as inorganic ions or organic molecules; the magnitude of these interactions depend enormously on the symmetry and the spatial arrangement of the interacting orbitals.

1.3 Phthalocyanine and metal phthalocyanines

Phthalocyanine was accidentally discovered in 1907 as a by-product during the synthesis of o-cyanobenzamide. Twenty years later the first accidental synthesis of copper phthalocyanine was reported. Phthalocyanines and their organo-metallic

complexes with transition metals are intensely coloured compounds with remarkable chemical and thermal stability. These properties aroused interest in their application as industrial dyes, which has been the largest application of these compounds since the first half of the twentieth century. However, the past four decades have witnessed a growing interest in advanced applications of phthalocyanines in a wide range of fields such as catalysis, chemical sensing, cancer therapy, molecular magnetism, optics, electronics and photovoltaics [68]. The chemical structure of the molecule, which was identified by Linstead and his collaborators in 1933, consists of a symmetrical planar macrocycle composed of four isoindoline units linked by aza nitrogen atoms, as shown in Figure 1.3. The macrocycle can accommodate cations, molecular groups or protons in the central cavity and at least 70 different phthalocyanine compounds have been reported. When Pc^{2-} binds to relatively small cations such as those from the first row of the d transition block and Pt(II), the planar geometry is retained and the molecule shows a D_{4h} point symmetry, while larger cations such as Pb(II) or the complex oxides (e.g. VO) induce a pyramidal deformation in the compound, reducing its symmetry. Even larger cations, such as lanthanides, form compounds where the cation is sandwiched between two phthalocyanine molecules. Metal phthalocyanines have very good thermal and chemical stability, and can generally be stored in ambient conditions without significant degradation [56]. Metal-free phthalocyanine is less stable to chemical attack and can undergo hydrolysis to phthalimide in strong acidic aqueous solutions.

Planar phthalocyanine molecules form various crystalline structures, which are labelled with Greek letters. All polymorphs are characterized by the presence of columns which consist of molecules stacked parallel to each other with a slight displacement in a direction parallel to the molecular plane, as shown in Figure 1.4.

The polymorphs differ in three aspects, defined in Figure 1.4 and 1.5: (i)

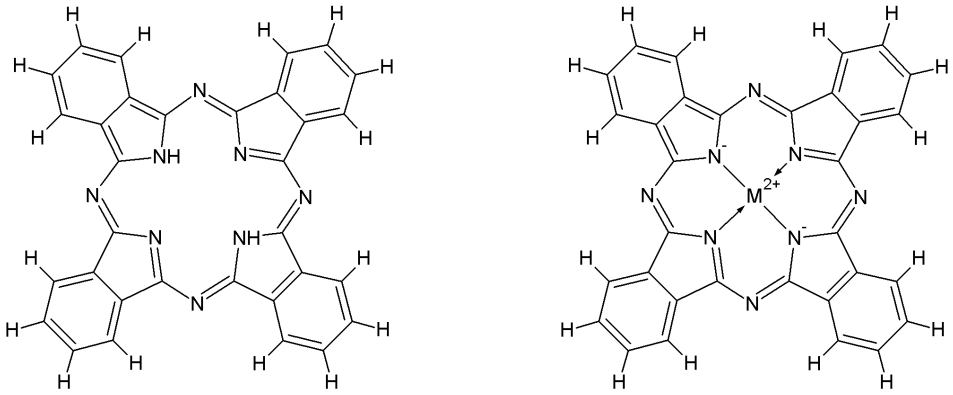


Figure 1.3: Chemical structure of metal free phthalocyanine H_2Pc (a) and of metal phthalocyanine MPc (b)

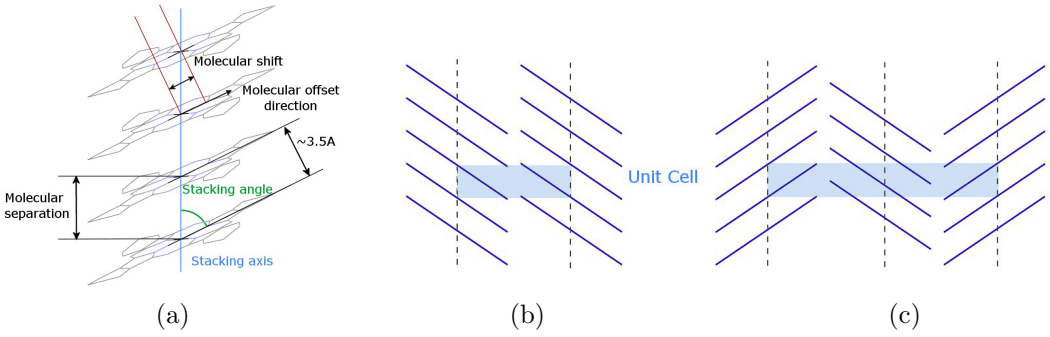
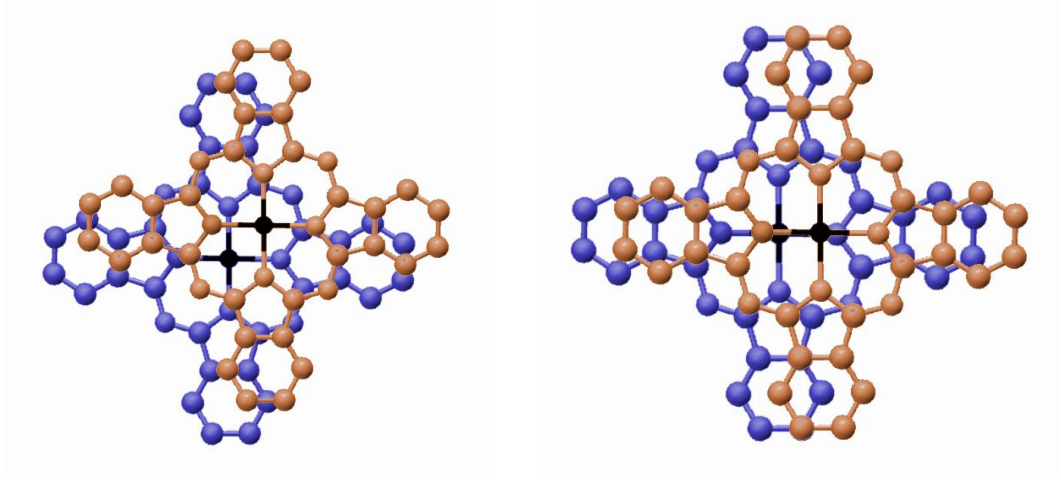


Figure 1.4: Definition of the geometrical parameters describing the arrangement of phthalocyanine molecules stacked in a column (a). Possible mutual arrangements of the columns in a crystal: (b) brick-stack and (c) herringbone arrangement. For the herringbone structure, the unit cell is doubled.



(a) (b)

Figure 1.5: Possible molecular displacement directions inside the phthalocyanine columns: at 45° with the directions defined by the four lobes of the molecule (a); along the direction of the lobes (b)

the stacking angle between the molecular plane and the column direction, (ii) the displacement direction and (iii) the mutual arrangement of the columns. It is believed that the polymorphs are isomorphous across the series of planar phthalocyanines, and only slight variations in the cell parameters are found between different phthalocyanines. The most common polymorphs are the α and β. The β polymorph, whose structure is shown in Figure 1.6, is thermodynamically more stable and this phase can be found in large needle-shaped single crystals obtained by sublimation, which allowed the determination of its crystal structure by X-ray diffraction. The β polymorph belongs to the monoclinic $P2_1/a$ space group with two non-equivalent molecules per unit cell and is characterized by a herringbone arrangement of the columns, with a stacking angle of about 45°; the direction of the molecular displacement inside the columns forms an angle of about 45° with the directions defined by the four lobes of the molecule.

The α polymorph is a metastable phase and this often prevents the growth of macroscopic single crystals; this polymorph undergoes a transition to the β phase at high temperature. The α phase can be obtained by vapor deposition of

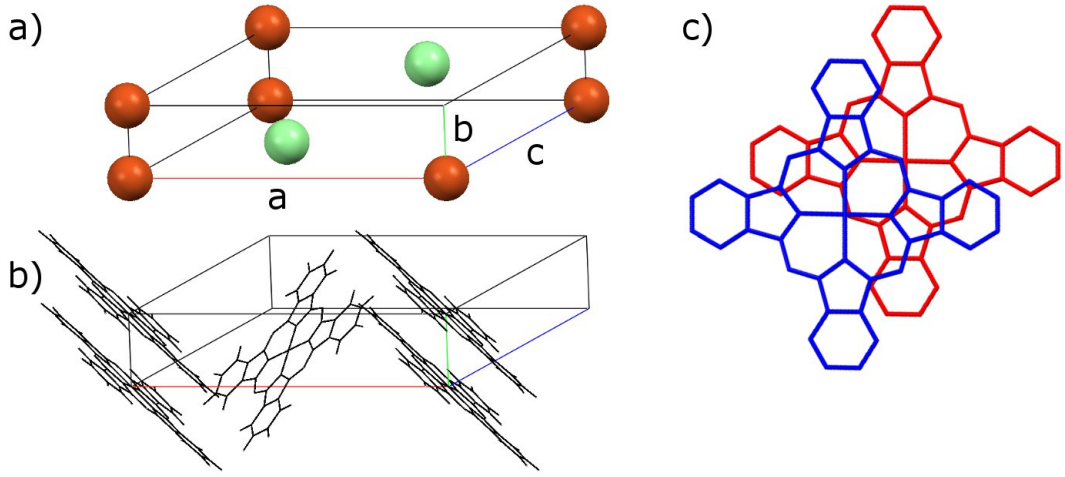


Figure 1.6: Crystal structure of β-CuPc, as determined by Brown [19]: a) is a representation of the crystal lattice, b) a schematics of the unit cell occupation by the phthalocyanine, c) is a projection of the stacking geometry on the plane of the molecules

thin films on substrates at room temperature or by re-crystallization in cold water of phthalocyanine solutions in concentrated sulphuric acid, a process referred to as *acid-paste*. Due to the absence of large single crystals, the structure determination of the α phase has been difficult and subject to controversy. According to recent studies [66] the most accurate structure determination seems to be the one obtained by Hoshino [43] on α-CuPc (Figure 1.7), who proposed a $P\bar{1}$ lattice with one molecule per cell, and a brick-stack arrangement of the phthalocyanine columns where molecules are stacked at an angle ϕ of about 65°; differently from the β phase, the molecular displacement is along the direction of the lobes.

The optical absorption spectrum of phthalocyanines in the visible region is largely determined by the properties of the organic ring, although the central atom can cause significant changes. Isolated phthalocyanine molecules with D_{4h} symmetry show a strong absorption band in the red portion of the spectrum, known as the Q band, and a Soret band (or B-band) occurring towards the UV region. The former band, occurring at energies around 1.8 eV-2 eV (620 nm-690 nm), is assigned to the first π-π^* transition of the organic ring and has a parallel polarization with

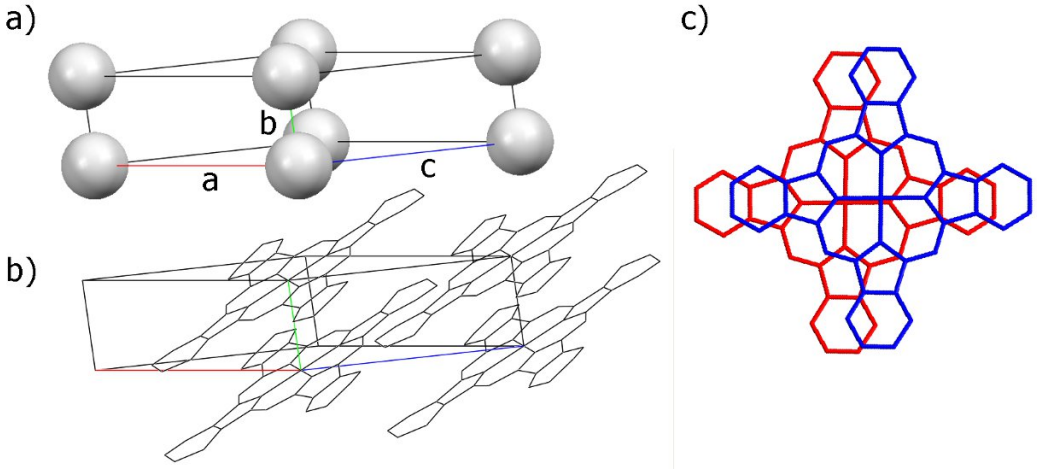


Figure 1.7: Crystal structure of α-CuPc, as determined by Hoshino [43]: a) is a representation of the crystal lattice, b) a schematics of the unit cell occupation by the phthalocyanine, c) is a projection of the stacking geometry on the plane of the molecules

respect to the molecular plane; the latter arise from higher energy transitions (e.g. to the first level above the lowest unoccupied molecular orbital, LUMO+1). Other bands, due to transitions having charge-transfer character between the metal and the ligand, can occur in some metal phthalocyanines. The absorption bands in phthalocyanine thin films are often split and significantly broadened, as shown for example by the spectrum of CuPc films presented in Figure 1.8; there are several explanations for these effects, which include, for example, the intermolecular coupling of the excited states, a possible lowering of the molecular symmetry in the crystal [63] or intermolecular charge transfer transitions.

Phthalocyanine films are p-type organic semiconductors; derivatives where peripheral hydrogen atoms have been substituted by electron withdrawing groups can show n-type character, as in the case of the perfluorinated phthalocyanine derivative which is presented in the next section. The hole mobility in single crystals is around $1\,\mathrm{cm^2\,V^{-1}\,s^{-1}}$ [79] along the stacking direction, where the overlap between the frontier orbitals (HOMO and LUMO) of neighbouring molecules is largest. Mobility is about three orders of magnitude lower along other crystal

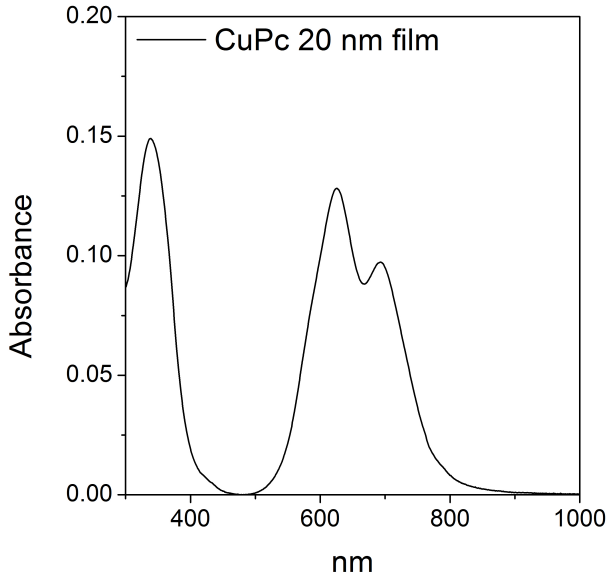


Figure 1.8: Absorption spectrum of a 20 nm copper phthalocyanine (CuPc) film deposited on glass

directions or in films [110], which show grain boundaries.

Many metal phthalocyanines have a magnetic moment resulting from the d electrons of the transition ion. As an example CuPc and CoPc have a spin $S = 1/2$, FePc has a triplet ($S = 1$) ground state, MnPc has spin number $S = 3/2$, while ZnPc, being a system with 10 d electrons (d^{10}), is diamagnetic. Despite having an incomplete d shell, NiPc (d^8) has no unpaired electrons because of its particular electronic structure. The electronic structure of the molecules, which determines their spin multiplicity and magnetic moment, depends on a number of factors, which are mainly: (i) the symmetry of the molecule, (ii) the amount of hybridization between the metal and the ligand orbitals, (iii) the magnitude of the spin orbit coupling in the metal ion, which increases with its atomic number. In the case of planar metal-phthalocyanines, the metal ion is surrounded by an environment with tetragonal symmetry; this is strictly true for molecules in vapour phase, but is a good approximation for phthalocyanine molecules in crystals, where the central atom is axially coordinated by nitrogen atoms from neighbouring molecules.

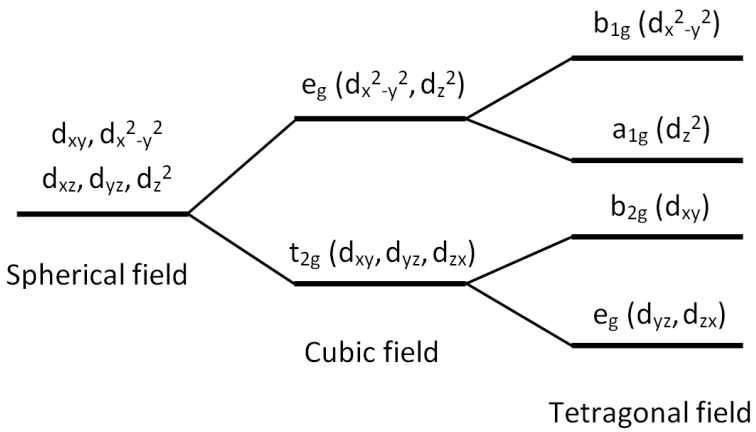


Figure 1.9: Splitting of the d levels of transition metals in ligand fields of cubic and tetragonal symmetry. The z axis is defined by the C_4 symmetry axis of the molecule

Figure 1.9 shows how a tetragonal configuration splits the 5 degenerate orbitals of the metal atom into four sets of orbitals; the highest orbital in energy is the $d_{x^2-y^2}$, which has b_{1g} symmetry, and the order in which the other orbitals are filled can vary between different metal-phthalocyanines.

1.3.1 Fluorinated phthalocyanines

Low atomic weight halogen elements like fluorine, chlorine and bromine are known for their high electronegativity, which gives them the ability to polarize the electronic density of the chemical bonds when attached to less electronegative atoms. Halogenation has been used to enhance the fire and chemical resistance of materials and to increase their hydrophobicity and lipophobicity [37]. In the field of organic electronics, it represents an important strategy used to improve device stability and optimize key processes such as charge injection/transport [91] or light absorption/emission [97] in organic semiconductors. The carbon-fluorine bonds can stabilize the HOMO and LUMO levels of the molecule by more than 1 eV [18], leading to less negative reduction potentials, which increases the stability against degradation by oxygen and moisture. The barriers for negative charge

injection in the LUMO also become smaller, reducing the need of highly reactive low workfunction metals in the cathode, like calcium, in favour of more stable alternatives, such as aluminium. Furthermore, electrons in deep LUMO levels are also less prone to trapping, resulting in considerably higher n-type mobility.

Fluorinated phthalocyanines form an important class of organic derivatives. The synthesis of F_{16}MPc was first described by Birchall in 1970 [12], however work on these compounds really thrived in the past 15 years, after the group of Zhenan Bao [7] published the first report of an air stable n-type FET transistor using F_{16}CuPc. Even if electron transporter organic semiconductors have become more available and efficient over the years, F_{16}CuPc still has competitive performances [96]. The interest in fluorinated phthalocyanines is not limited to organic electronics only, but encompasses the field of catalysis [10, 9, 61] and photodynamic therapy [75], in which they perform better than unsubstituted MPcs thanks to a higher chemical stability in harsh environments.

Density functional calculations show that the attachment of fluorine atoms to the organic ring of a phthalocyanine shifts the states around the Fermi level by a similar amount, meaning that the HOMO-LUMO gap and the relative position of the *d* levels of the transition metal are only weakly affected by the chemical modification [103]. The amount of the energy shift can be tuned by varying the amount of fluorine substitution [67], which is very useful for the optimization of charge injection in electronic devices [18]. Very recently, the group of Knupfer demonstrated that the increased electron affinity of F_{16}CoPc can be sufficient to promote the partial transfer of negative charge from an unsubstituted MnPc molecule in a co-deposited film [60], opening new engineering avenues for phthalocyanine materials. Mixed films of CoPc and F_{16}CoPc are studied in this work and presented in Chapter 6. Fluorinated phthalocyanines not only show interesting electronic properties, but also exhibit a growth behaviour of crystals and thin films which differs from MPcs, as discussed in Chapter 5.

1.3.2 Magnetic ordering in metal phthalocyanines

MnPc and FePc have attracted a lot of interest in the molecular magnets community because they show ferromagnetic ordering. β-MnPc was the first molecular magnet to be discovered [71], characterized by a positive Weiss constant of 23 K and a Curie transition temperature of 8.6 K. The material has been described as a *canted* ferromagnet, a behaviour schematized in Figure 1.10; a relatively large and negative magnetic anisotropy (zero field splitting) of the spin centre force the magnetic moments to be perpendicular to the molecular plane and this prevents a complete alignment of the spins with the magnetic field at moderate field strength. The

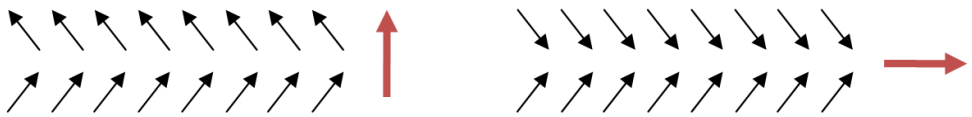


Figure 1.10: Canted ferromagnet with ordered (opposed) spins. Individual spins are represented by black arrows; the rows of spins represent spin chains coupled ferromagnetically. The resultant magnetization of the material is shown by the red arrow. The two possible orientations of the magnetization can be determined by an external magnetic field, or by the inter-chain magnetic coupling

magnetic properties are dramatically different in the α-MnPc polymorph, which is a weak antiferromagnet, with a Weiss constant around -3 K [106]. This highlights the importance of molecular overlap in the coupling (as explained in section 1.2.5). Indeed the switching of the magnetic properties in MnPc has been attributed to a change from the superexchange coupling mechanism in the β phase to the indirect exchange one in the α-phase [102]. On the contrary, ferromagnetic ordering was observed in the α polymorph of iron phthalocyanine with a Weiss constant of 40 K, while ordering is not observed in the weakly ferromagnetic β polymorph [34]. In the latter case, the positive magnetic anisotropy of FePc ($S = 1$) dominates over the ferromagnetic spin coupling interaction and forces the spins on the molecular plane (as in the XY model, section 1.2.3), determining a ground state with $S_z = 0$. A remarkably high magnetic coupling has recently been discovered in CoPc, where

Inelastic Electron Tunnelling Spectroscopy (IETS) highlighted antiferromagnetic coupling of the order of 200 K [23]. This result exceeds largely the magnitude of spin-spin couplings reported in phthalocyanine compounds so far, and it suggests, for the first time, that phthalocyanines may enable the fabrication of organic spin devices that operate at temperatures achievable with "cheap" refrigeration methods like, for example, cooling with liquid nitrogen. For these reasons my project initially focused on the fabrication and characterization of CoPc samples, with the aim of finding independent and complementary characterization of the spin coupling interaction, using experimental techniques such as SQUID magnetometry and electron spin resonance. The next section will expose a review of the literature available on cobalt phthalocyanine.

1.3.3 Cobalt phthalocyanine

Cobalt phthalocyanine (CoPc) is a planar organic molecule as most first row transition metal phthalocyanines (MPcs). The cobalt ion is in a 2+ oxidation state (d^7 electronic configuration) and is found in a low spin $S = 1/2$ state due to the square planar ligand field of the organic ring. CoPc is an organic semiconductor and has been studied in thin film field effect transistor devices, where it exhibits hole transport with mobilities (μ_h =$1.0 \times 10^{-4}\,\mathrm{cm^2\,V^{-1}\,s^{-1}}$–$2.6 \times 10^{-4}\,\mathrm{cm^2\,V^{-1}\,s^{-1}}$) comparable to those measured in copper phthalocyanine (CuPc) [110]. Among MPcs, CoPc demonstrated remarkable chemical sensing [100, 51, 110] and catalytic properties [47, 87, 81, 98, 88]. These qualities arise from the chemical stability of CoPc and the enhanced chemisorption of oxygen and other small molecules on the cobalt ion.

Recently several studies focused on the electronic properties of CoPc films and molecules adsorbed on metallic surfaces using scanning tunneling microscopy and spectroscopy [42, 113, 45, 23, 39], X-ray absorption and photoelectron spec-

troscopy [53, 65, 2, 54]. These studies helped to elucidate the ground state electronic structure of CoPc, since ab-initio calculations point towards at least two possible electronic configurations for the ground state [53]. The experimental evidence obtained on CoPc thin films points towards a ground state with a half filled cobalt d_{z^2} orbital [54]. The configuration might differ at the interface with metallic substrates, where hybridization of molecular and metal states or quenching of the magnetic moment due to charge transfer are often observed [23, 17]. A number of studies reported strong coupling of the magnetic moment of the first molecular layer with the substrate, including the observation of the Kondo effect in distorted CoPc molecules on gold [113] and ferromagnetic exchange with magnetic substrates such as iron [2], or cobalt [55]. Even when the magnetic moment is strongly reduced as in CoPc deposited on an Fe thin film [2], the magnetic substrate can still induce high local spin polarization on the organic molecule [17]. At the boundary between studying surface monolayers and molecular thin films, Chen and co-workers [23, 39] performed inelastic scanning tunneling spectroscopy to investigate CoPc nanostructures up to 5 monolayers (ML) thick on Pb islands at sub-Kelvin temperatures (T =400 mK). Their study showed that while the CoPc molecules directly in contact with the substrate are magnetically quenched, from the second ML CoPc preserves its $S = 1/2$ state. Most importantly, Chen *et al.* were able to measure tunneling resonances assigned to spin-flip excitations in antiferromagnetic chains formed by stacked CoPc molecules. By fitting the measurements of the excitation spectra in regions of different molecular thickness, a Heisenberg exchange energy $2J$ =18 meV was calculated for the CoPc antiferromagnetic chain [23]. This was the first example of spin exchange interactions in a phthalocyanine with an energy comparable to the temperature of the boiling point of liquid nitrogen (J/k_BT =105 K) and represents one of the highest exchange energies known in organic magnetic materials. STM images showed that the molecular stacking angle in the CoPc nanostructures studied by Chen

is $\approx 60°$, very close to the one found in the $\alpha-$CoPc phase, suggesting that this well known polymorph should exhibit a similar property. The initial part of my work, discussed in Chapter 3, aimed at demonstrating that Chen's result can be extended to thin $\alpha-$CoPc films with thickness of the order of 100 nm, more relevant to organic electronics applications. The antiferromangetic interactions in the sample were studied by using Superconducting Quantum Interference Device (SQUID) magnetometry, which, differently to Chen's experiment, can probe the spin correlations at temperatures around J/k_BT and above.

1.4 Thesis layout

In the subsequent chapters this thesis develops as follows. The second chapter will describe the experimental methods followed for the preparation of the samples and their characterization, providing also basic knowledge about the instruments and techniques used.

The third chapter will expose experimental results obtained on cobalt phthalocyanine thin films and powders, including magnetic, morphological, crystallographic and spectroscopic characterization of the material. The discussion will compare the properties of the α and β CoPc polymorphs and a great attention will be given to the magnetic behaviour, which differ dramatically between the two polymorphs. A detailed analysis of the magnetic data will be provided to quantify the strong antiferromagnetic coupling observed in the α polymorph of cobalt phthalocyanine. Chapter four will deal with the characterization of the structural, spectroscopic and magnetic properties of a novel CoPc nanowire phase obtained by vapour deposition.

The following two chapters present the investigation of organic films based on perfluorinated CoPc (F_{16}CoPc). Chapter five deals with pure F_{16}CoPc films and focuses on the study of the thickness dependence of the crystalline structure and

other properties, including magnetism, while chapter six introduces blending of functionalized phthalocyanines as a strategy for novel organic magnetic materials. This section will discuss preliminary results obtained on mixed films of F_{16}CoPc with CoPc grown by organic molecular beam deposition, with emphasis on the modification of the magnetic properties and the assessment of the degree of structural ordering and intercalation of the two molecules in the film.
Chapter seven concludes the thesis summarizing the main achievements and outlining future work.

Chapter 2

Experimental methods

2.1 Purification of materials

About 300 mg of unpurified powder were loaded in a ceramic crucible, which was positioned inside a quartz tube. A kapton film was inserted in the tube to cover the deposition zone and ease the collection of crystals. The quartz tube was introduced in a three zone furnace and was connected on one side to a nitrogen line through a flow meter, which kept the flow at 300 standard cubic centimetres (sccm); on the other side it was connected to a rotary vacuum pump. The pressure inside the tube was monitored with a pirani gauge and was kept around 6 mbar using a regulating valve to control the suction from the pump. During the growth, the three zones of the furnace were set to temperatures of 475°C, 465°C and 460°C going from the source side to the deposition side; this created a temperature gradient that allowed the separation of CoPc from impurities with a higher sublimation temperature, while the most volatile impurities were removed by the flow of carrier gas.

2.2 Growth of organic nanostructures

2.2.1 OMBD growth of thin films

Thin organic films were grown at room temperature on kapton (polyimide, DuPont), glass and crystalline silicon wafers using a "Spectros" organic molecular beam deposition (OMBD) system manufactured by Kurt J. Lesker, schematically shown in Figure 2.1. The substrates were cleaned prior to deposition by washing and sonicating in acetone for 10 minutes and then repeating the procedure in isopropanol. After cleaning, the substrates were dried with compressed air and subsequently mounted on a substrate holder for loading in the OMBD chamber. The holder has a 10 cm x 10 cm size, limited by the size of the substrate shelf inside the chamber. Ceramic crucibles were filled with the organic powder to be sublimed and were placed inside the chamber in thermal evaporation sources known as Knudsen cells. The chamber was pumped down; when the base pressure reached a value around 1×10^{-7} mbar–1×10^{-6} mbar, preheating of the Knudsen cells to a temperature slightly below the sublimation point of the compound was started in order to de-gas the source material; during this phase both the source shutter and the substrate shutter were held closed. After the source temperature was stable for at least 15 min, only the source shutter was opened, and the heating of the crucible was adjusted automatically by a feedback loop in order to achieve a stable deposition rate at the desired value. The deposition rate is monitored by quartz microbalances (QCM) placed close to the source: deposition on the surface of the quartz crystal changes its resonance frequency, which is converted to the actual deposition rate on the substrate by using appropriate calibration parameters. When the rate was stable at the desired value, the substrate shutter was opened and the software started to measure the thickness of the film deposited on the substrate; the substrate shutter was closed and the deposition stopped when the desired thickness was reached. The thickness and rate of deposition of CoPc

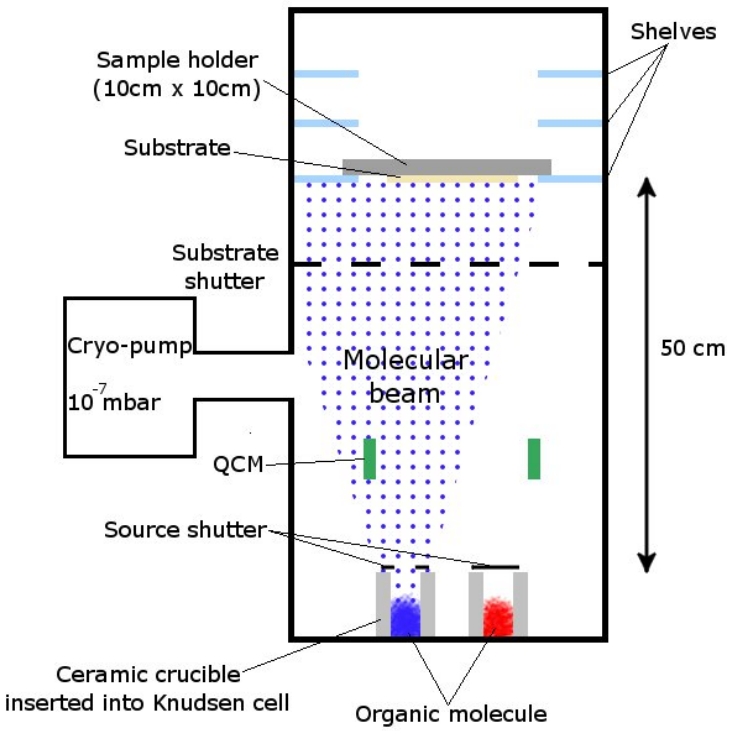


Figure 2.1: Schematics of the OMBD chamber. QCM are quartz-crystal microbalances used to monitor the growth rate; the substrate shutter is opened only when the sublimation rate stabilizes at the desired value, and is closed again when the desired thickness is achieved.

films was controlled using a set of calibration parameters obtained for copper phthalocyanine, assuming that cobalt phthalocyanine has similar adhesion energy on the substrates. CoPc films with a 200 nm and 400 nm thickness were deposited at a rate of 1 Å/s. In the case of templated CoPc films, the substrates were first coated with a perylene-3,4,9,10-tetracarboxylic dianhydride (PTCDA) templating layer (20 nm) grown at 0.2 Å/s, and then the CoPc layer was deposited. The OMBD system allows the use of masks to define the deposition area on the substrate. The masks are mounted on a specific holder which can be placed in front of the samples, or removed, with a mechanical arm without the need of breaking the vacuum. An aluminium mask was used during the growth of CoPc films for magnetic characterization, as described in section 2.3.7.

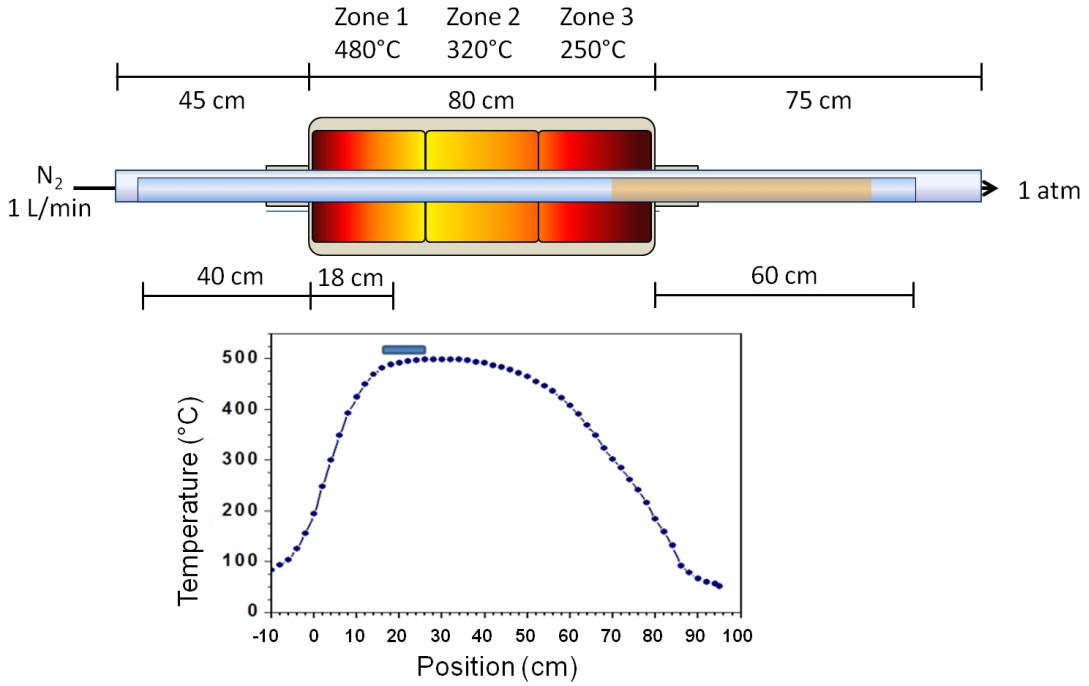


Figure 2.2: Schematics of the OVPD system used for the growth of CoPc nanowires. The steady-state temperature profile was measured by Zhenlin Wu [104]

2.2.2 OVPD growth of nanowires

The organic vapor phase growth method used for CoPc nanowires presents only minor modifications from the one described in [95]. The process is carried out on a setup is schematized in Figure 2.2. An Elite TMH12/75/750 furnace with three independently controlled heating zones, set to 480°C, 320°C and 250°C respectively, is loaded with an outer quartz tube (200 cm long and 5.4 cm in diameter) that contained an inner quartz tube (180 cm long and 4 cm in diameter). A rectangular alumina crucible (100 mm in length, 10 mm in width and 5 mm in depth) containing the organic material, is placed in the inner tube, in a position corresponding to the hottest part of the furnace, about 18 cm inside the first zone. The other end of the inner tube, where condensation of the material occurs, is lined with a film of kapton in order to ease the collection of the material and to reduce contamination of the tube. During the growth, the left end of the outer tube is

connected to a nitrogen line which provides inert gas at atmospheric pressure and constant flow rate (1000 sccm), while the opposite end leads to the exhaust line through a trap, which condenses residual vapours of organic molecules. Before heating the furnace, the tubes are purged with nitrogen for at least 30 minutes. After the system has reached a stationary state during the process, the thermal gradient through the furnace assumes the profile shown in Figure 2.2. The temperature reaches the maximum value of 480°C in the region between zones 1 and 2. The temperature in zone 2 overshoots the set values due to insufficient insulation which causes heat transfer between the zones. The temperature decreases smoothly through the third zone and reaches about 40°C just outside the furnace. A typical nanowire deposition takes place over two days.

2.2.3 Preparation of nanopowders (acid paste)

Acid pasting of cobalt phthalocyanine powder was used to produce α-CoPc nanocrystals. First, 0.5 ml of concentrated sulphuric acid (98% wt) and 15 ml of distilled water were poured inside different graduated glass cylinders and submerged in an ice/water bath for 15 minutes. 300 mg of cobalt phthalocyanine powder were dissolved in the cold sulphuric acid, obtaining a dark green solution which was then poured in the cylinder containing cold water. The blue precipitate obtained in water was filtered on a Buchner funnel using a water pump and washed twice with water and once with ethanol. The powder was dried overnight in a desiccator and then ground in a mortar.

Variations in acid paste CoPc powders characteristics

There are several variations of the acid pasting process for the preparation of the α phase phthalocyanines. In a typical experiment, the phthalocyanine solution in sulfuric acid is diluted into chilled water to induce precipitation of the phthalocyanine. The precipitate is the filtered and washed abundantly with water. Mauthoor

noted that this method could be optimized to minimize the hydrolysis of the phthalocyanine, especially H_2Pc, in acidic aqueous solutions [66]. In the modified process, cold isopropanol is used instead of water to precipitate phthalocyanine. Both methods were used to prepare α-CoPc powders. It was found that the use of isopropanol results in the formation of a suspension of CoPc particles of much finer size than when just water is used. Indeed, a qualitative filter paper with average pore size of 10 microns was sufficient for filtering the suspension in water, while a higher grade paper with pore size of ≈ 1 micron was needed for retaining the suspension in isopropanol. XRD measurements (Figure 2.3) show that the α form of CoPc is found in powders obtained with both methods, although there are visible differences in the diffraction peak widths and relative intensities. Powders precipitated in water show better resolved XRD patterns than those obtained from precipitation in isopropanol, which hints towards a larger crystallite size in the former. Therefore precipitation in water was the preferred method as the characteristics of the material can be studied with a higher degree of confidence. Other process parameters such as the temperature of the solutions or the duration of the individual steps have an effect on the final characteristics of the material, however these aspects were not thoroughly investigated as they were beyond the scope of this work.

2.3 Characterization of the organic nanostructures

The starting point in the characterization of a material is the study of the materials' morphology, purity, thickness (in the case of films), particle size, crystalline phase and preferential orientations. After an understanding of the materials' characteristics is obtained, more specific experiments are performed to determine the

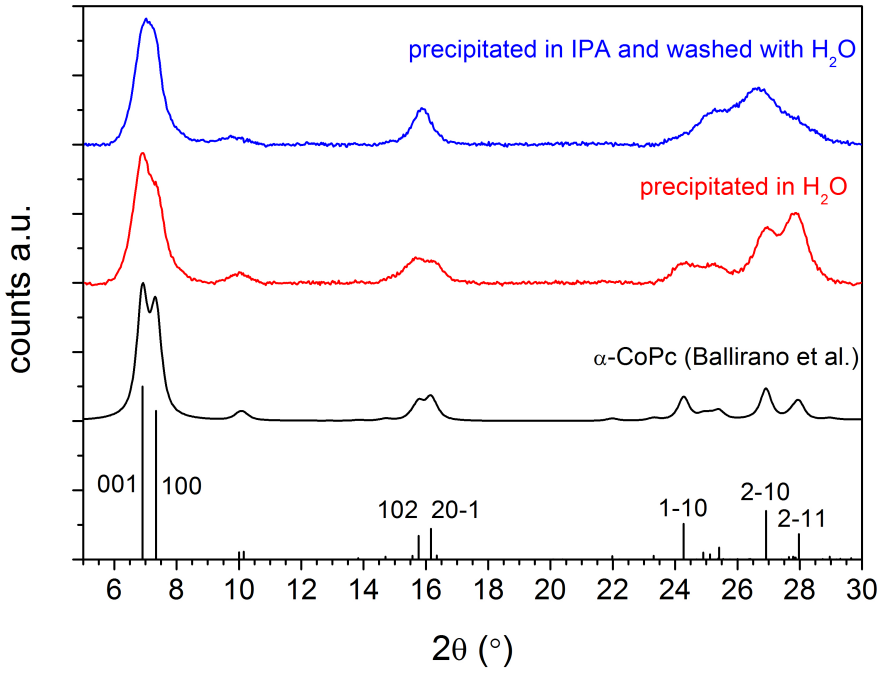


Figure 2.3: Differences in diffraction patterns of acid paste α-CoPc powders precipitated in isopropanol and water. The conditions of re-precipitation control the average grain size in the powder. A simulated α-CoPc pattern with a peak FWHM=0.424° is also shown

magnetic or electronic properties of the material. Finally, we aim at obtaining a unifying description of the material which correlates the magnetic and electronic properties with the structural characteristic of the sample. The following section will describe the techniques used to characterize the samples.

2.3.1 Scanning electron microscope

Scanning electron microscopy is a surface imaging technique that uses a focused electron beam to collect information about the sample's morphology or composition. The beam is formed by electrons emitted by a heated filament, or a field emission gun, which are then accelerated to an energy between 5 and 30 kV, collimated and focused by the microscope optics to a spot which is scanned on the surface of the sample. The impact of the beam on the sample causes the emission of low energy secondary electrons (SE), backscattered electron (BSE) and X-rays,

which can be separately detected to collect a two dimensional image of the surface of the sample. The secondary electrons are emitted with a high yield and have the shortest sampling depth, of the order of a 10 nm, so their intensity is strongly sensitive to the surface topography; therefore SE are preferred for high resolution imaging of the morphology of nanoscopic materials. The samples have to be conductive; insulating or poorly conducting materials can be coated with a thin layer of a metal (e.g. Cr) to ensure that the charges are dissipated.

Experimental

The SEM system used for both plane view and cross section imaging of the samples presented in this work is a LEO GEMINI 1525 FEGSEM which operates with a field emission gun and has a ultimate resolution of ≈3 nm. The system operates at a high vacuum (≈ 10^{-6} Torr). The images collected with an InLens detector for the secondary electrons, using a 5 kV electron beam and a working distance around 5 mm. A conductive layer of chromium is deposited on the films to prevent surface charging using an Emitech K-575X sputter coater. Normally samples were coated at a sputtering current of 100 mA for 1 minute, which yields a layer of ≈20 nm of chromium. Samples with a smaller particle size were coated for 30 seconds in order to obtain a thinner coating (≈10 nm). Cross-section images were only taken in films deposited on silicon, which were freshly cleaved before imaging.

2.3.2 X-ray diffraction

X-ray diffraction is a non destructive technique that allows the investigation of the crystallographic structures of materials. The measurement involves the irradiation of the sample with a collimated beam of X-rays with a specific wavelength and the measurement of the intensity of the radiation scattered by the sample. When an atom is hit by X-ray radiation, its electrons oscillate at the same frequency of the electromagnetic radiation producing a scattered wave of X-rays. In amorphous

materials where the atoms are arranged in a disordered array, the combination of the scattered waves will lead to destructive interference in all directions and little intensity will be recorded by the instrument. However, in a crystalline solid, where the atoms are organized in a periodic fashion, there will be a few directions in space where all waves scattered by the crystal are in phase, generating a diffracted beam.

Crystal lattice

A crystal is defined by a periodic arrangement of atoms in the three dimensions. The smallest repeating unit of the structure is called the unit cell, which is delimited by three unit vectors, named **a**, **b** and **c**. The directions of these vectors are called crystal axes, while their lengths a ,b, c, and the angles between them, α, β and γ are known as lattice constants or parameters. The crystallographic planes of the structure are indicated by integer Miller indices (hkl), which correspond to the reciprocal of the intercepts of the plane with the three crystal axes. Each crystallographic plane is periodically repeated in the structure with a spacing d which depends on the Miller indices and the lattice constants.

Bragg's law

A beam of X-ray radiation incident on a set of crystallographic planes will be specularly reflected if the angle of incidence θ satisfies the Bragg's law:

$$2d\sin(\theta) = n\lambda \tag{2.1}$$

where d is the inter-planar distance for a particular set of crystallographic planes, λ is the wavelength of the X-rays and n is an integer number. Values of θ for which Equation 2.1 is verified are also called Bragg angles. Since the wavelength of the radiation is known, the value of d can be calculated. Similarly, by knowing the crystal structure, the Bragg angle can be obtained from the equation. An

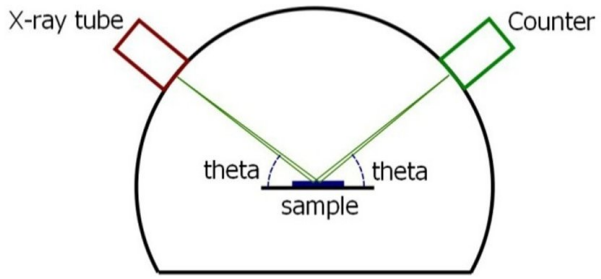


Figure 2.4: Schematics of the X-ray diffractometer in a Bragg-Brentano configuration

X-ray diffraction measurement is commonly done in the Bragg-Brentano (or θ-2θ) geometry (Figure 2.4), where the sample stage is held horizontal while the X-ray tube and the detector are moved at the same angular speed in opposite directions geometry shown in Figure 2.4; in this configuration only the crystallographic planes parallel to the sample plate can be detected.

Determination of crystallites sizes

When the size of a crystal is below 200 nm, the diffraction condition set by the Bragg's law is relaxed and some diffraction intensity will be measured near the Bragg angle. The result is an increase of the full width at half maximum (FWHM) of the peak of diffracted intensity as a function of the θ angle. Even in an infinite crystal, the peak would have a finite width due to an instrumental broadening, w_{inst}. The intrinsic width w due to a small crystal size and the instrumental contribution will be convoluted into a measurable experimental broadening w_{exp}. Two corrections have been proposed for calculating w [26], which apply in the case where the broadening functions can be represented by Lorentzian (Equation 2.2) or Gaussian (Equation 2.3) functions:

$$w = w_{exp} - w_{inst} \tag{2.2}$$

$$w^2 = w_{exp}^2 - w_{inst}^2 \tag{2.3}$$

The Scherrer equation (Equation 2.4) provides a means of estimating the size τ of the crystalline grains [26]:

$$\tau = \frac{K\lambda}{w_{2\theta}\cos(\theta)} \tag{2.4}$$

where K is a dimensionless shape factor, λ is the X-ray wavelength, $w_{2\theta}$ is the (corrected) full width at half maximum of the peak in 2θ radians, and θ is the Bragg diffraction angle.

Experimental

A Philips X'Pert PRO PANalytical X-Ray Diffraction system is used for the characterization of the structure and orientation of materials. The system operates in the θ-2θ mode (Figure 2.4). The sample stage was set spinning during the measurement in order to average signal at different orientations; this did not alter the results as the grain orientation of the samples studied has azimuthal symmetry. The X-ray tube uses the K_α emission of a copper target to generate X-ray radiation with a wavelength of 1.54 Å. Typical scans were performed in the range $5° < 2\theta < 30°$, with 2θ step size of 0.033° and a duration of approximately 10 minutes.

Except where otherwise stated, the peaks are fitted with Lorentzian functions, despite this was not always the best choice for fitting the entire peak profile. The intrinsic peak width w was estimated by correcting the FWHM of the fit (w_{exp}) with the instrumental broadening w_{inst}; this was taken equal to 0.08° in the $5° < 2\theta < 10°$ range and 0.13° in the $25° < 2\theta < 30°$, as determined from the measurement of large single crystals. The two values of w, obtained through Equation 2.2 and Equation 2.3, where used to calculate the crystallographic grain size using the Scherrer equation 2.4, with $K = 1$; the two results have been used as an estimate of the uncertainty of the size of the crystallites.

2.3.3 UV-Visible absorption spectroscopy

UV-visible absorption spectroscopy is a technique that probes electronic excitations in a material, usually a solution or an optically transparent film. The spectral range investigated normally spans from the near infrared ($\approx$ 1000 nm) to the UV ($\approx$ 300 nm). When light hits the sample, the electron density in certain parts of the molecules, called chromophores, can resonate with the electromagnetic radiation at particular wavelengths and bring the molecule in an excited electronic state, with the absorption of a photon during this process.

A particularly important transition is the one between the Highest Occupied Molecular Orbital (HOMO) and the Lowest Unoccupied Molecular Orbital (LUMO) of the molecule, whose energy determines the optical gap of the material. In organic conjugated molecules, these two orbitals usually correspond to the bonding (π) and antibonding (π^*) states of the conjugated system. In the case of phthalocyanines, the transition leads to the appearance of the Q absorption band, which is usually centred around 650 nm.

Exciton coupling

The electronic transitions characteristic of single molecules are affected in several ways by the intermolecular interactions occurring in solids. In general, a lowering of the symmetry and the elecrtostatic interactions between the chromophores (excitonic coupling) lead to shifts and splitting of the absorption bands. In the case depicted in Figure 2.5 an electronic transition splits into two excitations with different energy and oscillator strengths, f_1 and f_2. The oscillator strengths of these excitonic transitions depend on the geometry of the interaction between the chromophores. In a sideways alignment of the molecular transition dipoles, similar to that of a "H aggregate", the lowest excitonic energy state shows an out of phase relation between the oscillating electron densities on the two interacting

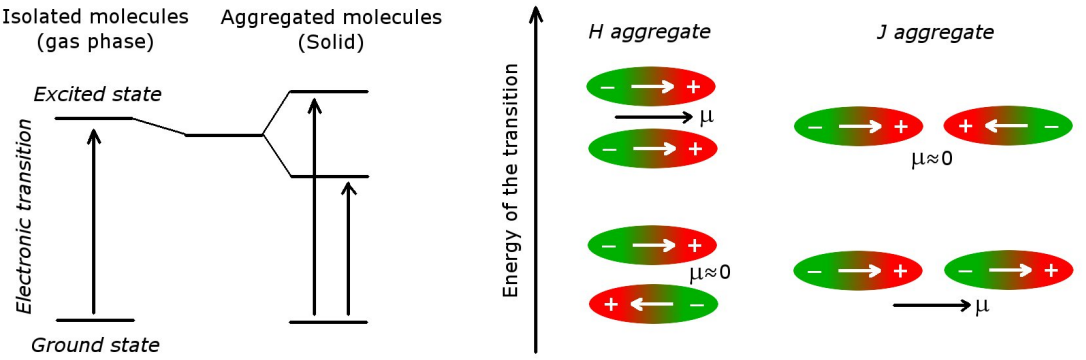


Figure 2.5: Left: energy diagram of an electronic transition in an isolated molecule and in a solid. The ground and excited levels can be modified by dispersion interactions in the solid state. The intermolecular interaction of the chromophores in the solid leads to a splitting of the excited state into, at least, two excitonic levels, with different oscillator strengths, f_1 and f_2. Right: the oscillator strengths of the excitonic transitions are shown in the case of a sideways (H aggregate) and a head to tail (J aggregate) alignment of the molecular transition dipoles.

molecules, which leads to a zero total oscillator strength. In the higher energy excitonic state the electron densities of the molecules oscillate in phase, and the oscillator strength is high, leading to a blue-shifted absorption compared to the isolated molecule. When the transition dipoles of the chromophores are aligned in a head to tail fashion, as in a "J aggregate", the lowest excitonic state has a large oscillator strength, causing a red-shift in the absorption spectrum. In the intermediate cases, both blue- and red-shifted components will occur in the spectrum, with splitting and relative intensities determined by the actual configuration of the chromophores in the solid. In phthalocyanine materials, the characterization of the Q band absorption pattern constitutes a valuable tool for the identification of the polymorph type.

Lambert-Beer law

The UV-Visible absorption measurement can be used to quantitatively measure the concentration of a solution or the thickness of a film of a light absorbing molecule. In order to quantify the amount of light absorbed by the sample, the

absorbance (A) is defined as the logarithmic ratio between the intensities of the incident (I_0) and transmitted light (I_T):

$$A = \log(\frac{I_0}{I_T}) \tag{2.5}$$

The relationship between the absorbance and the concentration of a solution is expressed by the Beer-Lambert Law, as in Equation 2.6:

$$A = \epsilon l c \tag{2.6}$$

where ϵ is the molar absorption coefficient, that is wavelength dependent and characteristic of each compound, l is the length of the optical path through the solution, and c is the molar concentration of the solution. An equivalent law exists for thin films, which links the absorbance to absorptivity of the material (α) and the film thickness (L), as shown by Equation 2.7:

$$A = \alpha L \tag{2.7}$$

Due to the broadening and splitting of the absorption bands in the solid state, in the case of thin films it is significantly more accurate to consider the integral of the absorbance of a particular band rather using a single wavelength.

Experimental

In this work a Perkin Elmer Lambda 25 UV-Vis spectrometer was used to obtain the UV-Vis absorption spectra, scanning a wavelength range between 300 and 1100 nm, with a resolution of 1 nm.

2.3.4 X-ray photoelectron spectroscopy

X-ray photoelectron spectroscopy (XPS) is a technique used for studying the elemental composition and the chemical environment of the different species at the surface of a solid sample; in a typical experiment, the first 10 nm from the surface are probed. During an XPS experiment, the samples are irradiated with monochromatic X-ray radiation, which is either transmitted, scattered or absorbed by the atoms in the material. In the latter case, the atoms may be ionized and the electrons that are emitted from within 10 nm from the surface, will be able to escape from the sample without loosing energy in inelastic collisions; therefore the maximum sampling depth is around 10 nm. The yield of the photoemitted electrons is measured as a function of their kinetic energy (K.E.). The photoelectron counts in an XPS spectra are usually shown as a function of binding energy (B.E.), *i.e.* the minimum energy needed by the electron to escape from the bound state, which can be calculated from Equation 2.8:

$$B.E. = h\nu - K.E. - \phi \tag{2.8}$$

where $h\nu$ is the energy of the X-ray photons and ϕ is a correction to take into account the workfunction of the instrument. As a first approximation, the binding energy can be assumed to be equal to that of the atomic level from which the electron was emitted (Koopmans' theorem). Therefore the presence of a particular element is revealed by peaks at characteristic values of binding energies. The position of these peaks can shift slightly depending on the oxidation state of the atom and its local chemical environment.

Experimental

The XPS measurements discussed in Chapter 6 were performed using a Thermo Scientific k-Alpha XPS (typical base pressure of $2\text{x}10^{-9}$ mbar). Al K_α X-rays with

photon energy of 1486.6 eV were incident upon the sample with a spot size of 400 μm. The photoelectrons were collected and their kinetic energy measured using a hemispherical electrostatic energy analyzer. The binding energy was calculated as in Equation 2.8, with ϕ equal to the workfunction of the spectrometer; no further correction was applied. The peak positions were found in reasonably good agreement (within 0.4 eV) with the literature [74, 76].

2.3.5 Inductively Coupled Plasma Atomic Emission Spectroscopy (ICP-AES)

Inductively coupled plasma atomic emission spectroscopy (ICP-AES) is a highly sensitive analytical technique used for detecting trace amounts of metal ions. The sample is dissolved in a solution which is nebulized into an argon gas plasma flame. Due to the high temperature, the analyte solution is immediately decomposed into its constituent atoms, which become electronically excited in the plasma and emit photons with a spectrum characteristic of the element. With the use of a monochromator and a photodetector, the intensity of a specific line of the atomic emission spectrum can be measured and used to quantify the concentration of a particular element; ICP-AES is able to detect most cations and some anions. Before any sample analysis, an instrumental calibration measurement, using a series of standard solutions of known concentrations of the elements of interest, is needed. There are several methods used for preparing a solution suitable for ICP-AES from a solid sample. The one used in this work is an "acid digestion" method adapted to phthalocyanines and is described in the following section.

Experimental

The solutions for ICP-AES analysis were prepared from CoPc powders using the following method. 5 mL of 98% H_2SO_4 was added under the fumehood to 83.03

mg of CoPc powder in a 100 mL glass beaker with a magnetic stirrer. The beaker was covered with a watch glass and heated to 80°C on a hot plate while stirring. After 30 minutes, when the powder was completely dissolved, the beaker was removed from heat and allowed to cool down to room temperature. 5 mL of HNO_3 (68%) were then added to the beaker, which was stirred on the hot plate at 80°C. After 35 minutes, a further amount of 5 mL of HNO_3 was added to the solution, which was left stirring at 80°C covered by the watch glass. Twenty minutes later, the temperature of the hot plate was set to 100°C. After 15 minutes at this temperature, the watch glass was removed from the beaker. A hour later, the temperature of the hot plate was set to 320 °C. HNO_3 fumes developed from the solution. Thirty minutes after the HNO_3 fumes had stopped, the temperature was raised to 330 °C, and 15 minutes later to 350°C, in order to boil the H_2SO_4 off the solution. When the volume of the solution was reduced to 1-2 mL, the beaker was removed from heat and allowed to cool down to room temperature. The acidic solution was diluted to 25 mL with double distilled water. The solution had a nominal cobalt concentration of 212 ppm, calculated as the weight fraction of cobalt over the mass of the solution.

2.3.6 Electron Paramagnetic Resonance

Experimental

A Bruker ESP300 spectrometer was used to measure the EPR spectra of the powder samples studied in Chapter 3. These were placed into a quartz tube, purged with argon and sealed. The tube was loaded into the resonator cavity and cryogenically cooled with liquid helium vapours. Microwaves of 9.37 GHz frequency (so called "X-band" measurements) were used to irradiate the sample, with their absorption measured by the spectrometer. The microwave cavity was situated between two electromagnets, with the magnetic field swept between 0

mT and 550 mT. Variations in microwave absorbance were then measured (in derivative mode) as a function of the applied magnetic field. Simulations of the spectra were performed using the Easyspin package available for MATLAB

2.3.7 Superconducting Quantum Interference Device (SQUID) magnetometry

The superconducting quantum interference device (SQUID) magnetometer is one of the most sensitive instruments for measuring magnetic moments. SQUID magnetometers are able to measure changes in the small magnetic moment of the sample with sensitivities down to $10^{-11}\,\mathrm{A\,m^2}$ ($10^{-8}\,\mathrm{emu}$), in a wide range of applied magnetic fields and sample temperatures. SQUID instruments are induction-based systems where the sample is moved along the direction of the applied field through a set of pick up loops, called gradiometer. The variable magnetic flux inside the coils caused by the moving sample induces a current in the gradiometer, according to Faraday's Law of induction. The gradiometer is inductively coupled to a SQUID which converts the magnetic flux to a voltage signal with high gain and low noise. The SQUID is made of a superconducting loop interrupted by thin tunnel barriers (Josephson junctions) and its operation relies on the Josephson effect. The signal measured on the SQUID is fitted to a model function in order to derive the magnetic moment of the sample. The instrument used in the experiments is a MPMS7 system manufactured by Quantum Design. A schematic cross section of the instrument is provided in Figure 2.6.

The instrument allows measurements of magnetic moments in a magnetic field up to $\pm 7\,\mathrm{T}$, in a temperature range comprised between $2\,\mathrm{K}$ and $400\,\mathrm{K}$. The instrument sensitivity depends on the magnetic field and the specifications are reported in Table 2.1.

The SQUID, the superconducting gradiometer and magnet only operate at

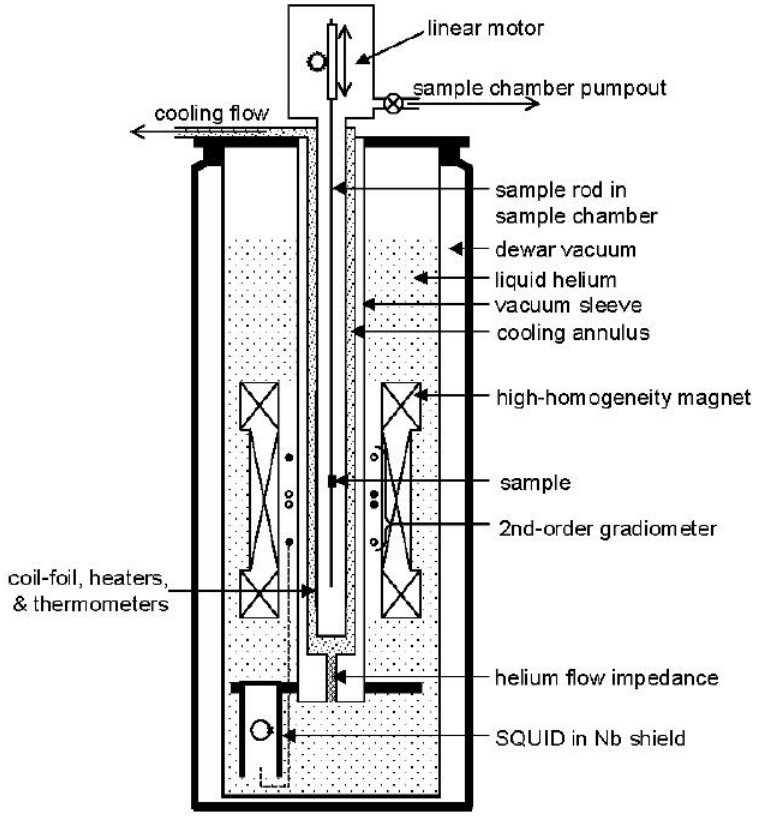


Figure 2.6: Schematics of the MPMS-7 Quantum Design system. From [24]

	Field strength		
	$\leq 1\,\mathrm{T}$	$1\,\mathrm{T}$–$2\,\mathrm{T}$	$2\,\mathrm{T}$–$7\,\mathrm{T}$
Absolute sensitivity	$\pm 10^{-7}\,\mathrm{emu}$	$\pm 10^{-6}\,\mathrm{emu}$	$\pm 10^{-6}\,\mathrm{emu}$
Differential sensitivity	$\pm 10^{-8}\,\mathrm{emu}$	$\pm 10^{-7}\,\mathrm{emu}$	$\pm 10^{-6}\,\mathrm{emu}$

Table 2.1: Sensitivity of the SQUID magnetometer in different ranges of magnetic field strength

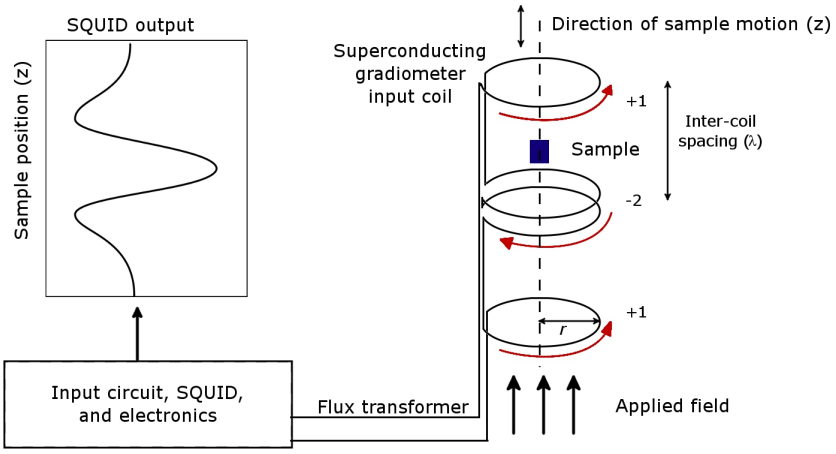


Figure 2.7: Schematics of the second order gradiometer in a SQUID magnetometer

cryogenic temperatures, therefore these parts of the instrument are kept in thermal equilibrium with a bath of liquid helium (4.22 K). The helium dewar is thermally insulated by a vacuum sleeve and surrounded by a liquid nitrogen dewar for further insulation (not shown in figure). The sample chamber is centred inside the magnet and is separated from the liquid helium bath by a vacuum sleeve. The chamber has thermometers for temperature control and can be heated by heaters in the chamber wall or cooled by a flow of cold helium through a gap between the chamber and the vacuum sleeve (cooling annulus). The sample is attached to a rod and located in the middle of the magnet; a linear motor drives the oscillation of the sample inside the gradiometer. The MPMS-7 makes use of a second order gradiometer, formed by three sets of coils equally spaced and connected in series; the first and the last coil have the same number of loops and are wound in the same direction, while the middle coil is wound in the opposite direction and has twice the number of loops, as shown in Figure 2.7. This arrangement of the coils ideally allows complete cancellation of background signals from the sample holder and strongly reduces the effect of field noise in the magnet. The response curve of the SQUID for a magnetic point dipole moving in the centre of gradiometer can be obtained from the Biot-Savart law. The voltage signal measured on the SQUID is fitted by

Equation 2.9.

$$V(z) = A\left[g(r, z-\delta-\lambda) - 2g(r, z-\delta) + g(r, z-\delta+\lambda)\right] + \rho z + V_0 \qquad (2.9)$$

A, δ, ρ , V_0 are fitting parameters, which correspond to the amplitude of the signal (A), the sample axial displacement from the centre of the z-range (δ), the signal drift (ρ) and the offset (V_0). The remaining parameters are instrumental constants: r is the gradiometer coil radius (0.97 cm), λ is the inter coil distance (1.519 cm). The response function $g(r, z')$ of each single gradiometer coil at axial distance z' from the sample is shown in Equation 2.10.

$$g(r, z') = (r^2 + z'^2)^{-3/2} \qquad (2.10)$$

In order for the point dipole approximation to hold with sufficient accuracy the sample size must be kept as small as possible, typically less than 3 mm in length and 5 mm in diameter. There are two operating modes for magnetic properties measurements in constant magnetic field; the standard one is called DC measurement, where the sample is moved through the coils in discrete steps, while the alternative one is called reciprocating sample option (RSO), in which the sample is oscillated over a length of a few centimetres by a servo motor, at a frequency of the order of 1 Hz. This last mode can achieve better sensitivity by eliminating low frequency noise and has therefore been used in the experiments.

Sample preparation and mounting

The MPMS-7 was used for measuring samples of different morphologies. Sample preparation and mounting varied from powder samples, to single crystals and thin films. In the case of powders, the sample is first gently ground in a glass mortar and then a small quantity (about 20 mg–30 mg) is loaded inside a gelatine

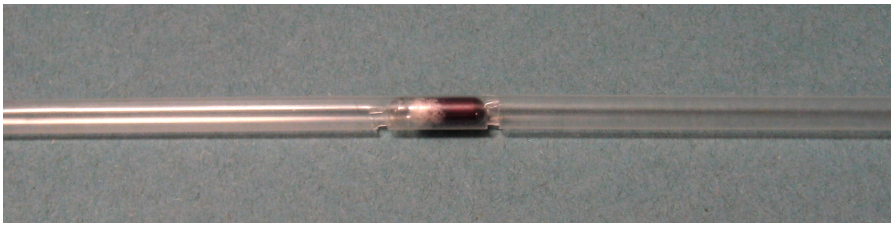


Figure 2.8: Mounting on a plastic straw of a capsule filled with CoPc powder for SQUID measurement

capsule. The powder is packed inside the capsule with some cotton wool to avoid displacement and reduce powder re-orientation during the measurement. Finally the capsule is loaded inside a clear plastic straw, 5 mm in diameter, and held in place by two plastic stripes cut transversally from the straw and folded inward, as shown in Figure 2.8. This way of mounting is expected to have a minimal impact on the background signal subtraction, since the amount of plastic material along the straw remains virtually constant. However the diamagnetic signal arising from the cotton wool and the gelatine capsule can represent a problem when measuring samples with a very diluted moment or virtually diamagnetic. The magnetic moment of phthalocyanine single crystals can be easily measured along the needle direction. The sample was held in the place in the holder between two concentric plastic straws, one of which was cut longitudinally in order to be able to slide into the other one. Thin films of CoPc for magnetic characterization were deposited on a 14 cm × 9 cm kapton substrate 25 µm thick. The deposition area was delimited by an aluminum mask which exposes only a 0.3 cm × 9 cm rectangular strip at in the middle of the long side of the substrate (Figure 2.9). This geometry leaves clear substrate on the sides of the CoPc strip, which allows cancellation of the magnetic signal of the substrate during the measurement in the SQUID. In the case of templated films, a 20 nm PTCDA film was grown on the substrate prior to CoPc deposition, covering the whole area available for deposition 10 cm × 10 cm: this allowed cancellation of most of the signal due to PTCDA, which is anyway very small. In order to reduce adsorption or oxidation of the organic film during

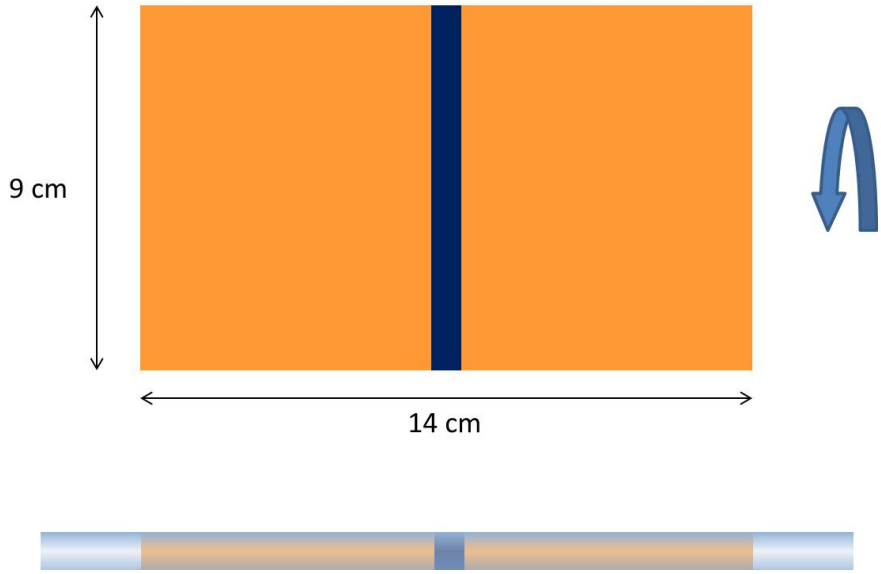


Figure 2.9: Organic film sample for SQUID characterization. The sample is shown rolled inside the sample straw (bottom)

sample transport, the samples were in some cases capped with 50 nm film of lithium fluoride grown on the whole deposition area. The samples are carefully rolled along the strip direction to fit inside the sample holder (plastic straw) for measurement, as shown in Figure 2.9.

Magnetic measurements

The magnetic characterization of the samples consisted in the measurements of the magnetic moment as a function of temperature (T) at constant magnetic field, or as a function of the magnetic field (H) at constant temperature. The measurement was always performed in the RSO mode of the SQUID magnetometer, oscillating the sample at 1 Hz, with end to end amplitude of 4 cm. The samples studied in this work are weakly magnetic, therefore the following approximation is used to relate the magnetic field strength H to the magnetic flux density B:

$$B = \mu_0(H + M_V) \approxeq \mu_0 H \tag{2.11}$$

where M_V is the magnetization density, which is much smaller than H. In this work, the net magnetic moment per molecule M, expressed in Bohr magneton (μ_B) units, is used; M is calculated by dividing the molar magnetization (in emu/mol) by the magnetic moment of a mole of Bohr magneton ($N_A\mu_B = 5584.9$ emu/mol). The $M(T)$ curves were measured from 2 K to 150 K or 310 K. Two different protocols for $M(T)$ measurements were used, which are called Zero Field Cooled (ZFC) and Field Cooled (FC). In the ZFC, the sample inside the SQUID was cooled down from 150 K to 2 K in absence of field, while in FC the cooling was done while applying the field used for the measurement. Comparison between the results of ZFC and FC measurements performed at low field (generally below 1000 Oe) may highlight some magnetic properties such as freezing of domain wall motion, slow spin relaxation or spin glass behaviour [72] in the sample. The susceptibility values in the text are given in $\mu_B T^{-1}$ units and the following definition of $\chi(T)$ is used:

$$\chi = \frac{\partial M}{\partial B} = \frac{V}{N\mu_0}\frac{\partial M_V}{\partial H} = \frac{V}{N\mu_0}\chi_{SI} \tag{2.12}$$

where N is the number of molecules in the sample, V is the sample volume, μ_0 is the vacuum permeability and χ_{SI} is the susceptibility definition normally used in the SI system, which is dimensionless. Note that the approximation in Equation 2.11 was used. The differential susceptibility was calculated as the incremental ratio of the $M(T)$ measurements with respect to magnetic field:

$$\chi(T) = \frac{\partial M}{\partial B} \approxeq \frac{1}{\mu_0}\frac{\partial M}{\partial H} \approxeq \frac{1}{\mu_0}\frac{M_{H_1}(T) - M_{H_2}(T)}{H_1 - H_2} \tag{2.13}$$

where $M_H(T)$ is measured at the field H. The use of a differential susceptibility allows the cancellation of field independent (constant) spurious contributions which may arise from ferromagnetic impurities saturating at low field. The choice of the H_1 and H_2 fields was determined by the interplay of two factors: the fields

have to be small in order to obtain a linear response from the material even at low temperature, but large enough to give a signal that could be easily detected by the SQUID. For the powder samples, which weighed tens of milligrams, the measurements were done at 500 Oe 1000 Oe; however, the mass of the thin films was about hundred times smaller and stronger fields were used (5000 Oe, 7500 Oe, 20 kOe and 70 kOe). The samples were prepared to a new $M(H)$ measurement by cooling them from 150 K to the desired temperature in zero applied field.

2.4 Calculation of the magnetic properties of antiferromangetic chains

The chains have been modelled with a Heisenberg Hamiltonian which contains an isotropic exchange interaction between nearest neighbours along a linear chain:

$$\hat{\mathcal{H}} = 2J\Sigma\hat{S}_i \cdot \hat{S}_{i+1} \tag{2.14}$$

The eigenvalues of the Heisenberg Hamiltonian of finite antiferromagnetic chains have been calculated using the method of Bonner and Fisher [15]. In a chain formed by N S=1/2 spins interacting with an exchange energy J, the magnetic moment $M(H)$ in units of μ_B per spin centre was calculated using the expression in Equation 2.15:

$$M(H) = \frac{1}{N} \frac{\sum_{m_z=-N/2}^{N/2} m_z g \exp(\frac{g m_z \mu_B \mu_0 H}{k_B T}) \sum_i \exp(\frac{-J\varepsilon^i_{m_z}}{k_B T})}{\sum_{m_z=-N/2}^{N/2} \exp(\frac{g m_z \mu_B \mu_0 H}{k_B T}) \sum_i \exp(\frac{-J\varepsilon^i_{m_z}}{k_B T})} \tag{2.15}$$

which is the Boltzmann average (thermal average) of the magnetic moment projection $m_z g$ of the eigenstates of the Heisenberg Hamiltonian of the chain, which have eigenvalues $\varepsilon^i_{m_z}$, expressed in units of J. The $M(H)$ curves at low tempera-

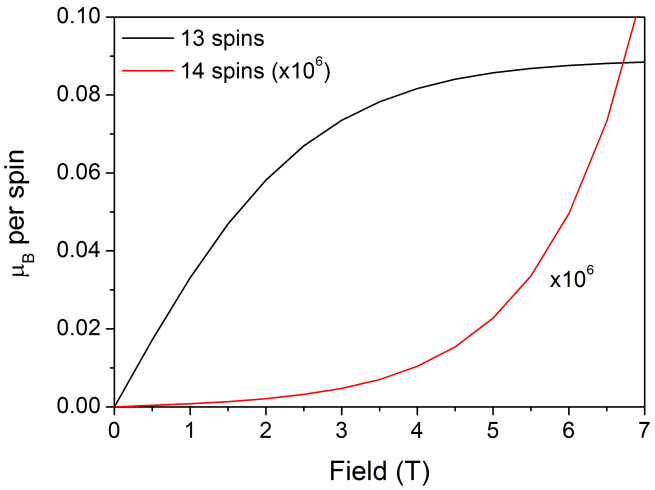


Figure 2.10: $M(H)$ curves for chains of 13 and 14 spins with $g = 2$ and $J/k_B = 80K$, calculated with the Bonner Fisher method. The curve of the 14 spins chain has been scaled by a factor of 10^6.

ture ($T \ll J/K_B$) are strongly dependent on the parity of the number of spins in the chain. Figure 2.10 shows that, between 0 and 7 Tesla, a chain with 13 spins behaves as a paramagnet, with an apparent saturation moment per spin equal to 1/13 μ_B, while the magnetic moment of the chain with 14 spins is cancelled out almost perfectly by the antiferromagnetic interaction.

The magnetic susceptibility $\chi(T)$ was calculated by differentiation of Equation 2.15 with respect to the field, as in Equation 2.13. Figure 2.11 shows that also $\chi(T)$ curves of finite chains exhibit a dependence on the parity of the chain at low temperature. Indeed, $\chi(T)$ diverges as T^{-1} as the absolute zero temperature is approached in an odd chain, while χ decreases to zero in an even chain. As the length of the chain is increased, the $\chi(T)$ curve converges rapidly to the infinite chain behaviour, which is expressed using the formula determined by Johnston *et al.* [48].

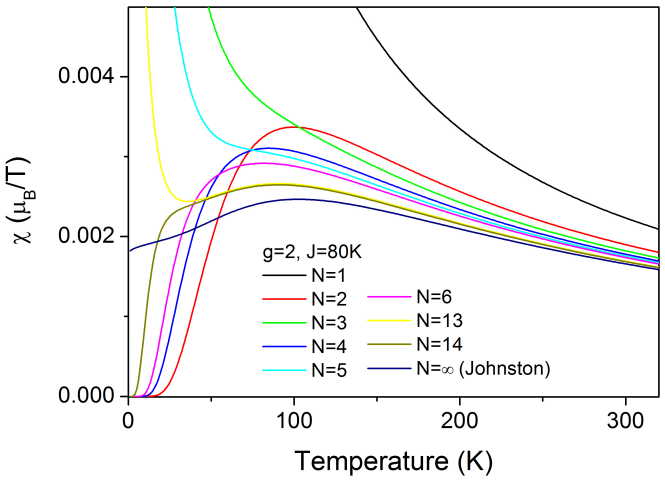


Figure 2.11: $\chi(T)$ curves for chains of length N, with $g = 2$ and $J/k_B = 80K$, calculated with the Bonner Fisher method. The infinite chain susceptibility was calculated with the Johnston formula [48]. For the definition of $\chi(T)$ and its units refer to Equation 2.12

Chapter 3

Cobalt phthalocyanine (CoPc) powders and thin films

This chapter will discuss the structural and physical properties of CoPc in the powder and thin film forms, with particular focus on magneto-structural correlations. The samples can be synthesized in either the α or β polymorph, which represent the two main crystal structures of phthalocyanines. The main result is the observation of spin correlations above $77\,\mathrm{K}$ *in* $\alpha-CoPc$ *thin fims, linked to an exceptionally high antiferromagnetic exchange constant for phthalocyanines and organic magnetic materials. The spin coupling mechanism and its dependence on the molecular stacking geometry is explained through the result of DFT calculations.*

3.1 Determination of the purity of CoPc

The electronic and magnetic properties of semiconducting materials are very sensitive to the presence of inadvertent impurities which may introduce structural and/or magnetic defects, traps for charge carriers, unwanted spin centres. For this reasons the purity of the material is paramount for characterizing the intrinsic

physiscal properties of magnetic materials.

The cobalt phthalocyanine used in this work was purchased from Sigma Aldrich with a nominal purity of 97%. It was purified once in our laboratory using the procedure described in section 2.1. The purity of the commercial and the purified material was then assessed by using inductively coupled plasma atomic emission spectroscopy (ICP-AES). This technique quantitatively measures the concentration of metal cations and some other species in the range from the ppm down to the ppb concentration range. Here ICP-AES is used to determine both the total cobalt content of the powder and to assess the amount of contaminants such as copper, manganese and iron.

Since only liquid solutions can be used, the phthalocyanine had to be decomposed by acid digestion, as described in section 2.3.5. The concentrated solution obtained from acid digestion needs to be diluted in order to have a concentration of the analyte approximately around 10 ppm, where the instrumental accuracy is highest. Since cobalt ions and possible impurities are likely to be found in largely different concentrations, solutions of different nominal cobalt concentrations were prepared. A less diluted solution containing cobalt in approximately 200 ppm was used to measure the impurities content, while a more diluted one, containing about 9 ppm of cobalt, was used for the quantification of the cobalt content. In order to have a baseline value of the ions concentrations in the reagents used, an acidic solution was prepared following the same acid digestion process, but without any CoPc added to it.

Before the measurement of the CoPc solutions took place, the ICP-AES instrument was calibrated by analysing solutions of standard concentration. The calibration samples were a blank solution containing only distilled water (0 ppm) and four other ones containing manganese, iron, cobalt, nickel, copper and other elements at individual concentrations of 5 ppm, 10 ppm, 15 ppm, 20 ppm. The calibration samples were prepared by dilution of a standard solution of certified concentra-

tion (100 ppm, 100 µg/ml) in 2 M nitric acid solution as a solvent. Since several elements showed interfering emission spectra, it was not always possible to select the strongest emission line for all the elements; in the case of iron and copper, the interference was unavoidable and two different lines were chosen for each element, in order to discriminate false positives.

The results of the calibration, shown in Figure 3.1, are characterized by excellent linear dependence of the signal on the solution concentration, demonstrating that the calibration solutions were prepared with sufficient accuracy.

Following the calibrations, the solutions made from commercial CoPc powders

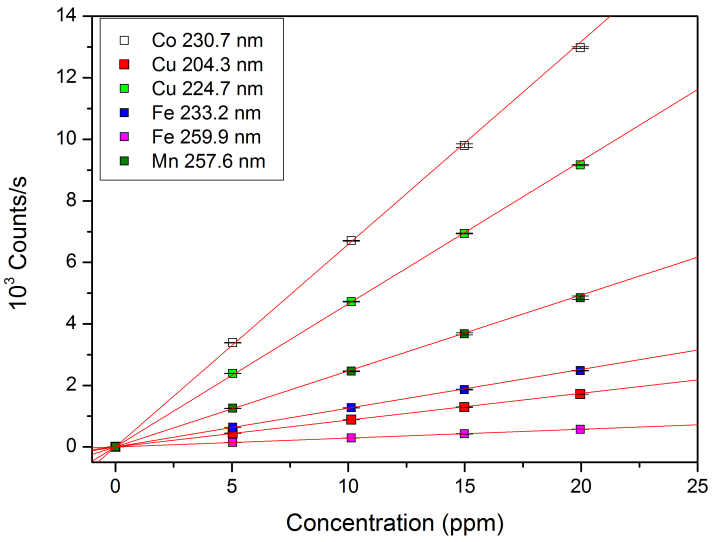


Figure 3.1: Results of the calibration procedure of the ICP analysis. The photon counts per second for the different elements (wavelengths) analysed are shown as a function of the concentration of the standard solution and fitted to a straight line

and CoPc purified crystals were analysed, starting from the two highly diluted solutions and finishing with the higher concentration ones. The results of the analysis are summarized in table 3.1. The cobalt content was in line with the values calculated. As expected, we found a smaller deviation in the solution of the purified CoPc, which demonstrates the effectiveness of the purification method. Based on

the measurements on the dilute solutions ($[Co]_{calc} \approx 9$ ppm) and correcting for the cobalt concentration in the blank solution, we conclude that the unpurified powder contains 92.9% of the expected cobalt amount, while after purification the cobalt content increased to 98.1%. These values express the lower bound of the cobalt content in the powders, since it could be possible that small amounts of the acid digested solutions were lost while preparing the solutions to be analysed. On the other hand, this analysis does not allow to distinguish between cobalt bound to the phthalocyanine ligand and other forms of cobalt present in the powder or crystals. However, the high stability of CoPc and the binding energy of the cobalt ion suggest that dissociation of the cobalt ion from the ligand is very unlikely.
Looking at the more concentrated solutions ($[Co]_{calc} \approx 200$ ppm) we observe that the other elements analysed are found in very low concentrations, which are comparable to those measured in the baseline solution and with the uncertainty of the measurement. Only in the case of Cu (λ=224.7 nm) and Fe (λ=233.2 nm), the concentrations in the CoPc solutions are well above the baseline values. However, this anomaly is only observed in one of the two wavelengths monitored in both Cu and Fe, suggesting that it could be an artifact. We can conclude that neither Mn, Fe or Cu should be found in CoPc powders in concentrations higher than 0.1%.

3.2 Characterization of α- and β-CoPc materials

3.2.1 Identification of the polymorph type

Organic materials exhibit striking correlations between the structural parameters and physical properties, with important implications for their technological application. The processing conditions can exert a control on the crystalline parameters offering a convenient way to modulate the materials characteristics. This is a well known fact in phthalocyanines, for which a large number of polymorphs has been

	Elemental concentrations (ppm)					
	Co λ=230.7 nm	Cu λ=204.3 nm	Cu λ=224.7 nm	Fe λ=233.2 nm	Fe λ=259.9 nm	Mn λ=257.6 nm
Blank						
	0.1145(1)	0.0396(15)	0.0383(24)	0.0527(63)	0.0467(323)	0.0008(23)
CoPc powder (Sigma Aldrich)						
$[Co]_{calc}$=9.13 ppm	8.604(21)	0.0036(47)	0.0029(8)	0.0063(19)	-0.0464(211)	0.0001(22)
$[Co]_{calc}$=218.6 ppm	197.2(3)	0.0153(19)	0.0653(11)	0.2511(65)	0.0003(235)	-0.0014(47)
CoPc purified crystals						
$[Co]_{calc}$=9.54 ppm	9.474(7)	0.0059(33)	0.0026(17)	0.0158(49)	0.0090(98)	0.0001(32)
$[Co]_{calc}$=216 ppm	209.0(5)	0.0140(22)	0.0668(19)	0.2742(19)	0.0076(155)	-0.0031(42)

Table 3.1: Results of the ICP analysis of CoPc samples. The first column shows the solutions analysed, with their theoretical concentration of cobalt indicated with the symbol $[Co]_{calc}$ in ppm units. The following columns report the measured concentration of each element (Co, Cu, Fe, Mn) and the line (λ) of the atomic emission spectrum used for the measurement. The standard deviation of the values of concentration are given in brackets.

identified.

This section discusses only the two main polymorphs of CoPc, α and β, in form of powders ad thin films. The novel η form of CoPc nanowires will be presented in Chapter 4. The α-CoPc powder was obtained using the acid paste method described in section 2.2.3, while β-CoPc powder was prepared by grinding in a glass mortar single crystals of β-CoPc obtained by the gradient purification of the commercial CoPc powder (Section 2.1). The α-CoPc films were grown by OMBD and subsequent annealing for 3 h in nitrogen atmosphere at 330 °C led to the transition to a β-CoPc film.

The polymorph composition of the samples was checked by X-ray diffraction scans in the 5°–30° range of 2θ angles, which are shown in Figure 3.2. This task is aided by the availability of high resolution structures for both α and β-CoPc [6] that provide guidance in the peak assignment. The good agreement of the observed peak positions and intensities with the prediction suggests that all samples consist of a single phase. β-CoPc exibit sharper diffraction peaks than the α-CoPc, which indicates larger crystalline domains in the former, as expected from the thermodynamic stability and the higher processing temperature of β phase samples. On the contrary, the acid paste method is known to yield nano-crystalline powders that exhibit broad envelopes of diffraction peaks. The α-CoPc powder data in Figure 3.2 exhibits a slight disagreement in peak intensity with the prediction, suggesting that the orientation of the grains in the powder might not be perfectly random.

The diffraction patterns of thin film samples exhibit only 1 or 2 strong peaks, which indicates a preferential orientation of the crystallites (*texture*) along the direction perpendicular to the film. The texture in α-CoPc films refers mainly to the (001) plane (2θ =6.90°) and, to a much lesser extent, the (100) plane (2θ =7.34°); the pattern varies slightly with film thickness and a slight increase of the (100) peak intensity is observed in a 400 nm film. The 200 nm β-CoPc film, which was obtained from an α-CoPc film by annealing, shows preferential orientation of the

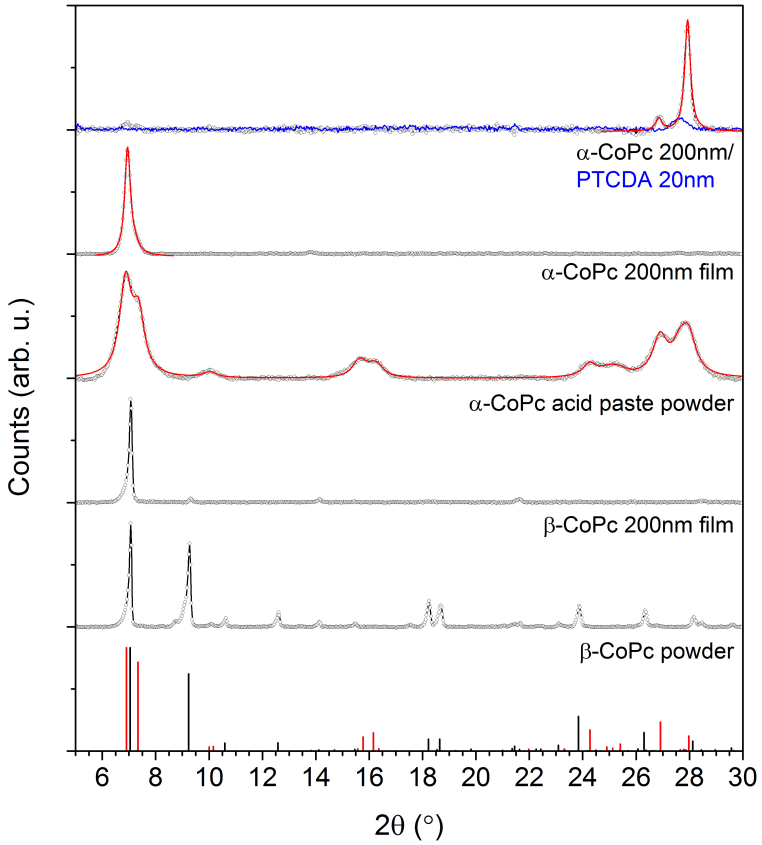


Figure 3.2: X-ray diffraction patterns of the four CoPc sample typologies investigated. The stick pattern of the α (red) and β-CoPc (black) shown were calculated using the structures published by Ballirano *et al.* [6]

(100) plane (2θ =7.04°); because of the sharp peak lines, other minor peaks are also visible in the background.

CoPc films are grown on glass, silicon wafer and kapton film (25 µm thickness) with very similar characteristics (Figure 3.4), due to the weaker strength of molecule substrate interactions compared to the intermolecular ones. The texture of the films can be drastically changed by growing CoPc onto a thin layer (20 nm) of perylene-3,4,9,10-tetracarboxylic dianhydride (PTCDA, Figure 3.3) previously deposited on the substrate. This effect, common to other phthalocyanines [41] and organic molecules, is called structural templating and it stems from the intrinsic preference of PTCDA to adhere to substrates with the molecular plane roughly parallel to the surface. This functionalizes the substrate surface with a π-conjugated sys-

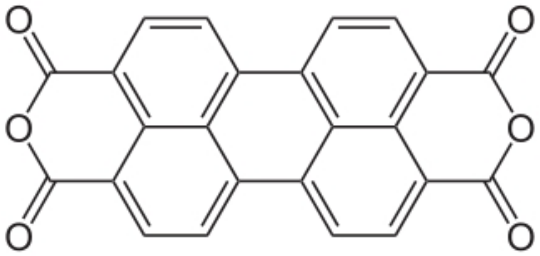


Figure 3.3: Structure of perylene-3,4,9,10-tetracarboxylic dianhydride (PTCDA), used in this work for templating the texture of phthalocyanine films

tem which provides anchoring for other planar conjugated molecules through π stacking interactions. When CoPc is grown on PTCDA, the film is preferentially oriented with the (2-11) (2θ =27.98°) and the (2-10) (2θ =26.91°) planes of α-CoPc parallel to the substrate, which results in an angle of 11.6° or 5.7° between the molecular plane and the substrate. The templating effect is progressively degraded as the film thickness increases beyond 200 nm. This is seen as a relative increase of the intensity on the (2-10) peak to the detriment of the (2-11) peak. In the case of films on glass, the texture of thick CoPc films is poorer than on kapton, resulting in the appearance of small diffraction intensities measured at the (001), (100), (1-10) and (1-11) peak positions. This difference could be due to a lower quality of the templating PTCDA film on glass.

3.2.2 UV-Visible spectroscopy of CoPc materials

An alternative technique that provides information about the crystal structure and orientation of CoPc films is optical absorption spectroscopy in the UV/Visible range. Phthalocyanine molecules exhibit highly anisotropic optical properties. The visible range typically shows the phthalocyanine Q band, the lowest electronic excitation, corresponding to π-π^* transitions in the organic ligand with transition dipoles in the plane of the molecule. In solution, the Q band of CoPc is peaked at 666 nm and accompanied by a vibronic satellite at 602 nm (Figure 3.5).

As explained in section 2.3.3, the intermolecular interactions in the solid state

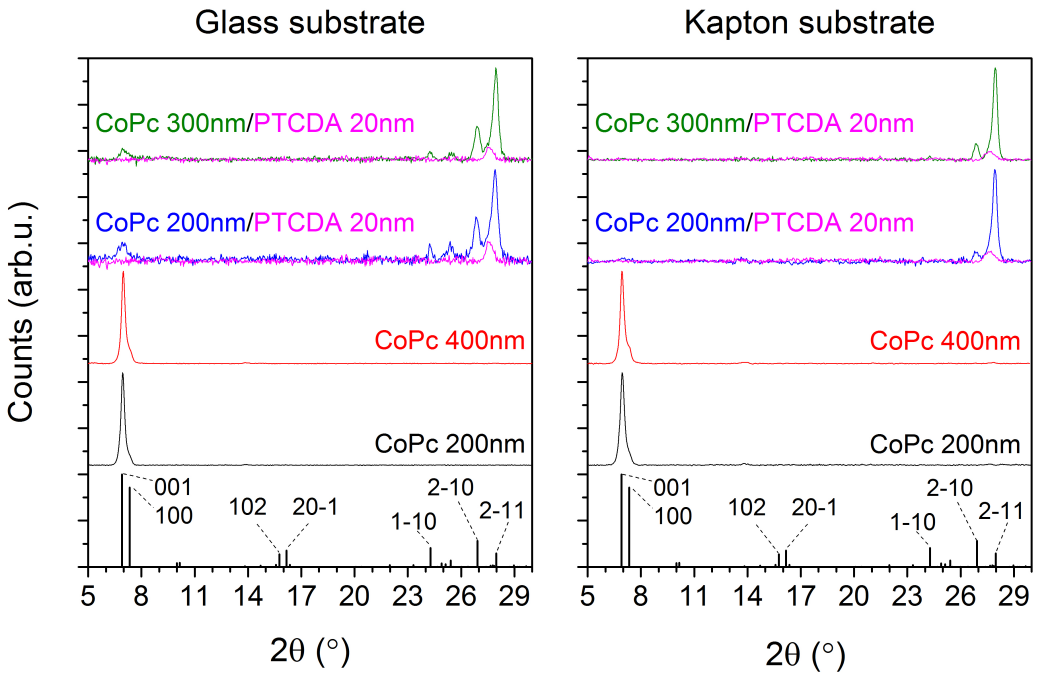


Figure 3.4: XRD scans of CoPc films grown on glass (left) and kapton film (right). The stick pattern at the bottom refers to the peaks of the α-CoPc structure

broaden and split the electronic transitions of the monomer molecule in a structure dependent fashion, providing a means to identify different polymorphs.

The spectra of the α phase consist of a broad envelope of two main bands centred at 612 nm and 685 nm, with at least two shoulders approximately at 576 nm and 721 nm. The relative intensity of these bands varies visibly between the films and the acid paste powder, which could be an effect of the smaller grain size in the powder.

The spectrum of the β-CoPc shows a sharper profile made of two bands at 635 nm and 703 nm. The shift to longer wavelengths is compatible with the larger lateral sliding of the molecules in the β-phase structure (Figure 1.6), which forms a stacking geometry closer to a J-aggregate structure [50]. The asymmetric peak profile in the β-CoPc sample may hint towards the presence of a small residual fraction of unconverted α phase after the annealing, which might not be detected by XRD because of the nanoscopic size of the domains.

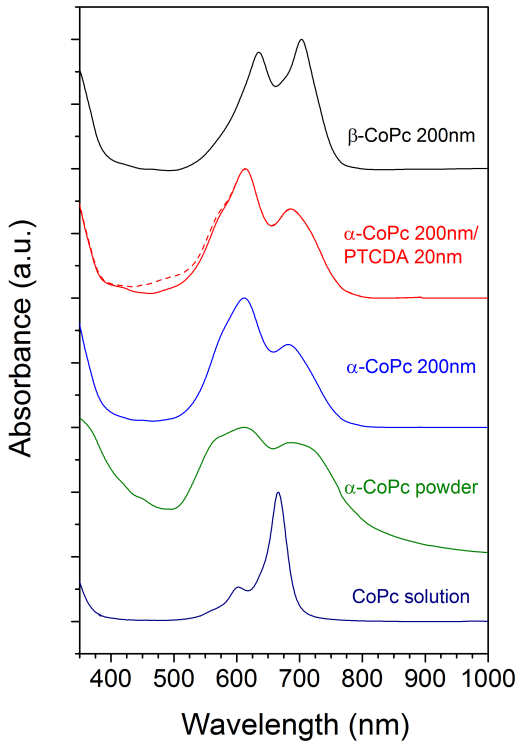
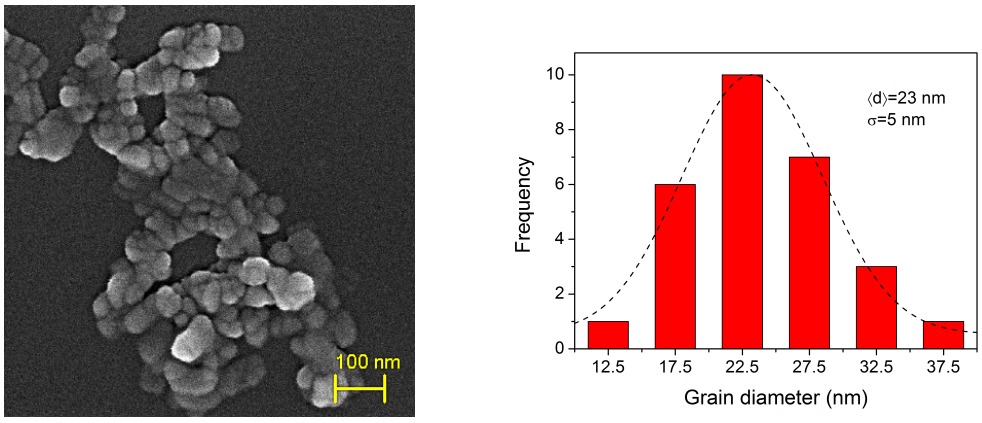


Figure 3.5: UV-Visibile absorption spectra of CoPc in solution and in α and β-CoPc solid samples (powders and films). The solution is 2.61 mg l^{-1} in 1-Chloronaphthalene:Pyridine (5:1). The spectrum of the α-CoPc powder was measured on a film obtained by drying a drop-casted suspension of the α-CoPc acid paste powder in hexane. The α-CoPc film was evaporated on bare glass or onto a 20 nm PTCDA layer (dashed (solid) line shows spectrum before (after) subtraction of PTCDA absorption). The β-CoPc film is the product of the annealing of an α-CoPc film deposited on glass.

3.2.3 Investigation of the morphology

Samples of the α and β phases of CoPc discussed above present distinct morphologies which are recognized with the scanning electron microscope. A distinction can be made based on the shape of the grains and their size, as anticipated by considerations on the differing widths of the XRD diffraction peaks. Both the CoPc acid paste powder (Figure 3.6) and the films grown by OMBD (Figure 3.7) display grains of approximately spherical shape. The distribution of particle sizes was estimated from the SEM images, although this procedure is not very accurate



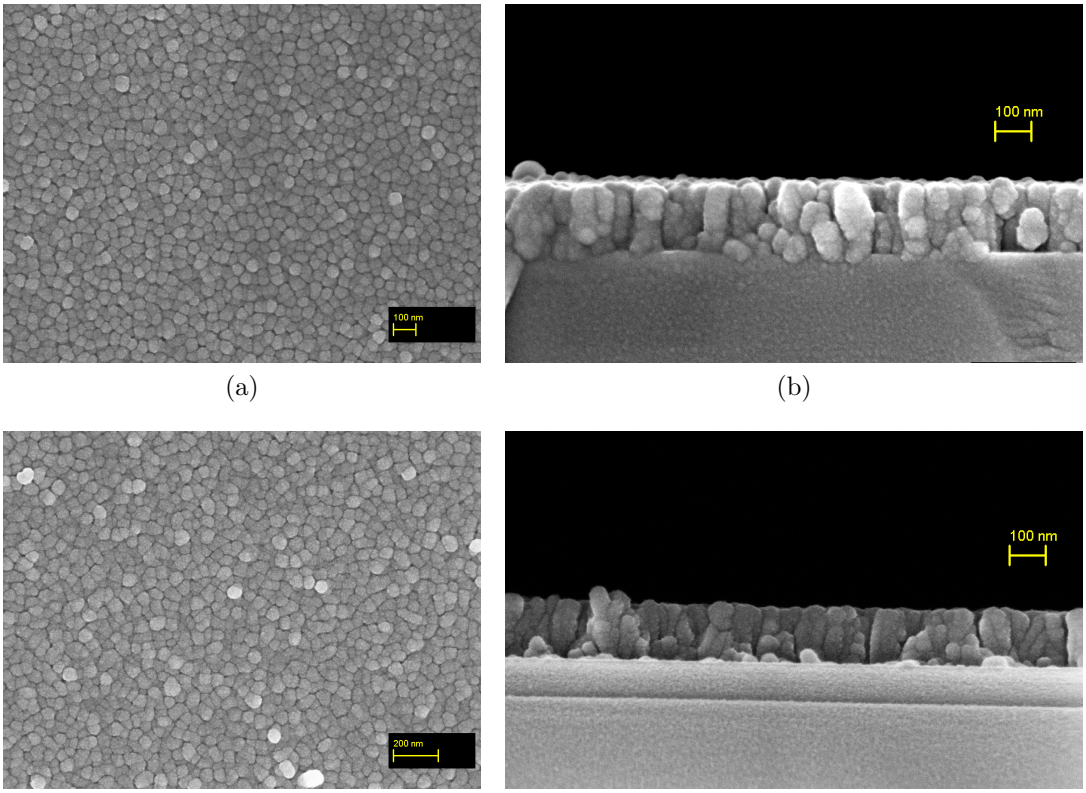
(a) (b)

Figure 3.6: Scanning electron microscope image (a) of particles found in CoPc powder re-precipitated with the acid paste method. (b) shows the distribution of particle sizes in a group of 28 particles

because the grains are not isolated (Figures 3.6b and 3.8), potentially leading to an underestimation of the size. The clusters observed in the acid paste powder contain grains with an apparent size of 23 ± 5 nm, while the templated α-CoPc film exhibits grain sizes of 54 ± 13 nm in the top view and 43 ± 13 nm in the cross-section images respectively. No significant difference in particle size is seen between templated and non-templated films. The films appear relatively smooth and homogeneous. The RMS roughness, quantified from the AFM topography images shown in Figure 3.9, is 5.6 nm for the non-templated film and 5.2 nm for the templated film.

The SEM images in Figure 3.10 show the different morphology of the β-CoPc film. The image at lower magnification (Figure 3.10a) shows domains several µm large, which are filled by elongated grains adopting a preferential orientation. The size of the grains varies considerably between domains, from about 0.5 µm to several µm in the elongated direction. At higher magnification (Figure 3.10(b)) a few small spherical grains less than 50 nm in diameter are visible, possibly indicating incomplete conversion of the α-CoPc film.

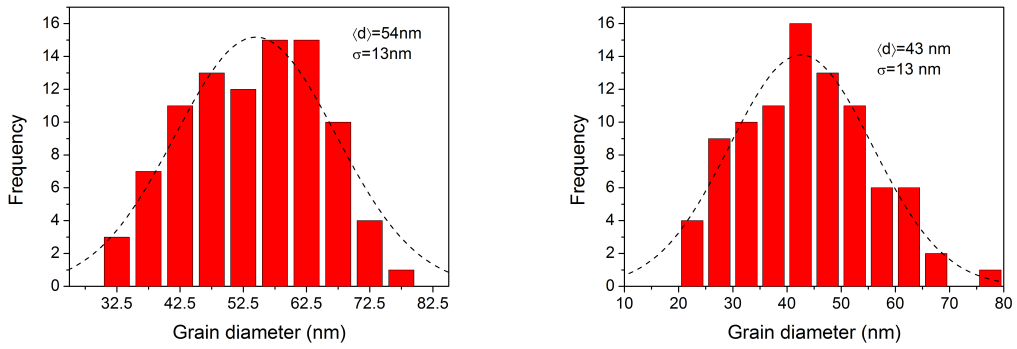
The relatively large size of the domains allows the study of the film morphology



(a) (b)

(c) (d)

Figure 3.7: Top view scanning electron microscope images of a 200nm CoPc non templated (a) and templated (c) films with their relative cross-sections (b) and (d)



(a) (b)

Figure 3.8: Statistics on the apparent size of randomly chosen grains visible in the SEM images of a 200 nm CoPc templated film. Figure (a) represents a group of 91 grains in the top view image 3.7c, while (b) refers to 89 grains in the cross section image 3.7d

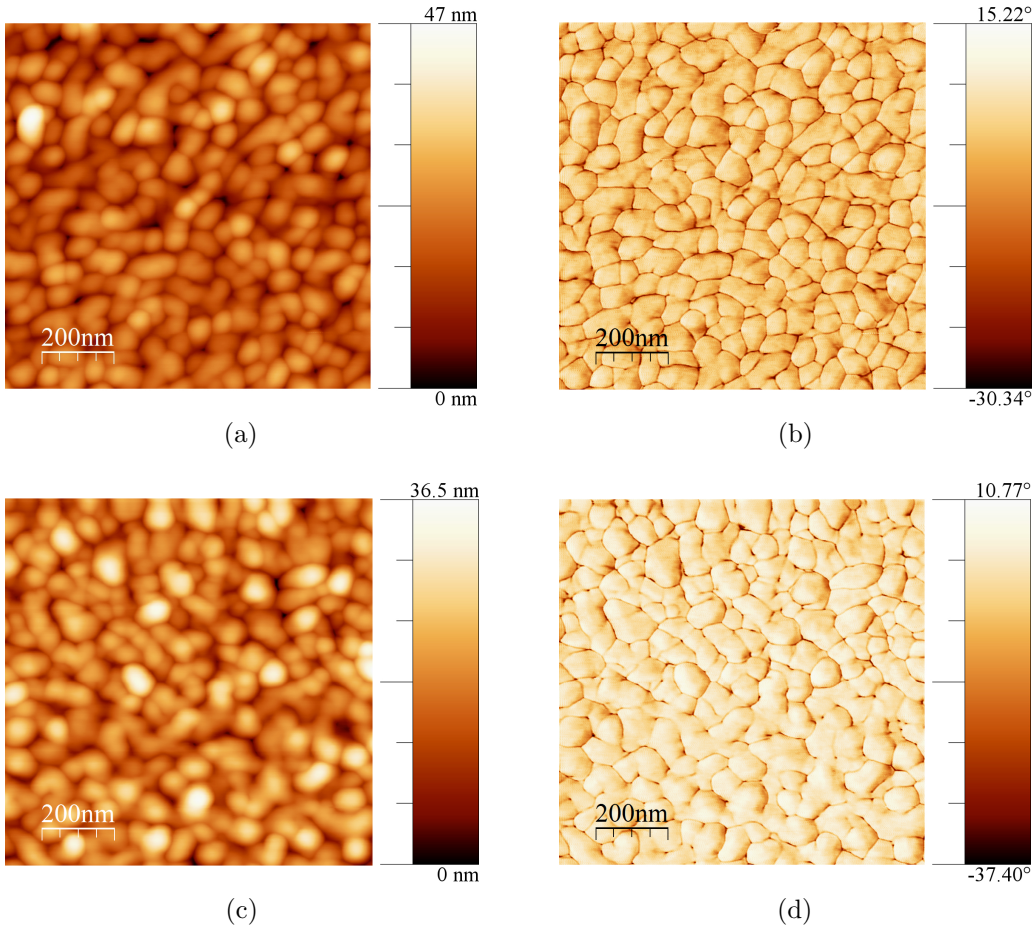


Figure 3.9: Atomic force microscope topography images of a 200nm CoPc non-templated (a) and templated (c) films on kapton with their relative phase images (b) and (d)

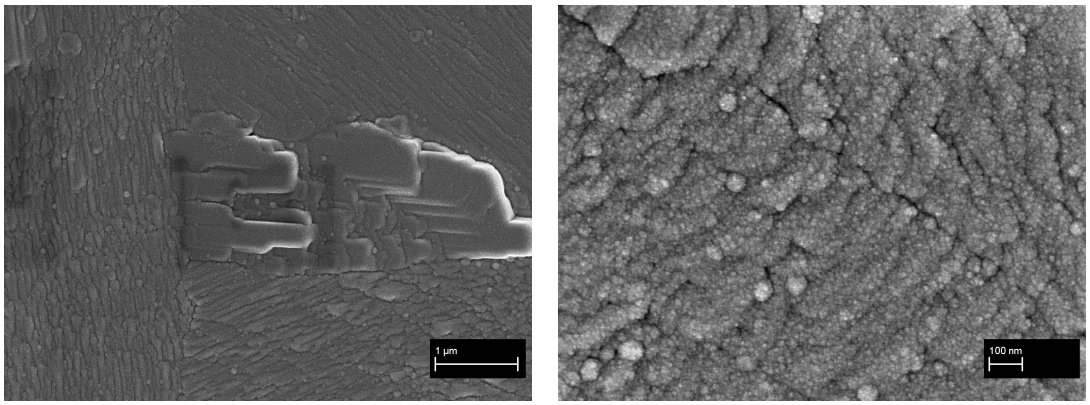
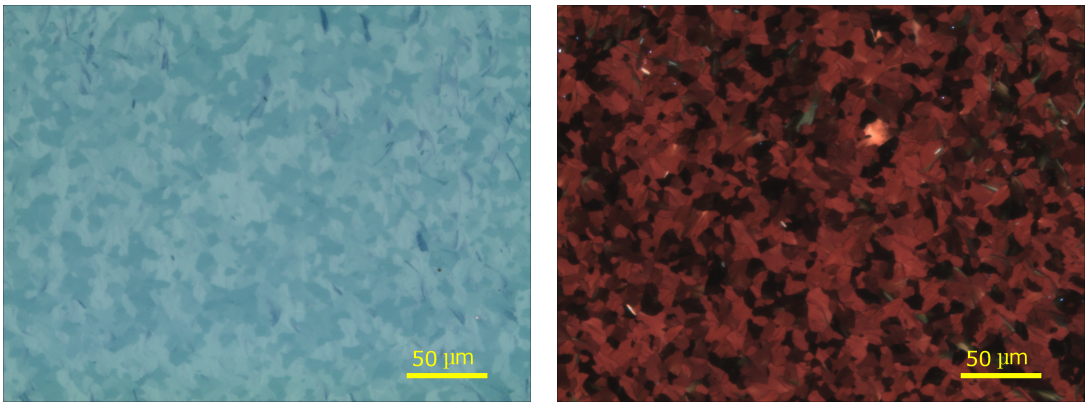


Figure 3.10: SEM images (50kX magnification in (a) and 200kX in (b)) of a β-CoPc film obtained by annealing of a 200 nm film on glass



(a) (b)

Figure 3.11: Bright field optical microscope transmission image (20x magnification) of a β-CoPc film on glass (a) The contrast highlights domains of different thickness. Same area observed with a 90° angle between the polariser and the analyser (b). The contrast highlights domains with different orientation

by optical microscopy. Variations of the colour intensity in Figure 3.11a suggest that domains vary in thickness, while the introduction of the analyser polarizer shows birefringence of the samples (Figure 3.11b) and highlights the different orientations of individual domains. This effect cannot be observed in the α-CoPc films, due to the nanometric size of the crystalline grains.

3.2.4 Analysis of the crystalline coherence length

This section completes the characterization of the structural properties of the CoPc samples by presenting a detailed study of the crystallite size, aimed at extracting the average length of the CoPc stacks along the b crystal axis, from which the size of the magnetic spin chains can be estimated. This analysis, combined with knowledge of the polymorph type, provides key information to understand the magnetic properties of the material.

A simple tool for assessing the size of structurally ordered domains is the Scherrer equation that relates the width of the XRD peak with the average crystallite size (see section 2.3.2). Red lines in Figure 3.2 show fits of the diffraction patterns of the α-CoPc samples with a Lorentzian peak shape. The position and the width of

Sample	(hkl)	$2\theta_0$ (°)	$w_{2\theta}^{obs}$ (°)	Size nm	N
α-CoPc powder	(001)	6.87	0.55	16–19	43–51
	(2-11)	27.97	0.67	14–17	37–45
α-CoPc 200 nm	(001)	6.95	0.26	37–51	99–136
α-CoPc 200 nm\ PTCDA 20 nm	(2-11)	27.93	0.26	40–70	107–189

Table 3.2: Summary of the Scherrer analysis performed on the α-CoPc samples XRD patterns. The peaks used in the calculation are the (001) and the (2-11) peaks of the α-CoPc structure. For each peak, the table shows the (hkl) index, the experimental diffraction angle ($2\theta_0$), the observed width of the peak ($w_{2\theta}^{obs}$), the Scherrer grain size (Size) and the estimated number of CoPc molecules (N) stacked along the b direction in an average crystallite. The number of molecules N was calculated by dividing the Scherrer size by the lattice constant b=3.75Å along the stacking direction

some representative peaks are shown in table 3.2. The widths must be corrected for the instrumental broadening in order to obtain the intrinsic width determined by grain size. This was done in two ways, as explained in section 2.3.2, yielding two limiting values of the grain size (Table 3.2). A further element of uncertainty in the analysis is represented by the value of the Scherrer constant, which for simplicity was set to 1 in this calculation.

It was estimated that the crystallite size in the α-CoPc acid paste powder is between 14 and 19 nm, on the lower end of the distribution estimated from the SEM images (Figure 3.6). This is not surprising as the particles seen under the microscope can contain more than a crystallite. The different average values obtained from the (001) and the (2-11) peaks could be due to a slight deviation from a spherical grain shape, or simply the uncertainty of this analysis. In the case of the films grown on kapton, the crystallite size lies between 37 and 51 nm in the non-templated sample, and in the 40 nm–70 nm range in the film deposited on PTCDA (templated film), in agreement with the SEM microscope images. Similarly to other phthalocyanine films grown at room temperature, the crystallite size

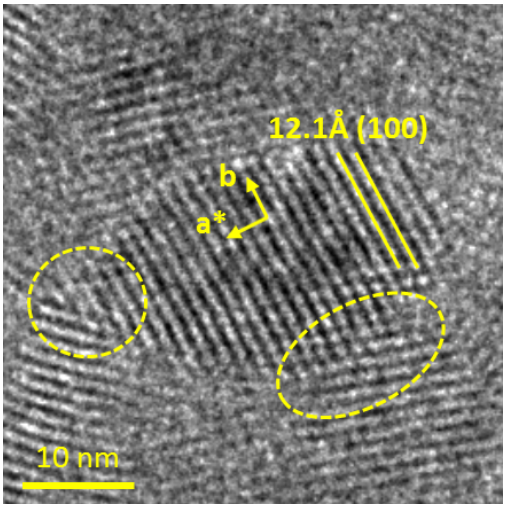


Figure 3.12: HRTEM image of a 50 nm CoPc film grown on a Cu grid with carbon film. The spacing between the fringes is 12.1 Å, in agreement with the 100 plane distance. Based on this observation, the a* direction of the reciprocal lattice is drawn perpendicular to the fringes, while the b direction of the unit cell lies along them. The regions highlighted by dashed lines contain grain boundaries with seemingly shorter fringes and possibly a higher concentration of structural defects. TEM image courtesy of Dr Luke Fleet

in relatively thick films (>100 nm) is determined by growth defects rather then the film thickness. The average number of CoPc molecules stacked in a grain along the b direction (N) is shown in the last column of table 3.2. This value most likely represents an overestimate of the effective length of the spin chains, as suggested by the magnetic data discussed later. Indeed, small structural imperfections, such as a random local strain, can potentially have a much more significant impact on the magnetic properties of the system than on the XRD peak shape.

In order to observe the degree of structual order at the microscopic scale, CoPc films were imaged by Dr. Luke Fleet using high resolution transmission electron microscopy (HRTEM). Figure 3.12 shows an image of a film of 50 nm, which is sufficiently transparent to the electron beam and allows imaging of individual grains.

The centre of the image shows a grain displaying well defined diffraction fringes from a set of crystallographic planes oriented perpendicular to the film; the periodicity (12.1 Å) matches well with the spacing between (100) planes. This orientation

is in agreement with the (001) plane being parallel to the film, as determined by XRD, since the dihedral angle between the two is 89.1°. Other grains with different in-plane orientation are also visible, indicating that the film is polycrystalline with azimuthal symmetry. The absence of fringes in some areas could be due unfavourable grain orientation, poor structural order in some grains or rapid beam damage. The XRD and the TEM measurements provide complementary in-plane and out-of-plane structural information, which set the orientation of the a* (100) and c* (001) axes of the reciprocal lattice along the direction perpendicular to the fringes and to the film respectively. It can be concluded that the fringes are aligned with the stacking direction b and represent individual molecular columns. The fringes extend up to 20 nm in the image, which equals to 53 molecules, while much shorter ones are also visible, especially at the grain boundaries. The brightness level along the fringes shows non periodic fluctuations which cannot be entirely attributed to noise. It is not clear whether these are indicative of defects or disorder within the chains or are instead attributable to beam damage. In the first case, the length of CoPc spin chains would be drastically shorter than the apparent grain size.

This concludes the characterization of the structure and morphology of the CoPc samples. The following section will focus on the characterization of the magnetic properties of CoPc materials and on the understanding the correlations between magnetism and structure.

3.3 Magnetism of α- and β-CoPc

3.3.1 Electron paramagnetic resonance of CoPc powders

A preliminary characterization of the magnetic properties of the CoPc samples was done using electron paramangetic spectroscopy (EPR) in the X microwave

band (≈9.40 GHz). This spectroscopic technique has the ability to resolve some spin parameters to a high accuracy, first of all the g factor and the hyperfine interactions between the electronic spins and the nuclear spins. Further information about the system, regarding the amount of interaction among the electronic spins, can be extracted from the analysis of the resonance peak shape. The integral of the microwave absorption is proportional to the average magnetization of the sample, however the accuracy of this measurement can be an issue, especially in the case of antiferromagnetic materials, which show broad and relatively weak resonance peaks. Therefore EPR and SQUID magnetometry are two complementary techniques.

In this work, EPR was mainly used to check the consistency of the g value of α and β-phase CoPc with those reported in the literature[3].

Figure 3.13 shows the EPR of α-phase powder at room temperature. The spectrum exhibits a fine structure overlaid on a broad profile, which have been de-convoluted using a low pass filter. Broad absorption spectra are typical of non-diluted (para)magnetic materials where spins are in close proximity and experience intense dipolar and exchange interactions. The shape of the derivative of the absorption is similar to that of a system with an axial g tensor [4]; in this case the position of the maximum and the minimum of the curve give estimates of the axial and perpendicular components of g. Here, it was estimated that $g_\perp = 2.72$ and a $g_\parallel = 2.08$. Due to the breadth of the peaks, this approach may lead to significant errors.

More surprising is the observation of the fine structure, due to spins much less coupled to the bulk. The positions of the oscillations are close to those in the simulation based on the parameters published by Assour *et al.* [3] for CoPc diluted in α-ZnPc. They contain two groups of lines, corresponding again to two values of an axial g tensor, each group split into 8 lines by the hyperfine interaction with the 7/2 nuclear spin of ^{59}Co. By slightly tweaking Assour's parameters to the

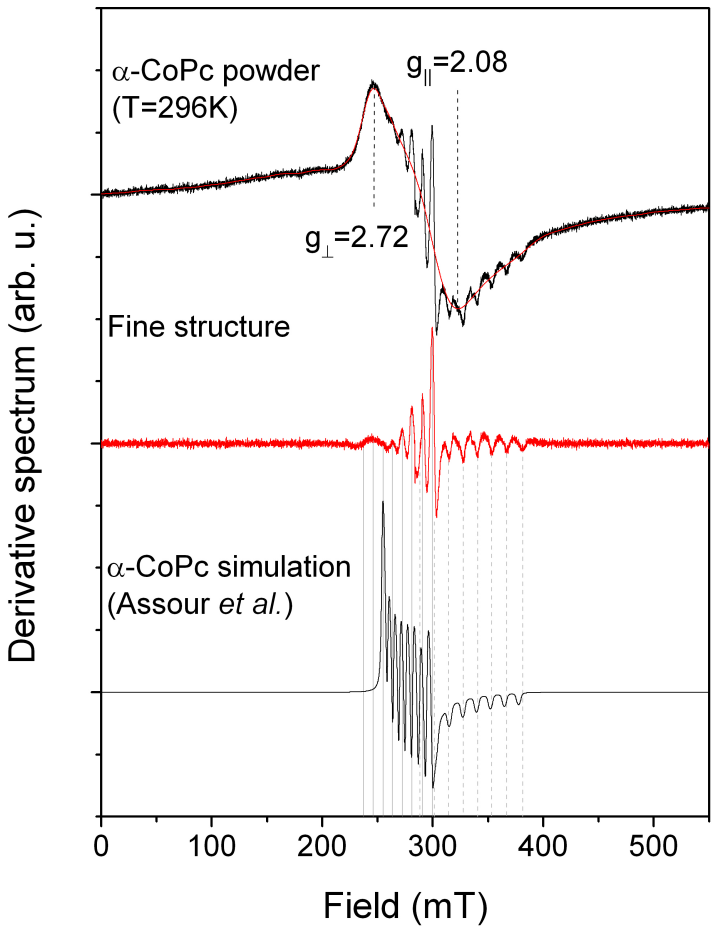


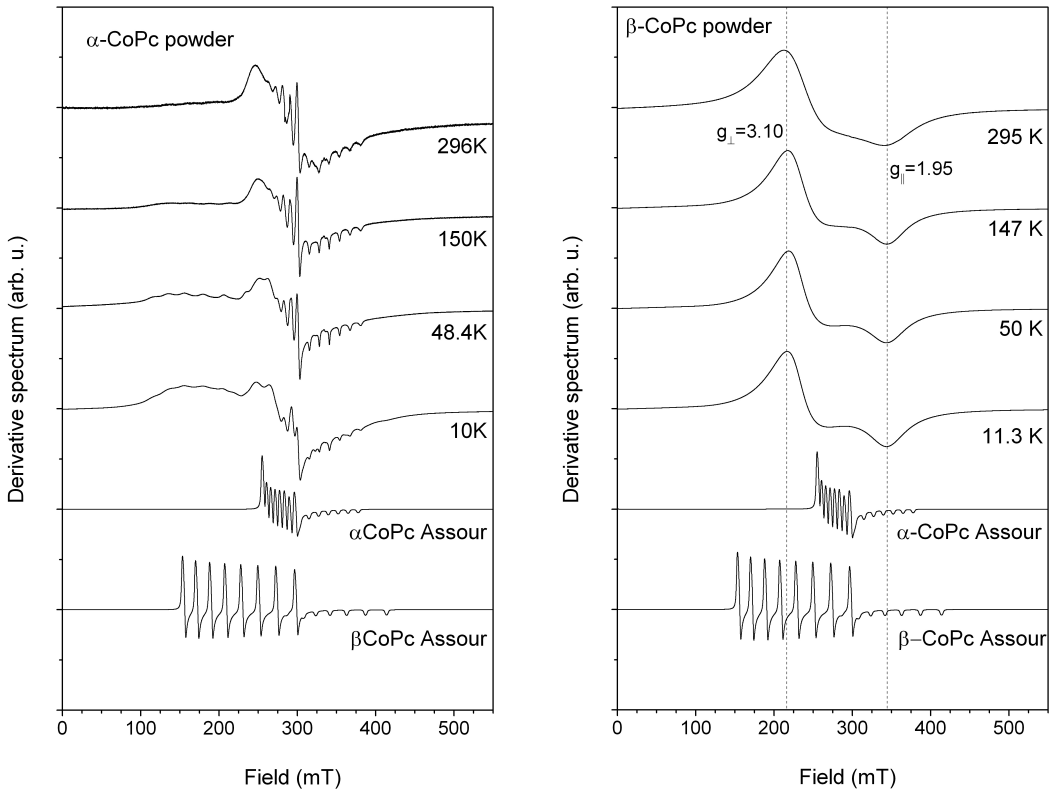
Figure 3.13: EPR spectrum (9.40 GHz) of α-CoPc acid paste powder at room temperature. The spectrum is composed of a broad component and a fine structure, which have been deconvoluted using a low pass and a high pass filter. The simulation of the spectrum of α-CoPc based on the parameters by Assour[3] (Table 3.3) was performed with Easyspin and is shown for reference

values listed in table 3.3, a good agreement is obtained. This suggests that the resonances are attributable to CoPc molecules. The fact that the hyperfine lines are spaced by the same amounts observed in a diluted sample suggests that the molecules responsible for this signal are not significantly coupled to other spins, *i.e.* the exchange energy J is much weaker than A, the hyperfine constant. In fact, the spectrum of an antiferromagnetically coupled dimer shows a halving of the distance between the hyperfine lines [11]. In more general terms, the spacing should be reduced by a factor equal to the number of coupled spins.

These observations suggest that the α-CoPc powder contains two spin environments. The majority of the spins are highly coupled and presumably form the bulk of the grains, while a minority of them are relatively uncoupled and are probably located at the surface of the grains.

The temperature dependence of the EPR spectrum is shown in Figure 3.14(a). The fine structure visible above 300 mT becomes sharper and more intense as the temperature is reduced, and then decays at 10 K, when other weak peaks become visible in the same field range. Below 100 K a new structure containing at least 8 peaks becomes visible between 100 mT and 260 mT. Interestingly, these features are quite close to those observed by Assour *et al.* in diluted β-CoPc powders. The XRD analysis excluded that the sample contained any β-phase, however this might be present in a disordered form which is not detected by diffraction. Another possibilty is that the CoPc molecules responsible for this signal are at the boundary of α-phase domains and are coordinated on the outer side by ligands in a position that mimic the environment experienced by the cobalt ion in the β-phase.

Differently from the EPR of the α-phase, the spectrum of β-CoPc powder shows only a broad unresolved absorption envelope without any fine structure from room temperature to 11.6 K (Figure 3.14b) with a modest narrowing of the spectrum occurring as the temperature is decreased. This matches with the higher crys-



(a) (b)

Figure 3.14: Temperature dependence of the EPR spectrum (9.40 GHz) of α-CoPc (a) and β-CoPc (b) powders. Simulations of the spectra using the spin paramenters by Assour (Table 3.3) were calculated using Easyspin and are shown here for reference

tallinity and much larger grain size in β-phase than in the α-phase powder, which decreases the contribution of surface molecules and defects to the EPR signal. The intensity was much higher than in α-CoPc, as shown by the different noise levels, which suggests that the spins in β-CoPc are coupled by weaker exchange interactions. The shape of the spectrum is again typical of an axial system and the maximum and minimum of the curve give $g_\perp = 3.10$ and $g_\parallel = 1.95$, which are close to the literature values (Table 3.3).

This work	$g_{\parallel}$	$g_{\perp}$	g_{powder}	$A_{\parallel}$ (cm^{-1})	$A_{\perp}$ (cm^{-1})
α-CoPc (RT)					
Fine structure	1.995	2.462	2.317	0.0117	0.0097
Broad envelope	2.08	2.72	2.52	N/A	N/A
β-CoPc (RT)					
Broad envelope	1.95	3.10	2.77	N/A	N/A
Assour *et al.*[3]	$g_{\parallel}$	$g_{\perp}$	g_{powder}	$A_{\parallel}$ (cm^{-1})	$A_{\perp}$ (cm^{-1})
α-CoPc					
1:1000 in α-ZnPc	2.007	2.422	2.292	0.0116±0.0003	0.0066±0.0003
β-CoPc					
1:1000 in β-H_2Pc	1.89	2.94	2.64	0.016±0.001	0.028±0.001

Table 3.3: Values of the g factors and hyperfine constants ($A_{\parallel}$, $A_{\perp}$) of CoPc extracted from EPR measurements on α-phase and β-phase samples. Fitting of the fine structure of the α-phase powder gave the values of both the g and the hyperfine tensors. When the fine structure was not resolved, values were estimated from the position of the maximum and minimum of the broad signal envelope. The values determined by Assour *et al.*[3] in spin diluted samples at low temperature (77 K) are also shown for reference.

3.3.2 SQUID magnetometry of CoPc samples

Low temperature magnetism

The isothermal magnetization curves $M(H)$ of the CoPc samples were measured at temperatures between 2 K and 15 K. Sweeping the magnetic field in a loop between 7 Tesla and -7 Tesla, no hysteretic behaviour was observed in any of the samples. At low temperature, the magnetism of the α and the β polymorphs of CoPc is remarkably different. Figure 3.15(a) shows the net magnetization per Co atom as a function of applied field at 2 K. The β-CoPc powder sample, whose data is scaled by a factor of 0.1 in the figure, reaches a value of 1.26 Bohr magnetons (μ_B) per Co atom under a field of 7 T, which is comparable with the saturation value ($1\mu_B$) of a $S = 1/2$ spin with $g \approx 2$. The magnetization increases almost linearly up to 5 T before the onset of saturation. The curve is not described by a Brillouin function, but it can be fitted very well with the Bonner Fisher model[15] (black line in Figure 3.15(a)) of a linear Heisenberg chain, defined by the Hamiltonian in Equation 3.1.

$$\hat{\mathcal{H}} = 2J\Sigma\hat{S}_i \cdot \hat{S}_{i+1} \tag{3.1}$$

The random orientation of the powder was simulated by averaging over all possible orientations of the chains. The values of the g tensor were taken from the literature (Table 3.3) and the g value was calculated at each angle θ between the field and the CoPc molecular plane using Equation 3.2.

$$g = \sqrt{g_{\parallel}^2 \sin\theta + g_{\perp}^2 \cos\theta} \tag{3.2}$$

The fit characterized β-CoPc as a weak antiferromagnetic material, with a value of the exchange constant J =1.86 K. The magnetic moment measured at 7 T in the α-CoPc samples is at least one order of magnitude smaller than in β-CoPc, which is the result of strong antiferromagnetic interactions in the α phase.

	α-CoPc powder	α-CoPc film (non templated)	α-CoPc/PTCDA film (templated)
g value	2.3	2.2	2.4

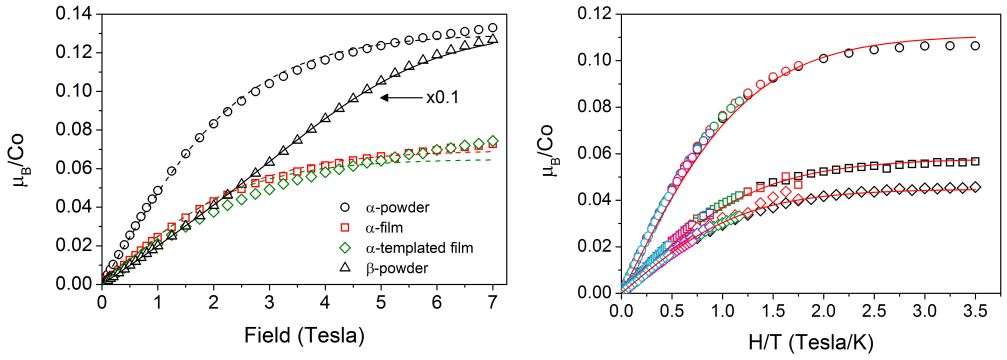
Table 3.4: Average value of g calculated for the orientation of α-CoPc powder, α-CoPc films and α-CoPc film on PTCDA. The calculation used the g tensor parameters from Assour (Table 3.3).

However, the magnetization is not entirely suppressed and the residual moment in α-CoPc samples could originate from magnetically uncoupled CoPc molecules, or short spin chain segments with an odd number of molecules, or impurities.

The curves of α-CoPc can be fitted, in a first approximation, with a Brillouin function that treats a fraction f of the Co spins as paramagnetic, and the remaining spins as non magnetic. Using the g values in table 3.4, this analysis estimates that the effective fraction of paramagnetic spins is 11 % in α-CoPc powder, 6.3 % and 5.4 % in the non-templated and templated films respectively. The agreement between the fit and the data is not excellent (dashed lines in Figure 3.15(a)), possibly due to the inadequacy of the model.

If the behaviour was truly paramagnetic, the magnetization would be a function of the ratio of the field over temperature (H/T), regardless of the temperature of the measurement. This scaling law is observed by α-CoPc samples between 2 K and 15 K only after the magnetization is corrected by subtraction of a term proportional to the field, $H\chi_0^{MH}$ (values of χ_0^{MH} in Table 3.5).

This indicates that the magnetization contains a paramagnetic part corresponding to a fraction f^{MH} of the total number of spins (see Table 3.5), which can be fitted with the Brillouin law (Figure 3.15b), and a small additional contribution described by a susceptibility χ_0^{MH} that is, at least in a first approximation, constant in temperature (between 2K and 15K) and field (up to 7 Tesla). A common source of a contribution of this kind would be diamagnetism. However the positive, rather than negative, sign of χ_0^{MH} (Table 3.5) indicates that other



(a) (b)

Figure 3.15: (a) Magnetic moment per Co atom as a function of field at 2 K in β-CoPc powder (black triangles, scaled by a factor of 0.1), α-CoPc powder (black circles), α-CoPc 200 nm film (red squares) and α-CoPc 200 nm/PTCDA 20 nm film (green diamonds). The black solid line represents the fit of the β-CoPc data with the Bonner Fisher model of a Heisenberg spin chain (S=1/2, g_z=1.9 $g_{x,y}$=2.9, J =1.86 K, average of two spin chains with 13 and 14 spins) (b) H/T scaling in α-CoPc powder (circles), 200 nm film (squares) and 200 nm film on 20 nm PTCDA (diamonds) after subtraction of field independent susceptibility χ_0^{MH} (values in Table 3.5). Colours indicate the temperature of the measurement: 2 K (black), 4 K (red), 6 K (green), 8 K (purple), 10 K (magenta), 15 K (cyan). Red lines are fit using the Brillouin function and g values in Table 3.4

mechanisms are dominant. In particular, Van Vleck paramagnetism can give an additional magnetic moment that is proportional to the field and is relatively constant with temperature. DFT calculations performed by our collaborators [101] and previous studies [53], predicted the existence of low energy orbital excited states in CoPc, which would justify a Van Vleck paramagnetic contribution larger than usual, since the effect is inversely proportional to the gap between the orbital excited state and the ground state. Finally, χ_0^{MH} can also include a contribution from long antiferromagnetic chains. The magnetization M of these systems is virtually temperature independent when T is much smaller than J/k_B. Furthermore, M increases linearly with H, as long as the applied field is small compared to saturation field H_{sat}, which scales with the exchange constant ($H_{sat}g\mu_B = 4|J|$) [15][40]. As long as J/k_B is higher than 10 K, this condition should be easily verified in our experiments.

The $M(H)$ data obtained at low temperature provided evidence of a substantial reduction of the magnetic moment in α-CoPc. In the following section the strength of the exchange interactions responsible for this effect will be determined by measuring the temperature dependence of susceptibility up to room temperature.

Characterization of the exchange coupling in α- and β-CoPc

The temperature dependent susceptibility $\chi(T)$ of CoPc, shown in Figure 3.16a, exhibits two distinct behaviours in the α and β phases.

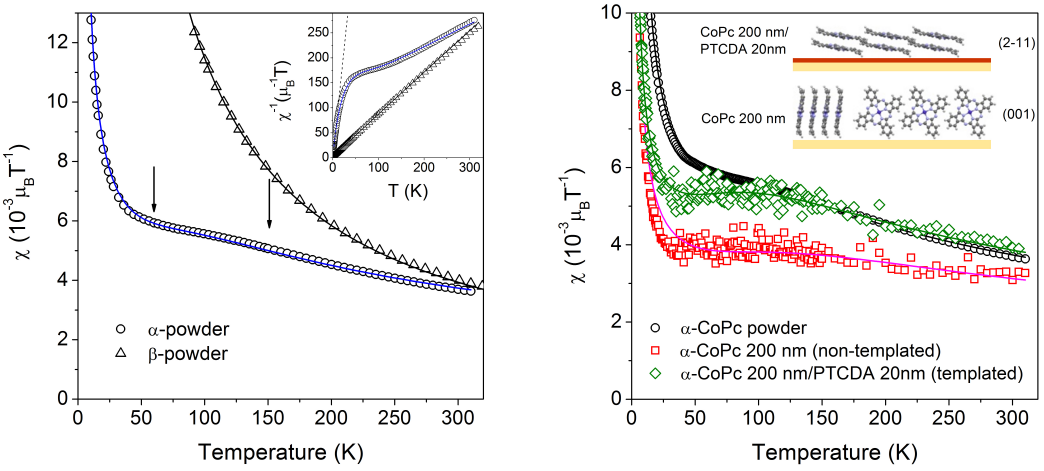
The $\chi(T)$ data of the β phase can be modelled with the standard Curie Weiss law between 8 K–310 K, extracting a Weiss temperature $\theta = -2.5$ K which is close to the exchange energy $J/k_B = -1.8$ K found by fitting the $M(H)$ curves; the exchange energy J/k_B and the θ temperature should be identical in the ideal case of a 1-dimensional S=1/2 system [13]. The Curie constant C=1.17 $\mu_B T^{-1} K$ corresponds to g=2.64, which is compatible with the value expected in the β-phase (Table 3.3).

In contrast to β-CoPc, the susceptibility of the α-phase powder is heavily suppressed, again symptomatic of antiferromagnetism, and displays inflection points around 50 K and 150 K, which mark an increase of the magnetic moment occurring around 100 K. Such effect cannot be attributed to the thermal population of a high spin state of CoPc, since DFT showed that the S=3/2 state and the S=1/2 ground state are separated by more than 1 eV[101]. Therefore the inflections in the curve are to be attributed to vanishing antiferromagnetic correlations in the chains at temperatures close to J/k_B.

Below 20 K, the trend of $\chi^{-1}(T)$ is linear (Inset of Figure 3.16b), following the behaviour of a paramagnet with a Curie constant corresponding to one tenth of the Co spins being paramagnetic (see analysis below), consistent with the field dependent data in Figure 3.15a. The change in curvature and transition to a regime dominated by the antiferromagnetism can again be clearly seen between 50 and

150 K.

Figure 3.16b shows that the $\chi(T)$ curves of the α-CoPc films grown on kapton



(a) (b)

Figure 3.16: (a) Magnetic susceptibility $\chi(T)$ of CoPc as a function of temperature: α-CoPc ($\circ$) and β-CoPc powders ($\triangle$); the main plot shows detail of the high temperature susceptibility, while the inset includes the full data range. The red line is a fit of $\chi(T)$ in α-CoPc powder with a model based on the Johnston antiferromagnetic chain formula and a Curie correction (Equation 3.3) to include finite size effects. The black line is the Curie Weiss fit of β-CoPc powder (8 K–310 K). $\chi(T)$ is calculated (Equation 2.13) as the incremental ratio of $M(T)$ between fields of 500 Oe and 1000 Oe; for an explanation of units refer to section 2.3.7 and Equation 2.12. Inset: Plot of the reciprocal of $\chi(T)$. Dashed black line is the linear fit of α-CoPc powder at low temperature. Solid lines represent the fits shown in the main figure. (b). Susceptibility of α-CoPc films and powders; the $\chi(T)$ values in the films are calculated from $M(T)$ measurements at 5000 Oe and 10 kOe (Equation 2.13). Solid lines are fits using Equation 3.3. Inset: preferential orientation of CoPc molecule in templated and non-templated films

exhibit similar features to those found in the powder of the same phase. The temperature dependent susceptibility is again characteristic of a strong antiferromagnet. The curvature around 50–150 K is more pronounced for the films, especially in the templated case.

Bonner and Fisher have shown in their calculations [15] that infinite Heisenberg antiferromagnetic chains exhibit a maximum in susceptibility at $T_{max} = 1.282 J/k_B$. The maximum of $\chi(T)$ is progressively obscured, as the chain length is reduced, by

the Curie-like divergence of the susceptibility that is characteristic of chains with an odd number of spins. Therefore, the different characteristics of the curvature of $\chi(T)$ in the α-phase samples suggest that the typical length of the spin chains is higher in the films than in the powder.

The overall shape of the curves is similar for all three α-phase samples. In particular, the position of the inflection points and local maxima in the $\chi(T)$ curves is not affected by the different molecular orientation found in the samples. This suggests an isotropic exchange mechanism, as expected for a spin = ½ system, and validates the analysis using the Heisenberg model.

In order to extract the values of the magnetic coupling, the $\chi(T)$ of the α-phase has been fitted with a model that includes three terms, namely the susceptibility of an infinite antiferromagnetic chain χ_{AF} [48], a Curie term C/T and a temperature independent correction χ_0^{χ} (Equation 3.3).

$$\chi(T) = \chi_{AF}(T) + \frac{C}{T} + \chi_0^{\chi} \tag{3.3}$$

The fit yields a value of the antiferromagnetic exchange interaction $J/k_B = 78.4\,\mathrm{K}$ in the powder. The value of the Curie constant is $C = 0.0955\mu_B T^{-1} K$ corresponds to a fraction $f^{\chi} = 10.6\%$ of the CoPc molecules exhibiting a moment $\mu_{eff} = 2.0\mu_B$ ($g = 2.3$ and S =½), consistently with the fit of the $M(H)$ data (Table 3.5). Since EPR did not show significant amounts of paramagnetic impurities in the α-phase powder (see section 3.3.1), it can be concluded that this Curie term can be traced back mainly to the presence of short spin chains in the material. The value of χ_0^{χ} is slightly smaller than χ_0^{MH} (Table 3.5), possibly because the Van Vleck paramagnetism is weakly temperature dependent and also because any contribution from the antiferromagnetic chain is now temperature dependent and included in $\chi_{AF}(T)$.

Similar fits were made for the films and are summarised in Table 3.5. The values of

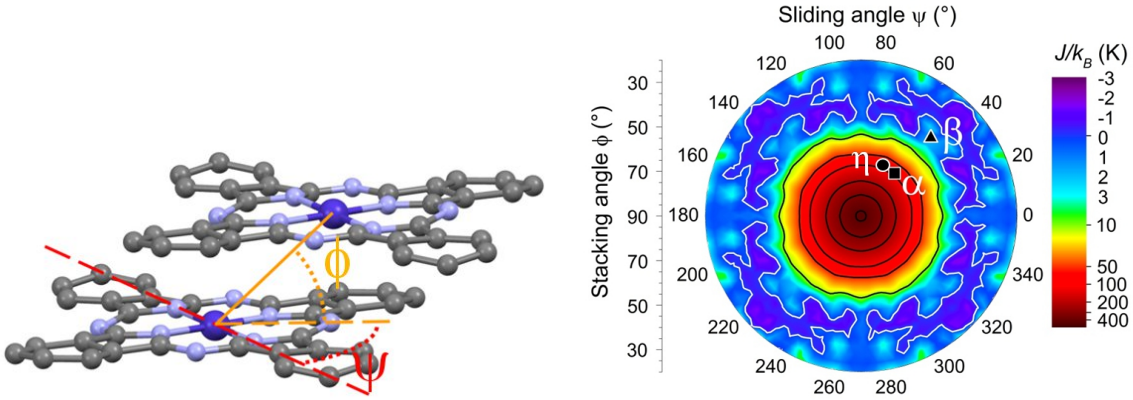
	$J/k_B(K)$	$\chi_0^{\chi}(\mu_B T^{-1})$	$\chi_0^{MH}(\mu_B T^{-1})$	f^{χ}	f^{MH}
α-CoPc powder	78.4	1.2×10^{-3}	3.8×10^{-3}	0.106	0.096
α-CoPc 200 nm	106.6	1.1×10^{-3}	2.3×10^{-3}	0.052	0.052
α-CoPc 200 nm\ PTCDA 20 nm	80.3	1.2×10^{-3}	4.1×10^{-3}	0.038	0.036

Table 3.5: Magnetic parameters extracted from SQUID measurements. J is the exchange energy, χ_0^{χ} is the temperature independent correction to the $\chi(T)$ curves, χ_0^{MH} is the temperature and field independent correction applied to M(H) curves, f^{χ} is the fraction of paramagnetic spins calculated from the Curie constant fitting the low temperature trend of $\chi(T)^{-1}$ (with g as in Table 3.4), while f^{MH} is the fraction of paramagnetic spins obtained by fitting the $M(H)$ curves.

exchange couplings are even higher with $J/k_B = 80\,\mathrm{K}$ and $106\,\mathrm{K}$ for the templated and non-templated films respectively, while the fraction of paramagnetic spins is significantly reduced.

The characterization of a large value of J was corroborated by the results of DFT calculations made by Dr Wu, which are the subject of a recent publication[101]. The theoretical analysis calculated antiferromagnetic J values of 81 K in the α phase and 2 K in the β phase, in very good agreement with the results of the fits of the experimental data. The calculations of the exchange energy considered also a variety of other stacking geometries. Figure 3.17 shows the contour plot of the exchange energy J/k_B as a function of the stacking (ϕ) and sliding (ψ) angles of the CoPc chains, which are defined in the figure. It can be seen that above a stacking angle of 50°, the exchange energy is rather insensitive to the sliding angle; within this regime, the coupling mechanism was described with the superexchange between the d_{z^2} orbitals of the Co atoms. As the stacking angle is increased above the value of the α phase ($\phi \approx 65°$) the value of J/k_B is predicted to further increase and surpass 400 K in a perfect cofacial stacking ($\phi \approx 90°$). For values of ϕ below 50°, the exchange constant shows variations as the sliding angle is varied. The pattern has the four-fould symmetry of the CoPc molecule because

the mechanism is increasingly relying on the organic ligand. These calculations show that there is scope for improving even further the magnetic interactions.



(a) (b)

Figure 3.17: (a) definition of the stacking (ϕ) and sliding (ψ) angles in CoPc chains. (b) contour plot of the calculated exchange energy as a function of the stacking and sliding angles in CoPc crystals. Note that the height scale is linear from -3K to 3K, and logarithmic thereafter. Contour lines are drawn at 0 K, 10 K, 50 K, and then for every 100 K increment from 100 K to 400 K. The points corresponding to the α, β and η CoPc structures have been highlighted with a square, a triangle and a circle respectively. The structure of η-CoPc is assumed to be identical to that of η-CuPc nanowires [95]; this assumption could be incorrect, as discussed in Chapter 4

Analysis of the magnetism in α-CoPc with a finite chain model

It was shown earlier that the behaviour of α-CoPc samples is described by a strong antiferromagnetic behaviour above 50 K, while at low temperature is characterized by a certain paramagnetism.

The previous analysis, which focussed on the quantification of the exchange interaction, used a simplified model where the antiferromagnetic susceptibility of an infinite chain was corrected by a Curie term to account for the low temperature diverging behaviour. Although that approximation was able to capture the essential characteristics of the system, the use of an infinite chain model can be questionable in nanocrystalline organic materials. Furthermore, that model lacked of a direct link with the structural properties of the material.

The TEM images of the α-CoPc particles (see Figure 3.12) showed that inside the grains, the CoPc columns may be intact across the whole size of the grain, while in the region of the grain boundary the lengths were drastically reduced. This observation suggested the use of a binomial distribution of chain lengths to fit the susceptibility. The simplest chain length distribution that could be used is expressed mathematically by Equation 3.4:

$$P(L) = \frac{A}{2}(\delta_{L,N} + \delta_{L,N+1}) + \frac{1-A}{2}(\delta_{L,M} + \delta_{L,M+1}) \tag{3.4}$$

where $P(L)$ is the probability of having a chain formed by L CoPc molecules, N and M are integer numbers, $\delta_{i,k}$ is the Kronecker delta, and A is an amplitude which can take values between 0 and 1. The distribution P(L), of which Figure 3.18 gives an example, describes a system with two characteristic chain sizes, by incorporating two pairs of chain lengths, each pair formed by chains of N (M) and N+1 (M+1) spins in equal fraction, ensuring a balance between odd and even chains. This latter property is very reasonable and is essential to avoid distortions in the results of the fit, due to the fact that the susceptibility of chains of opposite parity diverges at low temperature[15].

Averaging the susceptibility of finite chains over $P(L)$ and adding the temperature independent correction χ^{χ} gives the following expression for $\chi(T)$:

$$\chi(T) = A\frac{\chi_{N,J}(T) + \chi_{N+1,J}(T)}{2} + (1-A)\frac{\chi_{M,J}(T) + \chi_{M+1,J}(T)}{2} + \chi_0^{\chi} \tag{3.5}$$

where $\chi_{N,g,J}(T)$ is the suceptibility at a temperature T of a chain of N spins, coupled by an exchange interaction of energy J. The $\chi_{N,g,J}(T)$ functions were calculated using the Bonner-Fisher method[15]. In contrast to Equation 3.3, this model does not include the Curie term, since the $\chi(T) \propto T^{-1}$ behaviour at $T \ll J/k_B$ is intrinsic in finite chains with an odd number of molecules. Each pair in

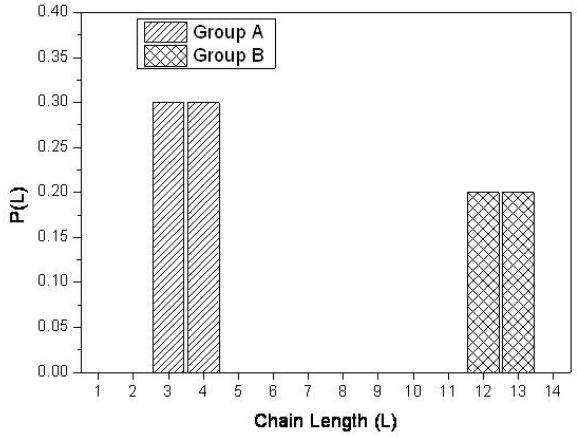


Figure 3.18: Example of a spin chain length distribution in CoPc materials reflecting a bimodal character, as defined in Equation 3.4. In this example 60 % of the CoPc molecules are part of the grain boundaries (group A), having an average length of 3.5 molecules, while the remaining 40 % belong to the core of the grains (group B) and have an average length of 12.5 molecules.

$P(L)$ contributes one uncompensated spin S=1/2 a low temperature, therefore the fraction f of paramagnetic spins is linked to the size distribution by the following expression:

$$f = A\frac{1}{2N+1} + (1-A)\frac{1}{2M+1} \tag{3.6}$$

The susceptibility of the α-CoPc powder was fitted to the equation 3.5 for all values of the chain lengths N and M between 1 and 14 spins; the upper limit of 14 molecules was determined by computational constraints. The map of the residuals as a function of the two characteristic chain lengths (Figure 3.19a) shows that the optimal chain distribution must include short (1–4 molecules) and longer chains (4–14 molecules) at the same time. Within the region of optimal size distribution, the agreement with the data is excellent (Figure 3.20) and the fit parameters are relatively constant (Table 3.6), with an average value of J/k_B, χ_0 and fraction f of paramagnetic spins of 73 K, $1.33 \times 10^{-3}\mu_B T^{-1}$ and 11.4 % respectively.

A similar analysis for the films yields exchange interactions of 103 K and 79 K for the non-templated and templated film respectively, and all values are in line

	Length range Group A Group B	WRMSE ($m\mu_B$/T) average min max	RMSE ($m\mu_B$/T) average min max	J/k_B (K) average min max	χ_0^χ (μ_B/T) average min max	f (%) average min max
α-CoPc	1–4	2.10	0.613	73	1.33	11.4
powder	4–14	1.23	0.431	72	1.27	8.9
		2.87	0.753	77	1.37	14.0
α-CoPc	8–14	1.64	0.311	103	1.19	6.2
200 nm	1–8	1.55	0.280	100	1.13	5.2
		1.74	0.336	106	1.22	7.0
α-CoPc	8–14	2.83	0.804	79	1.29	5.0
200 nm\	1–14	2.42	0.643	77	1.19	3.7
PTCDA		3.90	1.22	82	1.54	5.9

Table 3.6: Summary of the results of the finite chain fits of the CoPc susceptibility (Equation 3.5). The chain length range defines the chain distributions (Equation 3.4) that result in the best fits (*i.e.* WRMSE $<4 \times 10^{-3}\,\mu_{\mathrm{B}}\mathrm{T}^{-1}$); WRMSE is the weighted root mean of squared errors, where the squared errors are weighted by the density of data points at each temperature; RMSE is the root mean of squared errors. J/k_B is the exchange energy in K, χ_0^χ is the temperature independent correction, f is the fraction of paramagnetic spins predicted at low temperature, calculated with Equation 3.6

with the treatment based on the infinite chain (Table 3.5). The complete results of the fit of the films are given in section A.2 of the appendix. The analysis gave a less constrained chain length distribution in the films, showing that the chains are overall longer than in the powder. This approach proved that the magnetic properties of α-CoPc samples can be fully explained by an ensemble of antiferromagnetic chains of finite size and J/k_B between 73 K and 103 K.

The determination of the maximum length of the chains in the sample is elusive, because the $\chi_{N,g,J}(T)$ curves rapidly converge to the infinite chain limit as the length is increased. In order to check if the magnetic properties were compatible with chains extending throughout the crystal sizes (Table 3.2), the fraction of

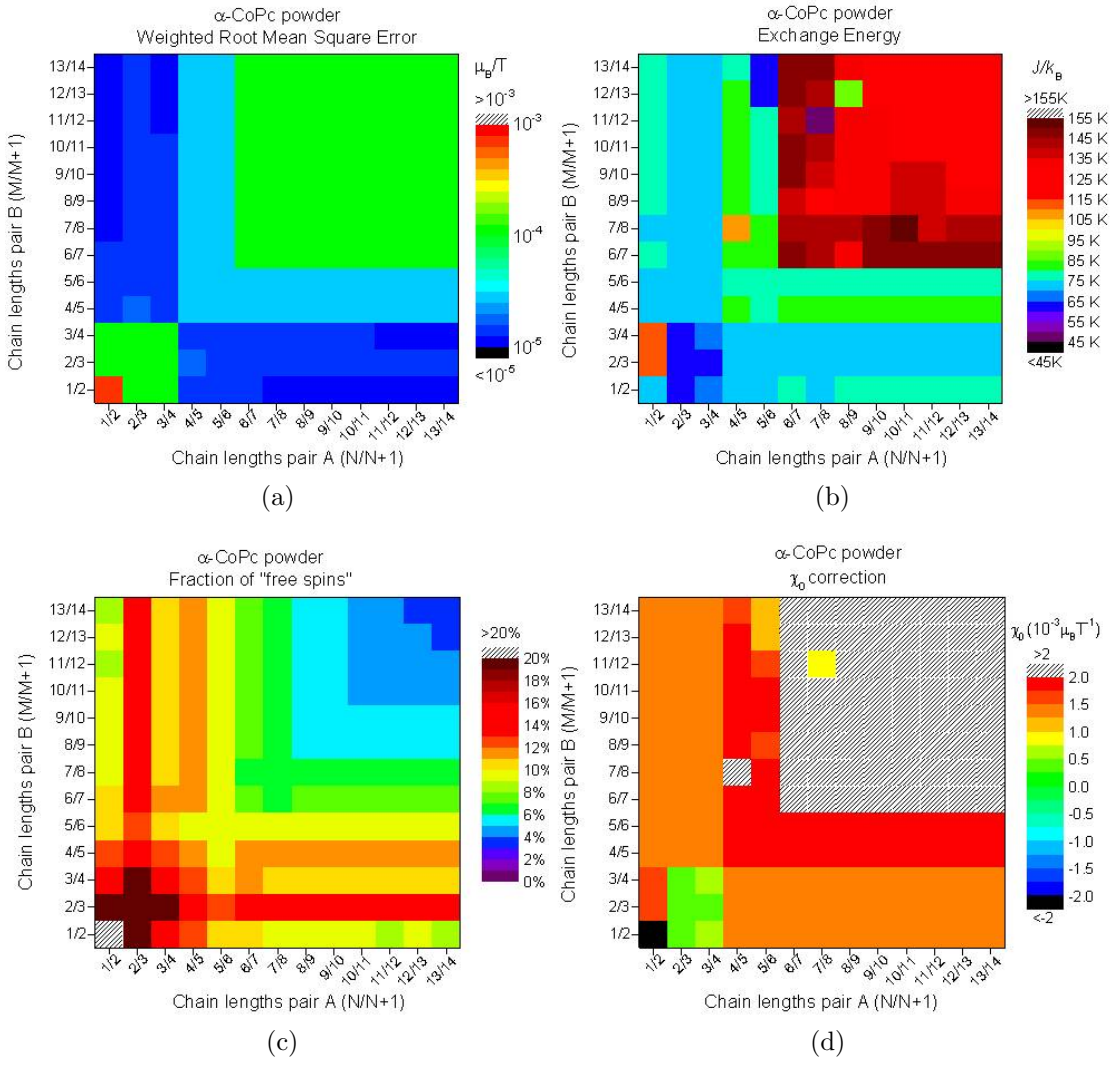


Figure 3.19: Results of the fit of the α-CoPc powder susceptibility using the finite chain model (Equation 3.5). Residuals and values of the fitted parameters are shown in the color map for all combinations of chain lengths. (a) Weighted root mean square error of the fit; (b) values of the exchange energy J/k_B; (c) values of the temperature independent correction χ_0; (d) fraction f of paramagnetic spins

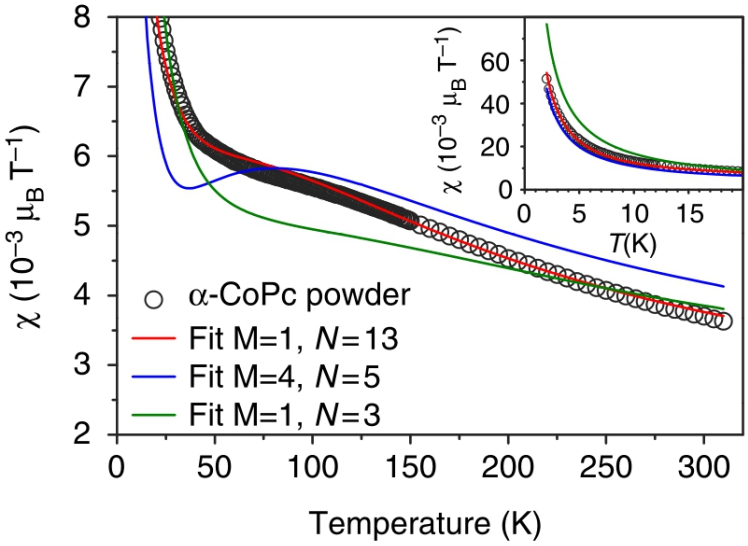
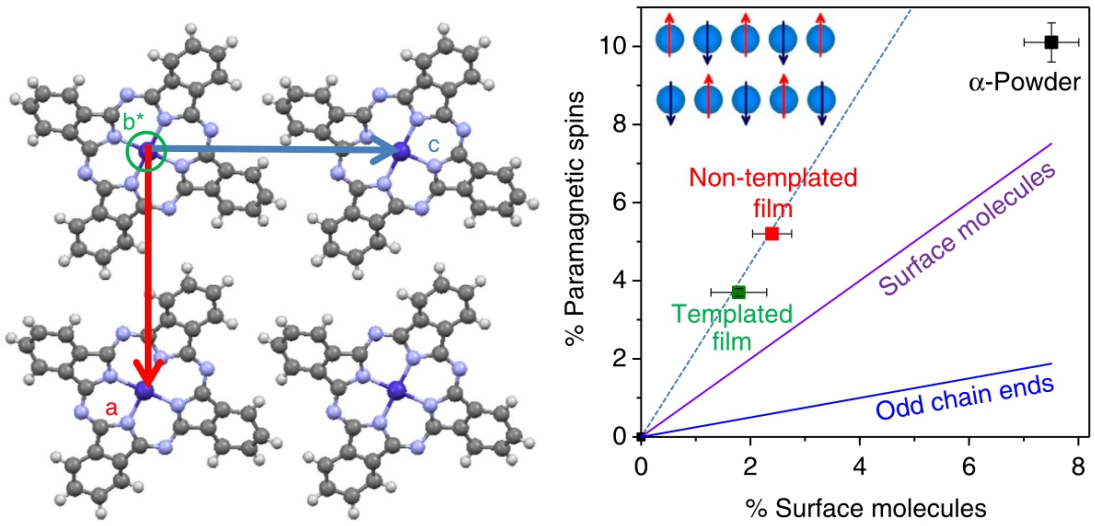


Figure 3.20: Characteristic fits of the susceptibility of α-CoPc powder highlighting that the inflection at low T ($\approx$ 30 K) (see inset) and the high temperature susceptibility requires contributions from both long and short chains

paramagnetic spins in the three typologies of α-CoPc samples was plotted against the ratio of surface molecules to the total number of molecule in the particles (Figure 3.21). It was found that the fraction of paramagnetic spins f nearly showed an inverse proportionality relation with the calculated fraction of molecules at the surface of the grains. The experimental values are compared in Figure 3.21 with trends corresponding to the case where the chains are not fragmented in the grain; in the blue line, only odd chains were contributing to f, while in the purple line it was assumed that all chain ends at the surface were paramagnetic. It can be seen that the experimental points lie above both trends, suggesting that, in addition to decoupling of the surface molecules, fragmentation of the spin chains within the grains should also contribute.



(a) (b)

Figure 3.21: (a) Projection of the CoPc unit cell along the b^* axis, highlighting that the cross-section area of a CoPc chain can be approximated by the product ac. (b) Scaling of the fraction of paramagnetic spins in α-CoPc samples with the fraction of surface molecules corresponding to chain ends, and which can be approximated by $3b/2r$, where b is the lattice vector ($b = 3.75$Å) and r is the particle radius as estimated from the Scherrer equation (Table 3.2). The fractions of spins and their error bars were determined by averaging the values obtained from the $M(H)$ and $\chi(T)$ experiments. The solid lines represent the fraction of paramagnetic spins expected if their origin is either all the surface molecules corresponding to chain ends (slope=1, purple) or only one spin per odd chain (slope=1/4, blue). The dotted line is a fit through the film data and has a slope of 2.2. The cartoon is a schematic representation of the S=1/2 ground state for a chain of 5 spins

Chapter 4

Cobalt phthalocyanine (CoPc) nanowires

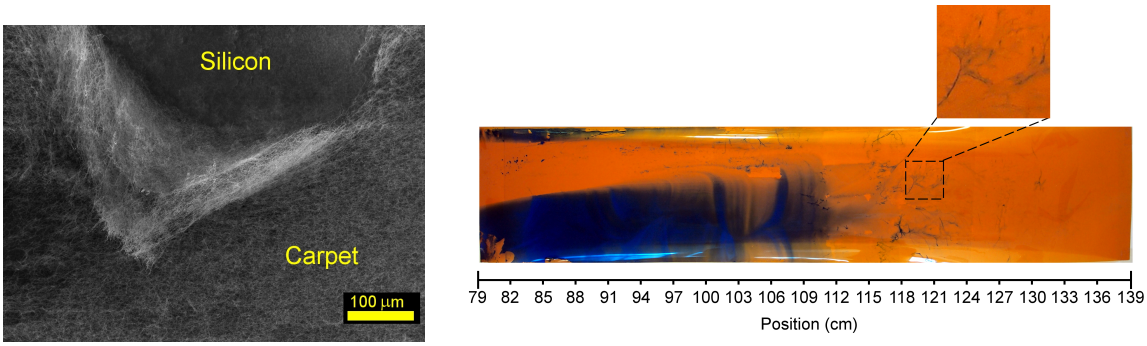
This chapter will present the structural and physical properties of cobalt phthalocyanine nanowires. This material was prepared for the first time in this work using a process adapted from the one used in the growth of copper phthalocyanine nanowires. CoPc nanowires are characterized by extremely high aspect ratios and exhibit signatures of a new polymorph of CoPc, which shows similarities with the η phase found in CuPc nanowires. In marked contrast with the DFT prediction of strong antiferromagnetism in a hypothetical η-CoPc, the nanowires were found to be almost paramagnetic. Possible reasons for this discrepancy are analysed.

There is an interest in investigating new morphologies and polymorphs of organic conjugated materials, as this often allows tailoring of their properties for some specific applications. Organic nanowires are particularly interesting since their low dimensionality enhances charge mobility, allows better control of carriers concentrations and offer high surface to volume for sensing applications, among other advantages. Our group has previously developed an organic vapour phase deposition method that produces copper phthalocyanine nanowires [95] which are characterized by extremely high aspect ratios and exhibit a previously unknown crystal structure which has been named the η phase. The prospect of producing

CoPc nanowires of the same polymorph is rather appealing, since the η structure exhibits a stacking angle similar to the α phase (66°) which, according to the DFT calculations discussed in chapter 3, should result in an antiferromagnetic coupling of the spins above the boiling point of liquid nitrogen (see Figure 3.17).
The method of Wang *et al.*[95] was adapted to a furnace of larger diameter, as described in 2.2.2, and successfully applied to the growth of CoPc. The nucleation of the CoPc structures during a deposition is visible by naked eye after 12 hours, however the typical growth duration is 2 to 3 days. The condensation of CoPc is initiated when the vapours are cooled below 280° and continues all the way out to the tube end. The changes in temperature and gas flow patterns encountered along the tube result in the formation of different polymorphs and morphologies, which will be characterized in the following sections.

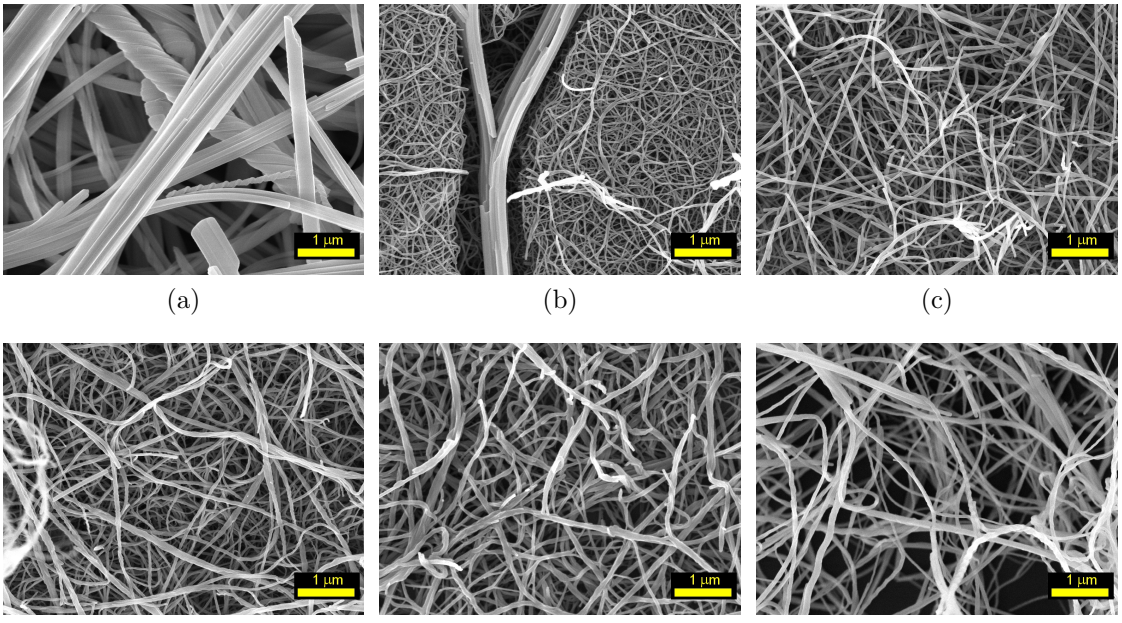
4.1 Identification of the nanowire phase

In this section we focus on samples collected between the hottest growth region, located 10 cm before the end of the coldest zone of the furnace (zone 3, see section 2.2.2), and the region which is 20 cm outside the furnace, which spans the growth temperature range between 280°C and 20°C. To help the identification of the samples, a labelling system that uses the distance between the sample and the beginning of the hottest zone of the furnace (zone 1) is adopted, in agreement with the one used for to express the temperature gradient in the furnace (see section 2.2.2). Figure 4.2 shows the evolution of the morphology, observed through a scanning electron microscope. The structures grown at the highest temperature (70 cm, 280°C) show a rod-like morphology (Figure 4.2a). The rods are generally straight or slightly bent. They have a lateral size comprised between 100 and 300 nm, but can form larger bundles. In some cases, twisting in the elongation direction is observed. Further along the tube, the morphology changes to a mixture



(a) (b)

Figure 4.1: (a) SEM image of a carpet of CoPc nanowires lifted from a silicon substrate after manipulation. (b) Photographic image of the kapton film covered by CoPc nanowires after the growth. The scale indicates the position in the tube, according to the convention defined in this chapter. In the inner part of the kapton film, the nanowires from a mesh with a film-like appearance; in the outer region strands of nanowires are observed.



(a) (b) (c)

(d) (e) (f)

Figure 4.2: SEM images (50kX) of CoPc nano-structures obtained by OVPD at different positions in the tube: (a) 70 cm, (b) 75 cm, (c) 80.5 cm, (d) 87.5 cm, (e) 95 cm, (f) 102.5 cm

of the rod-like structures and thin flexible fibres with a maximum diameter of 50 nm (Figure 4.2b) randomly woven to form a carpet. The morphology does not change significantly as the distance is further increased, indicating that the nanofibres are the most stable configuration outside the furnace (Figures from 4.2c to 4.2f). The carpet is relatively resistant and can be lifted off the kapton film with tweezers (Figure 4.1a).

A preliminary identification of the polymorph composition of the samples collected at various positions of the tube was carried out by visible light absorption (Figure 4.3a). The sample grown at the highest temperature (70 cm) gave poor optical measurements as it was heavily scattering. The remaining samples show very similar characteristics, namely a broad absorption profile that extends from 500 nm to 800 nm and features two main bands centred at 600 nm and 750 nm. After normalization of the intensity at 750 nm, the spectra of the samples overlap very well in the visible range, with the exception of the first sample of the series (75 cm), which shows slightly higher intensity at shorter wavelengths. The similarity points to a common polymorph type across the region between 80.5 cm and 102.5 cm, while the sample collected at 75 cm probably contains a mixture of polymorphs, matching the conclusions obtained from SEM images.

A comparison of the spectra with those of the α and β phases of CoPc emphasizes the increased breadth and the red-shifted onset of the absorption in the nanowire phase (Figure 4.3b). A close examination of the data in the range between 400 nm and 500 nm reveals a weak transition that is shown by all three CoPc polymorphs, suggesting that it should be intramolecular.

The juxtaposition of the CoPc and CuPc nanowire spectra in figure 4.3b shows that the Q band absorption is broadened to a similar extent in the two materials, but it also highlights important differences in the spectra. In particular the two broad peaks in the Q band have round maxima and similar intensity in CuPc, differently from CoPc where the absorption peak at 750 nm is clearly stronger and slightly

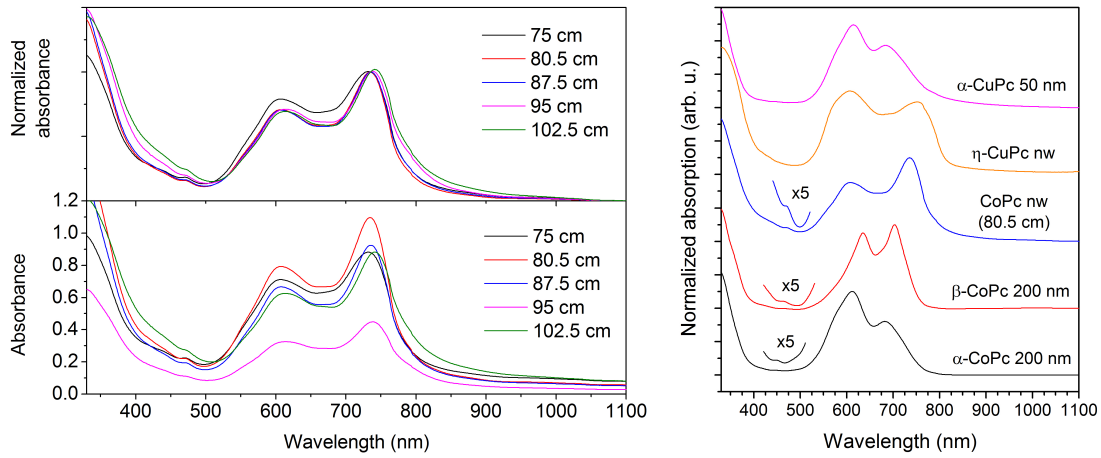


Figure 4.3: (a) UV-Vis absorption spectrum of CoPc nanostructures obtained by OVPD in different tube positions. The transition through a region of the OVPD tube where mixed phase growth occurs (75cm) is shown by the evolution of the spectrum. (b) Distinction from the α and β-CoPc spectra confirms the presence of a new polymorph. The absorption is remarkably similar to that of CuPc nanowires [95]

sharper. These observations may be a hint of a different crystalline structure of the CoPc and CuPc nanowires, since the two molecules exhibit a remarkably similar absorption in the α form, which indicates a comparable electronic structure.

Insight into the crystal structure of these samples is gained from X-ray diffraction measurements, shown in Figure 4.4. The sample grown at high temperature, showing a rod-like morphology (Figure 4.2a), manifests sharp peaks that match to the β-CoPc pattern. The narrow width of the peaks, close to the instrumental broadening, indicates that the X-rays are reflected by crystals larger than 100 nm. Less sharp β-phase reflections can also be observed in the sample collected at 75 cm, alongside with diffraction features that cannot be attributed to either the β or α phases, in agreement with the mixed morphology observed by electron microscope (Figure 4.2b). The strong reflection at $2\theta = 8.72°$ can be found also in the following samples of the series, demonstrating that it is characteristic of the nanowire phase. The Scherrer crystallite size calculated for this diffraction peak

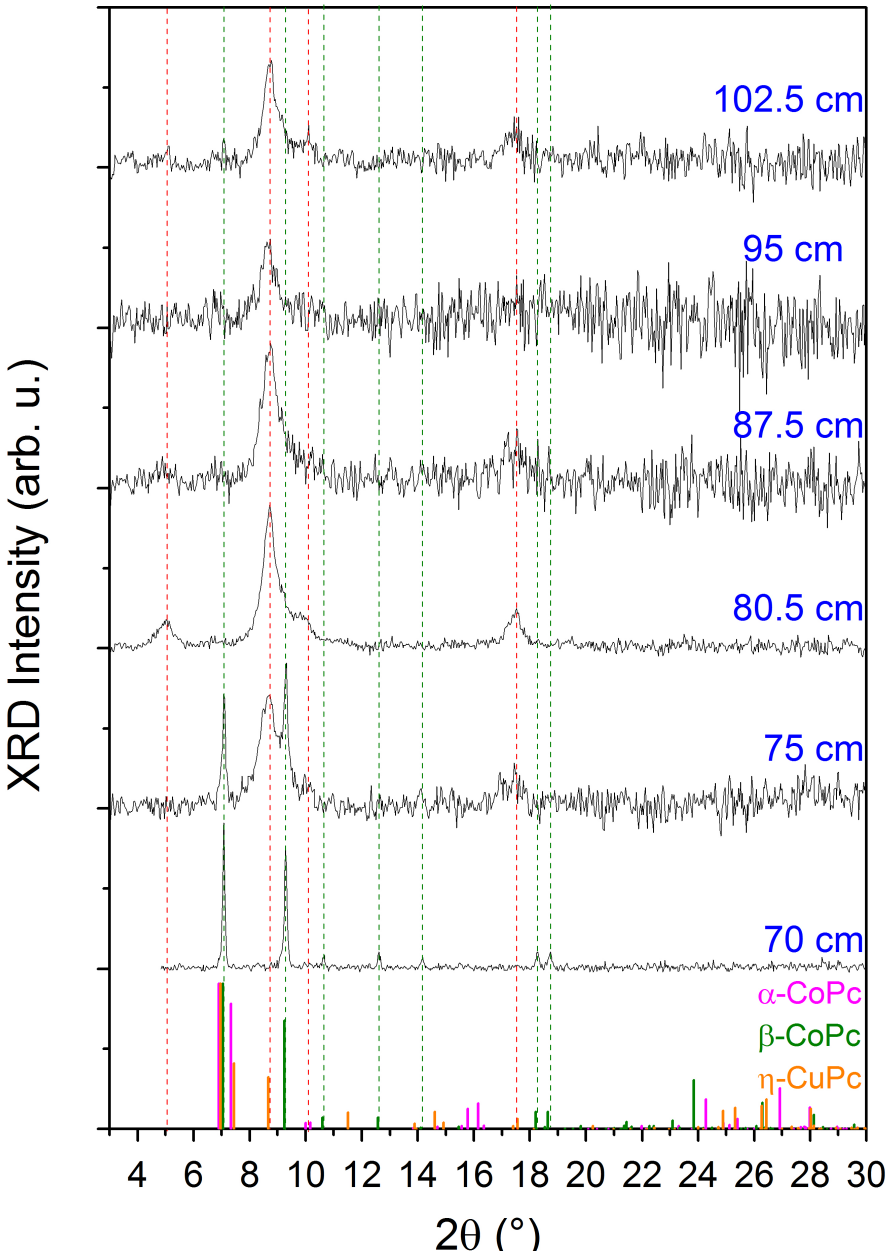


Figure 4.4: XRD of the CoPc nanostructures collected along the tube. Peak characteristic of the nanowire phase have been highlighted by red dashed lines at the following 2θ positions: 5.05°, 8.72°, 10.09°, 17.53°. Peaks that can be assigned to β-CoPc are highlighted by green vertical lines at these positions: 7.09°, 9.28°, 10.65°, 12.61°, 14.16°, 18.62°, 18.73°

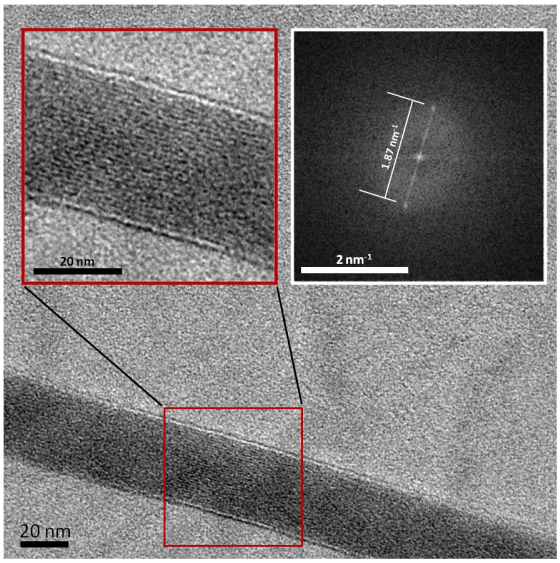
Position (cm)	Angle ($2\theta°$)	*width* ($2\theta°$)	*Area*	size (nm)	d (Å)	phase	plane
75	7.08	0.118	141.6	102–235	12.5	β	(100)
	8.66	0.70	891.4	13–14	10.2	η	(20-1)
	9.29	0.156	193.3	66–116	9.5	β	(10-2)
	10.05	0.40	58.5	23–28	8.8	?	
80.5	5.00	0.57	416.1	16–18	17.6	?	
	8.72	0.53	1984.9	17–20	10.1	η	(20-1)
	9.28	0.37	166.1	25–31	9.5	β	(10-2)
	9.89	0.58	361.3	15–18	8.9	?	
	17.46	0.53	489.7	17–21	5.1	η	(202)
87.5	8.71	0.69	666.0	13–14	10.1	η	(20-1)
95	8.67	0.60	242.6	15–17	10.2	η	(20-1)
102.5	8.71	0.56	575.0	16–19	10.1	η	(20-1)
	9.17	0.4	61	23–28	9.6	β	(10-2)
	10.06	0.7	182	13–14	8.8	?	

Table 4.1: Peak parameters of CoPc nanostructures samples grown by OVPD collected at different positions along the furnace tube. For each sample the table gives the Bragg angle of the peaks observed, their width and integrated area, the corresponding Scherrer size and lattice spacing, and the assignment to either the β or η polymorphs, with the relative Miller indices (hkl). The question mark indicate peaks that could not be assigned

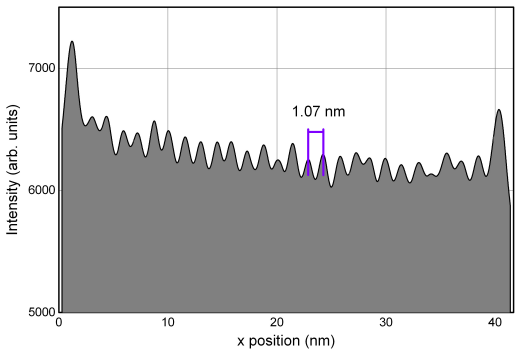
is between 10 nm and 30 nm and therefore correlates with the nanowire lateral size observed by electron microscopy. The peak position matches very well the (20-1) spacing (d=10.2Å) of the η structure reported in CuPc nanowires [95]. The $2\theta = 8.72°$ peak in the sample collected at 102.5 cm shows a shoulder at higher 2θ angle, in the position of the (10-2) peak of the β-phase, which might indicate some minor contamination by β crystals carried away by the gas flow from the high temperature growth region. Other weak reflections can also be identified. The diffracted intensity measured around 17.5° could be second order diffraction linked to the previously described peak or could be caused by the (202) set of planes in the η structure.

The interpretation of other features, not predicted by the η structure, is more challenging. The XRD pattern of the sample collected at 80.5 cm clearly shows a further peak at 5.05°, corresponding to an unusually large lattice spacing d=17.47Å, which is not reported in any known phthalocyanine structure. This reflection can only be observed in crystals of a relatively large molecule; the value of the plane spacing is close to diagonal dimension of a CoPc molecule (14.5Å), therefore it is compatible with the interchain distance in a CoPc polymorph. Further to this peak, a shoulder at 2θ=10.1° is also observed; the interplane spacing (d=8.74Å) is half the value calculated for the previous peak, so it seems likely that this is its second order reflection. The feature at 2θ=10.1° is also in the angle range of the (101) or the (10-1) diffraction in the α-phase, but this assignment is rather unconvincing given the absence of the much stronger (100) and (001) α-phase reflections, which are normally seen in thin films and form a close dihedral angle with the (101) and (10-1) planes. It should be stressed that these diffraction peaks of uncertain attribution were not reproduced in each growth. This aspect should be investigated more carefully in the future.

In order to gather microstructural information on the nanowires, Dr Luke Fleet performed a TEM analysis of the samples. The image in Figure 4.5 shows an



(a)



(b)

Figure 4.5: High Resolution TEM (HRTEM) image of a CoPc nanowire (a); the insets show a zoomed image of the diffraction fringes within the nanowire and its Fast Fourier Transform (FFT). The profile of the intensity across the wire is shown in (b), highlighting a spacing of 1.07 nm between the fringes. Courtesy of Dr Luke Fleet.

individual nanowire with a diameter of about 30 nm, close to the values estimated from XRD. A detail of the wire highlights the periodic pattern of diffraction fringes parallel to the wire length. This indicates crystalline order in the material and the presence of lattice planes aligned with the wires direction and perpendicular to the plane of the image. The Fast Fourier Transform (FFT) of the image shows spots at a distance of 0.935 nm^{-1} from the origin in reciprocal space, which corresponds to a lattice spacing of 10.7 Å in real space. Similar distances are obtained by measuring the periodicity of the intensity profile across the nanowire diameter. At the edges of the wire, brighter Fresnel fringes are seen, caused by the slight under focussed conditions used to improve contrast when the image was acquired. The lattice spacing measured across the wires by TEM is slightly larger from that observed in the XRD measurements (10.7Å against 10.1Å). It seems likely that the two values actually correspond to the same set of planes and that the disagreement

is caused by inaccurate calibration of the microscope magnification. It is worth to note that nanowires of other MPcs (CuPc, FePc) were previously studied and showed only fringes at a larger lattice spacing of 12.4Å, closely matching the (001) plane of the η phase. Since the nanowires are believed to grow with no preferential orientation, the absence of such lattice spacing in the CoPc sample could be interpreted as a sign of a different structure from the η phase. Unfortunately the CoPc material was particularly unstable under the electron beam, preventing the collection of transmission electron diffration (TED) patterns and limiting the understanding of the molecular packing in the nanowires.

4.2 Magnetic properties of CoPc nanowires

The investigation of the magnetic properties of CoPc nanowires represented one of the main goals of this part of the work. In order to be able to measure the nanowires in the SQUID magnetometer, a sample of 0.46±0.04 mg of the material was collected from a region of the tube between 81 cm and 96 cm from the beginning of the hottest end of the furnace. This particular region was chosen since it displayed a high coverage and the characterization suggested that it contained a pure nanowire phase. The intricate mesh of wires forms a carpet which was easily lifted off from the kapton substrate by gently pulling at the corners with tweezers. To reduce the size of the sample, the layers of nanowire carpet were gently folded multiple times with tweezers to form a ball of small size (< 3 mm). A piece of kapton film, accurately cut in a rectangular shape of 4 cm×14 cm, was rolled to form a cylinder of less than 5 mm in diameter and the ball made of nanowires was trapped in the folds of the film as illustrated in Figure 4.6. The kapton cylinder was introduced into the straw to be loaded in the SQUID.

The magnetization of the nanowire sample was measured between 2 K and 320 K at a constant field of 500 Oe and 1000 Oe, after cooling the sample with

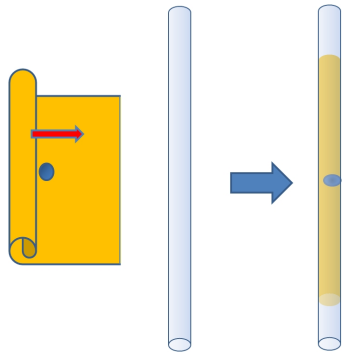


Figure 4.6: Schematics of the mounting of CoPc nanowires samples in plastic straws for SQUID measurements

the field applied. The differential susceptibility, which is shown in Figure 4.7a, exhibits a rapid monotonic decay as the temperature is increased. It is evident in the inset of the image, showing the reciprocal of χ, that the data is described by the Curie-Weiss law over the temperature range between 3 K and 320 K. The Curie constant $C = 1.19\mu_B T^{-1} K$ corresponds to $g = 2.42$ and the small negative Weiss temperature $\theta_{Weiss} = -0.9$ K (Table 4.2), indicates negligible antiferromagnetic interactions in the material. Accordingly, the magnetization increases with field at low temperature in a way similar to a paramagnet, as illustrated in Figure 4.7b. A high magnetic moment of $1.3 \pm 0.1\mu_B$ per cobalt atom, presumably close to the saturation value, is measured at 2 K in a 7 Tesla field, ruling out the presence of a strongly antiferromagnetic fraction in the material. The $M(H)$ curves shown as solid lines in Figure 4.7b are simulation of the Brillouin function that use the g-factor (g=2.42) calculated from the Curie constant of the $\chi(T)$ fit. The simulations slightly overestimate the experimental data but achieve similar values of magnetic moment at saturation, demonstrating that the material behaves almost as a paramagnet.

The fit of the data using the Brillouin function produced the dashed lines shown in the figure. The resulting values of the g-factor, listed in table 4.2, are close to the one previously calculated from the Curie constant, with an average value of 2.43. It can be seen that a much better agreement with the experimental data is

	θ_{Weiss} (K)	C_{Curie} ($\mu_B KT^{-1}$)	g
$\chi(T)$	-0.9	1.19	2.42
$M(H)$			
2 K	–	–	2.38
4.5 K	–	–	2.48

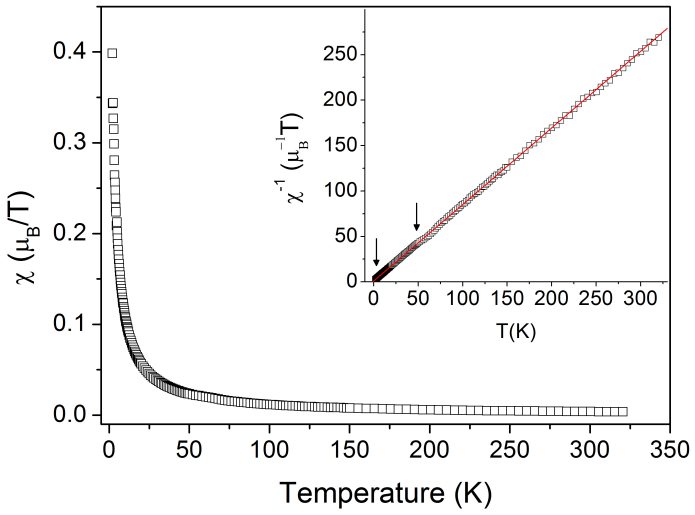
Table 4.2: Magnetic parameters extracted from the fit of the measurements in Figure 4.7

obtained at 4 K rather than at 2 K, indicating again that at the lowest temperature the behaviour deviates from the paramagnetic one due to weak antiferromagnetic interactions.

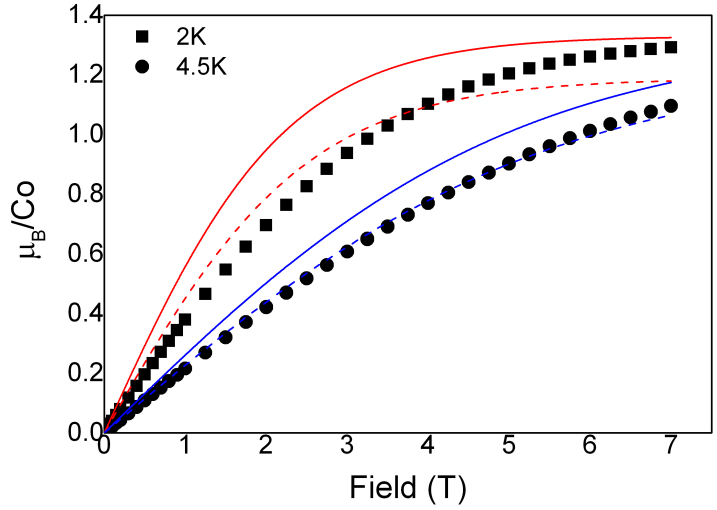
The g-factor is very sensitive to the crystal structure in CoPc. The values of the g-factor compare favourably with the in plane value in α-CoPc, or with the powder orientation average expected in the β-CoPc. Since the nanowire sample is not oriented, although it might not be perfectly isotropic, it seems more reasonable to have a comparison with the β-phase powder. This observation might suggest that cobalt atoms in the nanowire experience a chemical environment similar to the one in the β structure, having a significant amount of an axial coordination from the pyrrole nitrogen of the neighbouring molecule.

4.3 Discussion and conclusions

The OVPD process for the growth of nanowires was successfully applied to CoPc. X-ray diffraction and high resolution TEM imaging established that the nanowires constitute a new phase of CoPc, which is different from the known α and β polymorphs. The instability of the material under the electrom beam prevented the collection of the nanowires transmission electron diffraction, which hinders the determination of the unit cell of the material. Nevertheless, the XRD patterns and optical absorption spectra were mostly comparable with those measured in CuPc



(a)



(b)

Figure 4.7: Magnetic analysis of the CoPc nanowires. The susceptibility, shown in (a), follows the Curie-Weiss law. A fit of χ^{-1} between 3 K and 48 K extracts the parameters shown in table 4.2. The $\chi(T)$ values are calculated from $M(T)$ measurements at 500 Oe and 1000 Oe (Equation 2.13); for an explanation of the units refer to section 2.3.7 and Equation 2.12. The $M(H)$ curves in CoPc nanowires at 2 K and 4.5 K are shown in (b); the dashed lines represent the fits with the Brillouin function (S=1/2). Solid lines are simulations with the g value extracted from the $\chi(T)$ curve

nanowires, which points to a similar structure.

Magnetic measurements showed that CoPc nanowires can be classified as almost paramagnetic. The weak spin exchange interactions in the material are antiferromagnetic, with a value of J/k_B estimated around 0.9 K, two orders of magnitude lower than the one measured in the α-phase films. In the frame of the DFT calculations discussed in chapter 3, this behaviour is consistent with a decrease of the stacking angle to less than 50°, which determines an exchange mechanism possibly mediated by the organic ligand. This interpretation challenges our understanding of the CoPc nanowires structure, which was initially assumed to be identical to the η-phase derived from CuPc nanowires: the η and the α structures have a similar stacking angle, close to 66°, therefore both should exhibit similarly strong antiferromagnetic properties due to the efficient superexchange between the cobalt d_{z^2} orbitals.

There may be multiple factors determining this apparent contradiction between theory and experiment. It can be pointed out that the assumption that the cobalt phthalocyanine nanowires adopt the η structure is not substantiated by sufficient experimental evidence. Indeed, while XRD showed characteristic peaks of the η-phase in CoPc nanowires, it also showed other diffraction features which could not be assigned to any plane of that structure; furthermore, the spacing of the diffraction fringes observed in TEM imaging differs from the one usually detected in CuPc nanowires. While this could be indicative of differences in the structures, the general knowledge is that similarly processed planar phthalocyanines of different metals form roughly isostructural materials. The most common variations are in the direction of the sliding angle, as in the case of α-CuPc and α-CoPc, and in the preference for a brick-stack or herringbone arrangement of the MPc columns, although it cannot be excluded that the nanowires show different degrees of structural variations. The theory suggests that none of the aforementioned parameters should significantly influence the magnetism of CoPc as long as

the d_{z^2} superexchange mechanism is dominating, since the interaction is rotation invariant and essentially 1-dimensional.

Following these considerations, it can be speculated that either the calculations underestimate the role of competing ligand mediated exchange at high stacking angle, which might significantly decrease the magnitude of the exchange energy, or that the initial determination of the CuPc nanowire structure is incorrect.

Regarding the accuracy of the η unit cell parameters, it should be mentioned that, while the unit cell dimensions and angles were derived experimentally, the atomic positions were obtained by finding the packing geometry with the minimum potential energy. The algorithm used Lennard-Jones type potentials to describe the interactions between atoms of different molecules, not including the central metal atom. This simplistic approach could lead to incorrect conclusions, since it neglects the $\pi - \pi$ interactions between conjugated rings and the contribution of intermolecular coordination bonds between nitrogen and metal atom.

In conclusion, the study of the magnetic properties of CoPc nanowires stimulates further studies of their crystal structure, possibly using more sensitive techniques such as synchrotron diffraction. This might lead to a reconsideration of the η-phase structure reported in CuPc nanowires. More sophisticated theoretical methods would also be needed to determine whether the exchange pathways mediated by the organic ring are modelled with sufficient accuracy at all stacking angles.

Chapter 5

Hexadecafluoro cobalt phthalocyanine ($F_{16}CoPc$)

Fluorinated phthalocyanines are important organic semiconductors which exhibit exceptional air stability and n-type semiconducting behaviour. The substitution of the external positions of the organic ligand with fluorine atoms has profound implications on the molecular electronic structure, the intermolecular interactions and the interface between the organic film and the substrate. This introduces another tool for modifying the magnetism of metal phthalocyanine materials. In this chapter, the properties of thin films of the fluorinated derivative of cobalt phthalocyanine ($F_{16}CoPc$) are discussed. The growth mode of the films is significantly different and more complex than that of CoPc, showing signs of a transition induced by thickness. The films on kapton show weak antiferromagnetic interactions, comparable to those observed in the β-CoPc. This result is rationalized by the preference of $F_{16}CoPc$ to form structures with a low stacking angle, which weakens the super-exchange spin coupling pathway.

5.1 Introduction

Thin films of perfluorinated phthalocyanines are of interest to organic electronics for their application in n-type FET. The copper compound has been the most characterized and one of the first examples of relatively air stable n-type organic semiconductors [7]. DFT calculations [103] and valence band photoelectron spectroscopy [18] showed that the substitution of the peripheral hydrogen atoms with fluorine brings about a stabilization of both the HOMO and LUMO levels by about 1 eV, while the relative energy of the electronic states near the Fermi level, in particular of those levels that carry spin density, is unchanged [103]. This is an interesting prospect from the point of view of spintronics, since it allows tuning of the charge transport properties independently from the molecular spin structure[103].

The polarization of the electron density caused by the electronegative fluorine atoms modifies the pattern of intermolecular interactions in the solid state, resulting in the occurrence of crystal structures different from those observed in the unsubstituted phthalocyanines. The morphology [107, 109], crystalline order [29] and electric properties [7, 18] of F_{16}MPc films grown under different conditions are discussed in several studies. At present, there is no consensus about the crystal structure of the films, due to a complex growth behaviour that involves structural relaxation of the films.

The magnetic properties of the fluorinated phthalocyanines have not received wide attention and only thin films of F_{16}CuPc were characterized and found to be paramagnetic [103]. It has been suggested that stronger interactions between fluorinated molecules may lead to shorter intermolecular distances and enhanced exchange coupling between the spin centres [103]. Following the discovery of strong antiferromagnetism in evaporated thin films of CoPc, this chapter aims to investigate how the magnetic properties of the films are modified by the insertion of

fluorine atoms in the peripheral positions of the organic macrocycle. Due to the paramount importance of the molecular stacking geometry in deciding the sign and strength of the magnetic interactions, a preliminary study of the structure and morphology of the films is presented prior to the discussion of the magnetic measurement.

5.2 Morphology of F_{16}CoPc films

F_{16}CoPc films of different thickness were grown in parallel on kapton, silicon and glass by OBMD for the purpose of structural characterization. The use of different substrates gave access to a wider range of characterization techniques, including visible absorption spectroscopy, allowing a more complete analysis of the growth behaviour of the films. Figure 5.1 shows SEM micrographs of the films. The cross-sections of the films grown on silicon, obtained by cleaving the substrate after film deposition, show the evolution of the film surface roughness as a function of film thickness D. The thinnest film of the series (D=25 nm) exhibits a single layer of particles of fairly constant height. Films of higher thickness display overlapping grains and the nucleation of particles that grow higher than the average film thickness, contributing to a rapid increase of the roughness. In the thickest films (D=100 nm, 200 nm), the images show a very high density of protruding particles, growing at different angles with respect to the substrate. The apparent thickness of the films is significantly larger than the one measured by the QCM of the OMBD chamber, indicating the presence of voids in the films.

The top view micrographs allow the comparison between films grown on different substrates. The morphologies differ in the shape and the size of the particles already in the thinnest film thickness considered (D=25 nm). Films on silicon and kapton exhibit grains of irregular shape and diameter around 20 nm. A few particles are taller and appear as bright spots; they are sparsely distributed on

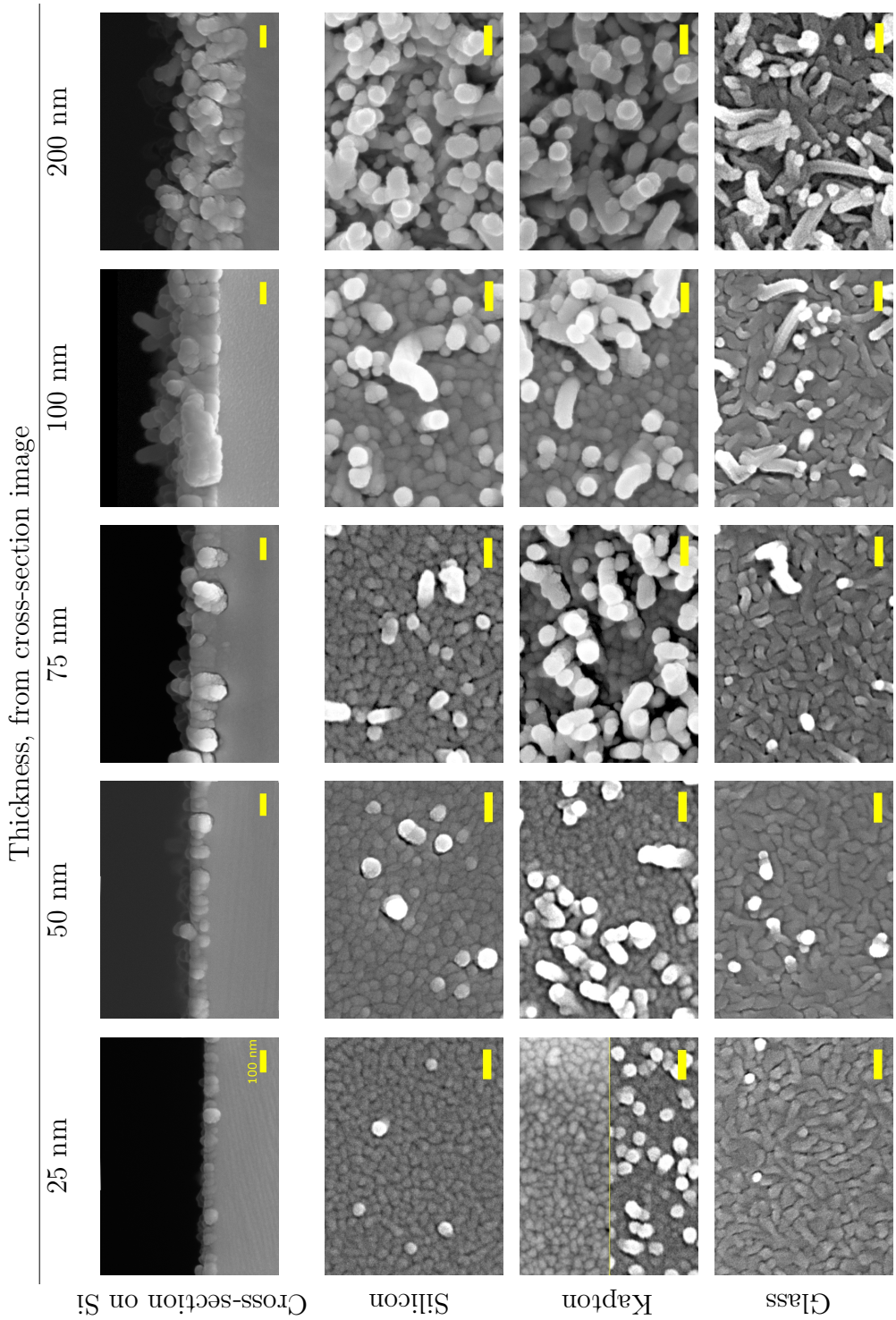


Figure 5.1: SEM images of F_{16}CoPc films grown at room temperature on kapton, glass and silicon. Cross-section images were obtained from freshly cleaved films grown on silicon. The scale bars correspond to 100 nm

the film grown on silicon, while on kapton they are concentrated in certain areas of the film. The 25 nm thick film grown on glass shows instead grains elongating in the plane of the substrate, with typical widths of 30 nm and approaching 100 nm in length; a few bright spots, indicating protruding grains, are also seen in the image.

The top-view morphology of the thicker films (D>25 nm) on all three substrates can be generically described as a combination of a compact underlying layer and needles that protrude out of the film surface. The shape of the particles in the underlying layer is identical to that observed in the smooth areas of the D=25 nm films, and their size also increases very slightly. Thick films exhibit a dramatic increase of the density and length of the needles, which eventually cover most of the film surface. These structures appear to have a wider diameter (about 50 nm) in the samples grown on silicon and kapton, while they appear thinner on glass (about 30 nm in diameter). In the D=100 nm and D=200 nm thick films, many needles are tilted close to the substrate plane. This growth behaviour is similar to the one reported by Yang *et al.*[107] in F_{16}CuPc films evaporated on ITO. The authors of the study suggested that the nucleation of elongated structures observed in thicker films could be caused by relaxation of strain in the structure which modifies the molecular orientation in the film and affects the surface diffusion of upcoming molecules during vapour deposition.

The effect of the substrate on the growth of F_{16}CoPc films is surprising, since CoPc films displayed similar morphologies on kapton, silicon and glass. The strongly electronegative fluorine atoms polarize the C-F bonds producing a negative charge density surrounding the F_{16}CoPc organic macrocycle, which may exacerbate or more simply enhance coulombic interactions with the substrate. Trapping of positive or negative static charges on the surface of insulating substrates such as glass or kapton, could affect the structure of films of fluorinated phthalocyanines significantly. Previous studies [62, 29] have also discussed the possibility that fluorine

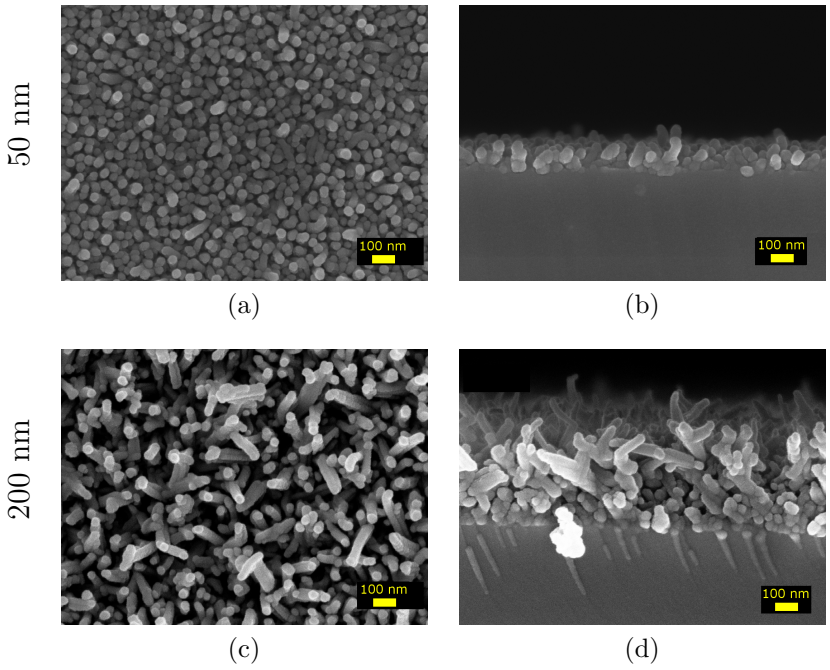


Figure 5.2: SEM images of F_{16}CoPc films deposited on a 20 nm PTCDA layer on a silicon substrate: (a) top view of a 50 nm F_{16}CoPc/20 nm PTCDA film and (b) relative cross-section view; (c) top and (d) cross-section view of a 200 nm F_{16}CoPc/20 nm PTCDA film

atoms may chemically react with SiO_2 in glass and oxidized silicon wafers.

When F_{16}CoPc films are grown on a thin layer of PTCDA (20 nm), the films display a different morphology, which was identical on kapton, silicon and glass because the interaction with the substrate is shielded by the PTCDA layer. A film of D=50 nm nominal thickness on silicon, shown in Figure 5.2a, looks homogeneously covered by a layer of particles, about 35 nm in diameter, separated from each other by small gaps. The particles have a propensity towards vertical growth, as inferred from the cross-section image of the film (Figure 5.2b), which is in general agreement with the description of F_{16}CuPc films on PTCDA made by Yang *et al.*[108]. Films of D=200 nm thickness appear very porous due to a disordered network of needles growing at different angles on the surface of the films (Figure 5.2c). The cross-section of the sample (Figure 5.2d) shows that the needles can reach a length of more than 100 nm, and some display a branched

structure. The image also shows that the bottom of the film contains a layer of closely packed spherical particles with an approximate size of 30 nm.

5.3 UV-Vis spectroscopy of films on glass

UV-visible absorption spectroscopy has been used as a tool to extract information about the chemical and crystal structure composition of phthalocyanine materials. Figure 5.3 compares the absorption spectra of F_{16}CoPc films on glass with those of CoPc materials. In both F_{16}CoPc films grown directly on glass or on a PTCDA coating, the spectrum consists of least four bands, three which are clearly visible at $\lambda \approx 645$ nm, 690 nm and 765 nm, and a faint shoulder around $\lambda = 580$ nm. The profile cannot be reproduced by linear combinations of the spectra of the α, β and nanowire CoPc. In particular, the band at λ=760 nm can only be observed in F_{16}CoPc films. On the contrary, the absorption of CoPc and F_{16}CoPc in solution looks identical in the visible range, demonstrating that the fluorination does not perturb the lowest intramolecular energy transition [103] (although absolute values of the HOMO and LUMO levels are shifted), and that the differences in the solid state must arise from the exciton coupling of distinct crystal structures.

The strong absorption band in the 700 nm–800 nm range seems a general feature of films of planar fluorinated phthalocyanines (F_{16}CuPc [1], F_{16}ZnPc [18]) which indicates excitonic coupling of the transition dipoles in a configuration close to a head to tail arrangement (as defined in section 2.3.3). This characteristic feature is also observed in films of axially ligated phthalocyanines (TiOPc, VOPc and ClAlPc, etc), where it is attributed to the arrangement of molecules into sheets where they form two dimensional square lattices [22]. Schlettwein suggested that a similar packing motif may be responsible for the red-shifted absorption of F_{16}ZnPc films [85].

The spectra of F_{16}CoPc have been measured in films of different thickness (Figure

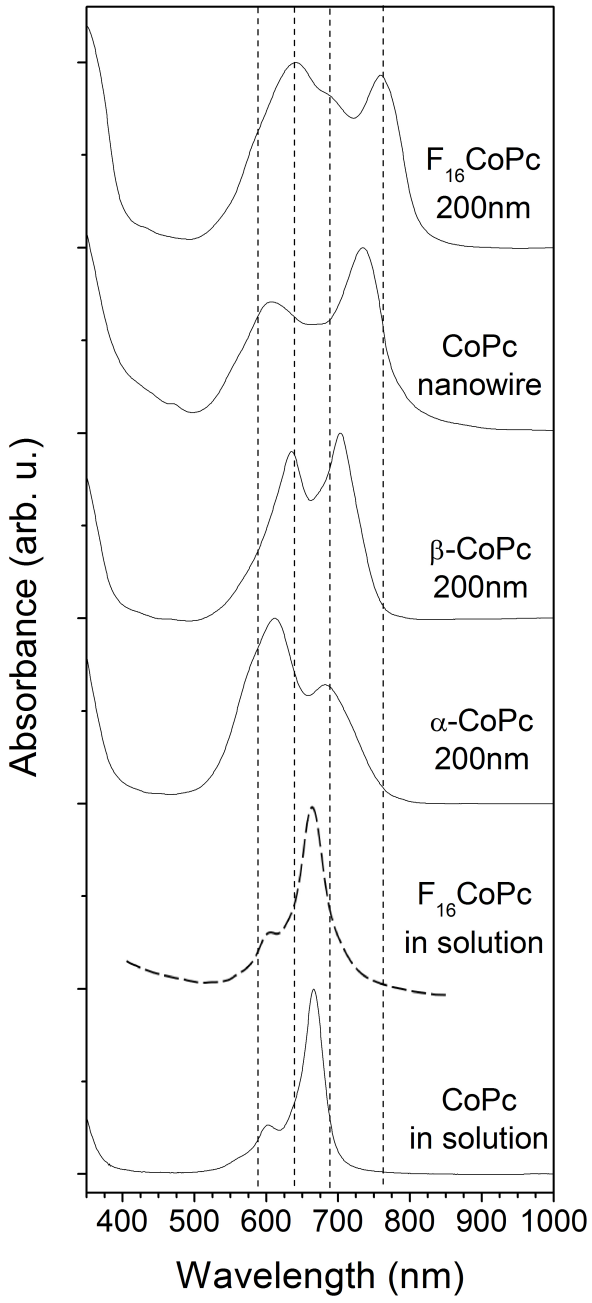
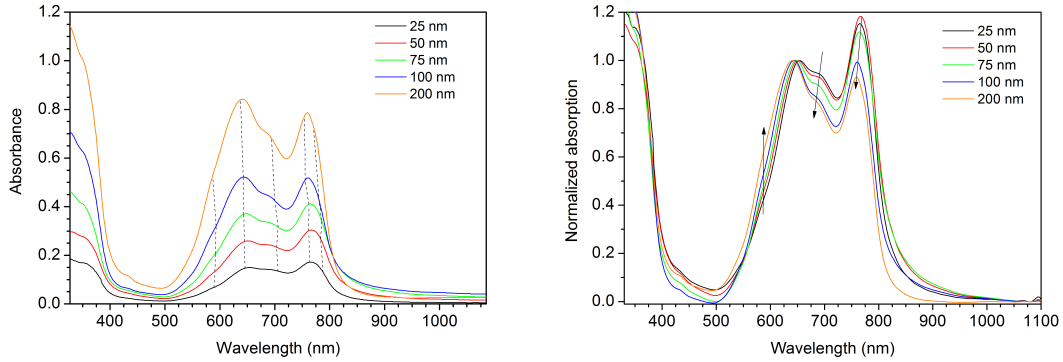


Figure 5.3: From top to bottom: normalized UV-visible absorption spectra of 200 nm F_{16}CoPc film, CoPc nanowires, 200 nm α-CoPc film, 200 nm β-CoPc film, F_{16}CoPc solution in pyridine and CoPc solution in 5:1 1-Chloronaphthalene/pyridine mixture. The spectrum of F_{16}CoPc in solution is taken from Schuster *et al.*[86].



(a) (b)

Figure 5.4: (a) Absorption spectra of films of increasing thickness on glass.(b) Spectra after normalization of the optical density at λ=645 nm.

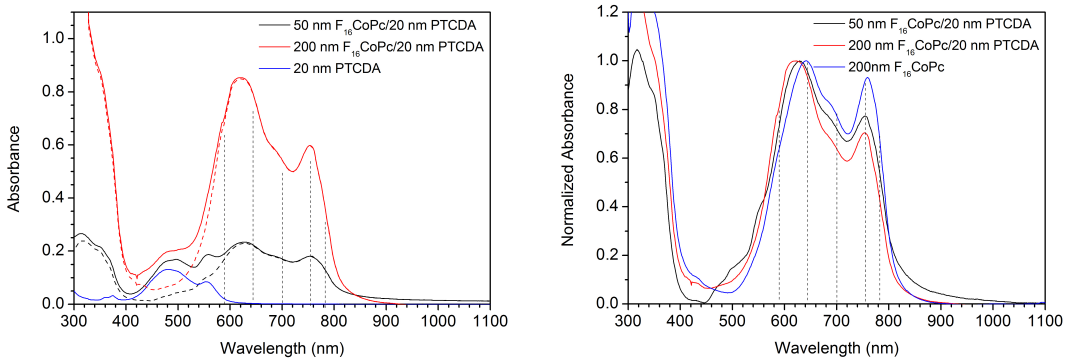
5.4a). If the optical density is normalized to unity at λ=645 nm, an evolution of the profile becomes evident (Figure 5.4b). The bands at $\lambda \approx$645 nm, 690 nm and 765 nm shift towards the blue by 8–10 nm and the relative intensity of the transitions is redistributed, with a weakening of the bands at $\lambda \approx$690 nm and $\lambda \approx$765 nm with respect to the bands at $\lambda \approx$645 nm and the shoulder at $\lambda \approx$590 nm. In F_{16}CoPc films grown on a PTCDA layer, the contribution from the bands at $\lambda \approx$690 nm and $\lambda \approx$765 nm is even weaker, and the thickness dependence very limited (Figure 5.5). The distinct shape of the absorption spectrum of films grown on glass or PTCDA may be due to different crystal structures, molecular orientation or structural disorder in the film.

5.4 X-ray diffraction of the F_{16}CoPc films

X-ray diffraction experiments allowed the study of crystalline order in the films as a function of their thickness (Figure 5.6). The films grown on the three substrates showed a diffraction peak at a Bragg angle $2\theta \approx 6°$, indicating textured film growth. The spacing between diffracting planes is comparable to the lateral dimension of the F_{16}CoPc molecule, thus the peak belongs to the (00l) plane family and indi-

	F_{16}CoPc on glass				
	25 nm	50 nm	75 nm	100 nm	200 nm
2θ	6.19	6.03	6.11	6.18	6.15
$w(2\theta)$	0.35	0.16	0.22	0.32	0.21
Scherrer size	33–26 nm	64–110 nm	43–63 nm	29–37 nm	46–68 nm
Area	16116	1139	2854	5956	3393
2θ	–	6.27	6.29	6.30	6.31
$w(2\theta)$	–	0.20	0.14	0.11	0.12
Scherrer size	–	48–74 nm	77–147 nm	>100 nm	>100 nm
Area	–	8196	6828	7622	11019
	F_{16}CoPc on silicon				
	25 nm	50 nm	75 nm	100 nm	200 nm
2θ	6.09	6.12	6.08	6.13	6.09
$w(2\theta)$	0.39	0.41	0.24	0.28	0.31
Scherrer size	23–29 nm	22–27 nm	39–55 nm	33–44 nm	30–38
Area	3710	2606	4544	5977	2666
2θ	–	–	6.26	6.27	6.26
$w(2\theta)$	–	–	0.15	0.11	0.14
Scherrer size	–	–	71–130 nm	>100 nm	77–147 nm
Area	–	–	3211	5782	870
	F_{16}CoPc on kapton				
	25 nm	200 nm			
2θ	5.94	6.03			
$w(2\theta)$	0.51	0.45			
Scherrer size	18 nm–21 nm	20 nm–24 nm			
Area	225	1192			
2θ	–	28.60			
$w(2\theta)$	–	0.48			
Scherrer size	–	20–26 nm			
Area	–	577			

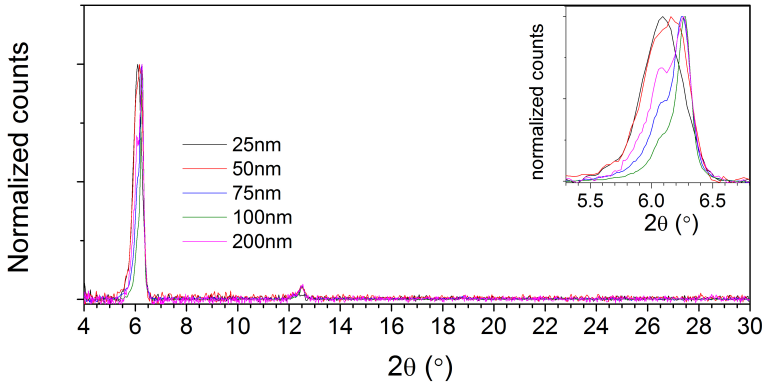
Table 5.1: Peak parameters from the fit of the XRD patterns of F_{16}CoPc samples, using pseudo-Voigt line shape.



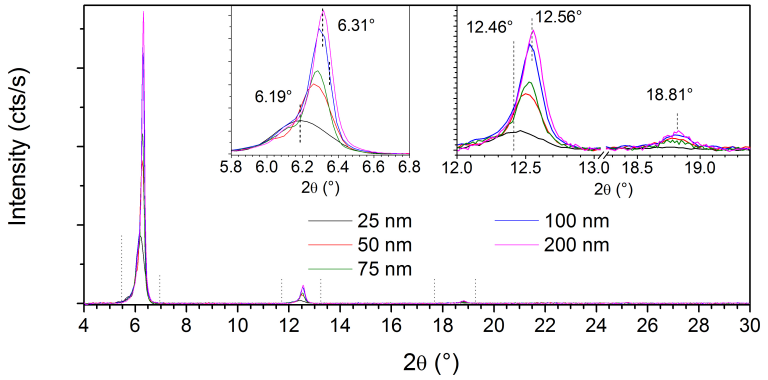
(a) (b)

Figure 5.5: UV-Visible absorption spectra of templated F_{16}CoPc films on glass. (a) shows the overall absorption of 50 nm and 200 nm thick F_{16}CoPc films grown on a 20 nm thick PTCDA layer. The dashed lines show the data after subtraction of the PTCDA absorption. In (b) the absorption profile of the same films, corrected for the PTCDA absorption and normalized to unity, is compared with the spectrum of a 253 nm thick film deposited directly on glass, also normalized. The vertical dashed lines suggest the position of the absorption bands

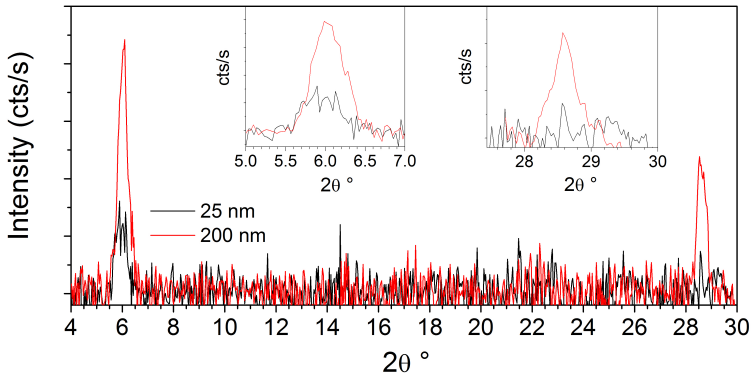
cates a preferential standing orientation. The exact peak position varies slightly between samples grown on different substrates and as a function of thickness. In the 25 nm thick film, the peak is centred at 2θ=6.0° on kapton, 2θ=6.1° on silicon and 2θ=6.2° on glass. This behaviour illustrates the ability of fluorinated phthalocyanines crystals to accommodate strain and to tweak the solid state molecular packing in response to different interactions with the substrate, but also constitute a hurdle towards a detailed understanding of their crystal structures. In the case of the 25 nm thick film on glass the diffraction angle coincides with the position of the (001) reflection in the bulk F_{16}CuPc structure determined by Pandey *et al.*[77], which could suggest the crystallization in an isomorphous structure. Second order diffraction is clearly seen at 12° in films grown on silicon and glass, which indicates a highly ordered structure. The crystalline order is also demonstrated by the similarity of the values of the Scherrer size (≈30 nm, Table 5.1) with the dimension of the particles seen in the cross-section image. A much weaker intensity of the diffraction signal indicates a low propensity of F_{16}CoPc to form ordered films on



(a)



(b)



(c)

Figure 5.6: XRD scans of films grown on (a) silicon (thickness 25 nm, 50 nm, 75 nm, 100 nm, 200 nm), (b) glass (thickness 25 nm, 50 nm, 75 nm, 100 nm, 200 nm) and (c) kapton (thickness 25 nm and 200 nm) substrates

kapton, which was already sensed in their inhomogeneous morphology. It can be inferred from the width of the diffraction peak that the Scherrer size of the ordered domains is limited to about 20 nm (Table 5.1). The diffraction pattern of samples grown on silicon and glass visibly changes by increasing the film thickness, indicating the crystallization in a different structure. The maximum diffraction intensity shifts to 2θ=6.26° on silicon, while a satellite peak at 6.1° is also visible. In films on glass, the profile evolves into a single peak centred at 2θ=6.31° with an asymmetric tail at lower angle. The data is compatible with the coexistence of two structures, the one observed in the thinnest film (D=25 nm) and another one observed only in thicker samples. The two contribution were deconvoluted by fitting the XRD profile with a two peaks model (Table 5.1). The new phase is characterized by sharper linewidths and a Scherrer size exceeding 100 nm, while the satellite/shoulder peaks are broader, compatibly with a Scherrer size of 50 nm or less. The maximum diffraction intensity in the 200 nm thick film on glass coincides with the position of the (002) diffraction of the F_{16}CuPc structure determined by Yoon *et al.*[112]. Although it might be just a coincidence, this demonstrates that the contraction of the lattice periodicity associated with the shift in 2θ is compatible with the switching from a brickstack to a herringbone structure. Figure 5.7 shows the corresponding model of thin film growth, also illustrating how defects in the packing motif could lead to the nucleation of the protruding needles observed in the SEM images. In contrast with the behaviour just described, the increase of the film thickness in the samples on kapton did not lead to a structural transition or the growth of larger crystallites. The only remarkable effect is the appearance of an additional peak at 2θ=28.6° in films of 253 nm, which can be interpreted as a loss of the film texture. The 2θ value corresponds to the typical periodicity along the stacking direction of phthalocyanine crystals, indicating that a fraction of the molecules reoriented their plane roughly parallel to the substrate.

In the case of films grown on substrates coated with a layer of PTCDA, a templat-

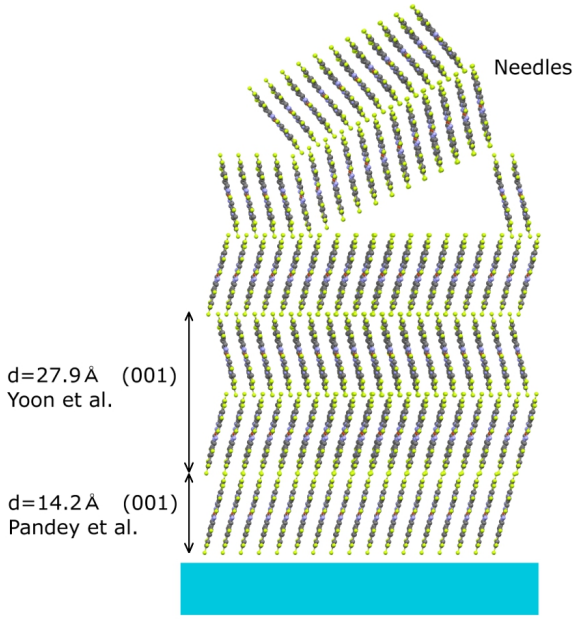


Figure 5.7: Schematics of the proposed crystalline structure of thick F_{16}CoPc films grown on non interacting substrates (glass, silicon, kapton). At the interface with the substrate, the film grows in the structure proposed by Pandey [77], with the (001) plane oriented parallel to the substrate. Above this interfacial layer, which might have a thickness of some tens of nm, the structure switches to the one proposed by Yoon *et al.*[112], which exhibits a herringbone pattern between consecutive layers. Stacking faults may lead to the growth in a tilted direction with respect to the substrate, causing the nucleation of needles.

ing effect, similar to the one observed in MPc films, is observed. The substrate did not have an appreciable effect of the crystalline properties of the film, since the F_{16}CoPc molecules interact solely with the PTCDA layer. The diffractograms of the thin films on glass, shown in Figure 5.8, exhibit a peak at 2θ=28.6°, attributed to F_{16}CoPc, and the peak at 2θ=27.6° corresponding to the (102) plane of PTCDA. The position of the F_{16}CoPc peak is identical to that of the extra peak detected in thick non-templated films on kapton, and again is consistent with a molecular orientation parallel to the substrate. The intensity of the diffraction at 2θ=28.6° increases when the film thickness is brought from 50 nm to 200 nm, as a result of a larger number of diffracting molecules, however the width of the peak is unchanged and indicates a typical Scherrer size of about 20 nm. This is consis-

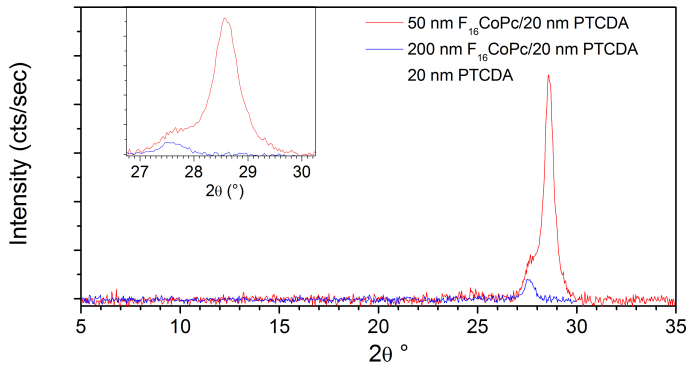


Figure 5.8: XRD patterns of 50 nm and 200 nm F_{16}CoPc films grown on a 20 nm thick PTCDA layer grown on a glass substrate. The diffraction from a 20 nm PTCDA film is shown for reference

tent with the structure seen in the SEM images, considering that the width of the diffraction peak probes just the cross-section size of the crystallites in the direction perpendicular to the film, and that the long axis of the needle is not aligned in a favourable orientation for diffraction in the θ-2θ geometry of the measurement. The position of the diffraction peak leads to two possible assignments, namely the (1-22) peak (2θ=28.49°) of the structure proposed by Yoon *et al.*[112] and the (1-2-2) plane (2θ=28.70°) of the structure proposed by Pandey *et al.*[77] (Figure 5.9). Between these two structures, the latter by Pandey seems the most likely since it allows a flat orientation of all phthalocyanine molecules on the PTCDA layer, thus maximizing π-π interactions. In Yoon's structure instead, the herringbone arrangement prevents half of the phthalocyanine molecules to have an optimal orientation for interacting with PTCDA.

5.5 Magnetic characterization of F_{16}CoPc films on kapton

The magnetic properties of F_{16}CoPc films were measured by SQUID magnetometry, using thick films (200 nm) in order to maximize the signal. Figure 5.10a

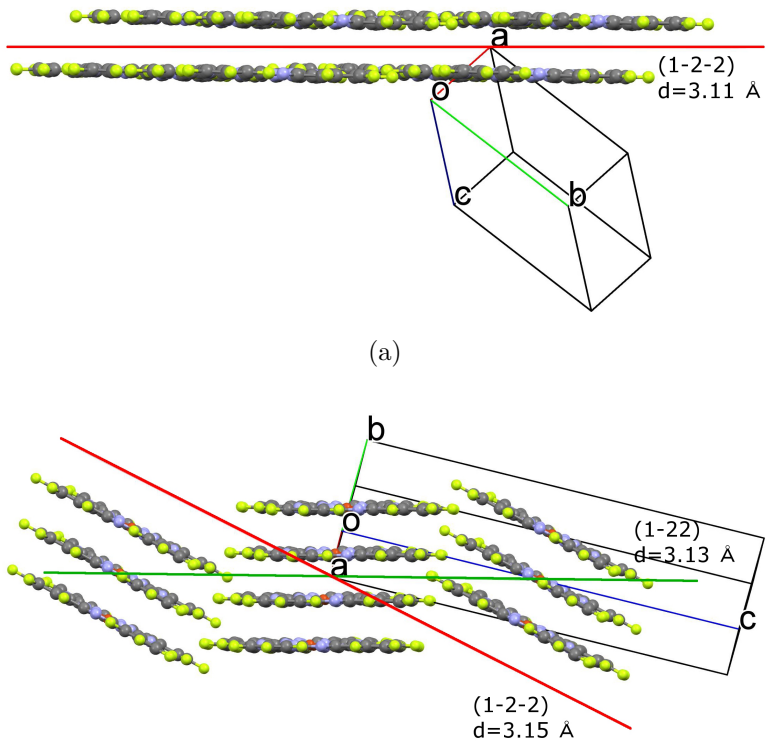


Figure 5.9: Possible crystallographic planes of texture in F_{16}MPc films grown on PTCDA and their respective interplanar spacing d: (a) shows the orientation of the (1-2-2) plane in the F_{16}CuPc crystal structure proposed by Pandey *et al.*[77], (b) depicts the orientation of the (1-22) and the (1-2-2) planes in the F_{16}CuPc crystal structure proposed by Yoon *et al.*[112]

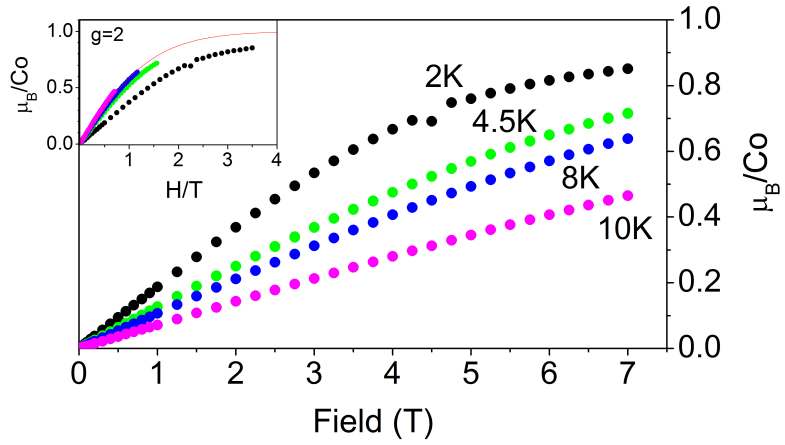
shows isothermal magnetization curves measured at 2, 4.5, 8 and 10 K in a 200 nm F_{16}CoPc film grown on kapton. The magnetic moment increases slowly with the applied field, similar to a paramagnetic spin. At 2 K, the moment approaches 1 μ_B at 7 Tesla, which is the saturation value for a spin S=1/2 with g=2. These observations indicate that the exchange interactions in the material are rather weak. The inset of figure 5.10a shows how the magnetic moment scales with the ratio of field to temperature in measurements conducted at different temperatures. It is observed that above 4.5 K, the data points collapse on a single curve, as in a paramagnetic S=1/2 spin with g=2; at a temperature of 2 K, the experimental values lie below the simulation, indicating a small reduction in magnetic moment due to weak antiferromagnetic interactions. The magnetization curves are almost

identical in a 200 nm film deposited onto a 20 nm PTCDA templating layer (Figure 5.11a), leading to the same conclusions.

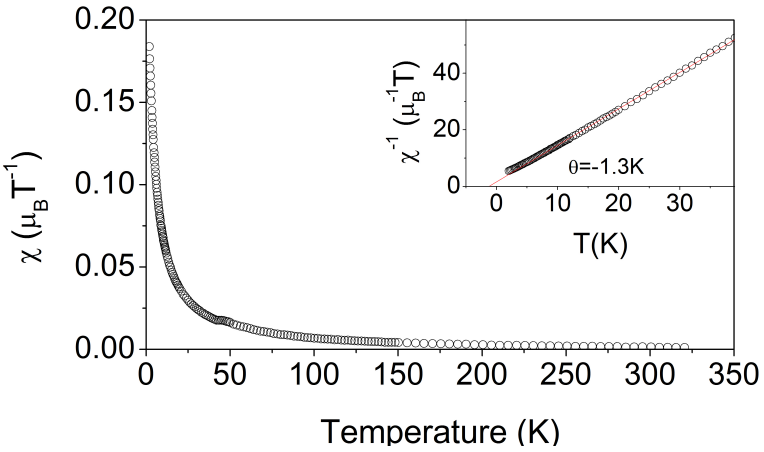
The temperature dependence of the magnetic susceptibility χ(T) allows a more precise quantification of the magnetic coupling. The value of χ(T) decreases rapidly and monothonically with increasing temperature in both the templated (Figure 5.11b) and non-templated (Figure 5.10b) 200 nm thick F_{16}CoPc films. The plot of the reciprocal of the susceptibility of both films shows that the magnetic behaviour is perfectly described the Curie-Weiss law up to 40 K, before it deviates slightly due to a small diamagnetism. The estimated values of the Weiss temperature are θ=-1.3 K in the non-templated film and θ=-2 K in the templated film, indicating weak antiferromagnetic interactions in the films. It is likely that small variations in the stacking geometry or in the crystalline order of the film are responsible for the small differences of magnetic coupling observed between non-templated and templated films. The g value of the films was calculated from the slope of the fit, returning $g = 2.15$ in the non-templated film and $g = 2.05$ in the templated film, in good agreement with the low temperature magnetization data.

The magnetic measurements show that evaporated thin films of F_{16}CoPc are characterized by weak antiferromagnetism. Having a structure similar to CoPc, F_{16}CoPc is likely to also form 1-dimensional spin chains, where the value of the exchange energy J/k_B is equal to the Weiss temperature. Due to the weakness of the interaction, it is not possible to ascertain the typical length of the magnetic chains or quantify the amount of uncoupled spins in the material. The fact that a Bonner Fisher fit did not reproduce accurately the shape of the curve may indicate that the magnetic properties are averaged over different crystalline environments.

The magnitude of the exchange interaction in F_{16}CoPc films is about two orders of magnitude smaller than in films of CoPc. To understand the origin of the different properties of the two materials, it may be instructive to look at the

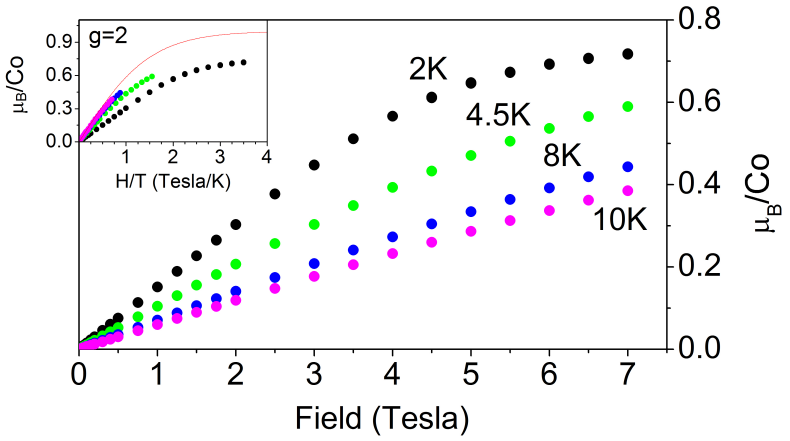


(a)

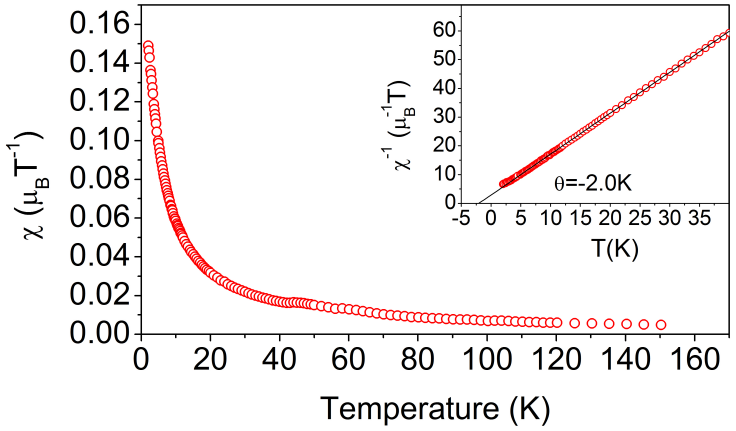


(b)

Figure 5.10: Magnetic characterization of F_{16}CoPc films. Isothermal magnetization curves of a 200 nm F_{16}CoPc film grown on kapton (a). The net magnetic moment per F_{16}CoPc molecule along the direction of the applied field is expressed in units of Bohr magnetons (μ_B). Inset: magnetic moment as a function of the ratio of field over temperature (H/T). The solid curve is a simulation of a paramagnet with S=1/2 and g=2. Temperature dependence of the differential susceptibility χ(T) (b). The $\chi(T)$ values are calculated from $M(T)$ measurements at 5000 Oe and 10 kOe (Equation 2.13); for an explanation of the units refer to section 2.3.7 and Equation 2.12. Inset: reciprocal of χ(T) and linear fit according to the Curie-Weiss law. The value of the Weiss temperature θ is equal to -1.3 K



(a)



(b)

Figure 5.11: Magnetic characterization of F_{16}CoPc films grown on PTCDA. Isothermal magnetization curves of a 200 nm F_{16}CoPc film grown on a 20 nm PTCDA layer on kapton (a). The net magnetic moment per F_{16}CoPc molecule along the direction of the applied field is expressed in units of Bohr magnetons (μ_B). Inset: magnetic moment as a function of the ratio of field over temperature (H/T). The solid curve is a simulation of a paramagnet with S=1/2 and g=2. Temperature dependence of the differential susceptibility χ(T) (b). Inset: reciprocal of χ(T) and linear fit according to the Curie-Weiss law. The $\chi(T)$ values are calculated from $M(T)$ measurements at 5000 Oe and 10 kOe (Equation 2.13); for an explanation of the units refer to section 2.3.7 and Equation 2.12. The value of the Weiss temperature θ is equal to -2 K

case of F_{16}CuPc films, which was studied both experimentally and theoretically [103]. The DFT calculations on F_{16}CuPc showed that the chemical modification does not perturb significantly the spin density distribution or the pathway of the exchange coupling, because the electronic states that are involved in the process are all shifted to lower energy by the same amount. In particular, it was shown that the exchange coupling had the same geometrical dependence on the stacking geometry, except for a possible enhancement (by a factor of 2) due to the reduction of the intermolecular spacing in the fluorinated compound. If the results can be extended to cobalt phthalocyanines, then the calculations of the exchange coupling in CoPc chains for different stacking geometries would be a valid starting point for interpreting the behaviour of F_{16}CoPc films. By comparing the estimated value of the exchange energy (1–2 K) with the contour plot of the calculated J values as a function of the chain geometry (Figure 3.17), it is excluded that the stacking angle ϕ is larger than 50° in F_{16}CoPc films. This conclusion is compatible with the two bulk F_{16}CuPc structures determined by Pandey*et al.*[77] and Yoon*et al.*[112], and also with those proposed for thin films [29], since they all replicate the stacking pattern of the β phase of phthalocyanines, although they differ in the relative orientation of the phthalocyanine chains in the crystal. In all these structures the metal ion axially coordinated to the pyrrole nitrogen of the two neighbouring molecules, leading to values of ϕ close to 45°. Such geometry is known to be the most thermodynamically stable in large phthalocyanine crystals, although the α phase structure is usually preferred in nanocrystalline materials [46] such as phthalocyanine films deposited on substrates held at room temperature. The inability of fluorinated phthalocyanines to form a high stacking angle structure equivalent to the α phase, might be due to the influence of repulsive interactions between the negatively charged fluorine atoms that can be relieved in a more slipped structure of the F_{16}CoPc columns.

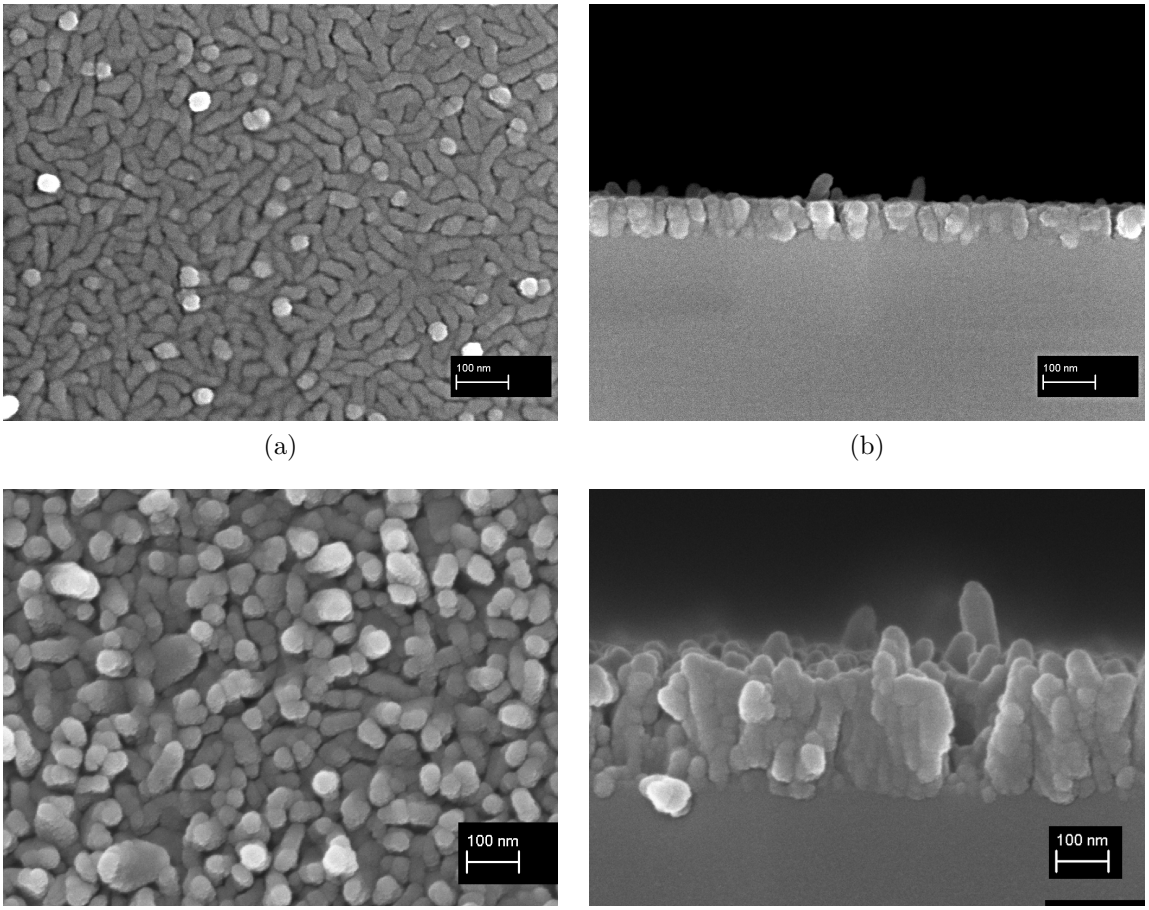
Chapter 6

Co-deposited CoPc:F_{16}CoPc films

This chapter will present the structural and physical properties of the mixed films of CoPc and F_{16}CoPc. This material was prepared and characterized for the first time in this work using co-deposition of the two materials in the organic molecular beam deposition. The two components form structurally ordered films demonstrating that an intimate mixing of the components is obtained in the film. The magnetic characterization showed that these materials exhibit antiferromagnetic coupling with exchange constants even higher than in α-CoPc.

6.1 Morphology of the films

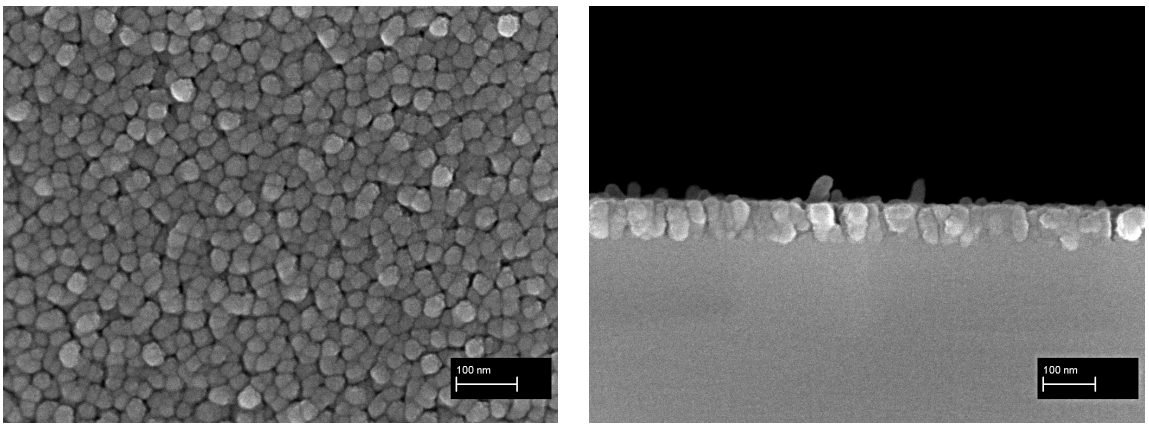
Once purified F_{16}CoPc and CoPc powders were co-evaporated in the OMBD chamber on glass, silicon and kapton substrates at individual deposition rates of 0.1Å/s, giving a 1 to 1 mixture in the film; the substrates were held at room temperature during deposition. Figure 6.1a shows an SEM micrograph of a 50 nm thick film grown on silicon. The surface of the film contains grains with an elongated shape, which are about 75 nm long and 25 nm wide. The morphology is similar to that of F_{16}CoPc films grown on glass (see Figure 5.1), although the grain size is smaller.



(a) (b)

(c) (d)

Figure 6.1: SEM top view image of a 50 nm F_{16}CoPc:CoPc (1:1) mixed film deposited on silicon (a) and its cross-section (b). Images (c) and (d) refer to films of the same composition but larger thickness (200 nm)



(a) (b)

Figure 6.2: SEM top view image of a 50 nm F_{16}CoPc:CoPc (1:1) mixed film deposited on a 20 nm PTCDA layer on silicon (a) and its cross-section (b).

	F_{16}CoPc:CoPc (1:1) 50 nm			
	Glass	Silicon	Kapton	Glass/PTCDA 20 nm
$2\theta_0(^\circ)$	6.49	6.52	6.49	27.92
$w_{2\theta}^{obs}(^\circ)$	0.23	0.21	0.29	0.33
Scherrer size (nm)	41–59	46–68	32–42	30–46

Table 6.1: Best fit parameters of the diffraction XRD peaks of F_{16}CoPc:CoPc (1:1) 50 nm films. The peaks are modelled with a Lorentzian function: $2\theta_0$ is the centre of the peak, $w_{2\theta}^{obs}$ is the experimental full width at half maximum in degrees of 2θ

A few grains appear higher then the rest of the film and have a circular shape with a diameter around 40 nm. The cross-section of the film (Figure 6.1b) shows a mostly uniform layer made of densely packed particles with vertical size between 30 and 70 nm; some needles elongate vertically up to 50 nm above the surface of the film. The 200 nm thick film on silicon displays a higher number of vertical needles, which creates a porous network at the surface of the film (Figure 6.1c and 6.1d). The growth on a 20 nm PTCDA layer induces a reduction of the lateral size of the grains, as shown by the 50 nm thick film in Figure 6.2a; the cross-section of the same film (Figure 6.2b) shows vertical elongation of the grains.

6.2 X-ray diffraction measurements of the films

The crystallinity of the films was studied by X-ray diffraction. Films grown on different substrates displayed similar characteristics (Figures 6.3, 6.4 and Table 6.1). Films grown on PTCDA exhibit a peak at $2\theta=(6.50 \pm 0.02)^\circ$. On glass and silicon this peak is very intense and has widths ($w_{2\theta}^{obs}$) of 0.21° and 0.23°, corresponding to Scherrer grain sizes in the range of the vertical particle size measured in the SEM cross-section image (Figure 6.1b). A very weak intensity can also be detected in the position of the second order peak ($2\theta\approx13^\circ$, Figure 6.3). The peak at $2\theta=6.5^\circ$ is also visible on kapton with less intensity and a slightly increased width (Figure 6.4 and Table 6.1). The measurements show that the

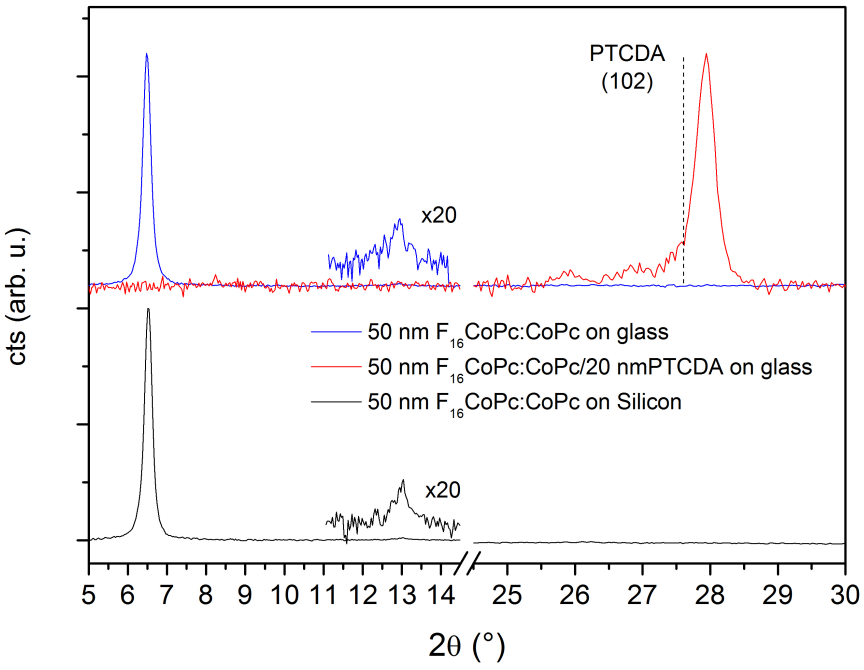


Figure 6.3: X-ray diffraction patterns of F_{16}CoPc:CoPc (1:1) mixed films; the background signal has been subtracted for clarity. The black line shows the measurement on a 50 nm film grown on silicon, the blue line refers to a 50 nm film grown on glass, while the red line represents the measurement of a 50 nm film grown on a 20 nm PTCDA layer on glass. All XRD scans have been normalized to unity. The data between 2θ=14.5°and 2θ=24.5°is omitted because it did not contain any diffraction peak. The position of the (102) peak of PTCDA has been marked for reference

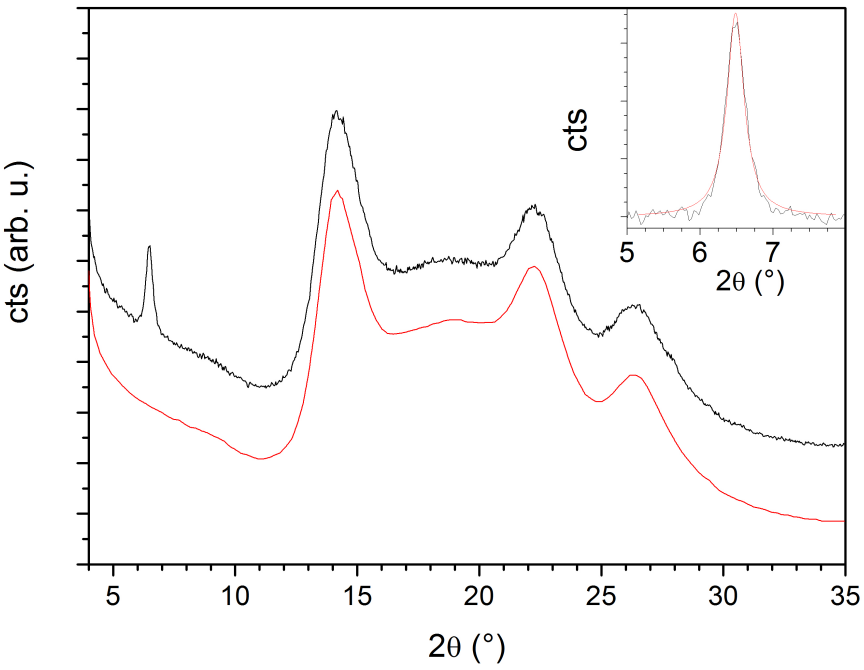


Figure 6.4: X-ray diffraction pattern of 50 nm F_{16}CoPc:CoPc (1:1) mixed films grown on kapton (black line); the background signal from the kapton substrate is shown for reference (red line). Inset: the diffraction peak of the organic film at 2θ=6.5°(black line) and fit with a Lorentzian function (red line)

films are textured and that the phthalocyanine molecules adhere on the substrate with a standing orientation, as suggested by the lattice spacing of the diffraction peak d=13.6Å in the range of lateral size of the molecules. The position of the peak is intermediate between those observed in films of CoPc and F_{16}CoPc on non-interacting substrates. Mixed CoPc:F_{16}CoPc films grown on a 20 nm PTCDA layer show diffraction peaks at higher angle (Figure 6.3). The main peak is observed at 2θ= 27.4° (d = 3.25Å), which denotes a flat orientation of the molecules on the PTCDA layer and demonstrates a templating effect on the film texture similar to that observed in CoPc and F_{16}CoPc films. The width of the peak is 0.33°, which corresponds to a Scherrer size of 46 nm (Table 6.1). The peak position is intermediate between that observed in templated films of F_{16}CoPc (2θ=28.59°), and CoPc (2-11) (2θ=27.95°). Other peaks may possibly be weakly diffracting at 2θ=26° and 2θ=26.75°

The XRD measurement shows that the two organic molecules can co-crystallize in a common structure, despite having very different electronic properties. The position of the diffraction peaks is intermediate between those measured in pure films of each individual component, which can have a few possible explanations. It was discussed in chapters 3 and 5 that the molecular packings of CoPc and F_{16}CoPc films are substantially different: compared to CoPc, the fluorinated compound has a preference for a larger lateral shift within the phthalocyanine columns, and possibly also for different relative arrangements of the columns in the crystal. When the two species are co-deposited, the molecular packing preferred by one the two components may prevail, or a novel structure, with intermediate characteristics, may be formed instead.

As will be discussed later, the UV-VIS absorption spectra and the magnetic properties point towards a stacking geometry close to the α-phase. The slightly longer (001) lattice spacing compared to α-CoPc films is compatible with the fact that fluorine atoms in F_{16}CoPc increase the molecular size and probably lead to

a larger electrostatic repulsion between the phthalocyanine chains than in a pure CoPc film.

Unfortunately the substitution of the peripheral hydrogen atoms with fluorine has a relatively small impact on the overall scattering of the X-rays by the phthalocyanine molecule; this means that the determination of the relative occupation of the lattice positions by the two molecules by XRD is almost impossible. The opposite character of the electric density distribution potential on fluorinated and regular phthalocyanine molecules suggests that electrostatic interactions would favour an alternation of the two species along the stacking direction, as observed in the case of crystals of benzene and hexafluorobenzene and other other phenyl-perfluorophenyl complexes [82]. However, the formation of a long range alternated structure would require film growth in conditions of (quasi)thermodynamic equilibrium, which are usually achieved only when the substrate is held near the sublimation temperature of the film. In the samples studied here the crystallization of the molecules in an ordered alternated structure is likely to be hindered for kinetics reasons, since growth occurs at room temperature. The films are therefore expected to display a random occupation of the crystal lattice by the two species. A completely random sequence would have on average 50% of the molecules of one species next to a molecule of the other type, while the remaining 50% would be paired to the same species; the balance might be slightly shifted towards the formation of pairs of CoPc and F_{16}CoPc by the favourable interaction of the two.

6.3 UV-Visible spectroscopy

The spectrum of a 50 nm F_{16}CoPc:CoPc (1:1) mixed film on glass exhibits a maximum of absorption at λ=620 nm and a weak shoulder around λ=680 nm, which are identically seen in the 200 nm thick film (Figures 6.6a and 6.6c).

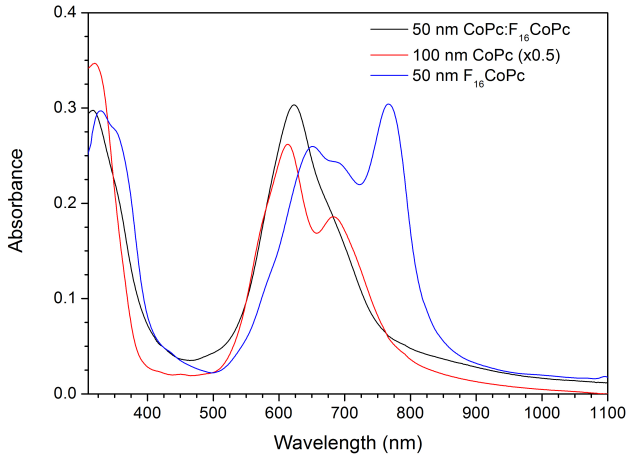


Figure 6.5: UV-Visible absorption spectrum of a 50 nm F_{16}CoPc:CoPc (1:1) mixed film (black line), compared with the spectra of a 100 nm CoPc film (red line, scaled by 0.5) and a 50 nm F_{16}CoPc film (blue line)

A similar shape of the spectrum, with a better resolved shoulder peak, is measured in the mixed films grown on a layer of PTCDA (Figures 6.6b and 6.6c); the absorbance is almost doubled compared to the 50 nm film directly grown on glass, in agreement with the change of the molecular orientation from standing to flat on the substrate, previously indicated by XRD. The films grown on PTCDA may also have a better grade of structural order, consistent with a reduced absorption around λ=665 nm, which is the maximum of absorption of monomers in solution (see Figure 5.3).

The spectra of the mixed films, both templated and non templated, bear no resemblance with those of F_{16}CoPc films and in particular do not show an intense absorption band at 760 nm. On the contrary, the position and intensity of the two main bands match quite well those of the α-CoPc spectrum. This suggests that the mixed films adopt a structure that is closely related to the one of the α-phase. This suggestion will be confirmed in the next section by the results of the magnetic characterization.

It should be noted that the spectra of the mixed films do not show evidence of intermolecular charge transfer transitions between F_{16}CoPc and CoPc, although

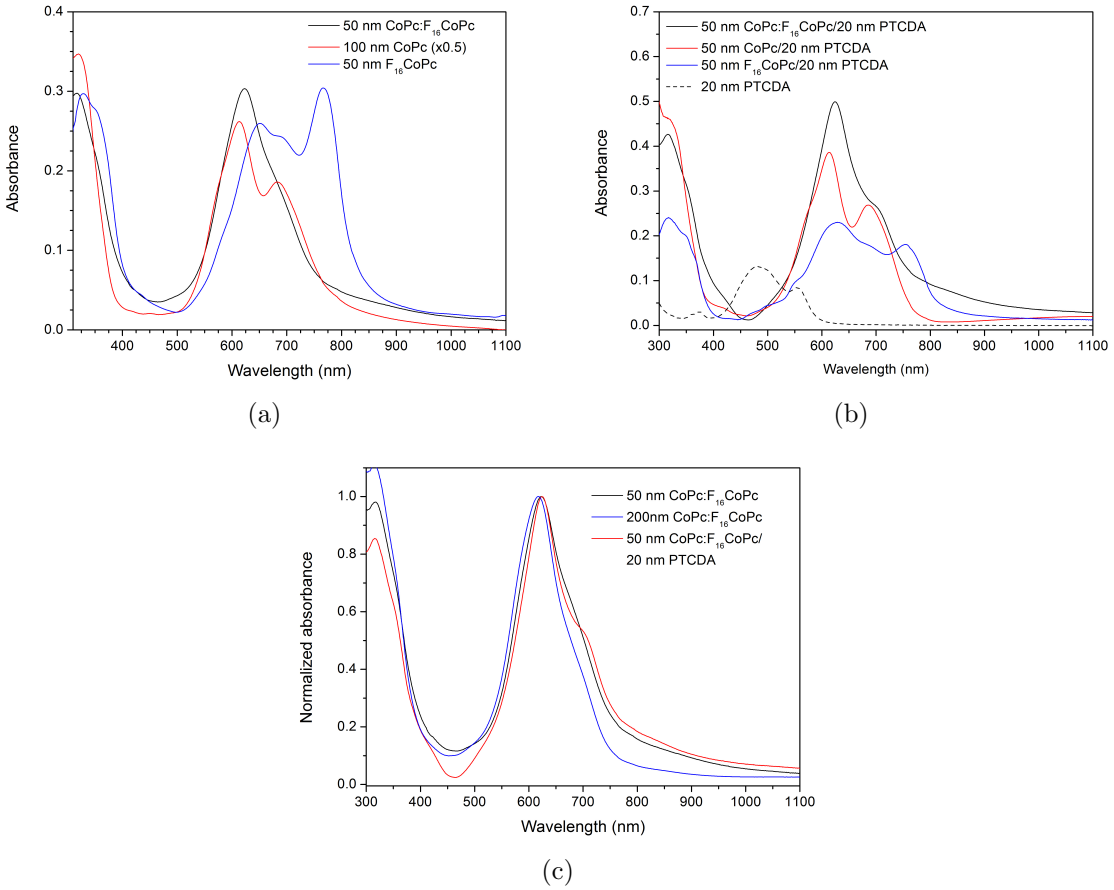


Figure 6.6: (a) UV-Visible absorption spectrum of a 50 nm F_{16}CoPc:CoPc (1:1) mixed film (black line), compared with the spectra of a 100 nm CoPc film (red line, scaled by 0.5) and a 50 nm F_{16}CoPc film (blue line). (b) spectra of 50 nm F_{16}CoPc:CoPc (1:1) mixed film on 20 nm PTCDA layer(black line), 50 nm CoPc film (red line, scaled by 0.5) and a 50 nm F_{16}CoPc film (blue line) both on PTCDA. The absorption of the 20 nm PTCDA layer (already subtracted from the other spectra) is shown for reference (dashed line). (c) Normalized spectra of F_{16}CoPc:CoPc (1:1) films: 50 nm film (black), 200 nm film (blue) and 50 nm film on 20 nm PTCDA (red); the absorption of PTCDA has been subtracted from all the spectra

these are expected due to the relative donor/acceptor character of the molecules. In a dimer of stacked F_{16}CoPc and CoPc molecules, the polarization of this transition would be close to the stacking direction, meaning that its absorption should be measurable in the films directly grown on glass, where phthalocyanines stack in the plane of the film. However, it is likely that the energy of the excitation falls below the range probed in the measurement (1.1eV–3.5 eV), as in the case of mixed films of MnPc and F_{16}CoPc, where it occurs at 0.6 eV ($\lambda \approx$2066 nm) [60].

6.4 X-ray Photoelectron Spectroscopy

X-ray core photoelectron spectroscopy (XPS) was used to determine the composition of the films and characterize possible electronic interactions between F_{16}CoPc and CoPc in the mixed films.

Figure 6.7 confronts the survey scans of single component films (CoPc or F_{16}CoPc) with those of mixed CoPc:F_{16}CoPc (1:1) films grown with or without a templating PTCDA layer. The thickness of the films varies between samples, however this does not affect the number of photoemitted electrons, because the thickness is always much larger than the sampling depth of XPS. Most of the features in the spectra have been assigned to the elements contained in the phthalocyanines. An exception is represented by the CoPc film, which displayed the O 1s peak of oxygen at a binding energy close to 530 eV, owing to a long ageing of the sample in air. The elemental abundance in the films has been calculated by comparing the integrals of the fits of the signal of each element (Figures 6.8 and 6.9), after correction of the different sensitivity factors [93] (Table 6.2).

In the single component CoPc film, the ratio of Co:N:C was 1:7:32, remarkably close to the theoretical 1:8:32. In the F_{16}CoPc film the ratio of Co:N:F:C was 1:7:14:30, also very close to the expected 1:8:16:32. The deviations could be explained by errors of the fit or by not having run a calibration of the sensitivity

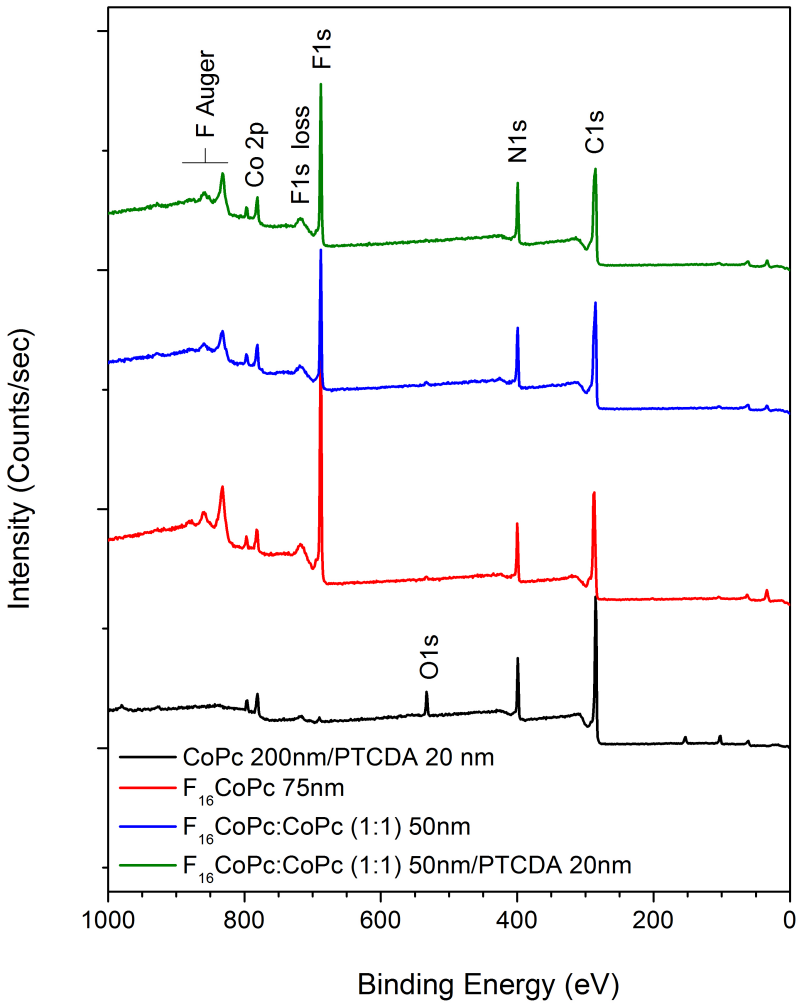


Figure 6.7: XPS survey data of CoPc, F_{16}CoPc and mixed F_{16}CoPc:CoPc films. The species responsible for the main peaks are labelled accordingly, whilst the data are offset for clarity.

Species (Orbital)	Sensitivity Factor	Relative abundance % (Theoretical %)			
		CoPc 200nm/ PTCDA 20nm	F_{16}CoPc 75nm	F_{16}CoPc:CoPc 50nm	F_{16}CoPc:CoPc 50nm/ PTCDA 20nm
C (1s)	0.25	77.2 (78.0)	57.3 (56.1)	66.8 (65.3)	64.6 (65.3)
N (1s)	0.42	15.6 (19.5)	13.0 (14.0)	15.0 (16.3)	14.5 (16.3)
O (1s)	0.66	4.8 (0)	0.8 (0)	0.7 (0)	0.2 (0)
F (1s)	1	N/A	27.1 (28.1)	15.5 (16.3)	18.5 (16.3)
Co ($2p_{3/2}$)	2.5	2.4 (2.4)	1.9 (1.8)	2.0 (2.0)	2.2 (2.0)

Table 6.2: Calculated relative abundance of the species detected in CoPc, F_{16}CoPc and mixed F_{16}CoPc:CoPc films (1:1 ratio) (from Figures 6.8 and 6.9) after correcting for the empirical sensitivity factors relative to the F(1s) level (from [93])

factors specific for the instrument in the laboratory.

The composition of the two F_{16}CoPc:CoPc mixed films is close to that one of an ideal 1:1 mixture of the two components, containing fluorine and nitrogen in the same amount. The larger abundance of fluorine in the mixed film grown on PTCDA seems to indicate a slight deviation in the composition, possibly due to unstable rate during the deposition. It is excluded that this effect is caused by the different molecular orientation of the films grown on PTCDA, since the spectra of templated and non-templated F_{16}CoPc films were fully consistent.

High resolution XPS scans of the C 1s, N 1s, O 1s, F 1s and Co 2p signals are shown in Figures 6.8 and 6.9. The C 1s signals in the single component CoPc and F_{16}CoPc films can be rationalized by the presence of C atoms in different chemical environments. The CoPc molecule contains 24 C atoms in the four benzenic rings, bonded to other carbon atoms and hydrogen, and eight C atoms in the four pyrrolic rings, each of them bonded to two N atoms and a C atom. These two components give rise to the two peaks observed at binding energies of 284.5 eV and 285.7 eV respectively, with intensity ratio of 2.6:1, close to the theoretical 3:1 (Figure 6.8a). The weak peak at a binding energy of 287.7 eV is a shake-up satellite commonly seen in phthalocyanines [74].

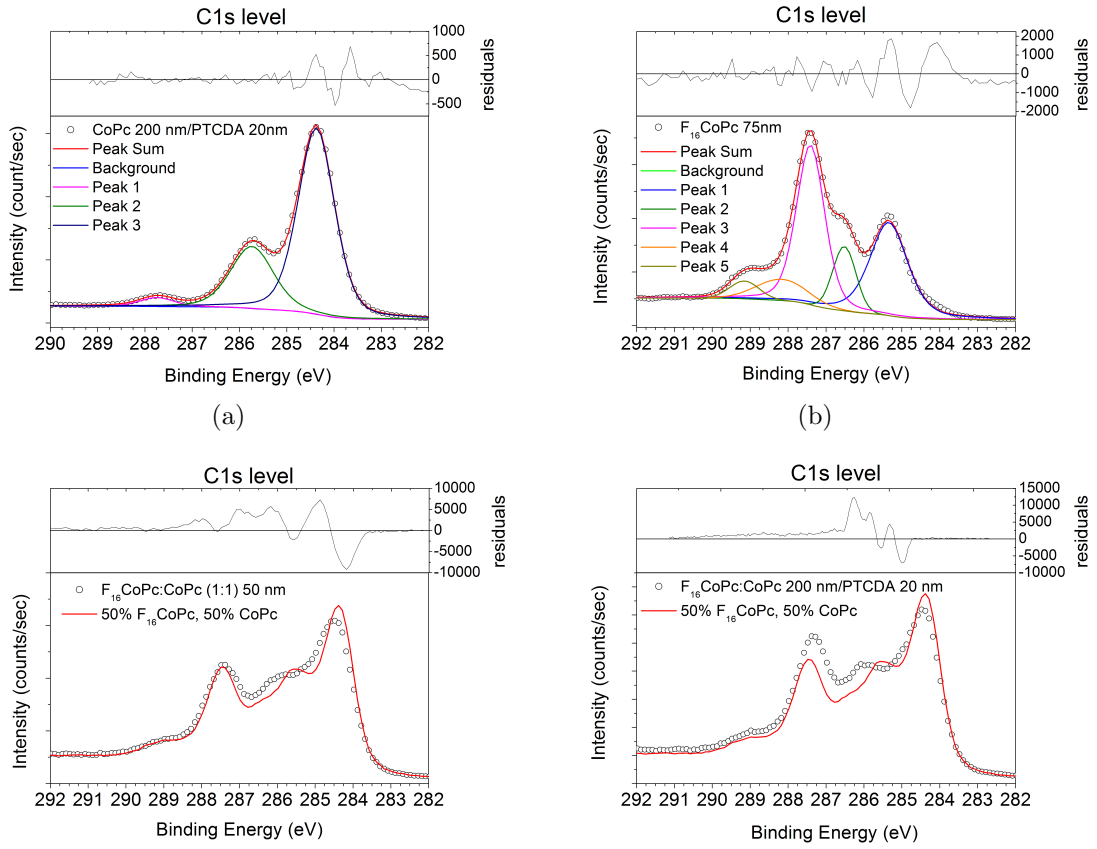


Figure 6.8: High resolution C 1s XPS profiles of the (a) CoPc 200nm/PTCDA 20 nm, (b) F_{16}CoPc 75nm, (c) F_{16}CoPc:CoPc 50nm and (d) F_{16}CoPc:CoPc 50nm/PTCDA 20nm films on silicon. The profiles in the pure CoPc and F_{16}CoPc films have been deconvoluted with Voigt peak shapes (30% Lorentzian, 70% Gaussian) and the background has been modelled by the Shirley algorithm. The spectra of the mixed films have been simulated by a 1:1 mixture of the spectra of the pure films. The top of each figure shows the residuals of the fit or of the simulation

The C atoms on the benzenic rings are not all equivalent in F_{16}CoPc, because some of them are bound to highly electronegative F atoms. Consequently, the three main components of the spectrum at binding energies of 285.3 eV, 286.5 eV and 287.4 eV (Figure 6.8b) are assigned to the eight benzenic C atoms not bound to F, to the 8 pyrrolic C atoms and to the 16 C atoms bound to fluorine respectively. The ratio of the integrated intensities (2.5:1:3.3) deviates from the theoretical one (1:1:2), possibly due to the overlap with a satellite peak. The broad, weaker feature at binding energy around 289 eV was reported also in F_{16}CuPc, and it has been attributed to two satellite peaks close in energy [76].

In the case of the mixed films, the C 1s spectrum presents the characteristics of both CoPc and F_{16}CoPc. Indeed, the profile measured in the mixed films can be approximated to a large extent with an average of the spectra of the individual components (Figures 6.8c and 6.8d). In the mixed film grown on PTCDA, the higher intensity of the 287.5 eV peak, characteristic of F_{16}CoPc, over the 284.5 eV peak suggests a F_{16}CoPc rich composition of the film, in agreement with the deviation in the nitrogen to fluorine ratio discussed previously (Table 6.2).

The spectra of the other elements showed a simpler structure and a weaker dependence on the film composition. The N 1s signal is described by an intense peak around 399 eV and a weak satellite located about 1.5 eV higher in binding energy, which is documented for other phthalocyanines as well [74]; Ottaviano *et al.* showed that the main peak is actually made by two components spaced by about 0.5 eV, corresponding to the non equivalent bridging aza and pyrrole nitrogen atoms [76], which has been taken into account in our fits. All peak components shift by 0.6 eV to higher binding energy going from the CoPc to F_{16}CoPc sample, with the mixed films showing half of the shift. This seems more than a fortuitous effect of sample charging, since the position of the F1s peak is remarkably constant at 687.6-687.7 eV across the series of F_{16}CoPc containing films (Figure 6.9c and Table 6.3).

The Co 2p spectrum is quite similar in the four samples. The signal is split in the $2p_{3/2}$ peak at 781 eV and $2p_{1/2}$ peak at 797 eV components separated by the spin orbit coupling upon ionization. The $2p_{3/2}$ peak shows a shoulder and a weak satellite about 1.8 eV and 9 eV higher in energy respectively, which have been characterized by Kroll *et al.* in CoPc and attributed to multiplet and covalence effects [54]. Differently from the case of mixed films of F_{16}CoPc and MnPc studied by Lindner *et al.*, there is no evidence of the shift of the $2p_{3/2}$ peak to 779 eV indicating reduction of the cobalt atom in F_{16}CoPc to the (I) oxidation state following charge transfer to F_{16}CoPc in the mixture [60]. It is noteworthy that even the CoPc film aged in air, which showed a high content of oxygen (in Figure 6.9b, the signal is scaled by 0.1 for the CoPc film), the Co 2p spectrum remains essentially the same as in the other samples, indicating stability of cobalt towards higher oxidation states.

To conclude, the results of the XPS investigation establish that the composition of the mixed films is close to the expected 1:1 ratio between CoPc and F_{16}CoPc. The analysis of the C 1s and the Co 2p spectra indicates that negative charge transfer to either the organic ligand or the cobalt centre of F_{16}CoPc does not occur in the mixtures with CoPc, contrarily with the case of mixtures with MnPc [60]. This can be attributed to ionisation potential in CoPc higher by 0.5 eV than in MnPc [38].

6.5 Magnetic characterization of the films

The magnetic properties of 200 nm mixed films of CoPc and F_{16}CoPc in a 1:1 ratio grown on kapton were studied by SQUID magnetometry.

Isothermal magnetization curves were measured between 0 and 7 Tesla. Figure 6.10a shows the net magnetic moment per phthalocyanine molecule at temperatures between 2 and 10 K. At 2 K, the curve shows a steady increase of the

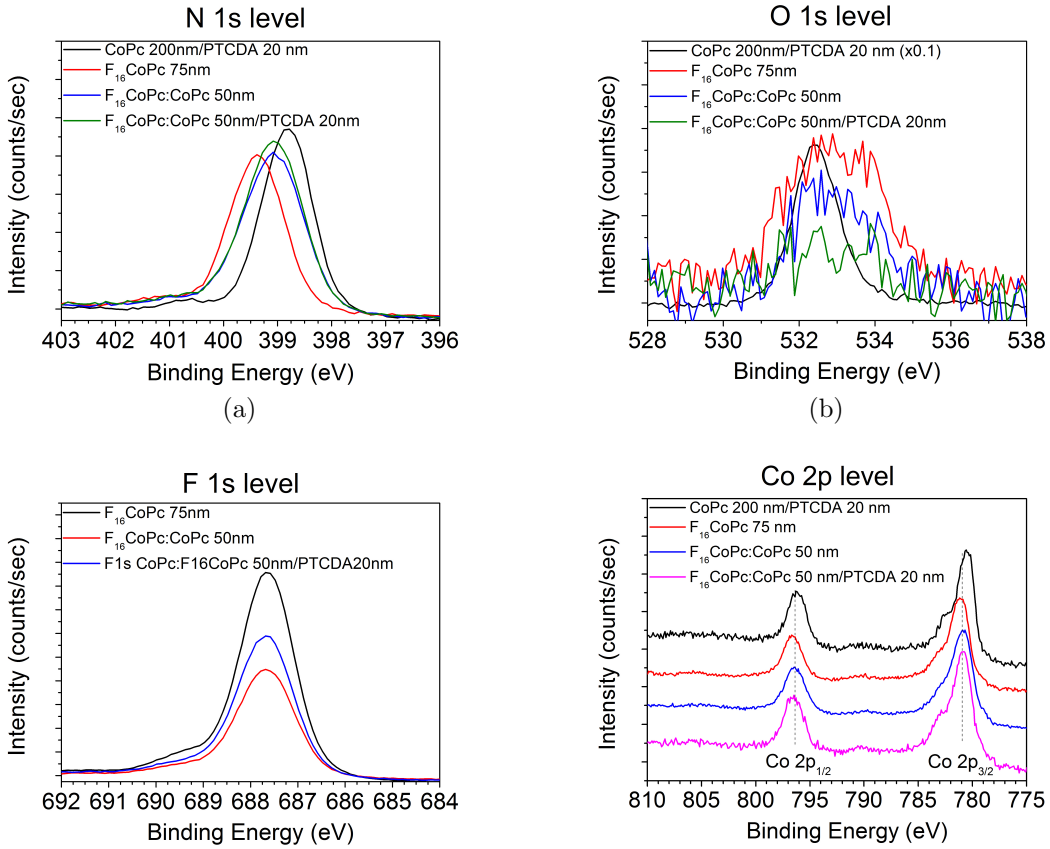


Figure 6.9: High resolution XPS profiles of the (a) N 1s, (b) O 1s, (c) F 1s and (d) Co 2p. In (d) the spectra are shifted for clarity.

	CoPc 200 nm/ PTCDA 20 nm		F_{16}CoPc 75 nm		F_{16}CoPc:CoPc 50 nm		F_{16}CoPc:CoPc 50 nm/ PTCDA 20nm	
	B.E. (eV)	%	B.E. (eV)	%	B.E. (eV)	%	B.E. (eV)	%
C 1s	284.5	69.8	285.3	32.0				
	285.7	27.1	286.5	13.0				
	287.7	3.1	287.4	43.5	N/A	N/A	N/A	N/A
			288.2	5.3				
			289.1	6.3				
N 1s	398.6	55.6	399.2	51.8	398.8	40.1	398.8	43.1
	399.1	42.6	399.6	45.8	399.3	56.8	399.3	55.9
	400.7	1.7	401.2	2.4	400.8	3.0	400.9	1.0
O 1s	532.4	100	532.3	56.4	532.5	65.0	532.9	100
			533.8	43.6	534.1	35.1		
F 1s	N/A	N/A	687.6	95.2	687.7	95.2	687.7	94.3
			689.4	4.8	689.4	4.8	689.2	5.7
Co $2p_{3/2}$	780.5	69.2	781.1	74.8	780.8	78.0	780.8	69.0
	782.3	30.8	783.0	25.2	782.6	22.0	782.5	31.0

Table 6.3: Binding energies and relative intensities of fitted peaks for the high resolution XPS spectra of CoPc, F_{16}CoPc and mixed F_{16}CoPc:CoPc films (1:1 ratio), in Figures 6.8 and 6.9. The intensity profiles are fitted using a Voigt line shape with 30 % Lorentzian and 70 % Gaussian component. The C 1s signal of the mixed films has not been fitted owing to its complex structure. Without any further correction, all values of the binding energy are in reasonably good agreement (within 0.4 eV) with those reported by Niwa *et al.*[74] and Ottaviano *et al.*[76]

magnetic moment with the applied field, followed by a change of slope around 3 Tesla marking the onset of an apparent saturation. The highest value of the magnetic moment, measured at 7 Tesla, is about 0.05 μ_B, which represents a 20-fold reduction from the hypothetical saturation moment of $\approx 1\mu_B$ expected for a spin S=1/2.

The low temperature magnetism of the films is analogous to that of CoPc films, which was discussed in chapter 3. Indeed, it is found that the magnetic moment has a temperature dependent paramagnetic component, which is a function of the H/T ratio, and a term characterized by a constant susceptibility χ_0^{MH} of positive sign. The value of this correction is $\chi_0^{MH} = 1.9\text{x}10^{-3}\mu_B T^{-1}$, which is comparable with those needed in fits of the CoPc films. The temperature dependent paramagnetic part could be fitted very well by the Brillouin function, extracting an average value of g equal to 2.0; the data could also be excellently fitted by fixing the value of g to that expected in a non-templated CoPc films ($g = 2.224$). The fraction of paramagnetic spins f estimated from the fit is $(4.05 \pm 0.25)\%$, where the uncertainty indicates the range of values obtained with the two values of g.

The low temperature behaviour of the templated mixed films, shown in Figure 6.11a, was similar to the one of the non-templated films, but with a smaller fraction of paramagnetic spins $f = (2.35 \pm 0.05)\%$ and a slightly larger temperature independent correction (χ_0^{MH}=2.5x$10^{-3}\mu_B T^{-1}$).

In analogy with the case of CoPc films, the substantial reduction of the magnetic moment at low temperature should arise from a strong antiferromagnetic spin coupling in the mixed films. In order to characterize the strength of the interaction, the temperature dependence of the magnetic properties was investigated. Figures 6.10c and 6.11c show that at temperatures of 50 K and above the magnetic moment of both non-templated and templated films increases linearly with the field between 0.5 and 7 Tesla. The extrapolation of the linear fit to zero applied field shows a finite intercept M_0, which has a negative sign in the non-

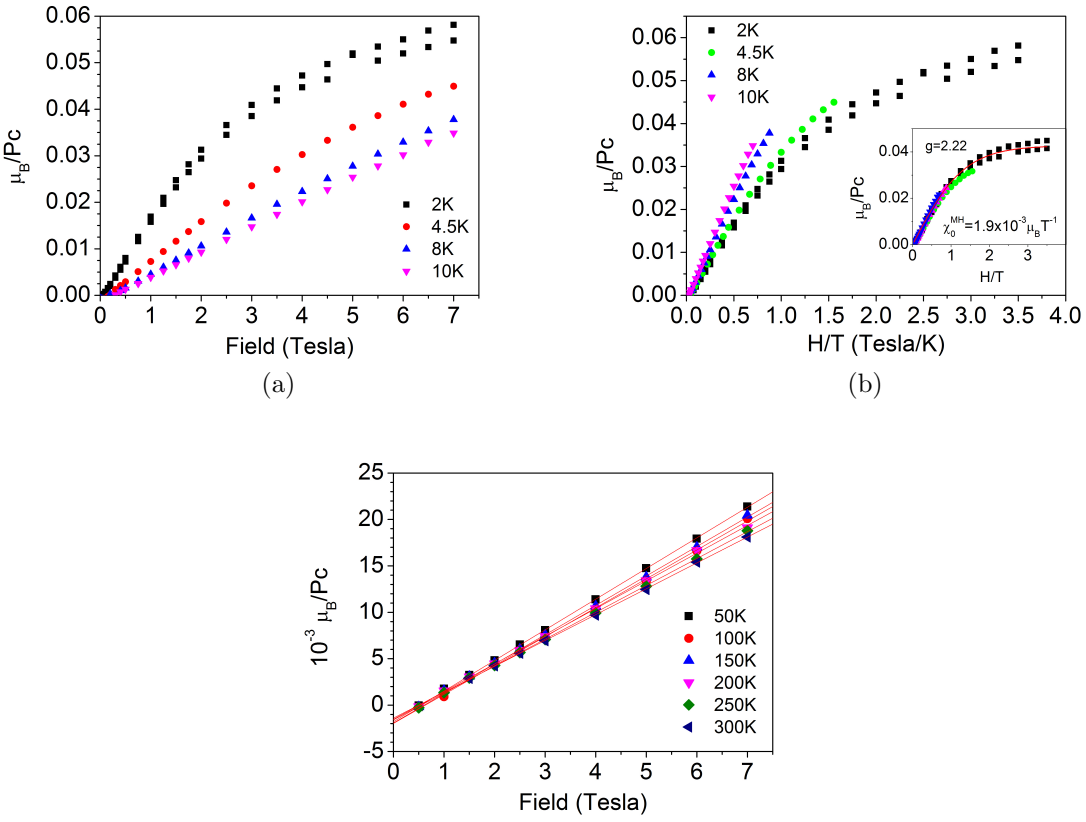


Figure 6.10: Magnetic characterization of F_{16}CoPc:CoPc (1:1) 200 nm film on kapton: (a) low temperature isothermal magnetization curve, expressed as the net magnetic moment in μ_B per phthalocyanine molecule. The magnetic moment as a function of the ratio of field over temperature (H/T) is shown in (b). Inset: the same data after subtraction of a magnetic moment $H\chi_0^{MH}$, where χ_0^{MH}=1.9x10$^{-3}\mu_B T^{-1}$. The red line shows the Brillouin function fit ($g = 2.224$) which returns a fraction of paramagnetic spins $f = 3.8\%$. The isothermal magnetization curves between 50 K and 300 K, shown in (c), exhibit a linear increase of the magnetization; lines of best fit are shown in red. The fits extrapolate to a negative intercept with the magnetization axis, owing to an impurity in the film (see text)

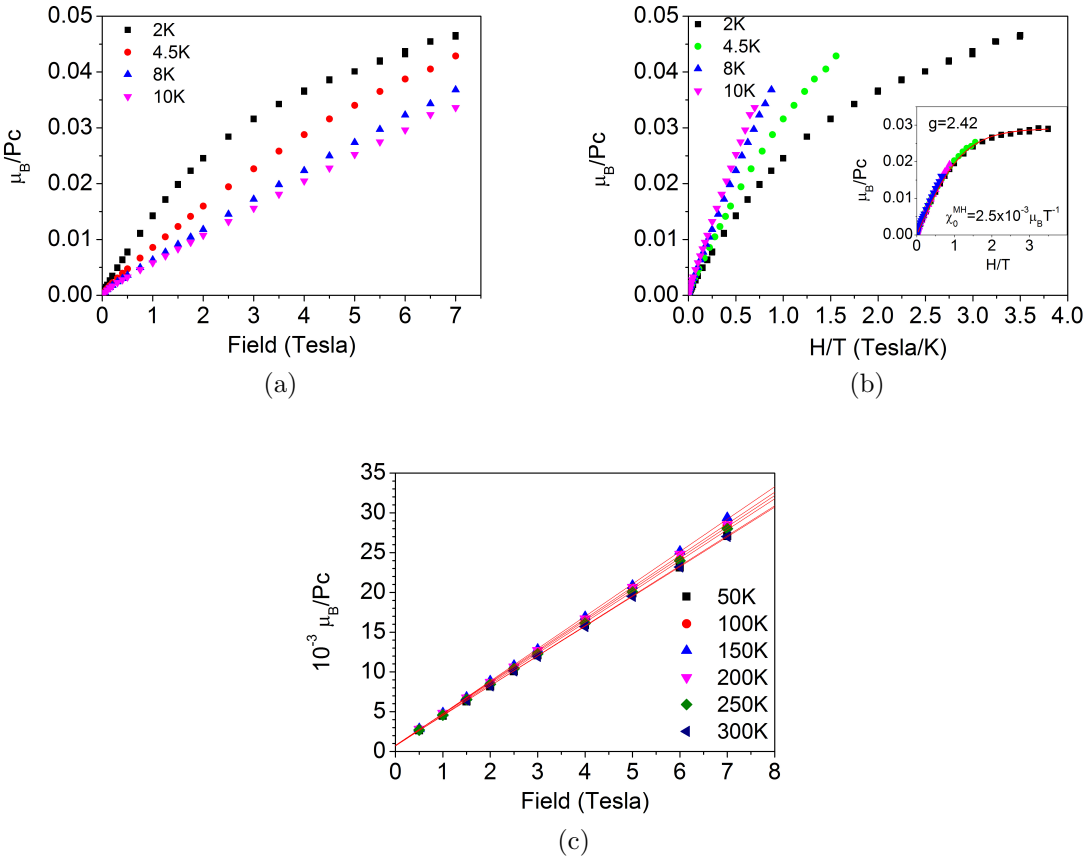
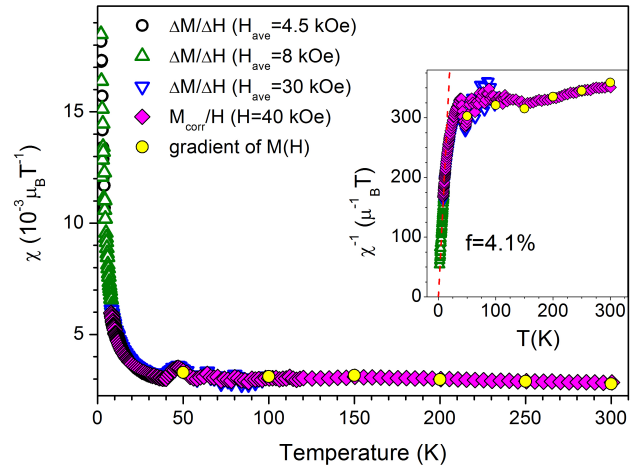


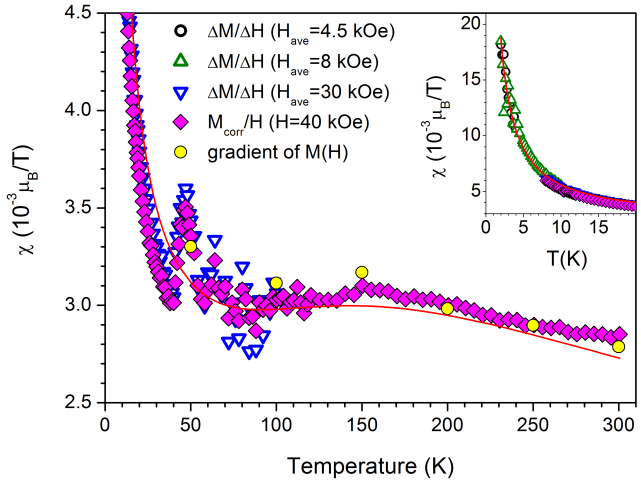
Figure 6.11: Magnetic characterization of F_{16}CoPc:CoPc (1:1) 200 nm film grown on a PTCDA layer on kapton: (a) low temperature isothermal magnetization curve, expressed as the net magnetic moment in μ_B per phthalocyanine molecule. The net magnetic moment per molecule as a function of the ratio of field over temperature (H/T) is shown in (b). Inset: the same data after subtraction of a magnetic moment $H\chi_0^{MH}$, where χ_0^{MH}=2.5x10$^{-3}\mu_B T^{-1}$. The red line shows the Brillouin function fit ($g = 2.42$) which returns a fraction of paramagnetic spins $f = 2.4\%$. The isothermal magnetization curves between 50 K and 300 K, shown in (c), exhibit a linear increase of the magnetization; lines of best fit are shown in red. The fits extrapolate to a positive intercept with the magnetization axis, owing to an impurity in the film (see text)

templated film $M_0 = (-3.4 \pm 0.5)\text{x}10^{-3}\mu_B$ and a positive sign in the templated film $M_0 = (7.43 \pm 0.4)\text{x}10^{-4}\mu_B$. It is likely that this spurious signal is due to a small ferromagnetic impurity in the sample or in the holder which saturates at a field lower than 0.5 Tesla; negative or positive contributions on the magnetic moment are both possible and depend on the position of the impurity in the sample. Since this small spurious signal is rather independent of temperature, it can be subtracted easily from the data; this correction will be applied when calculating the magnetic susceptibility, as explained in the caption of Figures 6.12 and 6.13.

The temperature dependent magnetic susceptibility of the non-templated film is shown in 6.12a; the measurement uses higher magnetic fields at higher temperatures, to compensate for the reduction of signal (further details given in the caption). The value of $\chi(T)$ decreases rapidly between 2 K and 20 K, and then shows a more stationary behaviour. The curve exhibits a broad peak centred at 50 K, which is characteristic of the antiferromagnetic to paramagnetic transition in frozen molecular oxygen [58]. This suggests that the sample is slightly contaminated by O_2 molecules, possibly chemisorbed/physisorbed on the cobalt ion; the effect was also observed, with a smaller magnitude, in CoPc films. The detail of the high temperature part of the $\chi(T)$ curve (Figure 6.12b), shows a faint maximum around 150 K, which is similar to the one seen in non-templated CoPc films (Figure 3.16b), but shifted to higher temperature. The reciprocal of susceptibility, shown in the inset of Figure 6.12a, follows a paramagnetic-like behaviour between 2 K and 25 K, highlighted by the linear relation with the temperature. The slope of the curve gives a Curie constant equal to 19.6 $\mu_B T^{-1} K$, which is equivalent to 4.1%–5.1% of the total number of spins, depending on the value assumed for g, in perfect agreement with the low temperature Brillouin fits of the magnetization. Above 50 K the $1/\chi(T)$ curve enters a different regime, characterized by a marked reduction of the slope and a large negative intercept, suggesting large antiferromagnetic interactions in the material, as in the case of CoPc films.

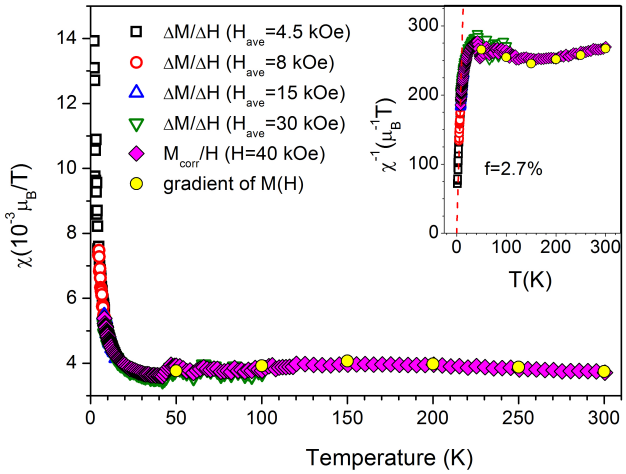


(a)

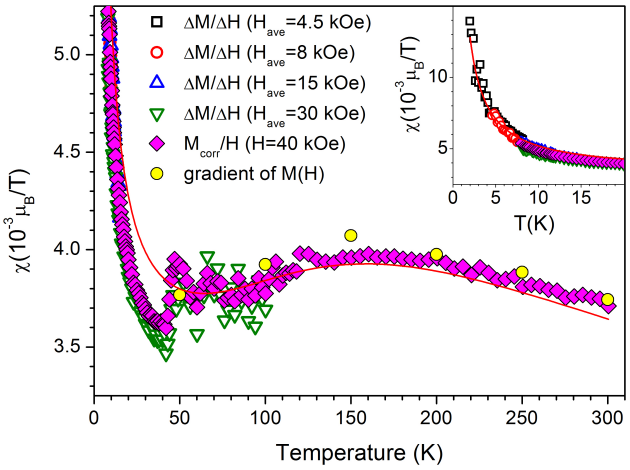


(b)

Figure 6.12: (a) Temperature dependence of the magnetic susceptibility $\chi(T)$ of a 200 nm F_{16}CoPc:CoPc (1:1) mixed film on kapton; empty symbols are values of differential susceptibility calculated as $\Delta M/\Delta H$ from two M(T) measurements at different fields (H_{ave} is the average field); filled (magenta) diamonds values were calculated as M_{corr}/H from a single M(T) measurement at H=40 kOe, where M_{corr} is the magnetization after subtraction of the spurious signal do to a ferromagnetic impurity (M_0=-3.4x10$^{-3}\mu_B$, see Figure 6.10c); the filled (yellow) circles are the gradients of the M(H) curves in Figure 6.10c. For an explanation of units refer to section 2.3.7 and Equation 2.12. (b) Detail of the high temperature part of $\chi(T)$ and fit with the model based on the infinite antiferromagnetic chain (Equation 3.3).



(a)



(b)

Figure 6.13: (a) Temperature dependence of the magnetic susceptibility $\chi(T)$ of a 200 nm F_{16}CoPc:CoPc (1:1) mixed film grown on 20 nm PTCDA on kapton; empty symbols are values of differential susceptibility calculated as $\Delta M/\Delta H$ from two M(T) measurements at different fields (H_{ave} is the average field); filled (magenta) diamonds values were calculated as M_{corr}/H from a single M(T) measurement at H=40 kOe, where M_{corr} is the magnetization after subtraction of the spurious signal do to a ferromagnetic impurity (M_0=+1.49$^{-3}\mu_B$, see Figure 6.11c); the filled (yellow) circles are the gradients of the M(H) curves in Figure 6.11c. For an explanation of units refer to section 2.3.7 and Equation 2.12. (b) Detail of the high temperature part of $\chi(T)$ and fit with the model based on the infinite antiferromagnetic chain (Equation 3.3).

The $\chi(T)$ curve of the templated F_{16}CoPc:CoPc films is shown in Figure 6.13; the behaviour below 20 K is dominated by a paramagnetic signal corresponding to 2.6–2.7% of the spins, and around 160 K the $\chi(T)$ curve displays a clearly defined maximum (Figure 6.13b).

The data was fitted to the infinite antiferromagnetic chain model defined in Equation 3.3, which includes a Curie term and a temperature independent correction χ_0^{χ}; it was shown in chapter 3, that this model is able to provide a reliable measure of the antiferromagnetic exchange in the CoPc films. The fit of the non-templated F_{16}CoPc:CoPc film measurement, shown in Figure 6.12b and relative inset, reproduces reasonably well the data in the whole temperature range using values of the exchange energy J/K_B =138 K, fraction of paramagnetic spins f =3.9% and temperature independent correction χ_0^{χ}=1.0x10$^{-3}\mu_B T^{-1}$. The value of f agrees well with the fit of the low temperature $M(H)$ curves, while χ_0^{χ} is of the same order of magnitude of χ_0^{MH} but 9x10$^{-4}\mu_B T^{-1}$ smaller. The best set of fit parameters for the templated F_{16}CoPc:CoPc film data were J/k_B =134 K, f =1.9% and χ_0^{χ}=1.7x10$^{-3}\mu_B T^{-1}$; the fit deviates slightly from the experimental curve between 20 and 50 K, possibly due to the simplification introduced by using an infinite chain model. The fit demonstrates that the antiferromagnetic exchange interactions in the mixed F_{16}CoPc:CoPc films are stronger than in the pure CoPc films.

Since the films are likely to be formed by a random mixture of two phthalocyanine forms, it is worth considering how a non uniform exchange interaction along the chain would affect the interpretation of the data. In general, pairs of F_{16}CoPc-CoPc,F_{16}CoPc-F_{16}CoPc and CoPc-CoPc along the chains could exhibit different values of J. Johnston *et al.*[48] considered the case of a S=1/2 antiferromagnetic chain where the exchange constant takes alternate J and αJ values. Their calculations show that as the value of the parameter α is decreased from 1 to 0, the height of the susceptibility maximum at T_{max} =0.64 ($2J/k_B$) progres-

sively increases and converges to the value of the dimer ($\alpha = 0$), which is about a third larger. Importantly, T_{max} only depends on the value of J, the largest exchange coupling in the chain. The most distinctive changes are observed at temperatures approaching 0 K: while uniform chains converge to a finite χ value, the susceptibility of a non uniform chain drops to 0 as the temperature is reduced. It seems reasonable to qualitatively apply Johnston's results to our case, although the mixed films studied here probably do not exhibit a regular alternation of the exchange constant values. Based on this assumption, it can be concluded that the J value obtained from the fits represents the strongest antiferromagnetic coupling in the material. Unfortunately, any detail regarding the variation of J along the chains is not accessible in the $\chi(T)$ data, since the key behaviour at low temperature is obscured by the larger paramagnetic signal deriving from odd chains and uncoupled molecules.

Chapter 7

Conclusions

The aim of this work was the growth and the characterization of the physical properties of films and nanostructures of cobalt phthalocyanine (CoPc) and its perfluorinated derivative (F_{16}CoPc). A particular focus was placed on the study of the magnetic properties and efforts were directed towards increasing the temperature up to which the spin correlations are preserved, in order to demonstrate the potential of phthalocyanine films as magnetic components in high temperature spintronic applications. The cobalt phthalocyanine system was chosen for this purpose because its singly occupied d_{z^2} orbital is expected to lead to stronger spin interactions in the solid state than in other metal phthalocyanines, owing to a larger projection of spin density out of the molecular plane.

The thesis first presented the investigation of the properties of CoPc materials in the α and β polymorph forms. Both structures contain columnar stacks of CoPc but differ for other geometrical parameters, like the angle between the stacking direction and the molecular plane (stacking angle). Large β-CoPc crystals were obtained during the purification of the commercially available CoPc powder. A nanocrystalline α-CoPc powder could be obtained by following the documented acid paste method [35]. Thin films grown by OMBD on substrates at room temperature also exhibited the crystal structure of the α polymorph, as reported for

other MPc films. XRD confirmed that CoPc films deposited on weakly interacting substrates, such as silicon, glass and kapton, and on a PTCDA layer exhibit different textures, corresponding to a standing molecular orientation in the first case, and an almost flat alignment of CoPc on the substrate in the latter case. The spin coupling interactions in the materials were investigated by SQUID magnetometry. While the β-CoPc powder was characterized as a weak antiferromagnet with an exchange energy J/k_B close to 2 K, in agreement with previous reports[71], the behaviour of the α-CoPc films and powder was consistent with a much strongly antiferromagnetic behaviour combined with a small paramagnetic contribution . The field and temperature dependence of the magnetization was analysed by two different models, which included either infinite antiferromagnetic chains with a paramagnetic contribution or finite chains with a binomial length distribution. The latter was chosen to represent the coexistence of highly ordered grain cores with disordered regions surrounding them. Both methods yielded consistent values of the exchange energy J/k_B ranging from 73 K to 106 K in all α-CoPc samples, demonstrating that the strong interaction is characteristic of the α structure only and is weakly affected by the sample morphology or orientation. On the contrary, the fraction of spins relative to the paramagnetic contribution was found to have an inverse correlation with the size of the particles in the samples, which is consistent with a higher concentration of magnetic defects at the surface of the grains. The conclusions of the magnetic analysis were strengthened by the DFT modelling of the spin interaction, which predicted values of the exchange energy in the α and the β phases very similar to those found experimentally[101].

The thesis then presented the growth and characterization of a previously unknown nanowire phase of CoPc. This new polymorph was obtained by the organic vapour phase deposition technique, using a process similar to the one that previously yielded CuPc [95] and FePc [104] nanowires. The novel CoPc material

exhibits an entangled mesh of nanowires with a lateral size below 50 nm and length of at least several μ m, resulting in a very high aspect ratio. The structure of the CoPc material was assumed to be the same as η-CuPc nanowires [95], based on the observation of characteristic XRD peaks and optical absorption spectra. The magnetic characterization of the η-CoPc led to the observation of weak antiferromagnetic spin couplings in the material quantified by an exchange J/k_B close to 1 K, although the similar stacking angles in the α and the η structures would have suggested a large antiferromagnetic coupling in the nanowires. Possible explanations were proposed for this unexpected behaviour. Firstly, the α and the η structures exhibit different directions of the molecular displacement within the phthalocyanine stacks, which could have consequences on the magnetic coupling which were initially underestimated. Secondly, the η structure could have been determined incorrectly or different in CoPc compared to CuPc.

A study of the growth and physical properties of fluorinated CoPc (F_{16}CoPc) films is then presented. The UV-Visible absorption spectra of the films were largely different from those of CoPc, indicating a distinctive molecular packing mode. The actual crystal structure of fluorinated phthtalocyanine films is still debated, but there is consensus about the molecular stacking geometry being similar to the one of the β phase. XRD indicates that in films grown on silicon, glass and kapton, the molecules adopt a standing orientation. Some inconsistencies in the lattice spacing between samples on different substrates hinted at an intrinsic ability of F_{16}CoPc to accommodate stress during growth. The growth behaviour of highly ordered films grown on silicon and glass was explained with the occurrence of a transition as the film thickness increases past 25 nm, as highlighted by changes in the XRD pattern. This modification of the structure also results in the transformation of the morphology from densely packed particles with a spherical or elongated shape to one characterized by needle-like structures protruding out of the film surface.

The films on kapton were the least crystalline, which could be the reason why the out-of-plane structural parameters did not show a similar transition at high film thickness. Growth of the F_{16}CoPc films onto a PTCDA layer eliminated the variability observed between different substrates and led to a templating effect similar to the one in CoPc. In the new molecular orientation, the phthalocyanine columns can grow vertically on the substrate, which significantly reduced the stress in the film, as demonstrated by the absence of any structural relaxation as the thickness was increased. The films of both textures exhibited a weak antiferromagnetic behaviour characterized by a value of J/k_B close to 2 K, leading to a temperature and field dependence of the magnetization similar to the one observed in β-CoPc; the result are therefore consistent with a β phase like stacking geometry in the F_{16}CoPc films.

The growth and characterization of mixed CoPc and F_{16}CoPc films is discussed in the final chapter. The films were prepared by the co-evaporation of CoPc and F_{16}CoPc from separate sources in the organic molecular beam deposition chamber, using identical growth rates of the two components to achieve a 1:1 composition ratio. The deposition on different substrates led to identical results. SEM and XRD peak patterns demonstrate that the CoPc and F_{16}CoPc can blend in an ordered structure in the mixed film. The phthalocyanine molecules in the films are likely to be randomly alternated along the stacking direction; the actual occupation of the lattice positions cannot at present be established from the XRD pattern, due to similar structure factors of CoPc and F_{16}CoPc. The optical absorption spectrum of the mixed film is strikingly similar to the one of the CoPc films, suggesting that the crystal structure of the mixture is closely related to the α phase of MPcs. Based on the XPS characterization it was excluded that the two components participate to a charge transfer. Indeed, the core level spectra of the carbon (C1s), nitrogen (N1s), fluorine (F1s) and cobalt (Co2p) were either identi-

cal or could be well approximated by an average of those measured in individual CoPc and F_{16}CoPc. The texture of the mixed films can be controlled by deposition onto a thin PTCDA layer, which leads to a parallel orientation of the molecules on the substrate, similarly to other phthalocyanine films. SEM cross-section image shows a vertical elongation of the grains, compatible with the anisotropic growth of phthalocyanine crystals. The optical properties were similar to those of the untemplated films, suggesting an identical structure. Mixed films of both textures were strongly antiferromagnetic, with exchange energy J/k_B approaching 140 K. This result indeed confirmed that the structure was similar to the α phase. The improvement of the coupling strength relative to α-CoPc could be explained by a reduction of the Co-Co distance, which could be brought about by an increase of the stacking angle or by a reduction of the spacing between the phthalocyanine rings. It is anticipated that the value of the exchange energy J might show variations along the chains, since the CoPc and F_{16}CoPc are likely to be randomly alternated.

The observation of spin coupling with exchange interactions J/k_B above the boiling point of liquid nitrogen in CoPc films was an unprecedented achievement for phthalocyanine materials. The ability to improve this result by a simple co-evaporation of two materials further demonstrated that phthalocyanine thin films represent viable options for applications in organic spintronics. The only other documented example of an undoped molecular material exhibiting both semiconducting behaviour and high temperature magnetism is the $V(TCNE)_x$ complex, which is a room temperature magnet [111]. Even if a direct comparison of the magnitude of the magnetic couplings is favourable to the vanadium material at the moment, metal phthalocyanines have a higher chemical stability and are more versatile, which broadens the scope of application and improvement of their properties.

This work gave some examples of how the physical properties of cobalt phthalocyanine based materials can be optimized for different applications. CoPc nanowires hold promise for application in high performance field effect transistors. CuPc nanowires FET devices have been previously been characterized in the group, highlighting that the threshold voltage can be lowered and the hole mobility improved by several orders of magnitude compared to the thin films, owing to the reduction of charge trapping at grain boundaries [32]. The characterization of CoPc nanowires FET is currently underway in our group and has shown improvements of the device performance similar to CuPc. The F_{16}CoPc films are also potentially interesting in FET applications as n-type semiconductor materials, similar to the successful F_{16}CuPc. The mixed CoPc:F_{16}CoPc films finally demonstrated that blending different phthalocyanines can be a successful strategy for increasing the strength of the antiferromagnetic coupling. A careful control of the mixing ratios could also lead to a parallel tuning of the charge transport properties.

Despite the advances made in this study, there are several areas that particularly deserve further investigation. A characterization of the α-CoPc and the CoPc:F_{16}CoPc mixed materials by neutron scattering should be considered, as it could provide more direct answers regarding the length of the spin chains, the origin of the paramagnetic contribution and the degree of variation of the exchange coupling energy throughout the materials.

The study of the CoPc:F_{16}CoPc mixed films is just at the beginning and their properties should be systematically studied, also as a function of the mixing ratio. A microstructural analysis of the films by TEM is needed to evaluate the degree of homogeneity of the films and complement the XRD characterization. An interesting aspect to consider is the evolution of the magnetic properties and structural parameters as the film composition is changed, which could lead to a better understanding of the magnetic interactions between the components and the way they mix. Finally, the effect of thermal annealing and high temperature

film growth should also be studied.

At the same time, mixtures of F_{16}CoPc with other transition metal phthtalocyanines should be also explored in a similar way. DFT calculations would be very useful to identify combinations of transition metal phthalocyanines that interact ferromagnetically in a mixed film. Preliminary work has already been done on mixed films containing either MnPc or FePc. In the former case, XPS showed the occurrence of charge transfer from Mn to Co, as reported by Lindner *et al.*[60]. However the film properties were found to be paramagnetic, although DFT calculations had suggested a ferromagnetic coupling within the material; the experiment should be repeated on a thicker sample, taking measures to protect the film from exposure to air. The FePe:F_{16}CoPc mixed films were found to be ferromagnetic, with a Curie temperature of approximately 20 K. The coercivity of the films at 2 K was significantly larger than that of pure α-CoPc films, therefore the two materials could be successful spin injectors and detectors in a spin valve. This concept is currently investigated in the group.

Bibliography

[1] **Alonso, M. I., Garriga, M., Osso, J. O., Schreiber, F., Barrena, E., and Dosch, H.** (**2003**). "Strong optical anisotropies of F_{16}CuPc thin films studied by spectroscopic ellipsometry." *The Journal of Chemical Physics*, 119(12): 6335–6340.

[2] **Annese, E., Fujii, J., Vobornik, I., Panaccione, G., and Rossi, G.** (**2011**). "Control of the magnetism of cobalt phthalocyanine by a ferromagnetic substrate." *Physical Review B*, 84(17).

[3] **Assour, J. M. and Kahn, W. K.** (**1965**). "Electron Spin Resonance of alpha and beta-Cobalt Phthalocyanine." *Journal of the American Chemical Society*, 87(2): 207–212.

[4] **Atherton, N. M.** (**1973**). *Electron spin resonance; theory and applications.* E. Horwood; Halsted Press, Chichester; New York.

[5] **Atodiresei, N., Brede, J., Lazicacute, P., Caciuc, V., Hoffmann, G., Wiesendanger, R., and Blugel, S.** (**2010**). "Design of the Local Spin Polarization at the Organic-Ferromagnetic Interface." *Physical Review Letters*, 105(6): 066 601.

[6] **Ballirano, P., Caminiti, R., Ercolani, C., Maras, A., and Orru, M. A.** (**1998**). "X-ray powder diffraction structure reinvestigation of the

alpha and beta forms of cobalt phthalocyanine and kinetics of the alpha to beta phase transition." *Journal of the American Chemical Society*, 120(49): 12 798–12 807.

[7] **Bao, Z., Lovinger, A. J., and Brown, J.** (**1998**). "New air-stable n-channel organic thin film transistors." *Journal of the American Chemical Society*, 120(1): 207–208.

[8] **Barraud, C., Seneor, P., Mattana, R., Fusil, S., Bouzehouane, K., Deranlot, C., Graziosi, P., Hueso, L., Bergenti, I., Dediu, V., Petroff, F., and Fert, A.** (**2010**). "Unravelling the role of the interface for spin injection into organic semiconductors." *Nat Phys*, 6(8): 615–620.

[9] **Bench, B. A., Beveridge, A., Sharman, W. M., Diebold, G. J., van Lier, J. E., and Gorun, S. M.** (**2002**). "Introduction of Bulky Perfluoroalkyl Groups at the Periphery of Zinc Perfluorophthalocyanine: Chemical, Structural, Electronic, and Preliminary Photophysical and Biological Effects." *Angewandte Chemie International Edition*, 41(5): 747–750.

[10] **Bench, B. A., Brennessel, W. W., Lee, H.-J., and Gorun, S. M.** (**2002**). "Synthesis and Structure of a Biconcave Cobalt Perfluorophthalocyanine and Its Catalysis of Novel Oxidative Carbon-Phosphorus Bonds Formation by Using Air." *Angewandte Chemie International Edition*, 41(5): 750–754.

[11] **Bencini, A. G. D.** (**1990**). *Electron paramagnetic resonance of exchange coupled systems*. Springer-Verlag, Berlin; New York.

[12] **Birchall, J. M., Haszeldine, R. N., and Morley, J. O.** (**1970**). "Polyfluoroarenes. Part XIV. Synthesis of halogenophthalocyanines." *Journal of the Chemical Society C: Organic*, (19): 2667–2672.

[13] **Blundell, S.** (**2001**). *Magnetism in condensed matter*. Oxford University Press, Oxford; New York.

[14] **Bogani, L. and Wernsdorfer, W.** (**2008**). "Molecular spintronics using single-molecule magnets." *Nat Mater*, 7(3): 179–186.

[15] **Bonner, J. C. and Fisher, M. E.** (**1964**). "Linear Magnetic Chains with Anisotropic Coupling." *Physical Review*, 135(3A): A640.

[16] **Brabec, C. J., Sariciftci, N. S., and Hummelen, J. C.** (**2001**). "Plastic Solar Cells." *Advanced Functional Materials*, 11(1): 15–26.

[17] **Brede, J., Atodiresei, N., Kuck, S., Lazicacute, P., Caciuc, V., Morikawa, Y., Hoffmann, G., Blugel, S., and Wiesendanger, R.** (**2010**). "Spin- and Energy-Dependent Tunneling through a Single Molecule with Intramolecular Spatial Resolution." *Physical Review Letters*, 105(4): 047 204.

[18] **Brinkmann, H., Kelting, C., Makarov, S., Tsaryova, O., Schnurpfeil, G., Wohrle, D., and Schlettwein, D.** (**2008**). "Fluorinated phthalocyanines as molecular semiconductor thin films." *Physica Status Solidi (a)*, 205(3): 409–420.

[19] **Brown, C. J.** (**1968**). "Crystal structure of beta-copper phthalocyanine." *Journal of the Chemical Society A: Inorganic, Physical, Theoretical*, pages 2488–2493.

[20] **Brustolon, M. and Giamello, G.** (**2009**). *Electron paramagnetic resonance : a practitioner's toolkit*. Wiley, Hoboken, N.J.

[21] **Burroughes, J. H., Bradley, D. D. C., Brown, A. R., Marks, R. N., Mackay, K., Friend, R. H., Burns, P. L., and Holmes, A. B.** (**1990**).

"Light-emitting diodes based on conjugated polymers." *Nature*, 347(6293): 539–541.

[22] **Chau, L. K., England, C. D., Chen, S., and Armstrong, N. R.** (**1993**). "Visible absorption and photocurrent spectra of epitaxially deposited phthalocyanine thin films: interpretation of exciton coupling effects." *The Journal of Physical Chemistry*, 97(11): 2699–2706.

[23] **Chen, X., Fu, Y.-S., Ji, S.-H., Zhang, T., Cheng, P., Ma, X.-C., Zou, X.-L., Duan, W.-H., Jia, J.-F., and Xue, Q.-K.** (**2008**). "Probing Superexchange Interaction in Molecular Magnets by Spin-Flip Spectroscopy and Microscopy." *Physical Review Letters*, 101(19): 197 208.

[24] **Clarke, J. and Braginski, A. I.** (**2006**). *The SQUID handbook. Vol. 2, Applications*. Wiley-VCH, Weinheim; Chichester.

[25] **Coulon, C., Miyasaka, H., and Clerac, R.** (**2006**). "Single-chain magnets: Theoretical approach and experimental systems." In R. Winpenny, editor, "Single-Molecule Magnets and Related Phenomena," volume 122 of *Structure and Bonding*, pages 163–206. Springer-Verlag Berlin, Berlin.

[26] **Cullity, B. D.** (**1956**). *Elements of X-ray diffraction*. Addison-Wesley Pub. Co., Reading, Mass.

[27] **De Fusco, G. C., Montanari, B., and Harrison, N. M.** (**2010**). "Half-metallicity in the ferrimagnet $Nb(TCNE)_2$ from first principles." *Physical Review B*, 82(22): 220 404.

[28] **De Fusco, G. C., Pisani, L., Montanari, B., and Harrison, N. M.** (**2009**). "Density functional study of the magnetic coupling in $V(TCNE)_2$." *Physical Review B*, 79(8): 085 201.

[29] **de Oteyza, D. G., Barrena, E., Osso, J. O., Sellner, S., and Dosch, H.** (**2006**). "Thickness-Dependent Structural Transitions in Fluorinated Copper-phthalocyanine (F16CuPc) Films." *Journal of the American Chemical Society*, 128(47): 15 052–15 053.

[30] **Dediu, V., Murgia, M., Matacotta, F. C., Taliani, C., and Barbanera, S.** (**2002**). "Room temperature spin polarized injection in organic semiconductor." *Solid State Communications*, 122(3-4): 181–184.

[31] **Dediu, V. A., Hueso, L. E., Bergenti, I., and Taliani, C.** (**2009**). "Spin routes in organic semiconductors." *Nat Mater*, 8(9): 707–716.

[32] **Din, S.** (**2011**). *Copper Phthalocyanine (CuPc) Thin Films and Nanostructures - Growth and Device Applications*. Ph.D. thesis, Imperial College London.

[33] **Drew, A. J., Hoppler, J., Schulz, L., Pratt, F. L., Desai, P., Shakya, P., Kreouzis, T., Gillin, W. P., Suter, A., Morley, N. A., Malik, V. K., Dubroka, A., Kim, K. W., Bouyanfif, H., Bourqui, F., Bernhard, C., Scheuermann, R., Nieuwenhuys, G. J., Prokscha, T., and Morenzoni, E.** (**2009**). "Direct measurement of the electronic spin diffusion length in a fully functional organic spin valve by low-energy muon spin rotation." *Nat Mater*, 8(2): 109–114.

[34] **Evangelisti, M., Bartolome, J., de Jongh, L. J., and Filoti, G.** (**2002**). "Magnetic properties of alpha-iron(II) phthalocyanine." *Physical Review B*, 66(14): 144 410.

[35] **Faulkner, E. B. and Schwartz, R. J.** (**2009**). *High performance pigments*. Wiley-VCH, Weinheim.

[36] **Fert, A.** (**2008**). "Nobel Lecture: Origin, development, and future of spintronics." *Reviews of Modern Physics*, 80(4): 1517.

[37] **Fried, J.** (**2003**). *Polymer science and technology*. Pearson Education.

[38] **Friedrich, R., Hahn, T., Kortus, J., Fronk, M., Haidu, F., Salvan, G., Zahn, D. R. T., Schlesinger, M., Mehring, M., Roth, F., Mahns, B., and Knupfer, M.** (**2012**). "Electronic states and the influence of oxygen addition on the optical absorption behaviour of manganese phthalocyanine." *The Journal of Chemical Physics*, 136(6): 064 704–8.

[39] **Fu, Y.-S., Zhang, T., Ji, S.-H., Chen, X., Ma, X.-C., Jia, J.-F., and Xue, Q.-K.** (**2009**). "Identifying Charge States of Molecules with Spin-Flip Spectroscopy." *Physical Review Letters*, 103(25): 257 202.

[40] **Griffiths, R. B.** (**1964**). "Magnetization Curve at Zero Temperature for the Antiferromagnetic Heisenberg Linear Chain." *Physical Review*, 133(3A): A768–A775.

[41] **Heutz, S., Cloots, R., and Jones, T. S.** (**2000**). "Structural templating effects in molecular heterostructures grown by organic molecular-beam deposition." *Applied Physics Letters*, 77(24): 3938–3940.

[42] **Hipps, K. W., Lu, X., Wang, X. D., and Mazur, U.** (**1996**). "Metal d-Orbital Occupation-Dependent Images in the Scanning Tunneling Microscopy of Metal Phthalocyanines." *The Journal of Physical Chemistry*, 100(27): 11 207–11 210.

[43] **Hoshino, A., Takenaka, Y., and Miyaji, H.** (**2003**). "Redetermination of the crystal structure of alpha-copper phthalocyanine grown on KCl." *Acta Crystallographica Section B*, 59(3): 393–403.

[44] **Hu, B., Yan, L., and Shao, M.** (**2009**). "Magnetic-Field Effects in Organic Semiconducting Materials and Devices." *Advanced Materials*, 21(14-15): 1500–1516.

[45] **Iacovita, C., Rastei, M. V., Heinrich, B. W., Brumme, T., Kortus, J., Limot, L., and Bucher, J. P.** (**2008**). "Visualizing the Spin of Individual Cobalt-Phthalocyanine Molecules." *Physical Review Letters*, 101(11): 116 602.

[46] **Iwatsu, F.** (**1988**). "Size effects on the alpha-beta transformation of phthalocyanine crystals." *The Journal of Physical Chemistry*, 92(6): 1678–1681.

[47] **Jasinski, R.** (**1965**). "Cobalt phthalocyanine as a fuel cell cathode." *Journal of The Electrochemical Society*, 112(5): 526–528.

[48] **Johnston, D. C., Kremer, R. K., Troyer, M., Wang, X., Klumper, A., Bud'ko, S. L., Panchula, A. F., and Canfield, P. C.** (**2000**). "Thermodynamics of spin S=1/2 antiferromagnetic uniform and alternating-exchange Heisenberg chains." *Physical Review B*, 61(14): 9558.

[49] **Jurchescu, O. D., Baas, J., and Palstra, T. T. M.** (**2004**). "Effect of impurities on the mobility of single crystal pentacene." *Applied Physics Letters*, 84(16): 3061–3063.

[50] **Kasha, M., Rawls, H., and El-Bayoumi, M. A.** (**1965**). "The exciton model in molecular spectroscopy." *Pure Appl. Chem*, 11(3-4): 371–392.

[51] **Kilinc, E., Erdem, A., Gokgunnec, L., Dalbasti, T., Karaoglan, M., and Ozsoz, M.** (**1998**). "Buttermilk Based Cobalt Phthalocyanine Dispersed Ferricyanide Mediated Amperometric Biosensor for the Determination of Xanthine." *Electroanalysis*, 10(4): 273–275.

[52] **Krinichnyi, V. I.** (**2000**). "2-mm Waveband electron paramagnetic resonance spectroscopy of conducting polymers." *Synthetic Metals*, 108(3): 173–222.

[53] **Kroll, T., Aristov, V. Y., Molodtsova, O. V., Ossipyan, Y. A., Vyalikh, D. V., Buchner, B., and Knupfer, M.** (**2009**). "Spin and Orbital Ground State of Co in Cobalt Phthalocyanine." *The Journal of Physical Chemistry A*, 113(31): 8917–8922.

[54] **Kroll, T., Kraus, R., Schonfelder, R., Aristov, V. Y., Molodtsova, O. V., Hoffmann, P., and Knupfer, M.** (**2012**). "Transition metal phthalocyanines: Insight into the electronic structure from soft x-ray spectroscopy." *The Journal of Chemical Physics*, 137(5): 054 306–7.

[55] **Lach, S., Altenhof, A., Tarafder, K., Schmitt, F., Ali, M. E., Vogel, M., Sauther, J., Oppeneer, P. M., and Ziegler, C.** (**2012**). "Metal-Organic Hybrid Interface States of A Ferromagnet/Organic Semiconductor Hybrid Junction as Basis For Engineering Spin Injection in Organic Spintronics." *Advanced Functional Materials*, 22(5): 989–997.

[56] **Lawton, E. A.** (**1958**). "The Thermal Stability of Copper Phthalocyanine." *The Journal of Physical Chemistry*, 62(3): 384–384.

[57] **Lever, A. B. P.** (**1986**). *Inorganic electronic spectroscopy*. Elsevier, Amsterdam.

[58] **Lewis, G. N.** (**1924**). "THE MAGNETISM OF OXYGEN AND THE MOLECULE O4." *Journal of the American Chemical Society*, 46(9): 2027–2032.

[59] **Li, B., Kao, C.-Y., Yoo, J.-W., Prigodin, V. N., and Epstein, A. J.**

(**2011**). "Magnetoresistance in an All-Organic-Based Spin Valve." *Advanced Materials*, 23(30): 3382–3386.

[60] **Lindner, S., Mahns, B., Konig, A., Roth, F., Knupfer, M., Friedrich, R., Hahn, T., and Kortus, J.** (**2013**). "Phthalocyanine dimers in a blend: Spectroscopic and theoretical studies of $MnPc^{\delta+}/F_{16}CoPc^{\delta-}$." *The Journal of Chemical Physics*, 138(2): 024 707–4.

[61] **Loas, A., Gerdes, R., Zhang, Y., and Gorun, S. M.** (**2011**). "Broadening the reactivity spectrum of a phthalocyanine catalyst while suppressing its nucleophilic, electrophilic and radical degradation pathways." *Dalton Transactions*, 40(19): 5162–5165.

[62] **Lozzi, L. and Santucci, S.** (**2003**). "XPS study of the $F_{16}CuPc/SiO_2$ interface." *Surface Science*, 532-535(0): 976–981.

[63] **Lucia, E. A. and Verderame, F. D.** (**1968**). "Spectra of Polycrystalline Phthalocyanines in the Visible Region." *The Journal of Chemical Physics*, 48(6): 2674–2681.

[64] **Manriquez, J. M., Yee, G. T., McLean, R. S., Epstein, A. J., and Miller, J. S.** (**1991**). "A Room-Temperature Molecular/Organic-Based Magnet." *Science*, 252(5011): 1415–1417.

[65] **Maslyuk, V., Aristov, V., Molodtsova, O., Vyalikh, D., Zhilin, V., Ossipyan, Y., Bredow, T., Mertig, I., and Knupfer, M.** (**2009**). "The electronic structure of cobalt phthalocyanine." *Applied Physics A: Materials Science and Processing*, 94(3): 485–489.

[66] **Mauthoor, S.** (**2010**). *Structural analysis of molecular nanostructures and thin films*. Ph.D. thesis, Imperial College London.

[67] **Mayer, T., Weiler, U., Kelting, C., Schlettwein, D., Makarov, S., Wohrle, D., Abdallah, O., Kunst, M., and Jaegermann, W.** (**2007**). "Silicon-organic pigment material hybrids for photovoltaic application." *Solar Energy Materials and Solar Cells*, 91(20): 1873–1886.

[68] **McKeown, N. B.** (**1998**). *Phthalocyanine materials: synthesis, structure, and function*. Cambridge University Press, Cambridge, U.K.; New York.

[69] **Miller, J. S.** (**2002**). "Organic Magnets – A History." *Advanced Materials*, 14(16): 1105–1110.

[70] **Miller, J. S. and Epstein, A. J.** (**1994**). "Organic and Organometallic Molecular Magnetic Materials – Designer Magnets." *Angewandte Chemie International Edition in English*, 33(4): 385–415.

[71] **Miyoshi, H., Ohyanish.H, and Deguchi, Y.** (**1973**). "Magnetic properties of Manganese(II) phthalocyanine." *Bulletin of the Chemical Society of Japan*, 46(9): 2724–2728.

[72] **Mydosh, J. A.** (**1993**). *Spin glasses : an experimental introduction*. Taylor & Francis, London; Washington, DC.

[73] **Naber, W. J. M. and et al.** (**2007**). "Organic spintronics." *Journal of Physics D: Applied Physics*, 40(12): R205.

[74] **Niwa, Y., Kobayashi, H., and Tsuchiya, T.** (**1974**). "X-ray photoelectron spectroscopy of tetraphenylporphin and phthalocyanine." *The Journal of Chemical Physics*, 60(3): 799–807.

[75] **Oda, K., Ogura, S.-i., and Okura, I.** (**2000**). "Preparation of a water-soluble fluorinated zinc phthalocyanine and its effect for photodynamic therapy." *Journal of Photochemistry and Photobiology B: Biology*, 59(1â€“3): 20–25.

[76] **Ottaviano, L., Lozzi, L., Ramondo, F., Picozzi, P., and Santucci, S.** (**1999**). "Copper hexadecafluoro phthalocyanine and naphthalocyanine: The role of shake up excitations in the interpretation and electronic distinction of high-resolution X-ray photoelectron spectroscopy measurements." *Journal of Electron Spectroscopy and Related Phenomena*, 105(2-3): 145–154.

[77] **Pandey, P. A., Rochford, L. A., Keeble, D. S., Rourke, J. P., Jones, T. S., Beanland, R., and Wilson, N. R.** (**2012**). "Resolving the Nanoscale Morphology and Crystallographic Structure of Molecular Thin Films: F_{16}CuPc on Graphene Oxide." *Chemistry of Materials*, 24(7): 1365–1370.

[78] **Podzorov, V., Menard, E., Borissov, A., Kiryukhin, V., Rogers, J. A., and Gershenson, M. E.** (**2004**). "Intrinsic Charge Transport on the Surface of Organic Semiconductors." *Physical Review Letters*, 93(8): 086 602.

[79] **Pope, M. and Swenberg, C. E.** (**1999**). *Electronic processes in organic crystals and polymers*. Oxford University Press, New York.

[80] **Pramanik, S., Stefanita, C. G., Patibandla, S., Bandyopadhyay, S., Garre, K., Harth, N., and Cahay, M.** (**2007**). "Observation of extremely long spin relaxation times in an organic nanowire spin valve." *Nat Nano*, 2(4): 216–219.

[81] **Qi, X. and Baldwin, R. P.** (**1996**). "Selective oxidation of thiols to disulfides at polymeric cobalt phthalocyanine chemically modified electrodes." *Journal of The Electrochemical Society*, 143(4): 1283–1287.

[82] **Reichenbacher, K., Suss, H. I., and Hulliger, J.** (**2005**). "Fluorine in crystal engineering–"the little atom that could"." *Chemical Society Reviews*, 34(1): 22–30.

[83] **Rocha, A. R., Garcia-suarez, V. M., Bailey, S. W., Lambert, C. J., Ferrer, J., and Sanvito, S.** (**2005**). "Towards molecular spintronics." *Nature Materials*, 4(4): 335–339.

[84] **Sanvito, S.** (**2007**). "Injecting and controlling spins in organic materials." *Journal of Materials Chemistry*, 17(42): 4455–4459.

[85] **Schlettwein, D., Hesse, K., Tada, H., Mashiko, S., Storm, U., and Binder, J.** (**2000**). "Ordered Growth of Substituted Phthalocyanine Thin Films: Hexadecafluorophthalocyaninatozinc on Alkali Halide (100) and Microstructured Si Surfaces." *Chemistry of Materials*, 12(4): 989–995.

[86] **Schuster, B.-E., Basova, T. V., Plyashkevich, V. A., Peisert, H., and Chasse, T.** (**2010**). "Effects of temperature on structural and morphological features of CoPc and $CoPcF_{16}$ thin films." *Thin Solid Films*, 518(23): 7161–7166.

[87] **Schutten, J. and Zwart, J.** (**1979**). "Autoxidation of mercaptans promoted by a bifunctional catalyst prepared by polymer attachment of cobaltphthalocyanine." *Journal of Molecular Catalysis*, 5(2): 109–123.

[88] **Sharma, V. B., Jain, S. L., and Sain, B.** (**2003**). "Cobalt phthalocyanine catalyzed aerobic oxidation of secondary alcohols: an efficient and simple synthesis of ketones." *Tetrahedron letters*, 44(2): 383–386.

[89] **Sun, D., Yin, L., Sun, C., Guo, H., Gai, Z., Zhang, X. G., Ward, T. Z., Cheng, Z., and Shen, J.** (**2010**). "Giant Magnetoresistance in Organic Spin Valves." *Physical Review Letters*, 104(23): 236 602.

[90] **Tang, C. W. and Vanslyke, S. A.** (**1987**). "Organic electroluminescent diodes." *Applied Physics Letters*, 51(12): 913–915.

[91] **Tang, M. L., Reichardt, A. D., Miyaki, N., Stoltenberg, R. M., and Bao, Z.** (**2008**). "Ambipolar, high performance, acene-based organic thin film transistors." *Journal of the American Chemical Society*, 130(19): 6064–6065.

[92] **Tsumura, A., Koezuka, H., and Ando, T.** (**1986**). "Macromolecular electronic device: Field-effect transistor with a polythiophene thin film." *Applied Physics Letters*, 49(18): 1210–1212.

[93] **Wagner, C. D., Davis, L. E., Zeller, M. V., Taylor, J. A., Raymond, R. H., and Gale, L. H.** (**1981**). "Empirical atomic sensitivity factors for quantitative analysis by electron spectroscopy for chemical analysis." *Surface and Interface Analysis*, 3(5): 211–225.

[94] **Wang, F. J., Xiong, Z. H., Wu, D., Shi, J., and Vardeny, Z. V.** (**2005**). "Organic spintronics: The case of Fe/Alq_3/Co spin-valve devices." *Synthetic Metals*, 155(1): 172–175.

[95] **Wang, H., Mauthoor, S., Din, S., Gardener, J. A., Chang, R., Warner, M., Aeppli, G., McComb, D. W., Ryan, M. P., Wu, W., Fisher, A. J., Stoneham, M., and Heutz, S.** (**2010**). "Ultralong Copper Phthalocyanine Nanowires with New Crystal Structure and Broad Optical Absorption." *ACS Nano*, 4(7): 3921–3926.

[96] **Wang, H., Zhu, F., Yang, J., Geng, Y., and Yan, D.** (**2007**). "Weak Epitaxy Growth Affording High-Mobility Thin Films of Disk-Like Organic Semiconductors." *Advanced Materials*, 19(16): 2168–2171.

[97] **Wang, Y., Herron, N., Grushin, V. V., LeCloux, D., and Petrov, V.** (**2001**). "Highly efficient electroluminescent materials based on fluorinated organometallic iridium compounds." *Applied Physics Letters*, 79(4): 449–451.

[98] **Wesley Owens, J., Perry, M., and Seybert, D. W.** (**1998**). "Adducts of nitric oxide with cobaltous tetraphenylporphyrin and phthalocyanines: potential nitric oxide sorbents." *Inorganica Chimica Acta*, 277(1): 1–7.

[99] **Wohrle, D. and Meissner, D.** (**1991**). "Organic solar-cells." *Advanced Materials*, 3(3): 129–138.

[100] **Wring, S. A., Hart, J. P., and Birch, B. J.** (**1989**). "Development of an improved carbon electrode chemically modified with cobalt phthalocyanine as a re-usable sensor for glutathione." *Analyst*, 114(12): 1563–1570.

[101] **Wu, W., Harrison, N., and Fisher, A.** (**2013**). "Electronic structure and exchange interactions in cobalt-phthalocyanine chains." *Physical Review B*, 88(2): 024 426.

[102] **Wu, W., Kerridge, A., Harker, A. H., and Fisher, A. J.** (**2008**). "Structure-dependent exchange in the organic magnets Cu(II)Pc and Mn(II)Pc." *Physical Review B*, 77(18): 184 403.

[103] **Wu, W., Rochford, L. A., Felton, S., Wu, Z., Yang, J. L., Heutz, S., Aeppli, G., Jones, T. S., Harrison, N. M., and Fisher, A. J.** (**2013**). "Magnetic properties of copper hexadecaphthalocyanine (F_{16}CuPc) thin films and powders." *Journal of Applied Physics*, 113(1): 013 914–8.

[104] **Wu, Z.** (**2012**). *Magnetic Properties of Transition Metal Phthalocyanine Molecular Thin Films and Nanostructures*. Ph.D. thesis, Imperial College London.

[105] **Xiong, Z. H., Wu, D., Valy Vardeny, Z., and Shi, J.** (**2004**). "Giant magnetoresistance in organic spin-valves." *Nature*, 427(6977): 821–824.

[106] **Yamada, H., Shimada, T., and Koma, A.** (**1998**). "Preparation and

magnetic properties of manganese(II) phthalocyanine thin films." *The Journal of Chemical Physics*, 108(24): 10 256–10 261.

[107] **Yang, J. L., Schumann, S., and Jones, T. S.** (**2009**). "Morphology and Structure Transitions of Copper Hexadecafluorophthalocyanine (F_{16}CuPc) Thin Films." *The Journal of Physical Chemistry C*, 114(2): 1057–1063.

[108] **Yang, J. L., Schumann, S., and Jones, T. S.** (**2011**). "Nanowire-array films of copper hexadecafluorophthalocyanine (F_{16}CuPc) fabricated by templated growth." *Journal of Materials Chemistry*, 21(15): 5812–5816.

[109] **Yang, J. L., Schumann, S., and Jones, T. S.** (**2011**). "Tuning the morphology and molecular orientation of copper hexadecafluorophthalocyanine thin films by solvent annealing." *Thin Solid Films*, 519(11): 3709–3715.

[110] **Yang, R. D., Gredig, T., Colesniuc, C. N., Park, J., Schuller, I. K., Trogler, W. C., and Kummel, A. C.** (**2007**). "Ultrathin organic transistors for chemical sensing." *Applied Physics Letters*, 90(26): 263 506.

[111] **Yoo, J.-W., Chen, C.-Y., Jang, H. W., Bark, C. W., Prigodin, V. N., Eom, C. B., and Epstein, A. J.** (**2010**). "Spin injection/detection using an organic-based magnetic semiconductor." *Nat Mater*, 9(8): 638–642.

[112] **Yoon, S. M., Song, H. J., Hwang, I.-C., Kim, K. S., and Choi, H. C.** (**2010**). "Single crystal structure of copper hexadecafluorophthalocyanine (F_{16}CuPc) ribbon." *Chemical Communications*, 46(2): 231–233.

[113] **Zhao, A., Li, Q., Chen, L., Xiang, H., Wang, W., Pan, S., Wang, B., Xiao, X., Yang, J., Hou, J. G., and Zhu, Q.** (**2005**). "Controlling the Kondo Effect of an Adsorbed Magnetic Ion Through Its Chemical Bonding." *Science*, 309(5740): 1542–1544.

[114] **Zutic, I., Fabian, J., and Das Sarma, S.** (**2004**). "Spintronics: Fundamentals and applications." *Reviews of Modern Physics*, 76(2): 323.

Appendix A

CoPc powders and films

A.1 Main ICP-AES lines of atomic emission spectra of Co and potential contaminants

Mn		Fe		Co	
λ (nm)	I (arb. u.)	λ (nm)	Intensity (arb. u.)	λ (nm)	I (arb. u.)
257.610	1×10^7 (II)	259.940	2×10^6 (II)	228.616	1×10^6 (II)
259.373	9×10^6 (II)	238.204	1.8×10^6 (II)	238.892	1×10^6 (II)
260.569	7×10^6 (II)	239.562	9×10^5 (II)	237.862	7×10^5 (II)
279.482	1.8×10^6 (I)	240.488	6×10^5 (II)	230.786	6×10^5 (II)
294.920	1.5×10^6 (II)	259.837	6×10^6 (II)	231.160	5×10^5 (II)
293.930	1.2×10^6 (II)	261.187	6×10^6 (II)	235.342	1.5×10^5 (II)
403.076	4×10^5 (I)	234.349	5×10^6 (II)	195.742	1.8×10^4 (II)
403.307	3×10^5 (I)	371.994	1.8×10^6 (I)		
191.510	6×10^4 (II)	233.280	1.5×10^6 (II)		
384.291	4.5×10^4 (II)	274.932	1×10^6 (II)		

Table A.1: Atomic emission lines for Mn, Fe, Co. For each element, the emission wavelength λ, the intensity and the oxidation state of the ion (in parentheses) are given

Cu		Ni	
λ (nm)	I (arb. u.)	λ (nm)	I (arb. u.)
324.754	5×10^6 (I)	221.647	6×10^5 (II)
327.396	3×10^6 (I)	231.604	6×10^5 (II)
224.700	1×10^6 (II)	341.476	3×10^5 (I)
219.958	5×10^5 (I)	216.556	2.5×10^5 (II)
221.810	4×10^5 (II)	232.003	2.5×10^5 (I)
217.894	3×10^5 (I)	352.454	2.5×10^5 (I)
213.598	2×10^5 (II)	361.939	2×10^5 (I)
204.379	9×10^4 (II)	230.300	1.5×10^5 (II)
214.897	4×10^4 (II)	243.789	5×10^4 (II)
211.209	3×10^4 (II)		

Table A.2: Atomic emission lines for Cu and Ni. For each element, the emission wavelength λ, the intensity and the oxidation state of the ion (in parentheses) are given

A.2 Finite chain fits of the magnetic properties of α-CoPc

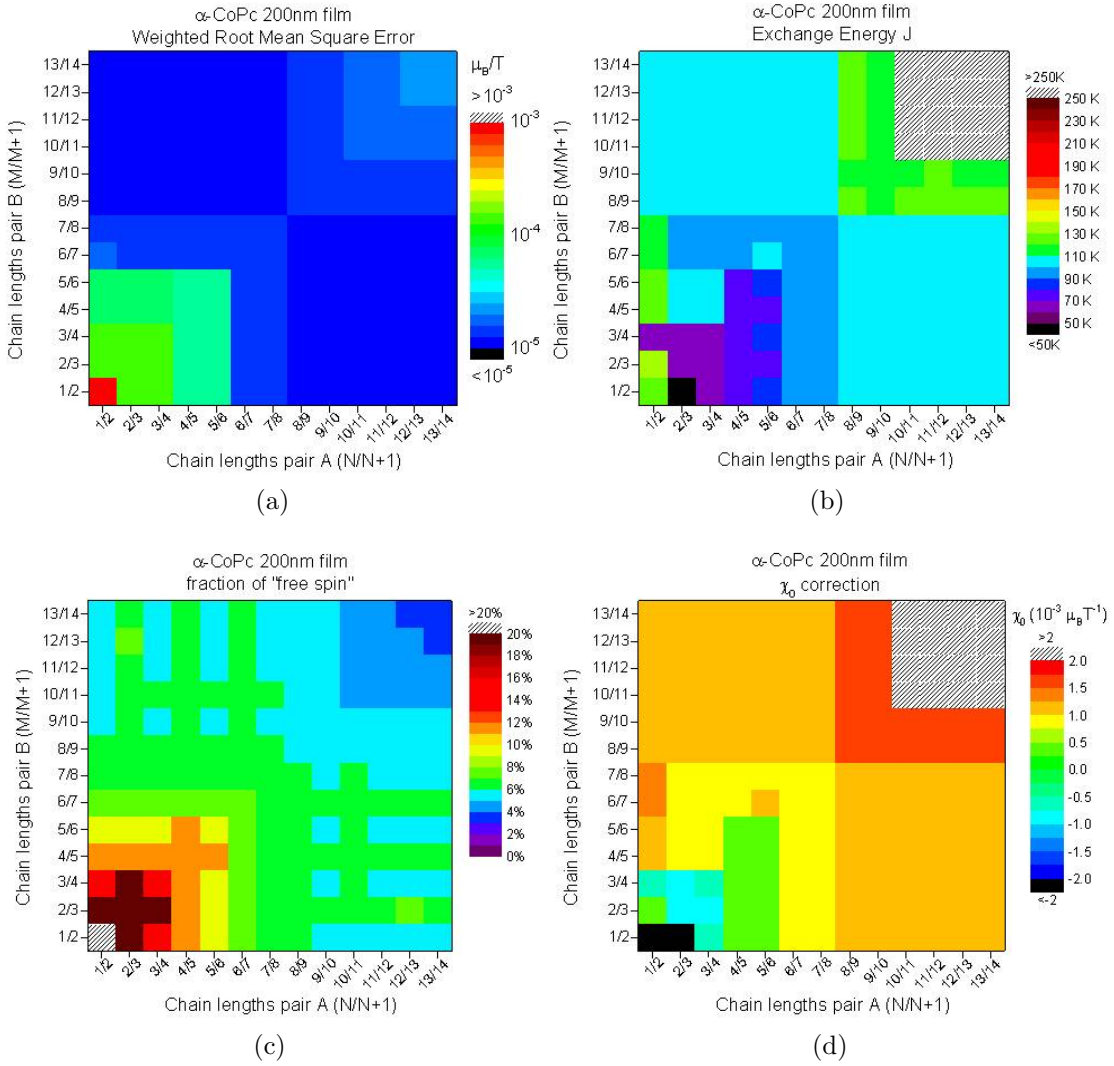


Figure A.1: Results of the fit of the magnetic susceptibility of α-CoPc 200 nm film on kapton using the finite chain model (Equation 3.5). Residuals and values of the fitted parameters are shown in the color map for all combinations of chain lengths. (a) Weighted root mean square error of the fit; (b) values of the exchange energy J/k_B; (c) values of the temperature independent correction χ_0; (d) fraction f of paramagnetic spins

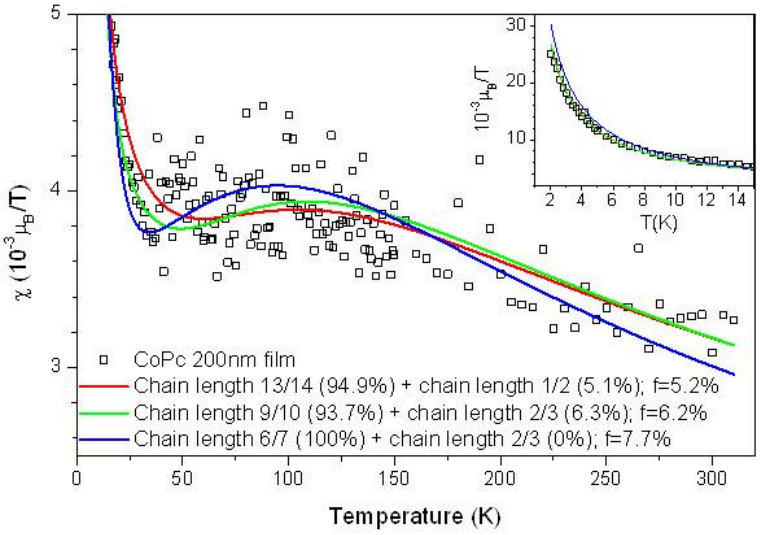


Figure A.2: Characteristic fits of the susceptibility of α-CoPc 200 nm film on kapton

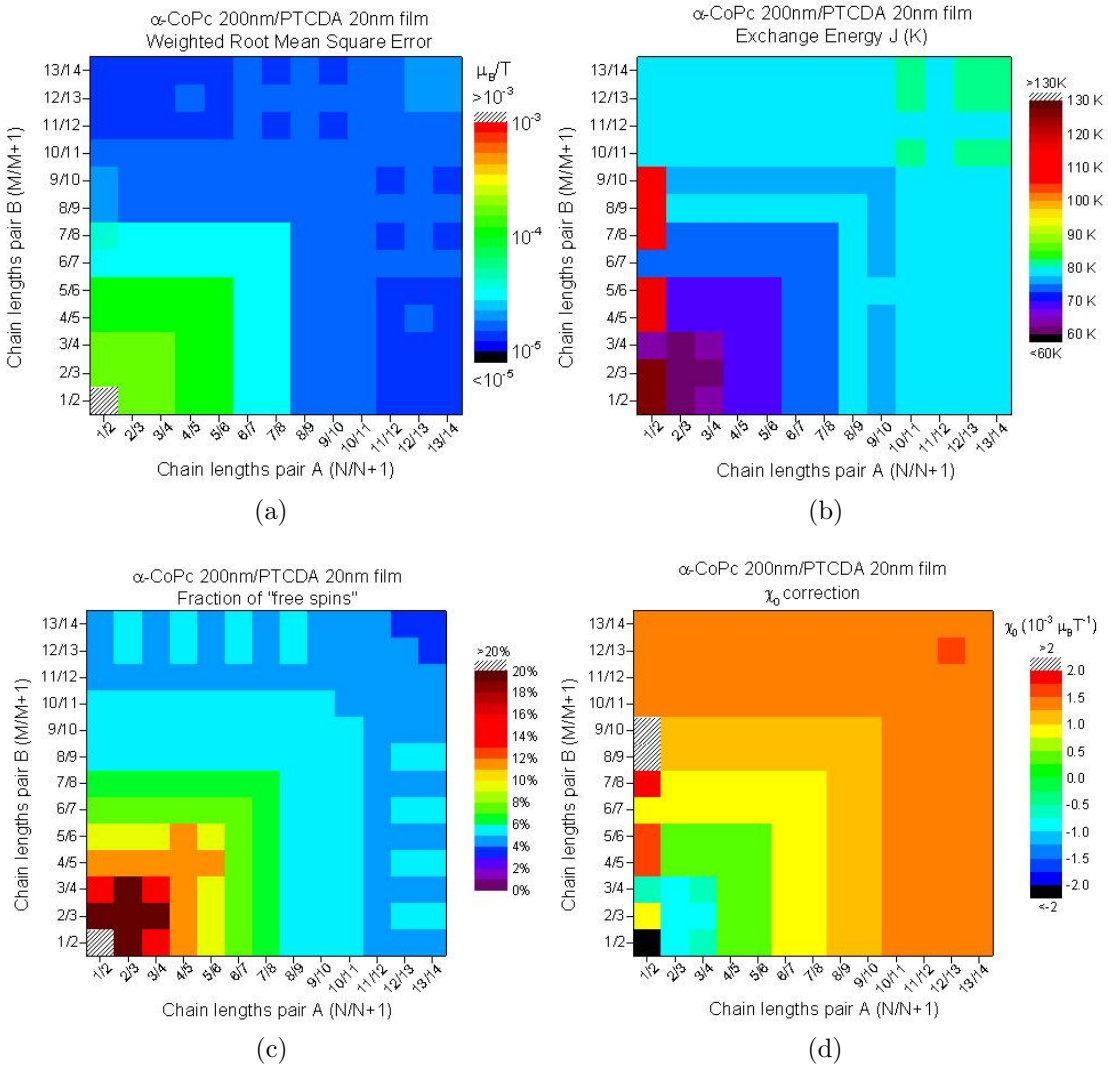


Figure A.3: Results of the fit of the susceptibility of the α-CoPc templated film (200 nm on 20 nm PTCDA) on kapton using the finite chain model (Equation 3.5). Residuals and values of the fitted parameters are shown in the color map for all combinations of chain lengths. (a) Weighted root mean square error of the fit; (b) values of the exchange energy J/k_B; (c) values of the temperature independent correction χ_0; (d) fraction f of paramagnetic spins

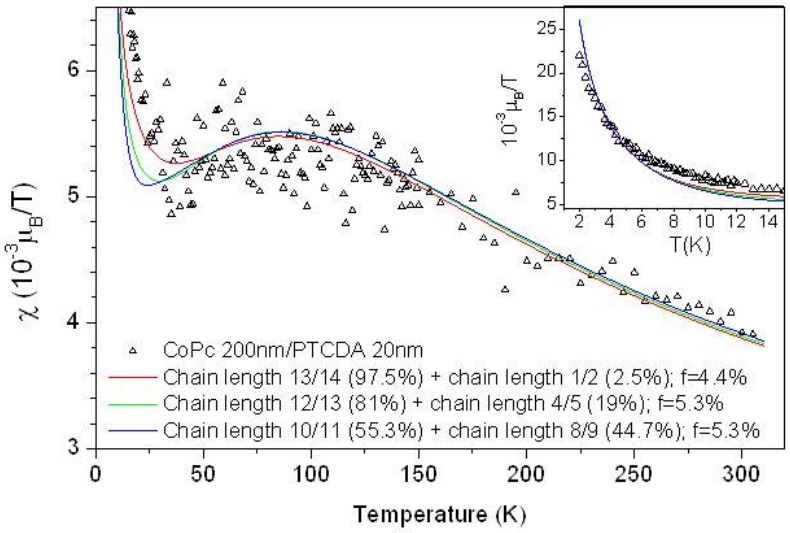


Figure A.4: Characteristic fits of the susceptibility of α-CoPc 200 nm templated film on kapton